Department of Chemical Engineering

Multiphase Transient Flow in Pipes

Hisham Kh Ben Mahmud

This thesis is presented for the Degree of
Doctor of Philosophy
of
Curtin University

February 2012

Declaration

To the best of my knowledge and belief this thesis contains no material previously published by any other person except where due acknowledgment has been made.

This thesis contains no material which has been accepted for the award of any other degree or diploma in any university.

Signature: …….

Date: ……...

List of publications

This research has led to the following International conferences:

1- Ben Mahmud, H. Kh., R. Utikar, M. O. Tadé and V. K. Pareek; CFD modeling of pressure drop and liquid holdup of gas-liquid two-phase flow in horizontal pipes, paper presented at 4th International Conference on Modeling, Simulation, and Applied Optimization, April 19-21,2011, Kuala Lumpur, Malaysia.

2- Ben Mahmud, H. Kh., R. Utikar, M. O. Tadé and V. K. Pareek; CFD simulation of gas-water in horizontal pipes, paper presented at 5th International Symposium on Design, Operation and Control of Chemical Processes, July 25-28, 2010, Singapore, Singapore.

Abstract

The development of oil and gas fields in offshore deep waters (more than 1000 m) will become more common in the future. Inevitably, production systems will operate under multiphase flow conditions. The two–phase flow of gas–liquid in pipes with different inclinations has been studied intensively for many years. The reliable prediction of flow pattern, pressure drop, and liquid holdup in a two–phase flow is thereby important.

With the increase of computer power and development of modelling software, the investigation of two–phase flows of gas–liquid problems using computational fluid dynamics (CFD) approaches is gradually becoming attractive in the various engineering disciplines. The use of CFD as a modelling tool in multiphase flow simulation has enormously increased in the last decades and is the focus of this thesis. Two basic CFD techniques are utilized to simulate the gas–liquid flow, the Volume of Fluid (VOF) model, and the Eulerian–Eulerian (E–E) model. The purpose of this thesis is to investigate the risk of hydrate formation in a low–spot flowline by assessing the flow pattern and droplet hydrodynamics in gas–dominated restarts using the VOF method, and also to develop and validate a model for gas–liquid two–phase flow in horizontal pipelines using the Eulerian–Eulerian method; the purpose of this is to predict the pressure drop and liquid holdup encountered during two–phase (i.e. gas–oil, gas–water) production at different flow conditions, such as fluid properties, volume fractions of liquid, superficial velocities, and mass fluxes.

In the first part of this thesis, the VOF approach was used to simulate the droplet formation and flow pattern at various levels of liquid patched and restart gas superficial velocities. The effect of restart gas superficial velocity on the liquid displacement from the low section of the pipe showed a decrease in the remaining liquid with an increase in gas superficial velocity, and the amount of liquid depends on the fluid properties, such as density and viscosity. Moreover, the flow pattern is also strongly dependent on the restart gas superficial velocity as well as the patched liquid in the low section. A low gas superficial velocity with different

patched liquids illustrated no risk of hydrate formation due to the observed flow pattern that is often a stratified flow. However, as the restart gas superficial velocity is increased, regardless of initial liquid patching, hydrate formation is more likely to be observed due to the observed flow pattern, such as annular, churn or dispersed flow.

In the second part, the E–E model was employed to establish a computational model to predict the pressure drop and liquid holdup in a horizontal pipeline. Due to the complicated process phenomena of two–phase flow, a new drag coefficient was implemented to model the pressure drop and liquid holdup in the 3D pipe. Different simulations were performed with various superficial velocities of two–phase and liquid volume fractions, and were carried out using RNG k-ε model to account for turbulence. Based on the results from the numerical model and previous experimental study, the currently used E–E model is improved to get more accurate prediction for the pressure drop and liquid holdup in horizontal pipes compared with the existing models of Hart *et al*. (1989) and Chen *et al*. (1997). The improved model is validated by previously reported experimental data (Badie *et al*., 2000). The deviation of pressure drop and liquid holdup obtained throughout the CFD simulation with regard to the experimental data was found to be relatively small at low superficial gas velocities. It was observed that the pressure gradient increased with the system parameters, such as the drop size, liquid and gas superficial velocity and the liquid volume fraction, where the liquid holdup decreased.

The developed model provided a basis for studying the pressure drop and liquid holdup in a horizontal pipe. Different parameters have been examined, such as gas and liquid mass flux and liquid volume fraction. Two empirical correlations have been examined (Beggs and Brill (1973), and Mukherjee and Brill (1985)) against the CFD simulation results of pressure drop and liquid holdup, it was noted that they gave better agreement with the air–oil system rather than the air–water system, but shows reasonable agreement over the entire gas mass flux.

In the third part, the coupling of Eulerian–Eulerian multiphase model with the population balance equation (PBE), accounting for droplet coalescence and

breakage, is considered. Strengths and weaknesses of each numerical approach for solving PBE have been given in details. The Quadrature Method of Moments (QMOM) is used and particular coalescence and breakup kernels were utilized to demonstrate the droplet size distribution behaviour. Numerical simulations on a two–phase flow in a horizontal pipe, including coalescence and breakage are performed. The QMOM is shown to give the solution of the PBE with reasonable agreement. The numerical data are compared with the experiment data of Simmons and Henratty (2001). The flow variables, such as liquid volume fractions, gas and liquid superficial velocities are employed to examine the droplet size distribution and the potential of the multiphase k–ε with population balance model for predicting the two–phase pressure drop and liquid holdup.

The significance of this work is to assist in understanding the risk of hydrate formation in bend pipes at gas–dominated restarts with different patched liquid values. The knowledge gained from this work can be utilized to avoid the hydrate formation operating conditions. The developed of multiphase flow E–E model will provide an accurate prediction for two–phase pressure drop and liquid holdup in a horizontal pipe which will be of benefit to the design of tubing and surface facilities.

ACKNOWLEDGEMENTS

I am most grateful to my supervisor Professor Moses Tadé for his excellent support and guidance throughout my PhD. I have been very fortunate to work under his supervision, and I thank him sincerely for his advice, encouragement, patience, the granted freedom and continued support in all phases of the work.

I would like to thank Professor Vishnu Pareek, for suggesting the project which is interesting and challenging topic and also for his continuous help with the software used in this work. I would also like to thank Dr Ranjeet Utikar for his effective help with CFD software issues and for providing valuable modelling advice.

I would also like to express my appreciation to the Libyan Higher Education, for the significant contribution in funding this work. I would also like to thank the Department of Chemical Engineering, Curtin University, for access to the office, computer facilities and to the cluster. I also thank all my friends (Adnan Ben Hukuma, Aziz Zankuli, Hisham Zereba, Abdullah Ashtewi, Tarek Murgham, Nabil Attarhouni, Mahamed Ben Swead, Esam & Ryiad Ben Mahmud, Osam Agetlawi & Al-Osta, and Khaled Alwefati) for all the free antistress therapy that I have received from them. A special thanks to Dr Mohamed Khalifa, Dr Walid Ben Mahmud, Dr Ebenezer Sholarin and Dr Sabri Mrayed.

Last but not least, I am most grateful to my Father (Deceased 2006), Mother (Al-Zhra), Brother (Bashar), Sisters and my cousin (Basher Ehmeda) without whose support and encouragement I could not have achieved so much. Special thanks are also extended to my lovely wife and daughter, Ibtesam and Omnia, who helped with supporting, encouragement and in many other ways.

Table of Contents

List of Figures

List of Tables

Nomenclature

Symbol	Description	Unit
C_D	= Drag coefficient	[-]
C_L	= Lift force	[-]
g	= Gravity acceleration (9.81)	m/s^2
$C_{1\varepsilon}, C_{2\varepsilon}, C_{3\varepsilon}, C_\mu$	= Empirical model constants	[-]
D	= Pipe diameter	m
A_p	= Pipe area	m^2
V	= Physical velocity	m/s
V_s	= Superficial velocity	m/s
Q	= Volumetric flow rate	m^3/s
G_k *and* G_b	= Turbulent kinetic energy due to velocity gradients and buoyancy	[-]
$\boldsymbol{I}$	= Unit tensor	[-]
$\dot{m}_{pq}$	= Rate of mass transfer per unit volume	$kg/m^3.s$
Re	= Reynolds number	[-]
t	= Time	sec
ΔP	= Pressure drop per unit length	Pa/m
S_k and S_ε	= User-defined sources terms	[-]
x	= Vapor quality	[-]
f	= Friction factor	[-]
N_v	= Velocity number	[-]
N_L	= Viscosity number	[-]

Greek letters

α_l	= Volume fraction/holdup	[-]
τ	= Stress tensor	N/m^2
σ	= Surface tension	N/m

μ	= Viscosity	kg/m.s
k	= Turbulent kinetic energy	m^2/s^2
μ_t	= Turbulent viscosity	Kg/m.s
ε	= Turbulent dissipation rate	m^2/s^3
λ_{RT}	= The Rayleigh–Taylor instability wavelength	m
α	= Under relaxation factor	[-]
ψ	= Backer chart dimensionless parameter	[-]
λ	= Backer chart dimensionless parameter	[-]

Subscripts

mix, m	= Mixture
p, d	= Dispersed phase (drop)
q, c	= Continuous phase (air)
t	= Turbulent

Superscripts

$-$	= Mean component
$'$	= Fluctuating component
$\rightarrow$	= Vector quantity
T	= Turbulent

Acronyms

MEG	= Methanol ethylene glycol
AA	= Anti–agglomerants
CFD	= Computational Fluid Dynamics
PDF	= Probability density function

Chapter 1. Introduction

1.1 Motivation for this thesis

Two–phase flow is a very common occurrence in many petroleum subsea systems where crude oil and gas is transported from offshore wells. In these applications, the two-phase flow can mix and form different flow regimes and patterns. The flow pattern is a very important feature of two–phase flow where the interface can be distributed in several shapes such as wavy, dispersed, and annular flow. During the hydrocarbon transportation process, the variation of phase temperature and pressure throughout the pipeline can cause the formation of a small quantity of liquid (water), to accumulate in the lowest section of the pipeline due to gravity as the pipeline profile is usually curved following the sea bed structure.

In two–phase flow water introduces new challenges related to flow assurance such as wax formation, scale deposits, and gas hydrate. Attention has been given to this phenomenon, which takes place in curved sections of the pipeline where the liquid is trapped. The critical velocity that is required at restart operation to sweep the liquid from the lower section can create different flow patterns. These could be undesirable for subsea system conditions. The understanding of flow behaviour is important for safety operation, control and design.

Design parameters such as pressure drop in a single–phase flow in conduits can be modelled easily. However the existence of a second phase such as water can lead to a significant increase in the pressure drop, and creates difficult challenges in the understanding and modelling of the flow system.

The flow hydrodynamics and mechanisms change significantly from one flow pattern to another. For instance, it has been illustrated (Cheremisinoff, 1986) that for similar flow conditions, slug flow and wavy flow may result in a difference in the pressure drop of a factor of two. In recent decades, researchers have given attention to two–phase flow because of its importance in the oil and gas industry, where the three most important hydrodynamic characteristics of two–phase flow in pipes are the flow pattern, the two–phase holdup, and the pressure drop. In order to predict the holdup

and pressure drop precisely, it is necessary to know the flow pattern under specific flow conditions. Different flow maps published over recent decades can be utilized to recognize the flow pattern. The most widely used flow pattern maps for predicting the two–phase flow regimes for adiabatic flow in horizontal pipelines are those of Baker (1954), Taitel and Dukler (1976), and Barnea and Taitel (1986).

A good understanding and an accurate description of fluid flow and drop size distribution in horizontal pipelines is necessary for the modelling of pressure drop, however accurate modelling of pressure drop and liquid holdup is complicated due to the complexity of flow configurations generated by the two–phase velocity. Over the last ten years, Computational Fluid Dynamics (CFD) has become an industrial simulation tool for an engineering system investigation which includes fluid flow, design, analysis, and performance determination. This improvement has been made due to the easy accessibility of robust in–house systems and the enormous increase in computer memory capacity and speed, resulting in a reduction in the costs of simulation compared to experimental work. With the CFD tool it is possible to get a detailed view of the flow, and specific data for liquid holdup and pressure drop behavior in horizontal pipelines.

It is also possible to model two–phase pressure drop and liquid holdup, accounting for a higher intensity explanation of the physical processes between the two–phase, and the coalescence and break–up phenomena of droplets influencing the dynamics of both phases, as well as the mass transfer between them. For this reason, the understanding of the droplet size distribution or of the droplet population evolution is of paramount significance for an accurate prediction of pressure drop and liquid holdup. Such a higher order physical model should integrate an Eulerian–Eulerian multiphase model and the Droplet Population Balance Equation (DPBE), which takes into account the breakage and aggregation of the droplet, which affects the final droplet size distribution and other system parameters.

1.2 Objectives

The aim of this research is to study two–phase flow behaviour in bend pipelines and to investigate the pressure drop and liquid holdup of two fluids in two areas: flow of gas–water and two–phase gas–oil flow. This research does not involve new numerical development codes; rather it utilizes the suitably existing CFD models with compiled user defined function (UDF) for the drag coefficient in order to conduct extensive simulations. These are validated using experimental data from the open literature or empirical correlations. The objectives of the study are:

1. To study the effect of restart gas superficial velocity, liquid loading and low section depth on flow behaviour.

2. To predict the flow pattern in curved pipelines and compare this with one of the flow pattern maps, and to develop a flow map for subsea systems based on the results obtained.

3. To set up an Eulerian–Eulerian model for predicting pressure drop and liquid holdup at fixed droplet size, and to compare this with experimental data and/or correlations.

4. To investigate the effects of droplet size, initial liquid holdup, and mass flux on the pressure drop and liquid holdup.

5. To evaluate the performance of CFD models with the population balance for predicting the pressure drop, liquid holdup and droplet size distribution.

1.3 Contributions of the Thesis

The current effort made contributions toward all of the above objectives, namely:

- It contributes to an understanding of the flow behaviour of two–phase in bend pipes at different restart gas velocities and initial liquid patching.

- It identifies the risk of hydrate formation based on the generated flow pattern map. This will assist the operators to understand the operating conditions which have a high risk of hydrate formation.

- It develops a two–phase flow model for modelling the pressure drop and liquid holdup by implementing a new drag coefficient. The Ishii–Chawla (1997) drag coefficient for gas–liquid flow has been implemented using a User Defined Function (UDF) and coupled with Eulerian–Eulerian multiphase flow.

- The developed CFD model predicts the pressure drop and liquid holdup data more accurately than the existing models such as Hart *et al*. (1989) and Chen *et al*. (1997) compared to the experimental data of Badie *et al*. (2000).

- The developed CFD model can be used to investigate the effect of various parameters on the pressure drop and liquid holdup in horizontal pipes with low liquid loading.

- The introduced population balance model combined with the CFD model develops the gas–liquid two–phase flow model prediction behaviour in terms of drop size distribution, pressure drop, and liquid holdup.

1.4 Thesis Overview

With the objectives provided by the current chapter, the remainder of this thesis provides a comprehensive development of research performed in the above areas. A brief description of the chapters is given as follows:

Chapter 2 commences with a literature review of the gas hydrate formation focusing on critical places where it can occur, such as the lower section of the pipe. It also provides the mechanism of an agglomeration process, and the way to avoid and dissociate hydrates using inhibitor injection, followed by real case studies. Furthermore, it also includes a literature review of two–phase flow in horizontal and

vertical conduits in terms of flow maps, flow patterns, and experimental work on pressure drop and liquid holdup.

A summary of the published correlations on liquid holdup and pressure drop is presented. The pressure drop correlations are classified based on a homogenous model, a two–phase friction multiplier model, direct empirical models, and flow regime specific models. In addition, a review of published experimental work on the effects of various parameters on the pressure drop, liquid holdup, and flow pattern in different pipe inclination angles are given.

Chapter 3 provides a general background to CFD including its applications, advantages, CFD analysis procedure, and methodology. It also outlines the numerical techniques used in this work.

Chapter 4 presents a brief review of published experimental work on gas hydrates in subsea systems, in which the key issues were identified. It also presents the Volume of Fluid (VOF) multiphase flow model for two and three–dimensional simulations and unsteady state numerical model of gas–liquid two–phase counter current horizontal flow regimes. Different restart gas velocities with initial liquid patching at the low section have been investigated numerically to find out the flow behaviour and to recognize the risk of hydrate formation. The simulation results were compared experimentally to those found in the open literature data (taken from the Baker (1954) chart).

Chapter 5 commences with published computational studies on two–phase flow pressure drop and liquid holdup in a horizontal pipeline, and defines the modelling problem. Controlling parameters (i.e. gas and liquid superficial velocity, and initial liquid holdup) and model assumptions were stated. Three turbulence models based on an Eulerian description were evaluated. The modelling adopts the RNG k–ε turbulence model in conjunction with the enhanced wall treatment method. The Eulerian–Eulerian two–phase flow model was developed by implementing the Ishii–Chawla drag coefficient using the User Defined Function (UDF) in which C^{+} program

is used for writing the UDF. The implemented UDF was used for modelling the pressure drop and liquid holdup. Various simulation case studies were conducted in order to demonstrate the applicability of the developed two–phase model.

The numerical results from the developed CFD model were compared with the existing models and with experimental data in order to test the accuracy and discuss the performance of the model and its limitations. Furthermore, the sensitivity analysis of different variables in the model was performed in order to test and find out the behaviour of system pressure drop and liquid holdup.

Chapter 6 introduces the Population Balance Equation for droplets that can break and aggregate due to droplet–droplet and droplet–fluid interactions. Under these circumstances a fixed droplet size model might not be suitable for predicting the correct thermo–fluid dynamics of the gas–liquid two–phase flow system. Many researchers have tried to solve the population balance equation in which several numerical methods are demonstrated. Most emphasis is given to studying the effect of different system factors on the particle size distribution, pressure drop and liquid holdup of two–phase flow in a horizontal conduit.

Finally, *Chapter 7* summarizes the main outcomes from this work and presents recommendations for further work.

Figure (1.1) gives a diagrammatic sketch of the thesis outline.

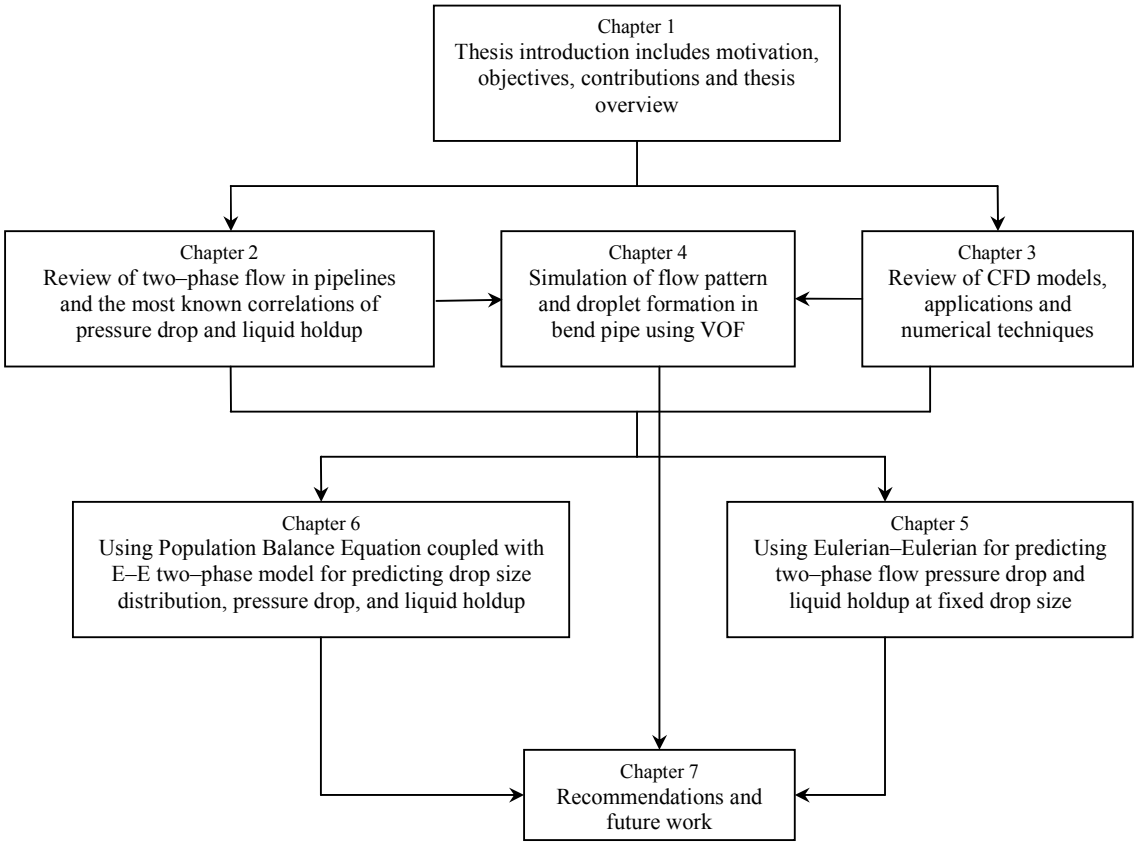

Figure 1.1: The thesis structure

1.5 Bibliography

Badie, S., C. P. Hale, C. J. Lawrence and G. F. Hewitt (2000). Pressure gradient and holdup in horizontal two-Phase gas-liquid flows with low liquid loading. *International Journal of Multiphase Flow*, 26, 1525-1543.

Baker, O. (1954). Design pipelines for simultaneous flow of oil and gas. *Oil and Gas Journal*, 53, 26.

Barnea, D. and Y. Taitel (1986). Flow pattern transition in two-phase gas-liquid flows. *Encyclopedia of Fluid Mechanics*, 3, 403-474.

Chen, X. T., X. D. Cai and J. P. Brill (1997). Gas–Liquid stratified-wavy flow in horizontal pipelines. *Journal of Energy Resources Technol*ogy, 119(4), 209-216.

Cheremisinoff N. P. (1986). Properties and concepts of single fluid flows. *Encyclopaedia of fluid mechanics*, V, 1, flow phenomena and measurement, 285-351

Hart, J., P. J. Hamersma and J. M. H. Fortuin (1989). Correlations predicting frictional pressure drop and liquid holdup during horizontal gas-liquid pipe flow with a small liquid holdup. *International Journal of Multiphase Flow*, 15(5), 947-964.

Ishii M. and T. C. Chawla (1979). Local drag laws in dispersed two-phase flow, NUREG/CR-1230, ANL-79-105.

Taitel, Y. and A. E. Dukler (1976). A model for predicting flow regime transitions in horizontal and near horizontal gas- liquid flow. *AIChE Journal*, 22(1), 47-55.

Chapter 2

Literature Review of Multiphase Flows in Pipelines

This chapter will cover some topics which are relevant to subsea system and hydrate. The first section describes the hydrate, for example: what is a hydrate? How does it form? How could it be prevented?

Hydrate formation is closely related to offshore operations and a review of two–phase flow in subsea systems particularly focused on pipelines will follow. Flow behavior in horizontal pipes will be reviewed, including the flow pattern and flow map. Then, operating factors that affect the pressure drop and liquid holdup will be covered with some case studies.

2.1 Hydrate Background

In general, oil and gas offshore production can be very expensive, especially in deep water due to the difficulty of access to crude oil reservoirs and because of the problems of flow assurance due to low temperatures encountered at the seabed. Since the production of oil and gas has moved to offshore, the flow assurance practice has become very important to finding out the cost effectiveness and technical feasibility of a deep water development. There are some flow assurance difficulties that are common which take place in multiphase flows in pipelines. These include hydrate formation which occurs because of the water and gas reaction. This leads to the formation of solid particles that can cause pipe plugging; wax deposition on the pipe wall which can reduce the diameter of the pipe until the flow is decreased and as a result it can also plug the pipe and kill the well; asphaltene deposition; scale precipitation; corrosion problems; and severe slugging. In order to reduce these problems which have both practical and economic implications, the water has to be removed.

Hydrates are usually crystalline particles created from the reaction between water and a hydrocarbon gas at low pressure and high temperature, conditions which are most likely to be found in deep water. Three hydrate crystal structures have been recognized, these are structure I, II and H. Structures I and II are the most common hydrate crystal structures and are composed mostly of light hydrocarbons, including methane, ethane, propane, and isobutane, as well as many nonpolar molecules (such as carbon dioxide, nitrogen, argon, krypton, and xenon). Larger molecules (e.g., 2,2-dimethylbutane, cycloheptane) can also stabilize the hydrate structure (fitting into the $5^{12}6^{8}$ cavities of structure H) in the presence of a smaller guest molecule (e.g., methane, xenon) that occupies the small cavities ($4^{3}5^{6}6^{3}$ and 5^{12}) (Amadeu *et al.*, 2009).

The formation of these structures is based on gas molecules trapped by water molecules. The pressure and temperature (P–T) hydrate curve diagram can be created by using one of the software programs such as PVTSim or Multiflash based on the fluids composition. Figure (2.1) shows that hydrate can form in the area to the left

side of the curve. Assuming equilibrium, the region to the right side of the line will be without hydrates during operations. An operator requires monitoring production for any changes. The hydrate blockage is more often expected to be formed at the low point of an offshore production pipeline, where the water can accumulate. It can also form in valves where the gas expands and can result in the Joule–Thompson cooling effect. Furthermore, at greater water depth, the possibility of forming hydrates is high due to the increase of hydrostatic head resulting from increasing operating pressure.

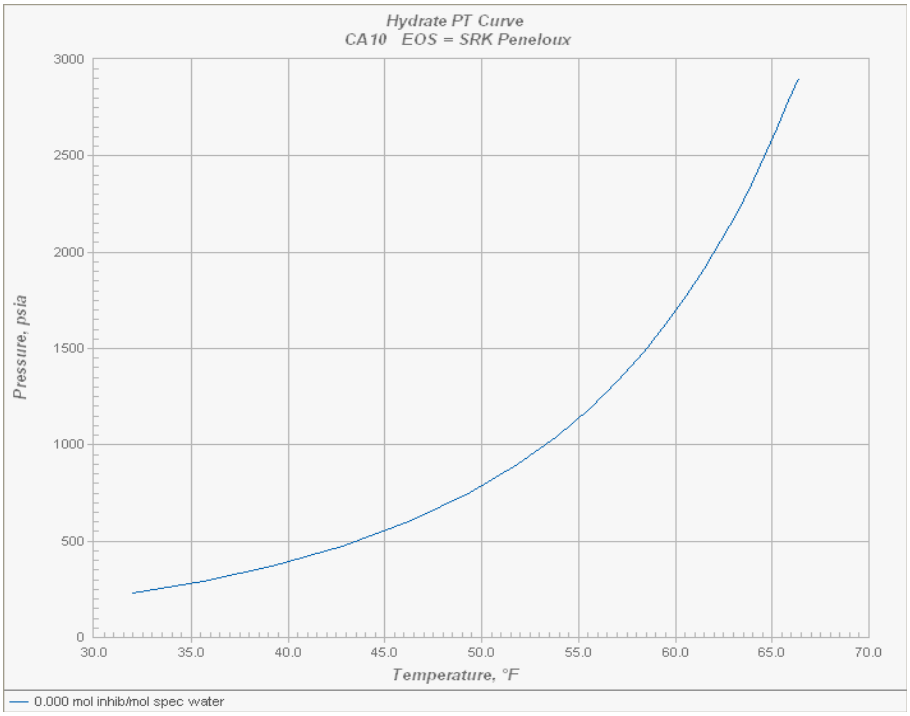

Figure 2.1: Typical hydrate curve (Volk *et al*., 2010)

When the hydrate plug takes place, it may require a long time to dissociate, causing production losses. It is also necessary to take into account the safety issues. Hydrate plugs can be created by two mechanisms, the agglomeration and slurry flow. The hydrate particles can agglomerate and build up in the pipe to form plugs, or the plugs may take place in the bulk where the particles are formed and flow as slurry until the viscosity of the slurry flow becomes so high that the flow ceases. The most typical hydrate prevention techniques are using chemical injection and insulation around the pipeline. The most appropriate insulation methods used are cast in place, where the

insulation layers are placed around the pipe, and pipe in pipe, where the production line is put inside another pipe and the space (annulus) between the pipes is filled with insulating material. This method of pipe–in–pipe is usually more costly.

Throughout the production of steady state, the insulation around the pipe may maintain the system away from the hydrate region, but when the shutdown takes place the fluids temperature in the pipeline may drop down to the sea temperature (typically around 5^{o}C). If the period of the shutdown does not go beyond the time of minimum cool down, no action is required before the restart production. On the other hand, if the time is longer, fluid conditions are more likely to occur inside the hydrate zone and mitigation procedures are taken immediately. In this case, the chemical injection technique is sufficient to avoid or delay hydrate formation, but is also expensive.

There are two common types of hydrate inhibitors; these are low dosage hydrate inhibitors and thermodynamic inhibitors. The addition of thermodynamic inhibitors such as methanol ethylene glycol (MEG) results in shifting the hydrate curve to a lower temperature, making the hydrate zone smaller. The other type of inhibitor (low dosage hydrate) is categorized as kinetic inhibitors, which cause a delay of the process of hydrate nucleation, growth and anti–agglomerants (AA) that allow hydrates to form without agglomeration. Other approaches that are available to prevent hydrate plugs are water removal, operating at low pressure, and active heating, but they are either too expensive or not practical. Even with these prevention methods, occasionally a hydrate plug still forms and the most practical solution to dissociate is to inject methanol. Other possible solutions used to dissociate hydrate plugs are heating the line, and two sided depressurization. In all situations, the dissociation must be made in a safe manner.

Many case studies of hydrate plug dissociation in subsea systems are presented by Sloan (2000), where the equipment was completely destroyed and lives were lost during an attempt to remove the hydrate plug. In 1991 there was an incident where operators were trying to remove the plug in a sour–gas flow pipeline. During the operation of plug dissociation, the pipeline was ruptured because of the effect of the

hydrate plug, resulting in loss of life. In another incident in the same year the method of two sided depressurization to remove the plug was utilized, but the multiple plugs could have resulted in the failure of a 3 inch Schedule 40 pipeline. Although engineers have attempted to design a hydrate free well, they still occur, sometimes leading to losses of life and equipment.

2.2 Fundamental Concepts of Two–phase Gas Liquid Flows

This section demonstrates some of the basic concepts and variables that are related to two–phase flow in pipelines. The flow behaviour encountered in vertical and horizontal pipelines is described, based on their characteristics. The flow pattern maps which describe the flow pattern information are also introduced.

2.2.1 Definition of Basic Parameters

The two–phase flow can be identified at the inlet boundary in different ways, as mentioned in section (3.7.3.2.1). One of them is the inlet velocity, which is also called the physical velocity. The physical velocity of each phase can be obtained based on the superficial velocity and the *in situ* volume fraction of each phase, as follows:

$$V_L = \frac{V_{SL}}{\alpha_L} \qquad \text{and} \qquad V_G = \frac{V_{SG}}{\alpha_G} \tag{2.1}$$

Where V_L and V_G are the physical (or called true average) velocities of liquid and gas phases respectively, and are larger than the superficial velocities.

The superficial velocities of the liquid and gas phases (V_{SL} and V_{SG}) are expressed as the volumetric flow rate for the phase divided by the cross sectional area of the pipe and can be written as:

$$V_{SL} = \frac{Q_L}{A_p} \qquad \text{and} \qquad V_{SG} = \frac{Q_G}{A_p} \tag{2.2}$$

Where Q_L and Q_G are the liquid and gas volumetric flow rate respectively and A_p refers to the pipe cross sectional area.

Mass flux is also another method that can be used to specify the inlet boundary, by dividing the mass flow rate by the inlet zone area. It is recommended that this is utilized in situations where it is needed to study the effect of particular parameters (i.e. volume fraction, flow rate) where a uniform mass flux is applied over the domain. It is calculated by using the following form:

$$M_{flux} = \frac{\dot{m}}{A_p} \tag{2.3}$$

When using the mixture model, it is necessary to use the mixture properties. Therefore, the mixture velocity is obtained by the sum of the gas and liquid superficial velocities:

$$V_m = V_{SL} + V_{SG} = (1-x)V_L + xV_G \tag{2.4}$$

In the homogeneous fluid flow, the two–phase volume fraction is calculated via dividing the volumetric flow rate of a particular phase by the total volumetric flow rate, where the sum of volume fractions of the liquid and gas phases (α_l and α_g) is equal to unity. It can be obtained as:

$$\alpha_l = \frac{Q_L}{Q_L + Q_G} = \frac{V_{SL}}{V_m} \tag{2.5}$$

$$\alpha_g = \frac{Q_G}{Q_L + Q_G} = \frac{V_{SG}}{V_m} \tag{2.6}$$

The typical feature of two–phase flow is that two phases are distinguished by viscosity and density, and flow counter or co–current. Typically the velocity of the

phase that is less dense and/or less viscous tends to flow fast in horizontal and uphill flows. Moreover, in this type of pipe inclination, the gas phase travels much faster than the liquid phase except in the situation of downward flow. Therefore, the difference in the *in situ* average velocities between the two phases results in a very important phenomenon , which is the "slip" of one phase relative to the other, or the "holdup" of one phase relative to the other (Govier and Aziz, 1972). This leads to different volume fractions between *in situ* and input. Although "holdup" can be described as the fraction of the pipe volume occupied by a specified phase, holdup is usually referred to as the *in situ* liquid volume fraction, while the term "void fraction" is typically utilized for the *in situ* gas volume fraction.

The liquid holdup and gas void fraction are obtained by dividing the cross sectional area that is occupied by one of the phases by the total area. The liquid holdup and gas volume fractions are defined as:

$$\alpha_L = \frac{A_L}{A_p} \quad \text{and} \quad \alpha_G = \frac{A_G}{A_p} \tag{2.7}$$

Where A_L and A_G are the cross sectional areas, occupied by liquid and gas, respectively.

Furthermore, the fluid property of each phase, such as density, viscosity and interfacial tension, and the pipe internal diameter and inclination angle also have an impact on the performance of the system. In the following sections the flow patterns in horizontal and vertical pipes, and the pressure drop as well as the liquid holdup in horizontal pipelines are reviewed and discussed.

2.2.2 Multiphase Flow Regimes

The flow regime typically is defined by a classification of flow pattern or a description of the morphological arrangement of the phases (Wallis, 1969). In addition, multiphase flow regimes are categorized into four classes, which are gas-solid flows, liquid-solid flows, gas-liquid or liquid-liquid flows and three phases flow

(ANSYS FLUENT 12.1 Theory Guide, 2010). In this work two–phase, gas-liquid flow in horizontal pipelines only is presented. Figure (2.2) shows a schematic chart of the multiphase flow regimes.

2.2.2.1 Classification of Gas–liquid Flow Patterns

The flow patterns are utilized to illustrate the interface distribution of two phases. In two-phase gas-liquid flow, the interface can take different configurations based on different parameters, such as the two-phase velocities, two-phase fluid properties, and the pipeline geometry. Three basic flow patterns are proposed by Hubbard and Dukler (1966) namely, separated, intermittent, and distributed flow.

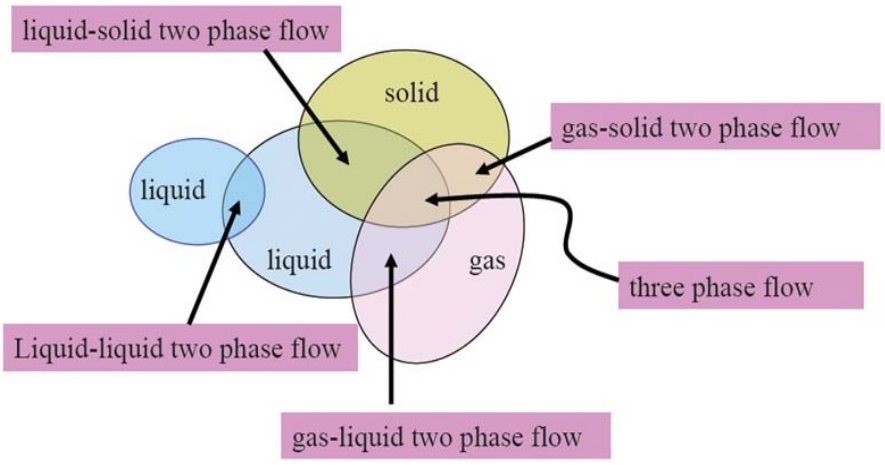

Figure 2.2: Multiphase flow regimes (ANSYS FLUENT 12.1 Theory Guide, 2010).

I. Separated flow patterns, where the two phases (gas-liquid) are continuous and some of the bubbles or droplets may form in either phase, or may not appear. Separated flow patterns can be classified into:
   - Stratified flows: These can be characterized into two types of stratified flows, which are described as smooth and wavy;
   - Annular flows: These include annular film flow and annular-mist flow, where liquid droplets can exist in the gas phase;

II. Intermittent flow patterns: At least one phase is discontinous. These flow regimes can consist of three sub-classes:
    - Elongated bubble flow;
    - Slug flow, plug flow;
    - Churn flow, which is a transition region between slug flow and annular-mist flow.

III. Dispersed flow patterns: These flow regimes can be described by the liquid phase as continuous and the gas phase as discontinous. The flow patterns that can be found are:
    - Bubble flow;
    - Dispersed bubble flow, in which the finely dispersed bubbles exist in a continuous flowing liquid phase.

We will describe in detail the features of these flow patterns for both horizontal and vertical flows.

2.2.3 Flow Patterns in Horizontal Pipes

The two-phase flow in a pipeline can take various physical distributions of the interface known as flow patterns or flow regimes. These flow patterns can be identified using different techniques which are categorized into traditional approaches, such as photography in transparent pipes or direct observation, and objective indicator approaches, that include x-rays, gamma-rays, fluorescent light, void fraction variations, pressure variations, tomography etc.

The typical flow patterns in horizontal circular pipes are demonstrated in Figure (2.3). The two-phase in this pipe geometry tends to separate out because of the asymmetry which is affected by the gravity acceleration. The flow patterns that can be observed are:

a) ***Bubbly flow:*** In horizontal flow the gas bubbles are created due to the turbulence of the liquid phase and tend to come together to flow at the top of the pipeline. Higher liquid velocities are likely to form identical bubbles, which are distributed and appear as froth.

b) ***Plug flow:*** This forms when large bubbles develop due to an increase of gas velocity. The formed bubbles coalesce to create long bubbles, which are recognized as plugs, and which keep travelling along the top side of the pipeline.

c) ***Stratified flow***: This also generates when the gas velocity is higher than the liquid phase that is specified by low flow rate. The gas phase separates out and flows separately on the top of the pipe with liquid flowing at the bottom due to the density difference. This type of flow can be classified into different configurations that are:

- *Stratified smooth flow* – where the interface of gas-liquid is observed as smooth.
- *Stratified wavy* – this is generated as the gas velocity is increased, the liquid wave amplitude increases (creating ripples and rolls), and therefore the smooth interface changes into waves.

d) ***Slug flow:*** This generates when the wave amplitude has become so big that the wave touches the top of the pipe, creating gas pockets in the pipe that are smooth from the front but keep on shedding gas bubbles from the tail area while flowing.

e) ***Annular flow:*** This is most likely to occur when the gas velocity has increased to a high value that is sufficient to push the liquid away at the same flow direction. In annular flow, the gas phase occupies the pipe core; while the liquid exists in two forms, as film around the pipe circumference and also as droplets in the core.

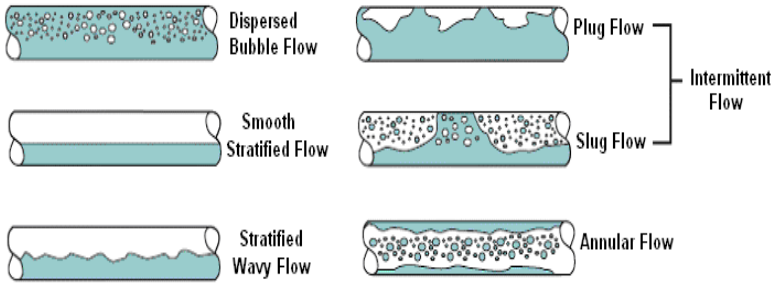

Figure 2.3: Flow regimes in horizontal gas–liquid (Ali, 2009).

2.2.4 Flow Patterns in Vertical Pipes

The flow regimes in vertical upward flows can be categorized into four typical flow patterns that are slug, churn, bubbly, and annular flow (Hewitt and Roberts, 1969; Spedding and Nguyen, 1980; Matsui, 1984; and Mishima and Ishii, 1984). These classes have been further differentiated by several investigators. The flow regimes that can be identified in vertical upward, co-current flows at various gas-liquid velocities are demonstrated in Figure (2.4). These are listed in order as the gas velocity is increased.

a) ***Bubbly flow*:** This flow is generated when the gas phase is dispersed in the continuous liquid phase. Further categorizing of this flow pattern has been made as: low liquid loading bubbly flow and dispersed bubbly flow (Taitel *et al.*, 1980; Weisman and Kang, 1981; McQuillan and Whalley, 1985; Barnea and Brauner, 1986 and Barnea 1987).

- *Low liquid loading bubbly flow*: This occurs when the liquid superficial velocity is low, and tends to form some gas bubbles, which are roughly the same size. They are presented and spread uniformly in the core phase of liquid where the coalescence mechanism can take place (Taitel *et al*., 1980).
- *Dispersed bubbly flow*: This flow is obtained over the entire pipe diameter variety and inclination (Barnea, 1987). The feature of this flow is that the gas phase is dispersed as small separate bubbles in the continuous phase of liquid.

The obvious distinction between these two flows is still not recognised by many investigators (Mishima and Ishii, 1984; Kokal and Stanislav, 1989; Weisman and Kang, 1981).

b) ***Slug flow*:** This generates as the gas superficial velocity is increased, in consequence of that, more gas bubbles are created and adhere together to form a long smooth bubble with a front cap as a bullet shape (also called nose). These bubbles are referred to as Taylor bubbles, which have a cross section that is comparable to the pipe. These bubbles are typically attached to the wall via a thin liquid film. Moreover, the two successive Taylor bubbles are separated by a liquid slug that may have small gas bubbles that are being shed from the tail of the leading Taylor bubble.

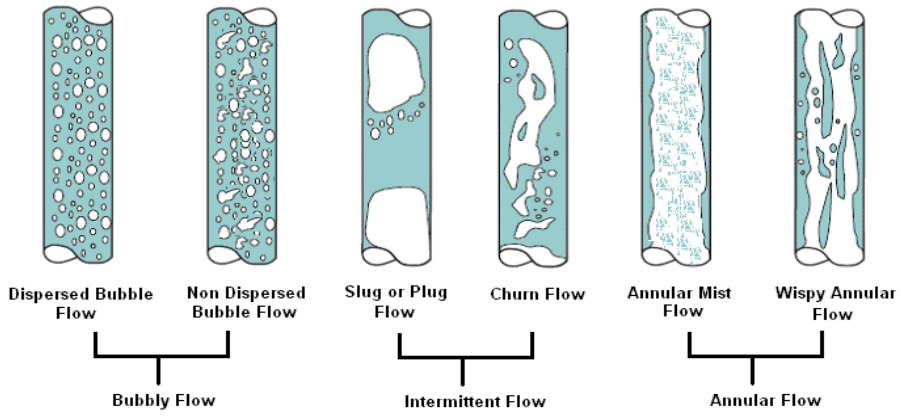

Figure 2.4: Flow regimes in vertical gas–liquid upflow (Ali, 2009).

c) ***Churn/ froth flow*:** This flow can be obtained as a result of increasing the gas superficial velocity in previous flow patterns (slug), where the Taylor bubble develops and becomes more distorted near the interface of liquid-gas. This distorted bubble moves in a motion which is similar to a churn motion, and this leads to it growing into irregular shaped portions of gas and liquid. This flow is identified as froth slug, dispersed slug, churn–turbulent flow, and pulsating annular (Brauner and Barnea, 1986). On the other hand, several researchers do not acknowledge churn/froth flow as a separate flow pattern, but consider it to be under the slug flow pattern (Hewitt and Jayanti, 1993).

d) ***Annular flow:*** This flow is described by the gas phase existence in the core of the pipe, which is surrounded by liquid film around its diameter. Some of the liquid also exists in the core phase as droplets. This flow can be distinguished by two different flows, namely (Hewitt, 1982):

- *Wispy annular flow*: The entrained liquid is found in quite large drops, while the liquid film holds gas bubbles.
- *Annular mist flow*: In this flow the pipe center is occupied by the gas phase with some liquid entrainment as droplets, while the liquid phase flows along the pipe circumference.

2.2.5 Flow Pattern Maps

To develop the co-current two–phase gas–liquid flow models for predicting performance, information about the flow patterns in the pipe is needed. Typically, detection of flow patterns is determined during visual experimental study, placing them on the flow map. Here, however, this information was collected by developing flow pattern maps. Consequently, several methods are presented to classify the flow regime.

Many flow regime maps for two–phase flow, both horizontal and vertical, are presented in the literature. Most of these maps use dimensional coordinates in terms of gas and liquid superficial velocities to identify the flow regime. In contrast, many other flow maps are presented with the coordinates' parameters, rather than superficial velocities, such as those by Hewitt and Roberts (1969) and Baker (1954).

Previously the majority of flow maps were constructed based on empirical correlations developed from experimental work that had limited application. The first mechanistic flow map used for horizontal flow was based on the physical transitions mechanism of each flow regime (Taitel *et al*., 1976). Later, Taitel *et al.* (1980) developed the Dukler and Taitel (1977) flow map for vertical up flow of gas-liquid flow in a 25 and 50mm diameter pipe at room temperature and atmospheric pressure. Weisman and Kang (1981) and McQuillan and Whalley (1985) introduced modified

flow maps for the vertical upward flow of air–water. Mishima and Ishii (1984) had implemented a similar concept, which was presented by Taitel *et al.* (1980) via a mechanistic flow pattern transition for two–phase flow rising in vertical pipes, the results of which agreed with other vertical flow maps. Barnea (1987) developed an integrated model for a wide rage of pipe deviation angles along with the vertical and the horizontal. Some of flow maps typically used for horizontal and vertical are shown in Figures (2.5, 2.6, and 2.7).

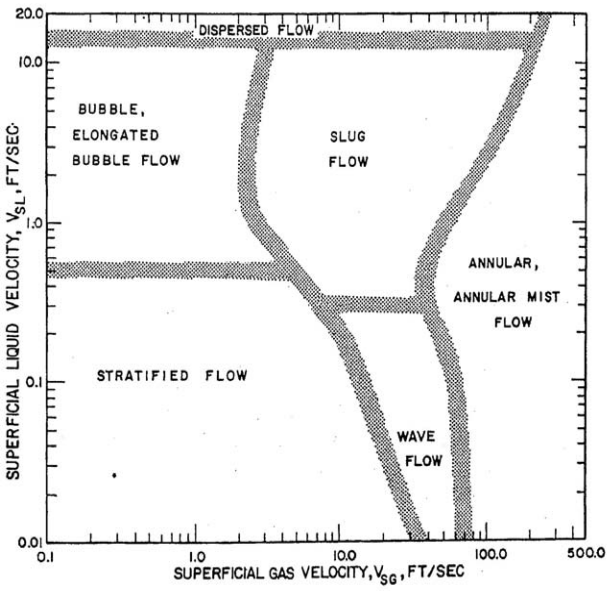

Figure 2.5: Mandhane (1974) flow pattern map for horizontal flow in a tube.

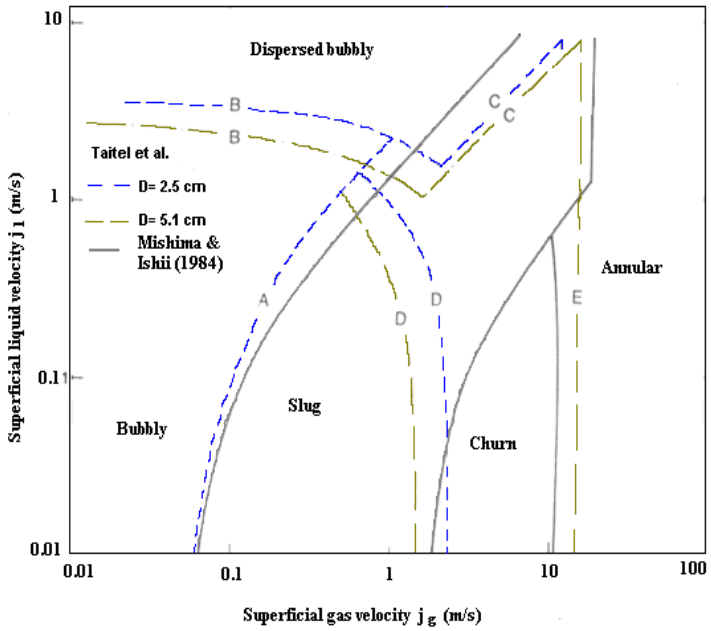

Figure 2.6: Flow regimes map for vertical upflow showing Taitel *et al.* (1980) and Mishima and Ishii (1984) transitions (Mishima and Ishii, 1984).

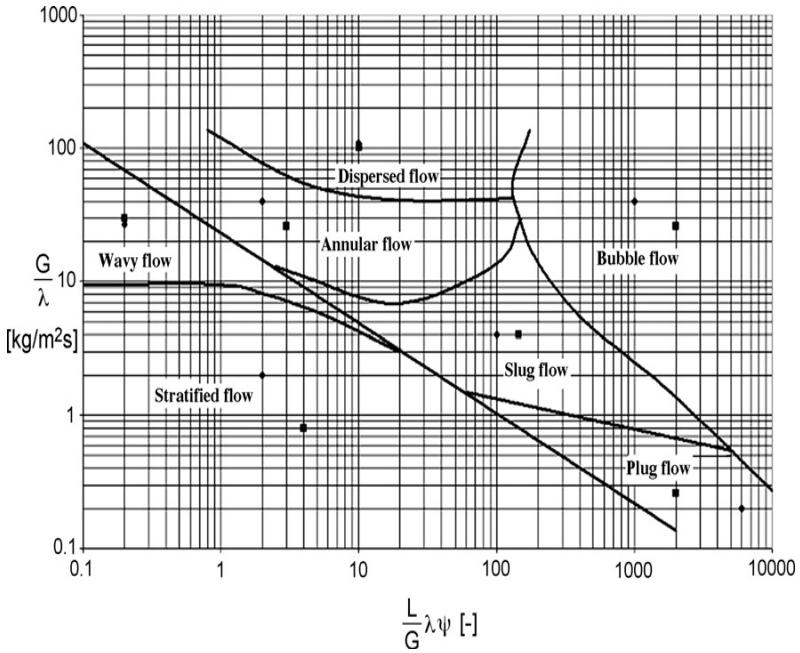

Figure 2.7: Baker chart. (●) Operating conditions for the simulations of water-air flow; (■) Operating conditions for the simulations of gas oil liquid-vapor flow.

2.3 Liquid Holdup and Pressure Drop in Horizontal Pipelines

2.3.1 Liquid Holdup Correlations of Adiabatic Two–phase Flow

In order to study co-current two–phase flows in a horizontal pipe, liquid holdup is one of the important factors to consider. In practice, the two–phase velocities do not move at the same rate, therefore the *in-situ* volume fraction will be completely different from the inlet volume fraction.

In the 1940s, researchers began to investigate the pressure drop and liquid holdup in the multiphase flow. Since then, data has been gathered for pressure drop and liquid holdup of two-phase flow for various pipeline inclinations, horizontal and vertical. The study of multiphase flow in pipelines has proven to be a very difficult concept because of various parameters, such as pipe roughness, pipe incline angle, pipe diameter, surface tension, two-phase densities, viscosities, velocities and the initial liquid fraction.

At a single phase flow, some of the factors such as flow regime characteristics and liquid holdup are not included. Based on the collected data, many empirical correlations have been developed, but they remain restricted for use in some applications due to accuracy. Moreover, these correlations cannot be extrapolated to the data rather than information that is based on or is valid for particular flow conditions. Different studies have been performed and a model has been developed to predict the pressure drop and liquid holdup. Table (2.1) shows different correlations that have been proposed for liquid holdup predictions.

Table 2.1: Most Common Liquid Holdup Correlations

Author	Flow Pattern	Correlation
Armand (1946)	Bubbly and slug	$\frac{H_G}{H_L} = \frac{1}{0.2 + 1.2(Q_G/Q_L)}$
Lockhart and Martinelli (1949)	Bubbly, stratified churn, slug, annular, and mist	$\frac{H_L}{H_G} = \sqrt{\frac{(dp/dl)_{SL}}{(dp/dl)_{SG}}}$
Flanigan (1958)	Annular and slug	$H_L = \frac{1}{1 + 0.3264\ U_{SL}^{1.006}}$
Hoogendoorn (1959)	Intermittent bubble and slug	$\frac{H_G}{H_L} = 0.6\left[U_{SG}\left(1 - \frac{H_G}{1-H_G}\frac{U_{SL}}{U_{SG}}\right)\right]^{0.85}$
Levy (1960)	Slug, dispersed bubble, annular, and stratified	$H_G = \frac{\phi_L - 1}{\phi_L}$, $\phi_L = \left[(dp/dl)_{TP}/(dp/dl)_{SL}\right]^{0.5}$
Hughmark (1962)	Bubble and slug	$x = \frac{1}{1 - \frac{\rho_L}{\rho_G}\left(1 - \frac{K}{H_G}\right)}$ $K = \frac{H_G}{\lambda_G}$ $\lambda_G \frac{Q_G}{Q_G + Q_L}$
Butterworth (1975)	Flow regime-independent	$\frac{H_L}{H_G} = \left(\frac{1-x}{x}\right)^{0.74}\left(\frac{\rho_G}{\rho_L}\right)^{0.65}\left(\frac{\mu_L}{\mu_G}\right)^{0.13}$
Nishino and Yamazaki (1963)	Annular	$H_G = 1 - \left[\frac{(1-x)\rho_G}{x\rho_L + (1-x)\rho_G}\right]^{1/2}$
Zivi (1963)	Annular and slug	$\frac{H_L}{H_G} = \frac{(1-x)}{x}\left(\frac{\rho_G}{\rho_L}\right)^{2/3}$
Thom (1964)	Stratified and annular	$\frac{H_L}{H_G} = \frac{(1-x)}{x}\left(\frac{\rho_G}{\rho_L}\right)^{0.89}\left(\frac{\mu_L}{\mu_G}\right)^{0.18}$
Turner and Wallis (1965)	Annular, slug, and stratified	$\frac{H_L}{H_G} = X^{0.8}$
Guzhov *et al*. (1967)	Stratified, plug, slug, and annular	$\frac{H_G}{\lambda_G} = 0.81\left[1 - \exp\left(-2.2\sqrt{Fr}\right)\right]$
Eaton *et al*. (1967)	Slug, stratified smooth and stratified	$H_L = \frac{Z}{0.2578 + 0.9555Z + 0.1397Z^{0.5}}$ $Z = \frac{1.84\ N_{Lv}^{0.575}}{N_{gv}\ N_{pd}^{0.0277}}\left(\frac{P}{P_b}\right)^{0.05} N_{L\mu}^{0.1}$
Bonnecaze *et al*. (1971)	Annular and stratified	$H_L = 1 - \frac{1-\lambda_L}{1.2 + 0.35(1-\rho_G/\rho_L)\delta/\sqrt{Fr}}$
Beggs and Brill (1973)	Segregated, intermittent and distributed	$H_L = H_{L(0)}\psi$, $H_{L(0)} = \frac{a\lambda_L^b}{Fr^c}$
Butterworth (1975)	Flow regime-independent	$\frac{H_L}{H_G} = \left(\frac{1-x}{x}\right)^{0.74}\left(\frac{\rho_G}{\rho_L}\right)^{0.65}\left(\frac{\mu_L}{\mu_G}\right)^{0.13}$

Gregory *et al*. (1978)	Stratified	$H_{LLS} = \dfrac{1}{1+\left(U_M/8.66\right)^{1.39}}$
Chen and Spedding (1981a)	Stratified	$H_L = \dfrac{X^{2/3}}{1+X^{2/3}}$
Chen and Spedding (1981b)	Stratified	$H_L = \dfrac{X^{2/3}}{k_i+X^{2/3}}$
Chen and Spedding (1983a)	Slug, bubble, annular, and stratified	$\dfrac{H_L}{H_G} = A\left[\dfrac{1-x}{x}\right]^p\left[\dfrac{\rho_G}{\rho_L}\right]^q\left[\dfrac{\mu_L}{\mu_G}\right]^r$
Chen and Spedding (1983b)	Slug, bubble, annular, and stratified	$\dfrac{H_G}{H_L} = K\left[\dfrac{Q_G}{Q_L}\right]^a\left[\dfrac{\rho_G}{\rho_L}\right]^b\left[\dfrac{\mu_G}{\mu_L}\right]^c$
Chen and Spedding (1983c)	Slug, bubble, annular, and stratified	$\dfrac{H_G}{H_L} = \left[W_1\dfrac{\rho_G}{\rho_L}\dfrac{q_G^{1.8}}{q_L}\dfrac{\nu_G^{0.2}}{\nu_L D^{0.8}}\right]^{1/\omega_1}$ $\dfrac{H_G}{H_L} = \left[W_2\dfrac{\rho_G}{\rho_L}\dfrac{q_G}{q_L^{1.8}}\dfrac{\nu_G D^{0.8}}{\nu_L^{0.2}}\right]^{1/\omega_2}$
Tandon *et al*. (1985)	Annular	$H_G = 1 - 1.928\ \mathrm{Re}_L^{-0.315}\left[F\left(X_{TT}\right)\right]^{-1} + 0.9293\ \mathrm{Re}_L^{-0.63}\left[F\left(X_{TT}\right)\right]^{-2}$, $H_G = 1 - 0.38\ \mathrm{Re}_L^{-0.088}\left[F\left(X_{TT}\right)\right]^{-1} + 0.0361\ \mathrm{Re}_L^{-0.176}\left[F\left(X_{TT}\right)\right]^{-2}$, $F\left(X_{TT}\right) = 0.15\left(X_{TT}^{-1} + 2.85\,X_{TT}^{-0.476}\right)$ $X_{TT} = \left(\dfrac{\mu_L}{\mu_G}\right)^{0.1}\left(\dfrac{1-x}{x}\right)^{0.9}\left(\dfrac{\rho_G}{\rho_L}\right)^{0.5}$
Minami and Brill (1987)	Annular, slug, and stratified wavy, and smooth	$H_L = 1 - \exp\left[-\left(\dfrac{\ln Z + 9.21}{8.7115}\right)^{4.3374}\right]$ $x_L = -0.0095 + 3.698x - 11.497x^2 + 65.22x^4$ $x = \dfrac{y_{nsL}^{0.8945}\,N_{pd}^{0.0796}}{N_{Lv}^{0.4076}} \qquad 0.0026 < x < 0.15$
Hart *et al*. (1989)	Stratified	$\dfrac{H_L}{H_G} = \dfrac{U_{SL}}{U_{SG}}\left[1 + 10.4\,\mathrm{Re}_{SL}^{0.363}\left(\dfrac{\rho_L}{\rho_G}\right)^{0.5}\right]$
Abdul–Majeed (1996)	Annular, slug, and stratified wavy, and smooth	$H_L = \exp\left(\begin{matrix}-0.9304919 + 0.5285852\,R - \\ 9.219634\times10^{-2}R^2 + 9.02418\times10^{-4}R^4\end{matrix}\right)$ $H_L = \exp\left(\begin{matrix}-1.099924 + 0.6788495\,R - 0.1232191 \\ \times10^{-2}R^2 - 1.778653\times10^{-3}R^3 + \\ 1.626819\times10^{-3}R^4\end{matrix}\right)$ R = ln (*X*), where $X^2 = \left[\dfrac{U_{SG}}{U_{SL}}\dfrac{\rho_G}{\rho_L}\dfrac{\mu_L}{\mu_G}\right]^m\dfrac{\rho_L U_{SL}^2}{\rho_G U_{SG}^2}$
Spedding *et al*. (1998)	Stratified	$H_L = \left(3.5 + D\right)\left(\dfrac{Q_L}{Q_T}\right)^{0.7}$
Gómez *et al*. (2000)	Stratified	$H_L = \exp\left(-0.45\theta_R - 2.48\times10^{-6}\,\mathrm{Re}_{LS}\right) \quad 0 \le \theta_R \le 157$ $\mathrm{Re}_{LS} = \dfrac{\rho_L U_M D}{\mu_L}$

2.3.2 Pressure Drop Correlations of Adiabatic Two–phase Flow

The pressure drop of two–phase flow depends on a different number of independent factors, such as conduit geometry, mass flux, conduit orientation (i.e. vertical, horizontal or inclined), two–phase properties (i.e. density, viscosity), volume fraction of each phase, flow direction (i.e. down flow, upward flow, or counter-current flow), and flow regimes. Moreover, in practical engineering applications, two–phase flow processes can be classified into different physical situations, such as adiabatic and diabatic, or in different flow components such as one–phase, two–phase or multi–phase. The pressure drop of these several applications has to be correlated for availability.

A number of correlations for two–phase pressure drop in a horizontal co–current flow can be found in the literature. Most of them in practice are realistically only valid for a limited range of parameters. Mechanistic models are derived based on specific assumptions, and careful assessment of a particular system is required to ensure that these assumptions are in close agreement.

The two–phase flow pressure drop correlations can be categorized into four groups. These are:

1- Empirical correlations based on a homogenous model.
2- Empirical correlations based on a two–phase friction multiplier model.
3- Direct empirical models.
4- Flow regime specific models.

Most of the widely utilized and frequently referred to correlations of these classes are given in Table (2.2).

Table 2.2: Commonly Used Correlations for Friction Factor Calculation of Circular Cross–section Pipes

Author	Equation
Blasius (1913)	$f = 0.316\,\mathrm{Re}^{-1/4}$ $\quad 3000 < \mathrm{Re} < 10^5$ $f = 0.184\,\mathrm{Re}^{-1/5}$ $\quad 3000 < \mathrm{Re} < 10^6$
Drew *et al*. (1932)	$f = 0.0056 + \frac{\mathrm{Re}^{-0.32}}{2}$ $\quad 3000 < \mathrm{Re} < 3\times10^6$
Nikuradse (1933)	$\frac{1}{\sqrt{f}} = 0.86\ln(\mathrm{Re}\sqrt{f}) - 0.8$
Colebrook (1938)	$\frac{1}{\sqrt{f}} = 0.86\ln\left(\frac{\varepsilon/D}{3.7} + \frac{2.51}{\mathrm{Re}\sqrt{f}}\right)$ $\quad \mathrm{Re} > 3000$
Filonenko (1948)	$f = (1.82\log(\mathrm{Re}) - 1.64)^{-2}$ $\quad 4\times10^3 \le \mathrm{Re} < 10^{12}$
Selander (1978)	$f = 4(3.8\log\left(\frac{10}{\mathrm{Re}} + \frac{0.2\varepsilon}{D}\right)^{-2}$

2.3.2.1 Correlation Based on Homogeneous Flow Model

The two–phase frictional pressure gradient in the homogeneous flow model is found in terms of a friction factor, as calculated in a single–phase flow, using one of the equations that are provided in Table (2.2), using the two–phase viscosity model in computing the Reynolds number. Various viscosity models have been published, some of which are given in Table (2.3).

For fully developed laminar flow, the friction factor of adiabatic single–phase in a pipeline with circle cross-section is calculated as:

$$f = \frac{64}{\mathrm{Re}} \qquad \mathrm{Re} < 2000 \tag{2.8}$$

In the case of turbulent flow, a number of correlations typically utilised for friction factor are developed. Some of the correlations for smooth pipes are expressed in Table (2.2) as follows:

Table 2.3: Existing Correlations for Homogeneous Model for Two–phase Pressure Drop

Category	Equation
Homogeneous Mode	$\frac{dP}{dz} = \frac{2 f G^2}{D \rho_{mix}}$ $\quad \mathrm{Re}_{mix} = \frac{GD}{\mu_{mix}}$
Author	**Viscosity model**
McAdams *et. al*., (1942)	$\mu_{mix} = \left(\frac{x}{\mu_g} + \frac{1-x}{\mu_l} \right)^{-1}$
Cicchitti (1960)	$\mu_{mix} = x\mu_g + (1-x)\mu_l$
Owens (1961)	$\mu_{mix} = \mu_l$
Dukler (1964)	$\mu_{mix} = (1-\beta)\mu_l + \beta\mu_g$
Weisman and Choe (1976)	$\mu_{mix} = \mu_l \exp\left(\frac{2.5}{1 - \frac{39\beta}{64}} \right)$ and $\mu_{mix} = \mu_g + (\mu_C - \mu_g)(\beta^{-1} - 1)$
Beattie and Whalley (1982)	$\mu_{mix} = \mu_l(1-\beta)(1+2.5\beta) + \mu_g\beta$

2.3.2.2 Correlations Based on the Multiplier Concept

In this approach, the pressure drop of two–phase flow is obtained using single–phase pressure drop via multiplying with the multiplier of a two–phase friction factor. A number of the multiplier correlations are reported in the literature and demonstrated in Table (2.4). In addition, there are many other correlations which are beyond the aim of this research work.

Table 2.4: Existing Correlations for Two–phase Pressure Drop Based on the Multiplier Concept in Horizontal Pipeline

Author	Correlation	Validity
Lockhart and Martinelli (1949)	$\Delta P_f = \frac{\Phi_L^2 \times \Delta P_L}{L}$; $\Phi_L^2 = 1 + \frac{C}{X} + \frac{1}{X^2}$ $X = \sqrt{\frac{\Delta P_L}{\Delta P_G}}$ or $X = \left(\frac{1-x}{x}\right)^{0.9}\left(\frac{\rho_G}{\rho_L}\right)^{0.5}\left(\frac{\mu_L}{\mu_G}\right)^{0.1}$ $\Delta P_i = \frac{2 f_i \rho_i V_i^2}{D}$ i represents gas or liquid phase	C value is dependent on the nature of the flow of individual phases: C = 20 for turbulent flow of both phases = 12 for laminar liquid and turbulent gas flow = 10 for turbulent liquid and laminar gas flow = 5 for laminar flow of both phases. It is valid near atmospheric pressure with mass velocities less than 1500 g/m^{2}s, and is applicable for vapor qualities from $0 < x \leq 1$
Bankoof (1960)	$\left(\frac{dP}{dL}\right)_{fric} = \frac{2 f_L m_{total}^2}{d\rho_L}\Phi_{Bf}^{7/4}$ $\Phi_{Bf} = \frac{1}{1-x}\left[1-\gamma(1-\frac{\rho_G}{\rho_L})\right]^{\frac{3}{7}}\left[1+x(\frac{\rho_L}{\rho_G}-1)\right]$ $\gamma = \frac{0.71 + 2.35\left(\frac{\rho_G}{\rho_L}\right)}{1+\left(\frac{1-x}{x}\right)\left(\frac{\rho_G}{\rho_L}\right)}$	It is applicable for vapor qualities from $0 < x < 1$
Chawla (1967)	$\left(\frac{dP}{dL}\right)_{fric} = \frac{2 f_G m_{total}^2}{d\rho_G}\Phi_{Chawla}$ $\Phi_{Chawla} = x^{1.75}\left[1+S\left(\frac{1-x}{x}\frac{\rho_G}{\rho_L}\right)\right]^{2.375}$ $S = \frac{1}{9.1\left[\frac{1-x}{x}(\mathrm{Re}_G Fr_H)^{-0.167}\left(\frac{\rho_L}{\rho_G}\right)^{-0.9}\left(\frac{\mu_L}{\mu_G}\right)^{-0.5}\right]}$	It is applicable for vapor qualities from $0 < x < 1$
Grönnerud (1972)	$\Delta P_{fric} = \frac{4 f_L L m_{total}^2}{2 d \rho_L}\Phi_{gd}$; $\Phi_{gd} = 1 + \left(\frac{dP}{dL}\right)_{Fr}\left[\frac{\left(\frac{\rho_L}{\rho_G}\right)}{\left(\frac{\mu_L}{\mu_G}\right)^{0.25} - 1}\right]$ $\left(\frac{dP}{dL}\right)_{Fr} = f_{Fr}\left[x + 4\left(x^{1.8} - x^{10} f_{Fr}^{0.5}\right)\right]$; $f_{Fr} = Fr_L^{0.3} + 0.0055\ (\ln\frac{1}{Fr_L})^2$;	Developed specifically for refrigerant. It is applicable for vapor qualities from $0 \leq x < 1$

	$Fr_L = \frac{m_{total}^2}{gd\rho_L^2}$ if $Fr_L \geq 1$ then $f_{Fr} = 1$	
Chisholm (1973)	$\left(\frac{dP}{dz}\right)_{fric} = \frac{2f_L m_t^2}{d\rho_L}\Phi_{Ch}^2$, $\left(\frac{dP}{dz}\right)_G = \frac{2f_G m_t^2}{d\rho_G}$, $\left(\frac{dP}{dz}\right)_L = \frac{2f_L m_t^2}{d\rho_G}$; $Y^2 = \frac{\left(dP/dz\right)_G}{\left(dP/dz\right)_L}$ $\Phi_{Ch}^2 = 1+(Y^2-1)\left[Bx^{(2-n)/2}(1-x)^{(2-n)/2}+x^{2-n}\right]$ *B* is function of mass flux and is calculated using different equations based on *Y* values	The flow is considered fully turbulent Re < 2000 to void undefined interval in the correlation. It is applicable for vapor qualities from $0 \leq x \leq 1$
Friedel (1979)	$\Delta P_{fric} = \frac{4f_L L m_{total}^2}{2d\rho_L}\Phi_{fr}^2$; $f_i = \frac{0.079}{\mathrm{Re}_i^{0.25}}$ $\mathrm{Re}_i = \frac{m_t d}{\mu_i}$ *i* can be gas or liquid phase $\Phi_{fr}^2 = \frac{E + 3.24FH}{Fr_H^{0.045} We_L^{0.035}}$; $Fr_H = \frac{m_t^2}{gd\rho_H^2}$ $We_L = \frac{m_t^2 d}{\sigma\rho_H}$, $E = (1-x)^2 + x^2\frac{\rho_L f_G}{\rho_G f_L}$ $F = x^{0.78}(1-x)^{0.224}$, $\rho_H = \left(\frac{x}{\rho_G}+\frac{1-x}{\rho_L}\right)^{-1}$ $H = \left(\frac{\rho_L}{\rho_G}\right)^{0.91}\left(\frac{\mu_G}{\mu_L}\right)^{0.19}\left(1-\frac{\mu_G}{\mu_L}\right)^{0.7}$	This correlation is applicable when the ratio of (μ_L/μ_G) < 1000 and is recommended for vapor qualities from $0 \leq x \leq 1$

2.3.2.3 Direct Empirical Models

In this model, the friction pressure drop of two–phase flow is described as a function of mixture density, mass flux, equivalent diameter, length, etc. without including the single phase pressure drop. Some of these models were developed by Lombardi–Pedrocchi (1972), Lombardi–Ceresa (1978), Bonfanti *et al*. (1982) and Lombardi–Carsana (1992). Furthermore, these correlations indicate the use of a homogeneous model to compute the accelerational and gravitational pressure drop. These correlations are believed to give more accurate results of the calculated total pressure drop rather than the individual terms of pressure drop.

This correlation is based on dimensionless terms and can be used only for adiabatic and diabatic conditions in a vertical upward single or two–phase flow. The total pressure drop is computed via the sum of pressure drop due to the acceleration,

elevation, and friction. In this method, therefore, the elevation pressure drop is proportional to the mixture density of two–phase flow, and the acceleration pressure drop is computed by the assumption of homogeneous flow. While the frictional pressure drop is obtained by one of the equations that are given in Table (2.2) for single–phase flow, this depends on the flow regime, and the specific volume is assumed to be equal to the homogeneous value. The most used correlation is described as follows:

Dimensionless terms are obtained as follows:

$$R_o = \frac{G^2 V_m D}{\sigma}\left(\frac{\mu_g}{\mu_l}\right)^{1/2} \tag{2.9}$$

$$C_e = \rho_l g \frac{(D - D_o)^2}{\sigma}\left(\frac{\mu_g}{\mu_l}\right) \qquad \text{where } D_o = 0.001 \text{ m} \tag{2.10}$$

$$C_e = 0, \quad \text{in case of } D \leq D_o \tag{2.11}$$

where the mixture viscosity can be calculated using equation (2.4) and the friction coefficient of the two–phase mixture, f_m can be obtained as follows:

$$f_m = \begin{cases} 0.046\, R_o^{-1/4} & R_o \supseteq 30\, C_e \\ 0.046\,(30\, C_e)\, R_o^{-1.25} & R_o \subset 30\, C_e \end{cases} \tag{2.12}$$

The total friction coefficient is obtained as:

$$f = f_g b_g + f_l b_l + f_m b_m \tag{2.13}$$

where f_g and f_l are the single–phase friction coefficients (Fanning type), calculated at the same total flow rate by one of the equations in Table (2.2), b_g b_l and b_m are the weight functions and are obtained as follows:

$$\left.\begin{aligned} b_g &= x^{600(V_l/V_g)} \\ b_l &= (1-x)^{2(V_g/V_l)} \\ \mathrm{b_m} &= 1 - b_g - b_l \end{aligned}\right\} \tag{2.14}$$

Then the pressure drop due to the friction, elevation and acceleration is calculated and added together to get the total pressure drop as follows:

$$\Delta P_f = \frac{2f}{D} G^2 V_m \Delta Z \tag{2.15}$$

$$\Delta P_e = \frac{g}{V_m} \Delta Z \tag{2.16}$$

$$\Delta P_a = G^2 \Delta V_m \tag{2.17}$$

$$\Delta P_T = \Delta P_f + \Delta P_e + \Delta P_a \tag{2.18}$$

where ΔP_f , ΔP_e , ΔP_a , and ΔP_T are friction, elevation, acceleration, and total pressure drop, respectively.

2.3.2.4 Flow Pattern Specific Models

Generally, two approaches are utilised to derive correlations for a specific flow pattern. The first approach is via empirical correlations that are found by correlating the experimental data of particular flow patterns. Many correlations have been developed, such as those from Baker (Govier and Aziz, 1972 and Hoogendoorn, 1959) for horizontal flows and Hughmark (1965) for horizontal slug flow. The second approach is to use a mechanistic model that takes into consideration the two–phase distribution in every flow pattern.

Several of these models have been introduced and developed. These include Taitel and Dukler (1976a) and Agrawal *et al*. (1973) for stratified flow; Wallis and Dobson (1973) and Dukler and Hubbard (1975) for slug flow and Hewitt; and Hall–Taylor (1970) for annular flow. Some of the empirical and mechanistic models for calculating pressure gradients for horizontal and vertical flows are given in Table (2.5).

Table 2.5: Existing Correlations for Flow Pattern Specific to Two–phase Pressure Drop for Horizontal, Vertical and Inclined Pipeline

Author	Flow type	Correlation
Hoogendoorn (1959)	Stratified smooth and wavy	$\frac{\Delta P}{\Delta Z} = \frac{Cx^{1.45} G^2}{2 D \rho_g}$, C is a constant depends on a pipe relative roughness and fluid used.
Duns and Ros (1963)	Bubbly	$\left(\frac{dP}{dz}\right)_f = \frac{f_m \rho_L V_{SL} V_m}{2 g_C D}$
	Mist	$\left(\frac{dP}{dz}\right)_f = \frac{f \rho_G V_{SG}^2}{2 g_C D}$
Govier and Aziz (1972)	Stratified	$\phi_g = \frac{15400 \quad X}{G_{SL}^{0.8}}$
Beggs and Brill (1973)	Any flow pattern	$\left(\frac{dP}{dx}\right)_f = \frac{2 f \rho_{mix} V_{mix}^2}{D}$, $f = f_{ns} \frac{f}{f_{ns}}$, $\frac{f}{f_{ns}} = e^S$ $S = \frac{\ln(y)}{-0.0523 + 3.182 \ln(y) - 0.8725 (\ln(y))^2 + 0.01853 (\ln(y))^4}$ $y = \frac{\lambda}{\alpha^2}$, $\lambda = \frac{V_{SL}}{V_{SL} + V_{SG}}$, $\alpha = \frac{A \lambda^B}{Fr^C}$ *A*, *B*, and *C* are constants depend on flow pattern
Dukler *et al*. (1976)	Stratified	$\left(-\frac{\Delta P}{\Delta Z}\right)_m = \frac{f_m G^2}{2 D \rho_m}$ $f_m = F \eta J$ $J = 0.0056 + 0.5 \mathrm{Re}^{-0.32}$ $\mathrm{Re} = \frac{DG}{\mu_m}$ $F = 1 + \frac{\gamma}{(1.281 - 0.478\gamma + 0.444\gamma^2 - 0.094\gamma^3 + 0.00843\gamma^4)}$ $\gamma = -\ln(1-\beta)$; $\eta = \frac{\left(\rho_l / \rho_m\right)(1-\beta)^2}{(1-\alpha) + \left(\rho_g / \rho_m\right)\beta^{2/\alpha}}$
Chawla (1967)	Stratified	$\left(\frac{\Delta P}{\Delta Z}\right)_m = \frac{0.3164 \quad G^2 x^{7/4}}{2 D \rho_g (GD/\mu_g)} \left(1 + \frac{(1-x)\rho_g}{x \varepsilon_c \rho_l}\right)^{19/8}$ $\varepsilon_c = 9.1((1-x)/x)(\mathrm{Re}_l Fr_l)^{-1/6} (\rho_g/\rho_l)^{0.9} (\mu_g/\mu_l)^{0.5}$ $\mathrm{Re}_l = \frac{DG(1-x)}{\mu_l}$; $Fr_l = \frac{G^2 (1-x)^2}{\rho_l^2 g D}$

Agrawal *et al*. (1973)	Stratified	$\left(\frac{\Delta P}{\Delta Z}\right)_L = \frac{(\tau_{wg} P_g + \tau_i W_i)}{A_g}$ $\left(\frac{\Delta P}{\Delta Z}\right)_G = \frac{(\tau_{wl} P_l + \tau_i W_i)}{A_l}$ $\tau_{wg} = \frac{f_g \rho_g u_g^2}{2}$; $\tau_{wl} = \frac{f_l \rho_l u_l^2}{2}$; $\tau_i = (0.804\ \mathrm{Re}_g^{-0.285})^2 \rho_g u_g^2$ $W_i = 2D\sqrt{(h_l/D) - (h_l/D)^2}$; $h_l/D = 0.5(1 - \cos(\gamma/2))$
Mukherjee and Brill (1985)	Bubble and Slug	$\Delta P_f = \frac{fLV_m^2 \gamma_m}{2gD}$; $V_m^2 = V_{sl} + V_{sg}$; $\gamma_m = H_l \gamma_l + H_g \gamma_g$
	Stratified	$A_g \frac{dP}{dL} = -(\tau_{wg} P_g + \tau_i W_i) - \gamma_g A_g \sin\theta$ pressure drop in the gas and liquid phase is calculated with the same manner.
	Annular	$\Delta P_f = \frac{f_c \gamma_{ns} V_m^2 L}{2gD}$; $f_c = f_r \times f_{ns}$

2.4 Review of the Effect of Some Parameters on Pressure Drop, Flow Pattern and Liquid Holdup

As mentioned earlier the co–current gas–liquid flow in pipelines is complicated by several variables, including gas and liquid velocities, viscosities, densities, surface tension, pipe inclination angle, pipe diameter, and roughness. This section presents a general review of the effect of some of these parameters on the pressure drop, liquid holdup, and flow regime in conduits with different positions provided.

2.4.1 Effect of Fluid Property

The existence of any flow pattern depends on different parameters, for instance the fluid properties of two–phase, the flow rate, and the pipe characteristics, including diameter, orientation angle, shape, etc. Generally, the transition from one flow pattern to another does not immediately occur, except the transition from the stratified flow to intermittent at low gas velocities. The following flow subregimes are considered as stratified flow and are identified by Andritsos and Hanratty (1987), Andritsos (1992), Barnea *et al*. (1980), Kokal and Stanislav (1989), and Johnson *et al*. (2009):

- A two–dimensional (2-D) wave regime in which the interface is covered by small amplitude waves. In the case of horizontal flows, these waves are

generated due to the pressure variations in the phase with the wave slop. They increase in amplitude and in wavelength as they propagate downstream.

- A Kelvin–Helmholtz (K–H) wave region with large amplitude irregular waves, also known as a roll wave. These waves are associated with pressure variations in phase with the wave height (K–H instability).
- An Atomization region, where droplets or liquid filaments are broken off from the crests of the K–H waves and deposited on the pipe wall. Moreover, the liquid begins to climb up the pipe wall and the average shape is not approximated by a flat horizontal plane, at least for small conduit diameters ($D_{pipe} < 5$ cm) and low viscosity liquids.

The effect of fluid properties is considered as one of the significant parameters in two–phase flow phenomena, and it directly influences flow pattern, pressure drop, and liquid holdup. Over the past five decades, several authors have studied this effect (Hoogendoorn, 1959, Weisman *et al*., 1979, and Andritsos, 1986). One of the most frequently examined fluid properties is liquid viscosity. Hoogendoorn (1959) performed a two–phase experiment that utilized air–water and air–oil in horizontal smooth pipelines with an inner diameter range from 0.024 to 0.14 m, and rough pipes with an inside diameter of 0.05 m under various operating conditions.

Based on the results obtained from this experiment, Hoogendoorn found that the pipe diameter and liquid viscosity had no significant effect on the transition among the flow patterns. This finding was contradicted later by Andritsos (1986) and Carson (1989). Hoogendoorn (1959) noted that stratified flow took place at higher air flow rates with air–oil mixtures because of the surface tension effect. Moreover, a few years later, Hoogendoorn (1961) investigated the effect of gas density using superheated Freon–11 as the gas fluid. The increase in gas density was reported not to have a significant influence on the transition to slug or plug flow, but reduces drastically the onset of atomization. Hanratty and Hershman (1961) studied the influence of fluid physical properties on the flow pattern in a horizontal pipeline. They found that the increase of liquid viscosity slightly reduces the needed gas

velocity for transition to roll ripples, while adding the surfactant reduced the disturbance of the surface.

The impact of fluid properties on two–phase flow patterns in horizontal conduits was also investigated by Weisman *et al*. (1979). He found that the flow pattern maps for glycerol–water solutions were slightly different from air–water system flow maps. A similar trend was noted when using a surface active agent (Aliquat 221), with the only difference being that the smooth–wavy transition was noted to take place at higher gas flow rates.

In the experiments with boiling Freon–113, the gas density fluctuated at pressure values of 1 and 4 atm, but the effect of the density was quite complicated compared to liquid viscosity and surface tension, which were simultaneously significantly decreased with respect to the air–water case. Andritsos and Hanratty (1987) and Andritsos *et al*. (1989) performed a systematic experimental study of the effect of liquid viscosity ranging from 0.001 to 0.08 Pa–s, on flow pattern. They reported that increasing liquid viscosity with a lower liquid loading was required for the slug transition at low gas flow rates. Furthermore, the region with two–dimensional waves reduces in size with increasing viscosity, while the transition to roll waves is only slightly affected.

The impact of gas density on the flow behaviour in gas–liquid flow in horizontal and inclined pipelines has been experimentally investigated by Christina *et al*. (2011) using air–carbon dioxide–helium fluid. They found that the gas density strongly affects the transition of smooth to 2-D waves and later to K–H waves. Furthermore, the increase of gas density destabilized the flow and the transition to 2-D and K–H waves that occur at low gas velocities. The same observation also was reported for the transition to the atomization region and annular flow patterns that are directly related to the roll wave's onset.

2.4.2 Effect of Surface Tension

A number of limited experimental results have been shown on the effect of surface agents on two–phase flow parameters (liquid holdup, pressure drop). This is in comparison to single–phase flow, where considerable attention has been focussed. The effect of surface tension reduction on flow pattern, liquid holdup and pressure drop has been investigated and the outcome of these studies is summarized as follows.

2.4.2.1 *Effect of Surfactant on Flow Pattern*

The reduction of surface tension is one of the factors that can influence the flow pattern. Hand *et al.* (1991) conducted a two–phase flow of air–water and air–surfactant solution in a horizontal "Perspex" pipe with 0.0935m diameter and around 13m in length. The air and water flow rates were delivered in the system up to 0.13 and 0.003m^3/s, respectively. They performed a sensitivity analysis of the effect of surface tension reduction on the flow pattern, liquid holdup and pressure drop. They added a small amount of surface–active agent with different liquid flow rates of 1×10^{-4} m^3/s, 3.33×10^{-4} m^3/s, and 1×10^{-3} m^3/s, respectively. The stratified flow pattern typically was observed at higher rates of air flow.

This is a well–known phenomenon and was given by Franklin (1965), Davies and Rose (1965) and Miles (1966) who noted that surface–active agents dampen capillary waves in a closed basin. That saturated air created some waves on the liquid film flowing on a flat plate was also seen by Craik (1968). Van Rossum (1959) observed that at fully developed velocity, regular two–dimensional waves (i.e. stratified with wave) occurred on the water film of 0.6 mm thickness in a horizontal rectangular pipe and increased from 7 to 10 m/s via adding the Teepol surfactant. Thwaites *et al*. (1976) studied the flow down of two–phase air–water flow co–current annular flows with and without surfactant (Separan AR30) in 0.0318 m diameter and 10m long. They concluded that the addition of surfactant (100 ppm) to water led to surface waves becoming moist. As a result of that the roll wave frequency decreases by half and increases the mean film thickness.

These results for annular flow have a similar behaviour to those observed in the study by Hand *et al.* (1991) for stratified category flow patterns. The techniques employed in Hand *et al* (1991) were unable to identify any change in the roll waves' frequency due to the addition of the surfactant (Chemtreat 271).

Hanratty and Hershman (1961) examined the effect of surfactant using (sodium lauyrl sulphate agent) on the transition to the roll wave flow in a rectangular pipeline. They noted that the stratified flow pattern was developed and the transition to stratified plus roll waves can take place from a smooth stratified liquid film. Furthermore, based on their results and suggestion, the reduction in the stratified with waves region could be due to the increase of flow rate at which energy is dissipated to the liquid phase, or to the increased the viscosity of the film surface. However, the effect of adding surfactant was noted to be insignificant on the transition to stratified with roll waves. Hanratty and Hershman (1961) also noted that the surface tension has no effect on the transition to roll wave flow. Moreover, Weisman *et al*. (1979) noted that the use of a surface active agent (Aliquat 221) has a slight impact on the flow maps of glycerol–water solution in comparison with the air–water flow maps, with the only difference at high gas flow rates where the smooth–wavy transition takes place.

Christina *et al*. (2011) investigated the reduction of surface tension of water from 0.072 to 0.035 N/m using a butanol aqueous solution on the flow pattern. It was reported that at the same liquid flow rate, a significant reduction for gas flow rate is needed for the onset of the first disturbances. Both transitions of smooth and later to 2-D and K–H waves respectively are moved to lower gas flow rates, therefore the 2-D wave transition is more obviously affected.

2.4.2.2 *The Effect of Surfactant on Holdup*

Minami *et al*. (1987) studied the effect of surfactant on two–phase liquid holdup in a horizontal pipe about 400 m long and 0.078 m diameter. Three different mixtures of two–phase flow were utilized (air–kerosene, air–water, and air–water–surfactant). For a very foamy mixture with very high two–phase superficial velocities, a crucial

decline in the liquid holdup was noted, while at very low velocity experiments the liquid holdup was not affected.

It was concluded that at high turbulence, generated due to high superficial velocities with very foamy mixture, small bubbles of air were expected to form in the liquid phase, which leads to a decrease in the actual liquid holdup. The existence of the foam near the interface therefore would be most likely to increase the interfacial stress, resulting in a decrease in the difference of slip velocity between the phases and thus reducing the final liquid holdup. In contrast to the results of air–water, and air–water with surfactant, they reported that the effect of surface tension was insignificant. In addition, at non–foamy water with surfactant mixture, the liquid holdup stayed constant compared to air–water flow liquid holdup.

Hand *et al.* (1991) has classified the effect of surfactant on holdup based on the gas flow rates. First of all, when the gas volumetric flow rate is less than 0.02 m^3/s the liquid holdup was not influenced via the reduction in surface tension where the flow pattern was observed as a smooth stratified flow. When the gas volumetric flow rate is increased to between 0.02 and 0.07 m^3/s a significant increase in the liquid holdup was noted, and different flow patterns were observed in this flow rate range. The observed flow patterns are stratified with wave, roll wave, and long roll wave with droplet. At gas volumetric flow rates above 0.08 m^3/s there was no significant difference between water and surfactant solution holdup. Also different flow patterns were observed, such as stratified roll wave with droplet and film with droplet.

In addition, Hart *et al*. (1989) studied the effect of surface tension reduction (from 0.072 to 0.046 N/m) on two–phase air–water flow in a horizontal “copper” pipeline with 0.051 m diameter and around 17 m long. They conducted experimental work considering a small amount of liquid, similar to conditions found in gas condensate pipelines ($0 < \alpha_l < 0.06$). The operating gas and liquid superficial velocities ranged from 5 to 30m/s and from 0.00025 to 0.08 m/s, respectively. The results concluded that the reduction of interfacial tension by adding 0.11 wt. % of Tween 80 solution

decreased the surface tension of water from 0.072 to 0.038 N/m, but had no influence on the liquid holdup and wetted wall fraction.

Hart *et al*. (1989) were concerned with flow rates in which the low liquid loading was less than 0.06, where it is likely that the holdup measurement technique used could not have been precise enough to identify small changes in the liquid holdup. An increase in the liquid holdup may be a consequence of the dampening of the surface disturbances owing to dissipation, or an increased resistance to pressure and shear stress forces in the viscous surface layer.

2.4.2.3 The Effect of Surfactant on Pressure Drop

In contrast, the pressure drop was reported as the only parameter affected by the reduction of surface tension at air flow velocities ranging from 0.02 and 0.08m/s when pressure drop was decreased (Hand *et al.*, 1991). Thwaites *et al.* (1976) found that the reduction of pressure drop as a result of surfactant is similar to those reported in the study by Hand *et al.* (1991). Hart *et al*. (1989) observed an increase in the pressure drop by 15% due to the addition of surfactant, but this observation was not substantiated by Hand *et al.* (1991).

2.4.3 Effect of Two–phase Superficial Velocity

The superficial velocity is expressed by the average velocity of the fluid that is spread into the pipe and is usually described as the volumetric flow rate divided via the pipe cross sectional area. It is considered as one of the factors that affect the system parameters of two–phase flow in a horizontal tube. The effect of two–phase superficial velocities was examined by Abdul–Majeed (1995). He performed an experimental study on two–phase air–kerosene flow in a horizontal pipe with 0.0508m diameter and 36 m long. The air and kerosene superficial velocities ranged from 0.3−50 m/s and 0.006−1.5 m/s, respectively. The liquid holdup obtained ranged from 0.009−0.61, where different flow patterns were observed. The flow pattern observed at low gas and liquid superficial velocities below 0.5 and 0.05 m/s respectively was a stratified flow, which is also observed at higher than 0.5 m/s of gas

velocity. The slug flow was observed when the gas superficial velocity was increased to between 1–13 m/s, and when the superficial velocity of the gas increased further the wavy and annular flow were observed.

In addition, based on Abdul–Majeed (1995) and Minami *et al.* (1987) data, a mechanistic model of Taitel *et al.* (1976) was developed for assessing the liquid holdup in two–phase horizontal pipes. Badie *et al.* (1999) collected experimental data for pressure gradient and liquid holdup for air–water and air–oil in a horizontal pipe with 0.079 m diameter. The result concluded that the increase of the liquid superficial velocity at a constant gas superficial velocity led to an increase in liquid holdup. In contrast, the pressure drop had a significant increase even for very low liquid superficial velocity and in particular at high gas superficial velocity. On the other hand, it was noted that the increase of gas superficial velocity at constant liquid superficial velocity decreased the liquid holdup because of the higher drag exerted on the liquid fluid at the interface by the faster travelling of the gas phase, while the pressure drop increased proportional to the gas velocity.

Meng *et al.* (2001) performed numerous experiments with a small amount of liquid loading in an acrylic pipeline with 0.05 m diameter and inclination angle between $-2 \geq \theta \leq 2$. The gas and liquid superficial velocities ranged from 5–25 m/s and 0.001–0.053 m/s, respectively. Based on the result reported, there is a wide range of gas superficial velocity that corresponds to a transition from stratified to intermittent flow at a low input liquid fraction. It was also noted that liquid entrainment can take place in the gas phase at relatively low velocities, and simultaneously the droplet deposition occurs. In other words, the increase of gas superficial velocity had no influence on the entrainment fraction of the liquid over various velocities. Furthermore, it was observed that the increase of liquid superficial velocity increased the liquid entrainment fraction. In the region of annular flow, it was noted that the increase of liquid flow rate led to a reduction in the liquid–film velocity, and also in liquid holdup and pressure gradient, while it increased the entrainment flow rate.

Olive *et al.* (2003) have studied the effect of low liquid loading in near horizontal pipes of gas–liquid flow. They investigated the effect of pipe inclination angle, low liquid loading, and viscosity using different liquid fluid (water and oil), on pressure drop and liquid holdup. The gas superficial velocity was constant at 5, 10, 15, 20, and 25 m/s, and the liquid loading ranged from 300 to 1800 m^3/MMm^3. In the case of air–oil two–phase flow, a remarkable phenomenon was noted at specific high gas velocities. An increase of liquid loading significantly decreased the liquid film flow rate, pressure gradient and liquid holdup. Nonetheless, this phenomenon was not reported at the same liquid loading and gas velocity for air–water flow as a result of the difference between water and oil physical properties.

In the case of air–water two–phase flow, two new remarkable phenomena were noted. At relatively high liquid loadings and specific low gas superficial velocities, the relationship between gas superficial velocity and the liquid holdup is proportional. The reason for this is due to the liquid film spreading up the pipe wall, leading to an increase of the wall frictional drag to the liquid film. Moreover, at relatively high liquid loading and a specific range of high gas velocities, they observed the same relationship; an increase of superficial gas velocity led to an increase of the liquid holdup. These conditions of gas velocities and liquid loading are referred to as a flow pattern transition from stratified wavy to annular flow. At relatively low liquid loading in the air–water flow, the wall perimeter that has been made wet by the water was not increased significantly with respect to increasing the gas superficial velocity from 5 to 10 m/s, while at relatively high liquid loadings, the wet wall fraction increased sharply with increasing gas velocity.

2.4.4 Effect of Initial Liquid Holdup

Badie *et al*. (1999) investigated the low liquid loading effect on the pressure drop and liquid holdup in horizontal pipelines. They observed that adding a small amount of liquid (water) leads to increase in the pressure gradient compared to a single gas phase flow, where a similar observation was reported by Meng *et al*. (2001). When oil was the liquid used, the pressure drop data increased compare to air–water pressure drop. The reason for that is because the oil phase creates a rougher interface with the gas

fluid in comparison to water. The oil phase also maintains a very thin liquid film along the upper wall and a thicker film on the bottom wall that increases the friction with the pipe wall.

Olive *et al*. (2003) have also investigated the effect of low liquid loading (less than 1100 m^3/MMm^3) in near horizontal pipes of gas–liquid flow on the pressure drop and liquid holdup. They noticed that the pressure gradient increases as the liquid loading increases, where the pressure drop of air–oil is higher than air–water. This was due to the viscosity difference between two liquid fluids.

2.4.5 The Effect of Inclination Angle

Several authors have investigated the two–phase gas–liquid flow in inclined pipelines. Beggs and Brill (1973) noted that the pipe deviation angle has an effect on the pressure drop and liquid holdup. Barnea *et al*. (1980) concluded that in the vertical pipe down flow, the stratified region was developed as the pipe inclination angle increases, and higher liquid flow rates are needed in order to get intermittent flow. On the other hand the flow in an upward inclination can lead to the expansion of the intermittent flow region while stratified flow shrinks in a small bell–shaped region. At angles greater than 10 degrees the observation of stratified flow is impossible.

Experimental studies with down flow inclinations were conducted by Kokal and Stanislav (1989) and Grolman *et al*. (1996). Woods *et al*. (2000) studied experimentally the transition to intermittent flow in downward incline tubes. They noted that large amplitude small wavelength waves, which become visible in horizontal flows at the transition to slug flow, are reduced in conduits that are deviated slightly downward from the horizontal.

Recently Lioumbas and co–workers (2005, 2006, and 2009) systematically studied the effects of surfactant on the interfacial structure and also on the transition from a smooth stratified to a wavy stratified flow in slightly inclined conduits. It has been proposed that the transition of smooth interface to wavy in a downward flow can be the result of transition from laminar to turbulent flow within the liquid layer. The

addition of a small amount of (non–ionic) surfactant strongly affects the interfacial features (e.g., damping of small–amplitude waves) and the flow field inside the liquid layer, leading to a significant reduction in the pressure drop.

The existence of surfactant has a significant influence on the transition to almost all flow patterns, such as the slug froth region, which was shown to shift to higher liquid flow rates than those seen for tap water, while the atomization flow pattern becomes narrower. Christina *et al*. (2011) investigated the effect of gas density and surface tension on the flow patterns of gas–liquid flow in horizontal and inclined pipes. They found that even a small inclination of the pipe angle downward can result in a significant expansion in the stratified flow region. It also noted that the smooth stratified flow is not observed at angles higher than nearly 1 degree. In addition, two different types of waves were observed in the horizontal conduit (low amplitude waves reminiscent of 2-D waves in horizontal flow K–H waves) for all studied pipe inclination.

2.5 Conclusions

The previous literature review provides information about gas hydrate formation focusing on critical places where this can occur, such as lower sections of the pipe. It is essential to conduct detailed numerical simulation experiments in standard and bend pipes using CFD codes, which are given more attention in Chapter 4, where different operating conditions were investigated to find out the effect on the flow pattern and droplet hydrodynamic. It also demonstrated different techniques that can be used when the hydrate plug happens.

Moreover, the fundamental concepts of two–phase flow in pipelines, including how the velocity, density and viscosity can be calculated at homogeneous and non–homogeneous flows have been reviewed. Various developed empirical correlations for liquid holdup and pressure drop were also illustrated. A specific correlation was used for validation of CFD results, which will be seen in Chapter 5. A large number of models have been produced and can be found in the literature (Fan *et al*., 2005).

Finally, the effect of various factors, such as gas and liquid superficial velocity, pipe inclination, fluid property, and the surface tension on the pressure drop, liquid holdup, and the flow pattern behaviour have been analysed. The experimental investigations that have been done for two–phase flow in horizontal, near horizontal and inclined pipelines have been reviewed. The study of two–phase flow in pipes is complicated because of the measurements of pressure drop and liquid holdup at varying initial liquid holdup, and gas–liquid velocity. Stratified and dispersed two–phase flows have not been studied in detail and not many numerical investigations have been performed. A comprehensive study is given in Chapter 5 for two–phase flow through horizontal pipelines at low liquid holdup to understand the behaviour of pressure drop and liquid holdup.

2.6 Bibliography

Abdul-Majeed, G. H. (1996). Liquid holdup in horizontal two-phase gas-liquid flow. *Journal of Petroleum Science and Engineering,* 15, 271-280.

Agrawal, S. S., G. A. Gregory and G. W. Govier (1973). An analysis of stratified two phase flow in pipes, *Canadian Journal of Chemical Engineering*, 51, 280-286.

Ali, S. F. (2009). Two phase flow in large diameter vertical riser. *PhD thesis*, Cranfield University.

Amadeu K. S., C. A. Koh, and E. D. Sloan (2009). Clathrate Hydrates: From Laboratory Science to Engineering Practice, *Ind. Eng. Chem. Res.*, *48,* 7457–7465.

Andritsos, N. (1986). Effect of pipe diameter and liquid viscosity on horizontal stratified flow. *Ph.D. Thesis***,** University of Illinois.

Andritsos, N., L. Williams and T. J. Hanratty (1989). Effect of Liquid Viscosity at the Stratified-Slug Transition in Horizontal Pipe Flow. *International Journal of Multiphase Flow*, 15(6), 877-892.

Andritsos, N. and T. J. Hanratty (1987). Interfacial Instabilities for Horizontal Gas-Liquid Flows in Pipelines. *International Journal of Multiphase Flow*, 13(5), 583-603.

ANSYS FLUENT 12.1, Theory Guide (2010).

Armand, A. A. (1946). The resistance during the movement of two-phase system in horizontal pipes. Izvestia Vses. Teplo. Inst. 1, 16-23.

Badie, S., C. P. Hale, C. J. Lawrence and G. F. Hewitt (2000). Pressure gradient and holdup in horizontal two-phase gas–liquid flows with low liquid loading. *International Journal of Multiphase Flow,* 26(9), 1525-1543.

Baker, O. (1954). Design pipelines for simultaneous flow of oil and gas. *Oil and Gas Journal*, 53, 26.

Bankoff, S. G. (1960). A variable density single-fluid model for two-phase flow with particular reference to steam-water flow. *Journal of Heat Transfer*, 82, 265–272.

Barnea, D. (1987). A unified model for predicting flow pattern transitions for the whole range of pipe inclinations. *International Journal of Multiphase flow*, 13(1), 1-12.

Barnea, D., O. Shoham, Y. Taitel and A. E. Dukler (1980). Flow pattern transition for gas-liquid flow in horizontal and inclined pipes. *International Journal of Multiphase Flow*, 6, 217-225.

Beattie, D. R. H. and P. B. Whalley (1982). A simple two-phase frictional pressure drop calculation method, *International Journal of Multiphase Flow*, 8, 83–87.

Beggs, H. and J. P. Brill (1973). A study of two-phase flow in inclined pipes. *Journal of Petroleum Technology*, 25, 607-617.

Blasius, H. (1913). Das Ähnlichkeitsgesetz bei Reibungsvorgängen in Flüssigkeiten. Forschungs-Arbeit des Ingenieur-Wesens 131.

Bonfanti, F., I. Ceresa and C. Lombardi (1982). Two-phase densities and pressure drops in the low flow rate region for different duct inclinations. *Proceedings in the 7th International Heat Transfer Conference*, Munich.

Bonnecaze, R., W. Erskine and E. Greskovich (1971). Holdup and pressure drop for two-phase slug flow in inclined pipelines. *AIChE Journal*, 17, 1109-1113.

Brauner, N. and D. Barnea (1986). Slug/Churn Transition Upward Gas-Liquid Flow. *Chemical Engineering Science*, 41, 159-163.

Butterworth, D. (1975). A comparison of some void-fraction relationships for concurrent gas liquid flow. *International Journal of Multiphase Flow*, 1, 845-850.

Carson, K. (1989). An analysis of flow regime maps using an air-water system at atmospheric conditions. *Bsc. Eng. Research Project*, Department of Chemical Engineering, The Queen's University of Belfast.

Chawla, J. M. (1967). Warmeubergang und Druckabfall in waagrechten Rohren bei der Stromung von verdampfenden Kaltemitteln. VDI-Forschungsheft, No. 523.

Chen, J. and P. Spedding (1981). An extension of the Lockahart–Martinelli theory of two phase pressure drop and holdup. *International Journal of Multiphase Flow*, 7, 659–675.

Chen, J. and P. Spedding (1983). An analysis of holdup in horizontal two-phase gas–liquid flow. *International Journal of Multiphase Flow*, 9, 147–159.

Chisholm, D. (1973). Pressure gradients due to friction during the flow of evaporating two-phase mixtures in smooth tubes and channels. *International Journal of Heat and Mass Transfer*, 16, 347–358.

Cicchitti, A., C. Lombardi, M. Silvestri, G. Soldaini and R. Zavttarelli (1960). Two-phase cooling experiments: pressure drop, heat transfer and burnout experiments, *Energia Nucleare*, 7 (6), 407-425.

Colebrook, C. F. (1938). Turbulent flow in pipes with particular reference to the transition region between the smooth and rough pipe laws. *Journal of Institution of Civil* Engineers, 11, 133-156.

Craik, A. D. D. (1968). Wind-generated waves in contaminated liquid films. *Journal of Fluid Mechanics*, 31(1), 141-161.

Davies J. D. and R. W. Rose (1965). On the damping of capillary waves by surface films, *Proceedings of the Royal Society of London*, *A*, 286, 218-234.

Drew, T. B., E. C. Koo and W. H. McAdams (1932). The friction factor for clean round pipes. *Trans. AIChE*, 28, 56-72.

Dukler, A. E and Y. Taitel (1977). Flow regime transitions for vertical upward gas-liquid flow. *Paper presented at 70th Annual meeting of AICh*E, New York.

Dukler, A. E. and M. G. Hubbard (1975). A model for gas-liquid slug flow in horizontal and near horizontal tubes. *Industrial and Engineering Chemistry Fundamentals*, 14(4), 337-347.

Dukler, A. E., M. Wicks, and R. G. Cleveland (1964). Frictional pressure drop and holdup in two-phase flow, Part A- A comparison of existing correlations for pressure drop and holdup, Part B- An approach through similarity analysis. *AIChE Journal*, 10, 38-51.

Duns**,** H. Jr. and N. C. J. Ros (1963). Vertical flow of gas and liquid mixtures in wells. *Proceedings in the 6th World Petroleum Congress*, Frankfurt, 451-465.

Eaton, B. A., D. E. Andrews, C. R. Knowles, I. H. Silberberg and K. E. Brown (1967). The prediction of flow patterns, liquid holdup and pressure losses occurring during continuous two-phase flow in horizontal pipelines. *Journal of Petroleum Engineering*, 19, 815–828.

Fan, Y. Q., Q. Wang, H. -Q Zhang, C. Sarica and T. J. Dannielson (2007). A model to predict liquid holdup and pressure gradient of near horizontal wet gas pipelines. *Society of Petroleum Engineering Project*, Facilities & Construction, 2(2), 1-8.

Filonenko, G. K. (1948). On friction factor for a smooth tube. *All Union Thermotechnical Institute*, Izvestija VTI, No. 10, Russia.

Flanigan, O. (1958). Effect of uphill flow on pressure drop in design of two-phase gathering systems. *Oil and Gas Journal*, 56, 132.

Frankhn, B. (1774). On the stilling waves by means of oil. *Philosophical Transactions of the Royal Society*, 64, 445-460.

Friedel, L. (1979). Improved friction pressure drop correlations for horizontal and vertical two-phase flow. *European Two-phase Flow Group Meeting*, Ispra, Italy.

Gómez, L., O. Shohan and Y. Taitel (2000). Prediction of slug liquid holdup: horizontal to upward vertical flow. *International Journal of Multiphase Flow*, 26, 517-521.

Govier, G. W. and K. Aziz (1972). The flow of complex mixtures in pipes. Van Nostrand Reinhold Company, New York, NY.

Gregory, G., M. Nicholson and K. Aziz (1978). Correlation of the liquid volume fraction in the slug for horizontal gas–liquid slug flow. *International Journal of Multiphase Flow*, 4, 33-39.

Grolman, E., N. C. J. Commandeur, E. C. Baat and J. M. H. Fortuin (1996). Wavy to slug flow transition in slightly inclined gas-liquid pipe flow. *AIChE Journal*, 42, 901.

Grönnerud, R. (1972). Investigation in liquid holdup, flow resistance and heat transfer in circular type evaporators, Part IV: Two-phase resistance in boiling refrigerants. *Bulletin de l'Inst. Du Froid*, Annexe 1972-1.

Guzhov, A., V. Mamayev and G. Odishariya (1967). A study of transportation in gas–liquid systems. *In 10th International Gas Conference*, Hamburg, Germany.

Hand, N. P., P. L. Spedding and S. J. Ralph (1992). The effect of surface tension on flow pattern, holdup and pressure drop during horizontal air-water pipe flow at atmospheric conditions. *Chemical Engineering Journal*, 48, 197-210.

Hanratty, T. J. and A. Hershman (1961). Initiation of Roll Waves. *AIChE Journal*, 7, 488-497.

Hart, J., P. J. Hamersma and J. M. Fortuin (1989). Correlations predicting frictional pressure drop and liquid holdup during horizontal gas–liquid pipe flow with a small liquid holdup. *International Journal of Multiphase Flow*, 15(6), 947-964.

Hewitt G. F. and S. Jayanti (1993). To churn or not to churn. *International Journal of Multiphase Flow*, 19, 527-529.

Hewitt, G. F. (1982). Chapter 2: flow regimes and Chapter 10: Measurement of Two-Phase Flow Parameters. In: *Handbook of Multiphase Systems*, Edited by Hetsroni, G. Publisher: Hemisphere/McGraw Hill, Washington.

Hewitt, G. F. and D. N. Roberts (1969). Studies of two-phase patterns by simultaneous x-ray and flash photography. *Atomic Energy Research Establishment Report*, AERE-M 2159, Harwell, England.

Hewitt, G.F. and N. S. Hall-Taylor (1970). Annular Two-Phase Flow. Pergamon Press, New York.

Hoogendom C. J. (1959). Gas-liquid flow in horizontal pipes. *Chemical Engineering Science*, 9, 205-217.

Hubbard, M.G. and A.E. Dukler (1966). The characterization of flow regimes for horizontal two-phase flow: statistical analysis of wall pressure fluctuations.

Proceedings of the 1966 Heat Transfer and Fluid Mechanics Institute, 100-121.

Hughmark, G. A. (1962). Holdup in gas–liquid flow. *Chemical Engineering Progress*, 58, 62-65.

Hughmark, G. A. (1965). Holdup and heat transfer in horizontal slug gas-liquid flow, *Chemical Engineering Science*, 20, 1007-1010.

Kokal, S. L., J. F. Stanislav and J. F (1989). An experimental study of two phase flows in slightly inclined pipes: flow patterns. *Chemical Engineering Science*, 44(3), 665-679.

Lioumbas, J. S., C. Kolimenos and S. V. Paras (2009). Liquid layer characteristics in gas-liquid flow in slightly inclined pipes: effect of non-ionic surfactant additives. *Chemical Engineering Science*, 64, 5162-5172.

Lioumbas, J. S., A. A. Mouza and S. V. Paras (2006). Effect of surfactant additives on co-current gas-liquid downflow. *Chemical Engineering Science*, 61, 4605-4616.

Lioumbas, J. S., S. V. Paras and A. J. Karabelas (2005). Cocurrent stratified gas-liquid downflow-influence of the liquid flow field on interfacial structure. *International Journal of Multiphase Flow*, 31, 869-896.

Lockhart, R. and R. Martinelli (1949). Proposed correlation of data for isothermal two-phase two component flow in pipes. *Chemical Engineering Progress*, 45, 39-48.

Lombardi, C. and C. G. Carsana (1992). A dimensionless pressure drop correlation for two phase mixtures flowing upflow in vertical ducts covering wide parameter ranges. *Heat and Technology*, 10, 125-141.

Lombardi, C. and E. Pedrocchi (1972). A pressure drop correlation in two-phase flow. *Energia Nucleare*, 19(2), 91-99.

Lombardi, C. and I. Ceresa (1978). A generalized pressure drop correlation in two-phase flow. *Energia Nucleare*, 25(4), 181-198.

Matsui, G. (1984). Identification of flow regimes in vertical gas-liquid two phase flow using differential pressure fluctuations. *International Journal of Multiphase flow*, 10(6), 711-720.

McAdams, W. H., W. K. Woods and R. H. Jr. Heroman (1942). Vaporization inside horizontal tubes. II. Benzene-oil mixtures, *Trans ASME*, 64, 193-200.

McQuillan, K. W. and P. B. Whalley (1985). Flow patterns in vertical two phase flow. *International Journal of Multiphase Flow*, 11, 161-175.

Meng, W., X. T. Chen, G. E. Kouba, C. Sarica and J. P. Brill (2001). Experimental study of low-liquid-loading gas-liquid flow in near-horizontal pipes. *Society of Petroleum Engineers*, 16(4), 240-249.

Miles, J. W. (1966). Surface-wave damping in closed basins. *Proceedings of the Royal Society of London*, Ser. A, 297, 459-475.

Minami. K. and J. P. Brill (1987). Liquid holdup in wet gas pipelines. *Society of Petroleum Engineering*, *Production Eng*ineering, 5, 36-44.

Mishima, K. and M. Ishii (1984). Flow regime transitions criteria for upward two phase flow in vertical tubes. *International Journal of Heat and Mass transfer*, 27(5), 723-737.

Mukherjee, H. and J. P. Brill (1985). Empirical models to predict flow-patterns in two-phase inclined flow, *International Journal Multiphase Flow*, 11 (3), 229-315.

Nikuradse, J. (1933). *Stromungsgesetz in rauhren rohren, vDI Forschungshefte* 361 (English translation: *Laws of flow in rough pipes*). Tech. Rep. NACA Technical Memorandum 1292. National Advisory Commission for Aeronautics, Washington, DC, USA (1950).

Nishino, H. and Y. Yamazaki (1963). A new method of evaluating steam volume fractions in boiling systems. *Journal of Society of Atomic Energy Japan*, 5, 39-46.

Olive, N. R., H. Q. Zhang, Q. Wang, C. L. Redus and J. P. Brill (2003). Experimental study of low liquid loading gas-liquid flow in near-horizontal pipes. *Journal of Energy Resources Technology*, 125(4), 294-299.

Owens, W. S. (1961). Two-phase pressure gradient. *International Developments in Heat Transfer*, Part II, ASME.

Selander, W. N. (1978). Explicit formulas for the computation of friction factors in turbulent pipe flow. AECL-6354, November.

Sloan, D. (2000). Hydrate Engineering. First Edition, *Society of Petroleum Engineering*, Richardson, TX.

Spedding, P., J. Watterson, S. Raghunathan and M. Fergusonn (1998). Two-phase co-current flow in inclined pipe. *International Journal of Heat Mass Transfer*, 41, 4205-4228.

Taitel, Y. and A. E. Dukler (1976). A model for predicting flow regime transitions in horizontal and near horizontal gas- liquid flow. *The AIChE Journal*, 22(1), 47-55.

Taitel, Y., D. Barnea and A. E. Dukler (1980). Modelling flow pattern transitions for steady upward gas-liquid flow in vertical tubes. *AIChE Journal*, 26(3), 345-354.

Tandon, T., H. Varma and C. Gupta (1985). A void fraction model for annular two-phase flow. *International Journal of Heat Mass Transfer*, 28, 191-198.

Thom, J. (1964). Prediction of pressure drop during forced circulation boiling water. *International Journal of Heat Mass Transfer*, 7, 709-724.

Thwaites, G. R., N. N. Kulor and R. M. Nedderman (1976). Liquid film properties in two phase annular flow. *Chemical Engineering Science*, 31, 481-486.

Turner, J. and G. Wallis (1965). The separate-cylinders model of two-phase flow. Report NYO-3114-6, Thayer School of Engineering, Daetmouth College.

Tzotzi, C., V. Bontozoglou and N. Andritsos (2011). Effect of fluid properties on flow patterns in two-phase gas-liquid flow in horizontal and downward pipes. *Industrial & Engineering Chemistry* R*esearch*, 50, 645-655.

Van Rossum, J. J. (1959). Experimental investigation of horizontal liquid films. *Chemical Engineering Science*, 11, 35-52.

Volk, M., E. Delle-Case and A. Coletta (2010). Investigations of flow behavior formation in well-head jumpers during restart with gas and liquid. Technical Report, Tulsa University.

Wallis, G. B. (1969). One-dimensional two-phase flow. McGraw-Hill Book Company, New York.

Wallis, G. B. and J. E. Dobson (1973). The onset of slugging in horizontal stratified air-water flow. *International Journal of Multiphase Flow*, 1, 173-193.

Weisman, J. and W. G. Choe (1976). Methods for calculation of pressure drop in co-current gas-liquid flow. *Proceedings of the Two-phase Flow and Heat Transfer Symposium Workshop*, Fort Lauderdale, Two-Phase Transport and Reactor Safety, 1.

Weisman, J., D. Duncan, J. Gibson and T. Crawford (1979). Effects of fluid properties and pipe diameter on two phase flow pattern in horizontal lines, *International Journal of Multiphase Flow*, 5, 437-462.

Woods, B. D., E. T. Hulburt and T. J. Hanratty (2000). Mechanism of slug formation in downwardly inclined pipes. *International Journal of Multiphase Flow*, 26, 977-298.

Zivi, S. (1963). Estimation of steady-state steam void fraction by means of the principal of minimum entropy production. ASME Preprint 63-HT-16. In: *6th National Heat Transfer Conference*, *AIChE-ASME*, Boston.

Chapter 3

General Background to Computational Fluid Dynamics (CFD) and Numerical Techniques

In this chapter, a review of various techniques for simulating two–phase flow using CFD is given. In particular, the discussion involves the different multiphase and turbulence modelling approaches used, followed by the handling of interphase force that is largely responsible for accurate prediction of dispersed phase distribution and other system parameters. Moreover, an introduction to Computational Fluid Dynamics (CFD) is given including applications, advantages and methodology. The steps of the CFD analysis procedure are described, and the three discretisation methods, namely finite element, finite difference, and finite volume schemes are outlined. The discretisation technique utilized by the adopted CFD code in this work in order to discretise each of the terms in the governing equations is explained, and the strategy used to solve the resulting numerical equations is described, including the coupled solver and the Algebraic Multigrid method. The basic tools used for analysing the results are also given.

3.1 Definition and History

Computational Fluid Dynamics (CFD) is an engineering tool based on a computer simulation that is used to assess the system performance, including the fluid flow, heat transfer and associated phenomena such as chemical reaction (Versteeg and Malalasekera, 1996). The set–up of CFD can be divided into two steps: firstly, a numerical model is created by a set of mathematical equations that express the flow; and secondly, these equations are solved by a computer program in order to gain the flow variables through the flow domain.

Since the invention and development of the digital computer, CFD has been given comprehensive attention and has been used extensively in the engineering industry to contemplate different aspects of fluid dynamics. The development and application of CFD has become a powerful tool for design and analysis in the oil and gas industry. At the beginning of 1980s, computers developed into a sufficiently powerful tool for general application CFD software to become accessible.

3.2 Applications of CFD

The earliest users of CFD were the nuclear, aerospace, and automotive industries (Bakker *et al.*, 2001). Further improvement in CFD and its capability to model complicated phenomena, such as evaporation, condensation, and two–phase flow in process engineering, in conjunction with the fast development in computer power have increased the range of CFD applications. It is now employed in a wide range of industries, such as petroleum, metallurgical, mechanical, mine, biomedical, and food industries.

For a wide range of process industries CFD techniques have been utilized to gain information about various flow phenomena, to investigate the design of different equipment or to evaluate performance under various operating conditions. Some examples of CFD practices in chemical processing industries include drying, combustion, separation, heat exchange, mass transfer, reaction, mixing, multiphase systems and material processing.

In addition, CFD has been made available for a range of multiphase flow systems, even though a few limitations exist. Multiphase CFD models have the ability to facilitate the understanding of complex two–phase interactions and provide specific information on 3-D transient, where experimental work might not be suitable. These applications illustrate the potential of CFD to simulate and investigate complex flows in different industrial processes.

3.3 Validation of CFD Models

In general, CFD model validation is required to examine the accuracy of the computational model. The validation process is carried out by comparison of CFD results with available experimental, theoretical, or analytical data. This evaluation can contribute to produce reliable CFD models. Validated models are eventually established as reliable, whereas those which are not validated due to incorrect physical models are required to be modified and revalidated. As a result many CFD models have been validated in a wide range of industrial fields, which made the CFD application a reliable tool for industry and research. However the validation of CFD data against an experimental or theoretical data is not always possible due to a lack of available data. A detailed review of CFD validation can be found in Oberkampf and Trucano (2002).

3.4 Benefits of CFD

The convergence solution of CFD may have some complications that can be minimized based on the user's experience, and are therefore not fundamental. These difficulties are far outweighed by its benefits (Bakker *et al*., 2001). There are some cases; however, where basic information needed is incomplete, and as a consequence of the assumptions made the mathematical model adopted may provide inaccurate results.

Some of the benefits of using CFD codes are:

i. It can be used to study any system numerically when it is complicated to do so through experimentation;

ii. CFD is able to provide different kinds of information which can be difficult to obtain through experimentation due to the limitation of equipment or technique;
iii. The complex physical interactions that take place in a flow condition can be modeled simultaneously since no limiting assumptions are usually required.
iv. CFD also enables the visualization of the flow behaviour of a system, and it is commonly used in industry as a flow visualisation tool (Gaylard, 2001).

3.5 CFD Analysis Procedure

To employ CFD in process system investigations, the following information is required:

i. *A grid of points* is used to store the variables calculated by CFD;
ii. *Boundary conditions* are needed for defining the conditions at the flow domain boundaries and to allow the boundary values of all variables to be estimated;
iii. *Fluid properties* are required to be specified, such as viscosity and density;
iv. *Flow models* describe the various characteristics of the flow, for instance mass, heat transfer, turbulence, and multiphase models;
v. *Initial conditions* are used to give the initial state of the flow for a transient simulation or an initial guess of the solution variables in a steady state simulation;
vi. *Solver control parameters* are necessary to manage the behaviour of the numerical solution process; and
vii. *Analysis of the results* is done to verify that the solution is satisfactory against reliable data or correlation and to estimate the flow data required.

The entire CFD analysis structure can be classified into six steps as follows.

3.5.1 Initial Thinking

One of the fundamentals of this stage is to know and understand the problem before simulation in order to select the correct physical model that describes the case. This stage also requires some data which are necessary for the simulation, such as geometry details, fluid properties, flow specifications, and boundary and initial conditions.

3.5.2 Geometry Construction

The flow domain geometry is created by special software for drawing called Gambit. First of all, 2-D sketches are typically drawn and then 3-D tools are employed to generate the full geometry, which gives more accurate information about the problem such as that taking place in reality.

3.5.3 Mesh Generation

The flow domain space is subdivided into sufficiently small discrete cells. These cells are allocated to determine the positions of the flow variables which are to be computed and stored up. Usually variable gradients are not accurately calculated on a coarse mesh but on a fine one. Therefore, a fine mesh is very significant in regions where the flow variables are expected to have large variations. More computational power and time are required with a fine mesh. The optimization of mesh size is considered as a critical test that examines the simulation results with respect to mesh refinement.

3.5.4 Flow Specification

This step consists of defining the flow models, fluid physical properties, flow boundary conditions, and initial flow conditions, as found in the initial thinking step.

3.5.5 Calculation of the Numerical Solution

When the simulation set up is done using all the required information, iterative calculations are carried out by the CFD to reach a solution to the numerical equations

describing the flow. The numerical solution process is controlled by information that is provided by the user.

3.5.6 Analysis of the Result

Once the solution is achieved, the results are subsequently analysed to find out the accuracy of the solution. If these results are not accurate, the source of error has to be identified, which could be an incorrect definition of one of the mentioned sections, such as flow specification, a poor quality of mesh, or a conceptual error in the problem formulation as shown in Figure (3.1), which demonstrates the flowchart of CFD analysis process given by Shaw (1992).

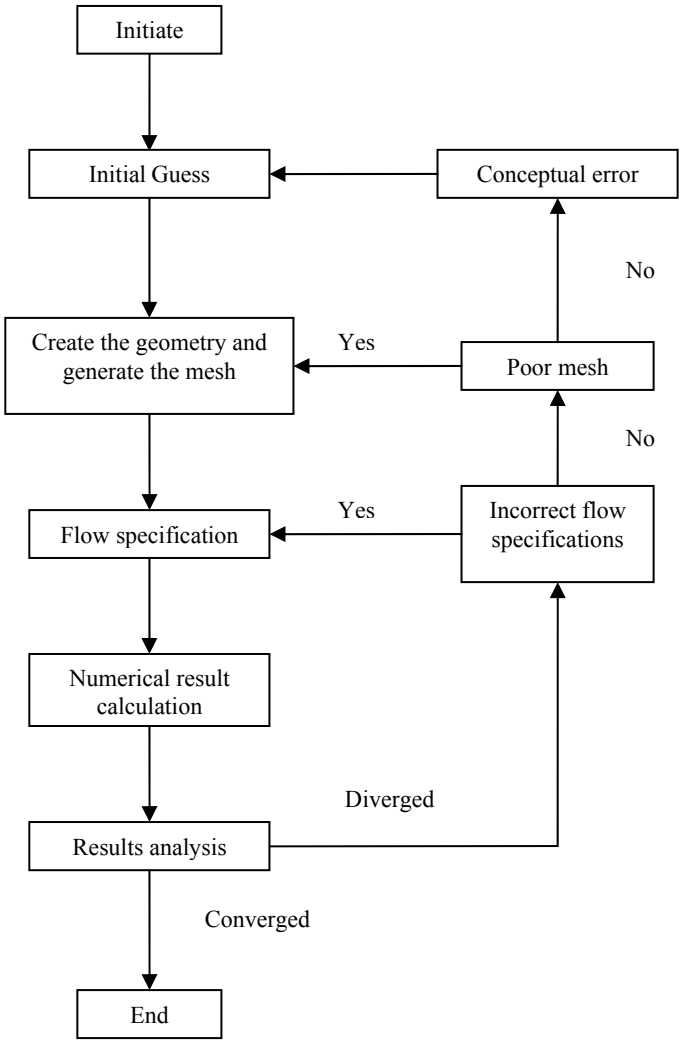

Figure 3.1: A flow diagram of the CFD analysis procedure.

3.6 Existing Commercial CFD Codes

In the last two decades, CFD has received interest from industry. This has led to the development of a variety of CFD codes that are available commercially, for instance CFX, FLUENT, PHOENICS, and STAR-CD. The benefit of these codes is that they can deal with many complex areas of fluid flow in industrial applications. Generally, the CFD package is made of three main components, which are:

a. A pre-processor
b. A solver
c. A post-processor

The first step is a pre-processor, which is considered the most important one because it involves the creation of geometry and mesh. After that the flow model, fluid properties and control parameters of the solver are specified, and then the boundary and initial conditions are applied. The second step is a solver that is used to discretise and solve the numerical transport equations based on the specified data. The final step is a post-processor, in which the output results of the simulation can be visualised and analysed.

3.7 Numerical Techniques

The governing equations are typically presented by partial differential equations (PDEs), such as Navier–Stokes equations. Such equations can not be solved directly using digital computers that are able to identify and operate with numerical data. However, the PDEs have to be converted into numerical equations that include only numbers and no derivates. This process of transferring the PDEs to a numerical analogue is called Numerical Discretisation, where various approaches are used for solving, including finite difference method, finite element method, and finite volume method.

The method of Finite–difference is derived based on the use of the Taylor series to change the partial differential equations into derivatives of dependent variables as there are differences among the variable values at various points in space and time.

Linear algebraic equations are produced as a result of PDEs being transferred so that they can be solved by one of the elimination approaches.

In the finite element method, the domain is separated into a finite number of small elements or sub–domains. A simple variant of the dependent variables is assumed over individual element, where this variable variant is computed based on the values of the variable at the element nodes. The obtained equations for individual elements are then placed in a matrix and boundary conditions are applied to solve the equations in the matrix.

The finite volume method is that most employed for numerical discretisation. It is a similar mode of application to the finite different method, while some of its implementations are driven on characteristics based on the finite element approach. This method takes into account the discretisation of the spatial domain into finite control volumes. A control volume usually covers many mesh elements that can be divided into sectors which belong to a different mesh element. The differential governing equations are integrated over individual control volumes. The result of this integration ensures the accurate conservation of related properties in individual finite volumes. Each integral term is transformed to a discrete term that results into discretised equations at the nodal, or centroids points of the control volumes. This method is similar to the finite difference method where the numerical equations at a particular point are derived from the values at neighbouring points.

3.8 CFD Modelling Approaches for Multiphase

The modelling of multi–phase flow is considered an enormous topic and includes a wide range of industrial processes. Multi–fluid flow has been given special treatment in oil and gas engineering due to its importance, and is significant in the current study of two–phase flows in horizontal pipelines. This section revises the multi–phase modelling aspects of dispersed and stratified flow, which are very common in low liquid loading two–phase flow. In reality most of the fluids flow as a turbulent due to the nature of the operating conditions. This section also discusses various turbulence modelling features in two–phase flow systems. Particular attention is given to the

treatment of interface forces that play an important role in the prediction of system parameters.

It is important to understand the need for modelling flow fields and turbulence in order to resolve them directly. A special technique which provides for an exact computation of the instantaneous flow fields and their turbulent fluctuations without resorting to any kind of modelling is discussed. This method has some limitations that are emphasized and, therefore, the requirement for modelling is demonstrated.

3.8.1 Dispersed Multi–fluid Flow Modelling

There are four recognized methods to modelling dispersed multi–phase flows (Ranade, 2002):

1. Volume of Fluid (the Eulerian framework for both phases with interface forces reformulation based on a volumetric basis).
2. Eulerian-Lagrangian (the continuous and dispersed phases are treated in the framework of Eulerian and Lagrangian respectively).
3. Eulerian-Eulerian (both phases are treated within the Eulerian framework, not including explicitly for the interface between phases), and
4. Mixture (it treats both phases as continuous and dispersed as a one mixture phase).

3.8.1.1 Volume of Fluid (VOF) Approach

The volume of fluid method tracks the motion of a distinct phase in each cell through the domain. In the VOF model, a single set of conservation equations is shared by the two–phase using mixture properties, when both phases share the same control volume. In addition, if the control volume is occupied by one of the phases, its related properties are utilized. The benefit of this is to avoid any unexpected changes in the physical properties of the fluid through a thin interface.

Usually, when the shape and flow processes taking place close to the interface are of interest, the VOF method is beneficially utilized because it is able to simulate the profile deformation of the dispersed phase particles (i.e. droplets, bubbles) as a result of the surrounding fluid flow (Delnoij, 1999). When the system is characterized by a great fraction of the dispersed phase, it requires substantial computational resources around every dispersed entity to determine the flow field. This approach, however, is considered as the easiest one among Eulerian–Eulerian and the Eulerian–Lagrangian method (discussed in the subsequent sections). It is appropriate to use as an application that focuses on simple flow pattern problems as seen in pipelines (slug) (Frank, 2005), flow around single objects (i.e. droplets, bubbles, and particles) and dispersed multi–phase flows which characterize the dispersed phase with extremely tiny fractions (Rashmi *et al*., 2009, De Schepper *et al*., 2008).

3.8.1.1.1 Governing Equations

In the VOF approach, the continuity equation is shared by the two phases where the tracking of the interface is achieved by solving the equation for one of the phases. The continuity equation can, therefore be written for the liquid phase as below:

$$\frac{\partial \alpha_l}{\partial t} + (U_i.\nabla)\alpha_l = 0 \tag{3.1}$$

The volume fraction equation is not solved for the gas phase as primary phase in the current study, but the gas volume fraction is calculated based on the limitation of total fraction being equal to unity as shown below:

$$\alpha_g + \alpha_l = 1 \tag{3.2}$$

Where α_g and α_l are the volume fraction of gas and liquid, respectively.

The equation of momentum conservation can be expressed by the Navier–Stokes equation, which is shared by both phases and solved throughout the domain as follows:

$$\frac{\partial}{\partial t}(\rho u_i) + \nabla.(\rho u_i u_j) = -\nabla p + \nabla.\left[\mu\left(\nabla u_i + \nabla u_j\right)\right] + \rho g_i + F_i \tag{3.3}$$

The left hand side corresponds to convection and the first term on the right hand side corresponds to pressure, while the other terms represent diffusion and the body force of gravity.

3.8.1.1.2 Physical Properties

The properties and variables of two–phase are presented purely or as a mixture in the cell, and are found by the distribution of the volume fraction. However, the mixture of the two phases that is shown in the transport equations is calculated based on the fraction of each phase in the control volume. The density and viscosity in each cell are given by:

$$\rho_m = \alpha_l \rho_l + \alpha_g \rho_g = \alpha_l \rho_l + (1 - \alpha_l)\rho_g \tag{3.4}$$

$$\mu_m = \alpha_l \mu_l + \alpha_g \mu_g = \alpha_l \mu_l + (1 - \alpha_l)\mu_g \tag{3.5}$$

where ρ_l , ρ_g μ_l and μ_g are the density and viscosity of the liquid and gas phase.

3.8.1.1.3 Interpolation near the Interface

Generally, the Volume of Fluid algorithm (Zaleski, 2005) solves the problem of updating the phase volume fraction field, providing the fixed grid, the phase volume fraction, and the velocity field as obtained in the previous time step. In a two–dimensional system problem, the interface is considered to be a continuous, piecewise smooth line. This kind of problem can be reduced to the reconstruction of an

approximation of the interface in each cell, knowing only the volume fraction of each phase in the cell itself and in the neighbouring cells.

The simplest VOF interface tracking schemes are the simple line interface calculation (SLIC) algorithms (Noh and Woodward, 1976). They are first order in the accuracy for the interface reconstruction. Usually, the reconstructed interface is made up of a sequence of segments aligned with the grid that composes the reconstruction relatively roughly. Figure (3.2–c) demonstrates the interface reconstruction by means of a SLIC algorithm.

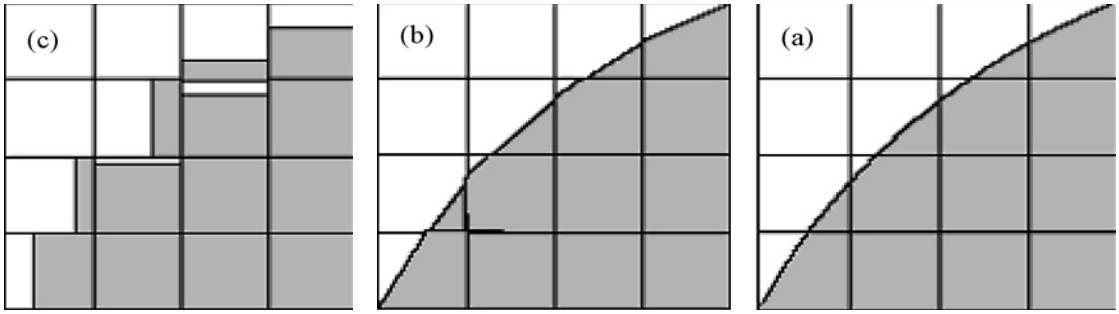

Figure.3.2: VOF interface reconstruction methods: (a) actual interface shape, (b) interface reconstruction by means of the second-order or PLIC method, and (c) interface reconstruction by means of the first-order or SLIC method (Fluent 6.2 User's Guide, 2005).

More accurate techniques of VOF attempt to fit the interface through piecewise linear sections. These techniques are known as the piecewise linear interface calculation (PLIC) algorithms (Li, 1995). In the PLIC method, the interface in the computational cell is approximated by a straight line segment with a slope obtained from the interface normal. The line segment cuts the computational cell such that the fractional fluid volume equals the phase volume fraction value in that cell. The outcome of the fluid polygon is then utilised to find out fluxes through any cell face. Figure (3.2–b) demonstrates the interface reconstruction by means of a second–order or PLIC algorithm.

One of the significant simplifying characteristics of VOF/PLIC algorithms is that it does not attempt to reconstruct the interface as a continuous chain of segments. Therefore, the alternating chain with small discontinuities is retained. When the curvature is small, the scheme will be more accurate. A VOF/PLIC algorithm involves a two–step that is both a reconstruction and a propagation step. In the reconstruction step, a linear interface that separates the computational cell into two sections containing an appropriate area of each of the two–phase is constructed. The orientation of the segment is found through the calculation of the unit normal vector to the segment.

Many algorithms have been developed for the calculation of the unit normal vector (Puckett, 1991). This unit normal vector, together with the value of phase volume fraction in the cell, uniquely establishes the linear interface in the cell. The second step of the VOF algorithm is propagation (Puckett, 1997). Once the interface has been constructed, the interface motion caused by the velocity field must be modeled with a suitable advection algorithm.

In the existing CFD code, this scheme is the most accurate one and it is applicable for general unstructured meshes as used here. As typical for the PLIC method, this interpolation scheme assumes that the interface between two fluids has a linear slope within each cell and this linear shape is used for the calculation of the advection of the fluid through the cell interfaces.

The first step in this reconstruction scheme consists of the calculation of the position of the linear interface relative to the center of each partially filled cell, based on information concerning the volume fraction and its derivatives in the cell. The second step is the calculation of the advecting amount of fluid through each interface using the computed linear interface representation and information about the normal and tangential velocity distribution at the interface. In the third step, the volume fraction in each cell is determined using the balance of fluid mass fluxes calculated in the previous time step.

The Compressive Interface Capturing Scheme for Arbitrary Meshes (CICSAM) is another method to improve the accuracy of the interface in the VOF approach and is based on Ubbink's research (1997). This method is suitable for flows with high ratios of viscosity differences between the phases. It is implemented in FLUENT as an explicit approach and provides an advantage of producing a sharp interface that is similar to that produced by a geometric reconstruction method. During all simulations in the current work in Chapter 4, the CICSAM interface reconstruction approach has been utilized for interpolation in a cell.

3.8.1.2 Eulerian–Lagrangian (E–L) Approach

In the Eulerian–Lagrangian method, the fluid phase is considered as a continuum. This is solved by time averaged of Navier–Stokes equations in the same way as it solved for a single phase system, whilst the dispersed phase is solved by the equation of motion for each dispersed phase entity where the explicit motion of the interface is not modeled in this approach.

This method is able to capture the dispersed fluid dynamics accurately. Particle–level processes (e.g. chemical reactions, heat and mass transfer effects etc) can be simulated in sufficient manner and detailed and accounts for interaction between particles and size distribution. However, a large number of particles are required in turbulent flow simulation in order to achieve a significant average. Subsequently, as the number of dispersed droplets, bubbles or particles increases, the computational cost increases proportionally, and as result this approach is limited to simulating two–phase flow with low fraction of less than 10% of dispersed flow (Domgin *et al*., 1997; Jaworski and Pianko–Oprych, 2002).

3.8.1.2.1 Governing Equations

This approach is used for modelling a hydrodynamic or multiphase flow, where the particle models are integrated with an Eulerian model for the continuous fluid in order to simulate the disperse fluid. The fluid phase movement is attained by calculating the

average two–phase governing equations in a similar manner of Eulerian–Eulerian approach. The continuity equation for one of the phases can be written as follows:

$$\frac{\partial}{\partial t}(\alpha_i \rho_i) + \nabla \cdot (\alpha_i \rho_i \vec{v}_i) = \sum_{j=1}^{n} \dot{m}_{ji} \tag{3.6}$$

And the momentum equation is expressed by the Navier–Stokes equation as:

$$\begin{aligned} &\frac{\partial}{\partial t}(\alpha_i \rho_i \vec{v}_i) = -\nabla \cdot (\alpha_i \rho_i \vec{v}_i^2) - \alpha_i \nabla p - \nabla \cdot (\alpha_i \tau_i) + \alpha_i \rho_i \vec{g} \\ &+ \alpha_i \rho_i (\vec{F}_i + \vec{F}_{lift,i} + \vec{F}_{vm,i}) \end{aligned} \tag{3.7}$$

where the stress tensor of the compressible fluid phase is identified as:

$$\tau_i = \alpha_i \mu_i (\nabla \vec{v}_i + \nabla \vec{v}_i^T) + \alpha_i (\lambda_i - \frac{2}{3}\mu_i) \nabla \cdot \vec{v}_i \mathrm{I} \tag{3.8}$$

The motion of dispersed phase (e.g. droplet, bubble, or particle) is presented by combining the force balance on the object that is expressed in the Lagrangian framework. Therefore the momentum balance equation is written in terms of particle acceleration as (Van Wachem *et al*., 2003):

$$m_d a_d = m_d g + V_d \nabla \cdot \tau_i - V_d \nabla P + \beta \frac{V_d}{\alpha_d} (\vec{v}_i + \vec{v}_d) \tag{3.9}$$

where m_d, V_d, v_d and α_s are the mass, acceleration, velocity and volume fraction of the dispersed phase respectively. Whereas P and β are the local pressure and interface momentum transfer coefficient.

3.8.1.3 Eulerian–Eulerian (E–E) Approach

In the Eulerian–Eulerian method, the flow of all phases is modelled by an Eulerian framework, and therefore is based on the assumption that all phases share the domain

and may interpenetrate as they get moving all the way through it. Every phase is described by velocity and volume fraction. The interface forces such as drag, lift, and virtual mass must be specified in order to effectively handle the coupling among the phases (closure). The Eulerian–Eulerian approach is considered more sufficient in terms of CPU time due to the continuum approach for the dispersed phase. Comparison of the Volume of Fluid approach and the Eulerian–Lagrangian approach demonstrates that the Eulerian–Eulerian method is well accommodated to modelling systems which account for high volume fractions of the dispersed phase, such as the current research of two–phase flow in horizontal pipelines, bubble–column reactors etc.

However the Eulerian–Eulerian method is not well suited to handling complex phenomena at the particle–level, such as dynamic size distribution of a discrete phase when compared to the Eulerian–Lagrangian method. The advantages of the latter make it attractive for modelling dense multiphase flows whose dealing with the Eulerian–Lagrangian approach is complicated owing to the unaffordable computational resource requirements.

3.8.1.3.1 Governing Equations

The governing equations of Eulerian–Eulerian method are derived by averaging all of the conservation equations for each one of the phases as mentioned by Drew (1983) and Lopez de Bertodano *et al*. (1990). The equation of volume average continuity for i^{th} interpenetrating phase is provided by Ranade (2002):

$$\frac{\partial}{\partial t}\left(\alpha_i \rho_i\right) + \nabla.\left(\alpha_i \rho_i \vec{v}_i\right) = \sum_{j=1}^{n} \dot{m}_{ji} \tag{3.10}$$

where α, ρ, v are expressed as the macroscopic volume fraction, density, and velocity of phase (i) respectively, while m_{ji} is the mass transfer from the phase j^{th} to the phase i^{th}.

Momentum equation of phase (i) is given by the Navier–Stokes equation as follows:

$$\frac{\partial}{\partial t}(\alpha_i \rho_i \vec{v}_i) = -\nabla.(\alpha_i \rho_i \vec{v}_i \vec{v}_i) - \alpha_i \nabla p - \nabla.(\alpha_i \tau_i) + \alpha_i \rho_i \vec{g} + \alpha_i \rho_i (\vec{F}_i + \vec{F}_{lift,i} + \vec{F}_{vm,i}) \quad (3.11)$$

where p, g, F_i, $F_{lift,i}$, and $F_{vm,i}$ are expressed as hydrodynamic pressure, gravity, external body force, lift force and virtual mass force respectively, while τ_q represents the viscous stress tensor for i^{th} phase, which can be expressed by:

$$\alpha_q \mu_q (\nabla \vec{v}_q + \nabla \vec{v}_q^T) + \alpha_q (\lambda_q - \frac{2}{3}\mu_q) \nabla.\vec{v}_q I \quad (3.12)$$

In the Eulerian multiphase applications, the energy conservation equation can be expressed by the enthalpy equation of each phase as:

$$\frac{\partial}{\partial t}(\alpha_q \rho_q h_q) = -\nabla.(\alpha_q \rho_q h_q \vec{v}_q) - \alpha_q \frac{\partial P_q}{\partial t} + \tau_q : \nabla \vec{v}_q - \nabla \vec{q}_q + S_q + \sum_{p=1}^{n} (\vec{Q}_{pq} + \dot{m}_{pq} h_{pq}) \quad (3.13)$$

where h_i, q_i , S_i , Q_{pq} and h_{pq} represent the specific enthalpy of phase i^{th} , the heat flux, the source term that takes into account sources of enthalpy due to chemical reaction or radiation, the intensity of heat exchange between the two phases, and the interphase enthalpy respectively.

3.8.1.3.2 Lift Force

Generally in multi–phase systems, FLUENT has the ability to take into account the effect of lift force on a spherical object (e.g. droplet, bubble, or particle). The influence of this force on a particle is mainly as a result of velocity gradients in the primary phase flow. The lift force on large particles is considered to be more significant, although the FLUENT model assumes that the inter-particle spacing is greater than the particle diameter. The enclosure of lift forces, therefore, is not suitable for very small particles and closely packed particles. In most of the situations, the lift force is not important in contrast to the drag force, but if the lift force is significant, such as in the case of two–phase separation, where both phases might be

quickly separated. In that situation, it could be appropriate to take into account the effect of this term. By default, the lift force is not included, but if it is required for multiphase system, the lift coefficient can be specified.

The influence of lift force on dispersed phase *j* in a primary phase *i*, is obtained as:

$$\vec{F}_{lift,i} = \frac{1}{2}\rho_i \varepsilon_i \left|\vec{v}_j - \vec{v}_i\right| \times (\nabla \vec{v}_i) \tag{3.14}$$

where F_{lift} is the lift force that will be added to the right–hand side of the momentum Equation (3.11).

3.8.1.3.3 Momentum Exchange Term

In multiphase flows such as gas–liquid, one of the phases presents less than the other one in the system, but whether it is expected to create some bubbles or droplets depends on the dispersed phase. This has influence on the two–phase flow behaviour. Therefore, the predominant phase in the system has to be modeled as a primary phase and the other one is more likely to produce droplets or bubbles. Thus, the term of exchange coefficient of the two fluids flow system can be expressed by the following equation:

$$K_{ji} = \frac{\varepsilon_j \rho_j f_{ji}}{\tau_{ji}} \tag{3.15}$$

where f_{ji} is the drag function that is formulated differently based on different exchange–coefficient models (as given below) and τ_{ji} represents the "particulate relaxation time" is given as:

$$\tau_{ji} = \frac{\rho_j d_j^2}{18\mu_i} \tag{3.16}$$

The drag function (f_{ji}) can be found using different empirical correlations, some of which are provided within the FLUENT code. The most widely used correlation is given by Morsi and Alexander (1972) as follows:

$$f_{ji} = \frac{C_D \, \mathrm{Re}_{ji}}{24} \tag{3.17}$$

where C_D is the drag coefficient which can be modeled by different formulates, of which some are available by default in the FLUENT code. It can also be written as user defined function (UDF) for a particular system, as takes place in current study and will be shown in Chapter 5. The drag coefficient for Morsi and Alexander correlation can be written as:

$$C_D = a_1 + \frac{a_2}{\mathrm{Re}_{ji}} + \frac{a_3}{\mathrm{Re}_{ji}^2} \tag{3.18}$$

where a_1, a_2, a_3 are empirical constants and Re_{ji} is the relative Reynolds number is calculated as:

$$\mathrm{Re}_{ji} = \frac{\rho_i \left| \vec{v}_j - \vec{v}_i \right| d_p}{\mu_i} \tag{3.19}$$

3.8.1.3.3 Wall Forces

The wall force is considered one of the significant forces which have an effect on the droplets, bubbles or particles when they approach the wall. Under these conditions, the normal uniform drainage of the fluid around the dispersed phase changes dramatically. Owing to exerted force, the walls slow the drainage rate between the droplet and the wall, which in turn enhances the drainage rate on the opposite side. The net effect is the force which acts to drive the droplet away from the wall.

3.8.1.4 Mixture

The mixture model is one of the simplified multi–fluid approaches, which can be utilized to simulate two phases of different or same velocities, but assumes the local equilibrium within small spatial length scales (FLUENT, 2005). As a result, the accelerating entities of dispersed fluid reach the terminal velocity after travelling a distance in which the length scale of the system is become greater (Chen *et al.*, 2005). The relative velocity among the fluids is described by using an algebraic equation, which is based on the local equilibrium assumption (Hossain *et al*., 2003, and Chen *et al*., 2005). In contrast to the Volume of Fluid (VOF) model, the two phases into the mixture approach are permitted to interpenetrating, where the dispersed phase is characterised by a volume fraction equation. Each dispersed phase has its individual transport equation, which allows for the slip velocity between the phases (dispersed and continuous).

Based on the mixture model theory, it treats both phases of continuous and dispersed as a single phase. This is considered as a mixture phase in which physical properties, such as density and viscosity of the mixture, are found based on each phase fraction. These properties are employed in the governing equation. Furthermore, the homogeneous multiphase flows can be simulated by the mixture model with very strong coupling between the phases, which flow nearly with the same velocity. The computational time of this model is much lower than other multiphase models which have been discussed before, because it solves the minimum number of equations. Nevertheless, there is a strong compromise in the level of flow information it can present when compared with the inclusive Eulerian–Eulerian method. In addition, none of drag interphase forces such as the lift and virtual mass forces are calculated into the mixture model. The mixture model can be used in many industrial applications, for instance sedimentation, bubbly flows where the dispersed phase fraction remains low and particle–laden flows with low loading.

The mixture model also solves most of the equations for the mixture, such as the continuity, momentum, and energy equation. The volume fraction equation is solved

for the secondary phases and algebraic expressions for the relative velocities in the case of phases travelling at different velocities.

3.8.1.4.1 Governing Equations

The mixture continuity equation is obtained based on the average properties of two–phase and can be written as:

$$\frac{\partial}{\partial t}(\rho_m) + \nabla.(\rho_m \overrightarrow{v_m}) = \dot{m} \tag{3.20}$$

where $\dot{m}$, v_m, and ρ_m represents the mass transfer between phases, the mass–averaged velocity, and the mixture density. The mass–averaged velocity and mixture density can be expressed by:

$$\vec{v}_m = \frac{\sum_{k=1}^{n} \alpha_k \rho_k \vec{v}_k}{\rho_m} \tag{3.21}$$

$$\rho_m = \sum_{k=1}^{n} \alpha_k \rho_k \tag{3.22}$$

where α_k and ρ_k are the volume fraction and density of a corresponding phase.

The momentum equation for the mixture can be computed by the sum of individual momentum equations for all phases, which can be written as:

$$\begin{aligned} &\frac{\partial}{\partial t}(\rho_m \vec{v}_m) + \nabla.(\rho_m \vec{v}_m^{\,2}) = -\nabla p + \nabla.\left[(\mu_m(\nabla \vec{v}_m + \vec{v}_m^{\,T})\right] + \rho_m \vec{g} + \overrightarrow{F} \\ &+ \nabla.(\alpha_g \rho_g (\vec{v}_g - \vec{v}_m)^2 + \alpha_l \rho_l (\vec{v}_l - \vec{v}_m)^2) \end{aligned} \tag{3.23}$$

where F and μ_m are the body force and the mixture viscosity, which is expressed by:

$$\mu_m = \sum_{k=1}^{n} \alpha_k \mu_k \tag{3.24}$$

where α_k and μ_k are the volume fraction and viscosity of a corresponding phase.

The energy equation for the mixture takes the following form:

$$\frac{\partial}{\partial t}\sum_{k=1}^{n}(\alpha_k \rho_k E_k) + \nabla.\sum(\alpha_k \vec{v}_k(\rho_k E_k + p)) = \nabla.(k_{eff}\nabla T) + S_E \tag{3.25}$$

where k_{eff} is the effective conductivity which can be obtained by the sum of each phase, thermal conductivity (k_i) and the turbulent thermal conductivity (k_t) , defined according to the used turbulence model. The first term on the right–hand side represents the conduction term due to energy transfer which is obtained by the expression below and S_E is any other volumetric heat sources.

$$E_k = h_k - \frac{p}{\rho_k} + \frac{\upsilon_k^2}{2} \tag{3.26}$$

This expression is for a compressible phase, while for an incompressible phase, E_k = h_k, where h_k is the sensible enthalpy for phase k.

The continuity equation and the volume fraction equation for secondary phase p can be obtained as:

$$\frac{\partial}{\partial t}(\alpha_p \rho_p) + \nabla.(\alpha_p \rho_p \vec{\upsilon}_m) = -\nabla.(\alpha_p \rho_p \vec{\upsilon}_{dr,p}) \tag{3.27}$$

3.8.2 Direct Numerical Simulations (DNS)

For any category of fluid flow, it is theoretically possible to find out the entire turbulent flow fields for three dimensions without resorting to any type of modelling. The direct solution of the governing equations (referred to as Direct Numerical Simulation) has limitations to its accuracy throughout the numerical method used.

This method produces a lot of data including the *time history* of all flow variables at each point in the domain. The characteristic of direct numerical simulation (DNS) therefore is a beneficial way to study and understand the fundamentals of fluid flow dynamics and turbulence phenomena, and as a result this assists in the evaluation and development of existing models.

The DNS method however is not sufficient for practical engineering problems, mainly owing to the excessive mesh sizes that are required to resolve all scales of motion in the three spatial dimensions (FLUENT, 2005). Furthermore, the requirement of initial and boundary conditions is considered as one of the most significant and difficult stages in using the concept of DNS (Ranade, 2002). Further to the complexity of this approach, the simulation would have to be a transient one with very small time steps. Consequently, a computational power is needed to solve the highly dispersed phase fraction, and usually turbulent and multi–phase flows are beyond the abilities of even modern computers.

3.8.3 Treatment of Turbulence in Multi–fluid Flows

Multi–fluid dispersions detected in Chemical Process Industries (CPI) are basically turbulent in nature and are thus classified based on velocity fields fluctuation. These variations combine transported quantities such as energy and momentum, as well as species concentration, and cause them to fluctuate as well. As these fluctuations can be of small scale and high frequency, they become extremely expensive to be simulated directly by DNS in terms of computational process time, as discussed in Section 3.8.2. As an alternative, the instantaneous governing equations can be time–averaged, ensemble–averaged, or otherwise controlled to remove the small scales of Large Eddy simulation (LES), leading to reformulate a set of equations, which then be developed and become computationally less expensive to solve. Nevertheless, the modified equations have additional unidentified variables, and turbulence models are required in order to find these variables in terms of known quantities (closure).

3.8.3.1 Large Eddy Simulations (LES)

Large Eddy Simulations (LES) are based on the assumption that the relevant scales in turbulent flows can be divided into large and small–scale (also referred to as sub–grid) components as shown in Figure (3.3). In this approach, it is implicitly assumed that such separation does not considerably affect the evolution of large–scale turbulent motions. The large–scale motions are generally much more energetic than the small–scale motions, and as a result of that they contribute more to the transport of conserved quantities. However, LES aims to simulate these large–scale motions much more specifically than small–scale motions, which are considered to be more general in character and hence more easily to be modeled.

The requirements of mesh resolution and time–step sizes are less restrictive in contrast with the DNS approach. Even though LES have many advantages, they still have some problems, similar to the shortcomings of DNS such as difficulties in specifying boundary conditions and generating a huge amount of information which is not useful for practical purposes (Bakker and Oshinowo, 2004).

The restricted ability (due to computational limitations) of using the DNS or LES methods to flows of practical interest in CPI conducts the use of computationally more tractable turbulence models based on the Reynolds Averaged Navier Stokes (RANS) equation (Prasad *et al*., 1998; Bakker and Oshinowo, 2004), which is explained in the next section. It should be noted that the latest advances in modelling have resulted in a hybrid approach that combines RANS modelling with LES, known as Detached Eddy Simulation (DES). Basically, DES reduces to RANS in regions which are close to the walls, and changes to LES in regions away from the walls (Constantinescu and Squires, 2003).

The outcome of this leads to a decrease in the computational effort significantly, while providing more accurate flow features when compared to RANS.

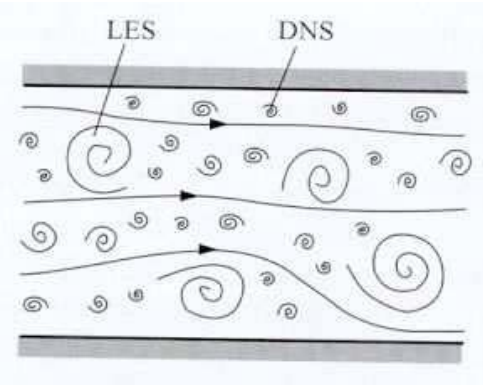

Figure 3.3: Schematic representation of scales in turbulent flows (adapted from Ferziger and Peric, 1995).

3.8.3.2 Turbulence Models Based on RANS

In this approach of RANS, the instantaneous value of any flow variable (ϕ) is decomposed into a mean ($\overline{\phi}$) and a fluctuating component (ϕ'):

$$\phi = \overline{\phi} + \phi' \tag{3.28}$$

whereϕ, $\overline{\phi}$, and ϕ' are the Instantaneous value, Time averaged mean, and Fluctuating component, respectively.

The mean value can be found by averaging over an appropriate time interval, where the Reynolds averaging obeys the following properties:

$$\overline{\overline{\phi}} = \overline{\phi} \quad \text{and} \quad \overline{\phi'} = 0 \tag{3.29}$$

where the over bar describes time averaging. Equation (3.28) is substituted in the basic governing equations for the flow variable (ϕ) (e.g. velocity of a phase) followed by time averaging, subject to the conditions listed in Equation (3.29) in order to yield governing equations for the mean quantities. When simplified the equation is led to a new averaged equation featuring an extra term which takes into account the turbulent transport of 'ϕ'. As the fluctuation of time averaged quantities takes place at much

larger scales, resolving the smaller spatial and temporal scales is not needed in the RANS–based approach.

The variation of fluid velocity with time is shown in Figure (3.4) and also demonstrates a comparison between the RANS based approach with the DNS and LES approaches.

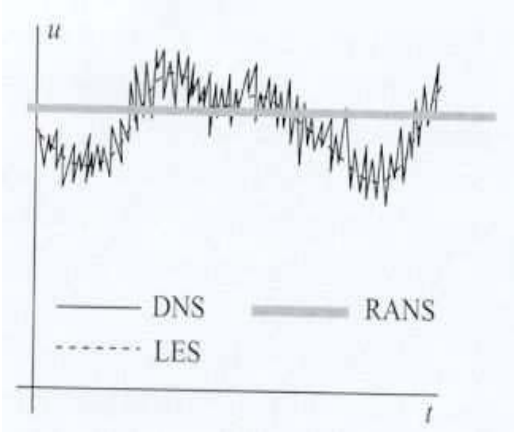

Figure 3.4: A comparison of DNS, LES and RANS (Ranade, 2002).

The averaging of RANS approach requires considerably less computational power compared to the LES or DNS methods. However, time averaging the basic governing equations results in the creation of new terms which lead to a closure difficulty. These new expressions might be integrated as apparent stress gradients and heat/mass fluxes associated with turbulent motion (Ranade, 2002). The governing equations for these new expressions can be derived theoretically. On the other hand, the obtained equations would also have more unknown expressions. Therefore, it becomes very important to establish a turbulence model, which relates these unidentified terms to known ones in order to complete the set of governing equations. During the last three decades, several turbulence models have been developed and utilized in simulations that have confirmed different degrees of achievement. In the next section, a comprehensive description of two–equation models will be given, such as standard *k*–

ε, Renormalization Group (RNG) *k*–ε, and *k*–ω. That discussion will focus on the advantages, limitations and the range of applicability of each model.

3.8.3.2.1 k−ε Model

Generally, the *k*–ε model is the most utilized turbulence model to simulate turbulence eddies. The *k*–ε turbulence model is described by a semi–empirical model, which is based on model transport equations for the turbulence kinetic energy (*k*) and its dissipation rate (ε). The transport equation for turbulence kinetic energy (*k*) is obtained from the explicit equation, whereas the equation of dissipation rate (ε) is derived using a physical hypothesis, and bears little resemblance to its mathematically exact counterpart. Both turbulence kinetic energy *k* and its dissipation rate ε are found from the following form of transport equations (FLUENT 6.2 User's Guide 2005):

$$\frac{\partial}{\partial t}(k\rho_k)+\frac{\partial}{\partial x_i}(k\rho_k U_k)=\frac{\partial}{\partial x_j}\left[\left(\mu+\frac{\mu_t}{\sigma_k}\right)\frac{\partial k}{\partial x_i}\right]+G_k+G_b-\rho\varepsilon-Y_M+S_k \tag{3.30}$$

and

$$\frac{\partial}{\partial t}(\varepsilon\rho_k)+\frac{\partial}{\partial x_i}(\varepsilon\rho_k U_k)=\frac{\partial}{\partial x_j}\left[\left(\mu+\frac{\mu_t}{\sigma_\varepsilon}\right)\frac{\partial \varepsilon}{\partial x_i}\right]+C_{1\varepsilon}\frac{\varepsilon}{k}(G_k+C_{3\varepsilon}G_b) - C_{2\varepsilon}\rho\frac{\varepsilon^2}{k}+S_\varepsilon \tag{3.31}$$

where G_k and G_b are the turbulence kinetic energy created as a result of the mean velocity gradients and buoyancy respectively. Y_M presents the involvement of the fluctuating dilatation in compressible turbulence to the total dissipation rate. S_k and S_ε are utilized to define the source terms, while the turbulent viscosity, μ_t is calculated using the combination of *k* and ε as given below:

$$\mu_t=\frac{C_\mu\rho k^2}{\varepsilon} \tag{3.32}$$

where C_μ is an empirical constant. In turbulence layers, diffusion and the production terms are equal to zero, thus $C_{2\varepsilon}$ is a constant appearing in the equation (3.4). Nevertheless, $C_{2\varepsilon}$ might be found directly from the decay measurement of turbulent kinetic rate (k) and was computed to be in a range of 1.8−2. For local equilibrium shear layers C_μ is equal to 0.09. The values of these empirical model constants $C_{1\varepsilon}$, $C_{2\varepsilon}$, $C_{3\varepsilon}$, C_μ, σ_k and σ_ε are recommended by Launder and Spalding (1974) for dispersed multiphase system as 1.44, 1.92, 1.3, 1.0, and 1.3, respectively.

3.8.3.2.2 RNG k−ε Model

This model is developed from the instantaneous Navier–Stokes equations, using a mathematical technique entitled the "Renormalization Group" (RNG) approach. This model is derived using analytical derivation, which generated dissimilar constants to those in the standard k–ε model. Moreover, additional terms and functions also are produced in the transport equations for k and ε. The impact that is caused by small scale turbulence is usually recognised by a random forcing function in the Navier–Stokes equations (Hjertager *et al*., 2002).

$$C_1^o = C_1 - \frac{\mu(1-\mu/\mu_o)}{1+\beta\mu^3} \tag{3.33}$$

$$\mu = \left[2\left\{ \left(\frac{\partial U_x}{\partial x}\right)^2 + \left(\frac{\partial U_y}{\partial y}\right)^2 + \left(\frac{\partial U_z}{\partial z}\right)^2 \right\} + \left\{ \left(\frac{\partial U_x}{\partial x}\right) + \left(\frac{\partial U_y}{\partial y}\right) + \left(\frac{\partial U_z}{\partial z}\right) \right\}^2 \right]^{0.5} \tag{3.34}$$

The empirical constants of this model recommended with (FLUENT 6.2 User's Guide 2005), are 1.42, 1.68, 0.0845, 0.72, 0.72, 4.377, and 0.012 correspond to $C_{1\varepsilon}$, $C_{2\varepsilon}$, $C_{3\varepsilon}$, σ_k, σ_ε, μ_o, and β, respectively.

3.8.3.2.3 k−ω Model

The present model is also based on model transport equations that are expressed by two terms, which are the turbulence kinetic energy (k) and the specific dissipation rate (ω), which can also be evaluated as the ratio of ε and k. The turbulence kinetic energy

k and specific dissipation rate ω are calculated from the given transport equations (FLUENT 6.2 User's Guide 2005) as:

$$\frac{\partial}{\partial t}(k\rho_k)+\frac{\partial}{\partial x_i}(k\rho_k U_k)=\frac{\partial}{\partial x_j}\left[\left(\mu+\frac{\mu_t}{\sigma_\varepsilon}\right)\frac{\partial k}{\partial x_i}\right]+G_k+G_\omega-\rho\omega-Y_M+S_k \tag{3.35}$$

$$\frac{\partial}{\partial t}(\omega\rho_k)+\frac{\partial}{\partial x_i}(\omega\rho_k U_k)=\frac{\partial}{\partial x_j}\left[\left(\mu+\frac{\mu_t}{\sigma_\varepsilon}\right)\frac{\partial \omega}{\partial x_i}\right]+C_{1\varepsilon}\frac{\varepsilon}{k}(G_k+G_{3\omega}G_\omega) - C_{2\omega}\rho\frac{\omega^2}{k}+S_\omega \tag{3.36}$$

Since the k–ω model has been developed during last two decades, additional terms have been included for both k and ω equations. This has resulted in an improvement in the accuracy of the model for predicting free shear flows. In the above two Equations (3.8) and (3.9), the term of G_k, and G_ω express the turbulence kinetic energy that is generated owing to the mean velocity gradients and buoyancy respectively, Y_M presents the compressible turbulence to the all dissipation rate due to the contribution of the fluctuating dilatation and S_k as well as S_ω are terms of user defined source, while the turbulent viscosity, μ_t is calculated by involving k and ω as follows:

$$\mu_t=\frac{C_\mu\rho k}{\omega} \tag{3.37}$$

The values of empirical constants of $C_{1\varepsilon}$, $C_{2\varepsilon}$, $C_{3\varepsilon}$, σ_k, and σ_ε, are given as 1.44, 1.92, 0.09, 1.0, and 1.3 respectively (FLUENT 6.2 User's Guide, 2005).

3.8.4 Numerical Simulation

3.8.4.1 Initial Conditions

The initial conditions are required to be specified for all dependent variables for the flow phase solution before using CFD simulation in order to obtain unique solutions

for the governing equations. Moreover, the initial solutions have to be taken carefully into consideration in order to provide a desired ultimate solution and abstain from numerical difficulties. Usually the initial pressure field is initialized using the gravity force, resulting in the pressure drop at the fluid phase being equal to the atmospheric pressure. Two different techniques are used in the existing CFD codes to initialize the solution (FLUENT 6.2 User's Guide, 2005). These are:

a. Initialize the whole flow field
b. Patch value in selected zone cell for chosen flow variables

3.8.4.2 Boundary Conditions

Boundary conditions are used to identify the flow and thermal variables on the system boundaries under consideration and are significant factors of dynamic simulations. Two types of boundary conditions for two–phase pipeline simulations are typically employed in simulations of fluid flow:

i- inlet and outlet boundary conditions
ii- wall boundaries

3.8.4.3 Inlet and Outlet Boundary Conditions

The appropriate specifications of inlet and outlet boundaries are required in order to obtain reliable solutions for the simulation. Different available boundaries for inlet and outlet might be applied, such as velocity inlet, mass flow inlet, and inlet and outlet pressure, where the velocity inlet is more commonly used to define the velocity as well as other phase's scalar properties at the inlet boundary such as turbulent parameters, volume fraction, etc. On the other hand, the outlet boundary condition could be described using outflow and pressure outlet. The assigned pressure outlet as a boundary condition is more helpful if the objective is phase separation.

In this simulation study of two–phase flows in a horizontal pipe, the velocity inlet condition is specified at the pipe inlet where the both phases are assumed

incompressible, and the physical velocity of two phases are defined and the volume fraction of the secondary phase is also defined. While at the outlet of the pipe, the pressure outlet condition is specified due to the convergence improvements, and to avoid backflow problems. In this situation atmospheric pressure is used at the pipe outlet. When investigated, because of the effect of different parameters on the pressure drop and liquid holdup in the system, the mass flux is used at inlet boundary condition in order to keep the mass flow rate constant through the domain.

3.8.4.4 Wall Boundaries

Wall boundary conditions can be applied using different terms that depend on the situation, such as symmetry and periodic axis, and can be utilized to bound fluid and solid regions. In the case of viscous flows, the wall boundary condition can be specified as no–slip boundary condition rather than being described as a tangential velocity component in terms of the rotational or translational motion of the wall boundary, or by describing shear (slip wall). It could therefore be modelled as slip wall with zero shears using the symmetry boundary.

3.8.4.5 Turbulence Parameters

When using the k–ε model, two turbulence properties have to be provided for two phases. Three combinations are given with CFD code to identify these values as follows:

a. Turbulence intensity (I) and length scale (l)
b. Turbulence intensity and viscosity ratio (μ_t/μ)
c. Turbulence intensity and hydraulic diameter

The turbulent intensity term can be calculated as:

$$I = 0.16\,\mathrm{Re}^{-1/8} \tag{3.38}$$

Usually the turbulence intensity is between 1–10%, but sometimes it is greater 10%, which is considered extremely high. In contrast 1% or less of turbulence intensity is considered low. The above equation is the best practice for predicting the turbulent intensity value. In contrast, in the situation of fully developed pipe flows, turbulent length scales is limited by the flow path length because the turbulent eddies cannot be greater than the conduit length. Nevertheless, the turbulence length scale can be taken as between 5–10% of the pipe diameter or can be estimated approximately by the following equation:

$$l = 0.07\ \mathrm{D} \tag{3.39}$$

where D expresses the pipe diameter and 0.07 is an empirical constant based on the maximum value of the mixing length in a fully developed turbulent flow (FLUENT 6.2 User's Guide, 2005).

The turbulent kinetic energy and dissipation rate can be calculated as follows:

$$k = \left(IU_{inlet}\right)^2 \tag{3.40}$$

$$\varepsilon = C_{\mu}^{3/2}\frac{k^{3/2}}{l} \tag{3.41}$$

The turbulent intensity (I) and turbulent length scale (l) can be found from Equations (3.38) and (3.39), respectively, U_{inlet} is the mixture velocity at the inlet and C_{μ} is an empirical constant given by 0.09.

3.9 Numerical Solver

The commercial CFD codes are mainly based on two categories of solvers, which are a coupled and segregated solver. In the coupled solver, the governing equations for momentum, mass, and energy are solved simultaneously, but the segregated solver equations of transport governing are solved sequentially. Moreover, governing equations of additional scalars are calculated sequentially for both formulations.

Several iterations of the solution loop have to be performed before a converged solution is obtained, the reason behind that is because of the non-linear nature of the governing equations. In general, the segregated solver is utilized for incompressible and mildly compressible flows. The performance of each solver is determined using discretisation schemes specification, therefore the current capabilities of FLUENT do not permit the coupled solver with multiphase flow modelling. The segregated solver is now used generally for multiphase flow modelling.

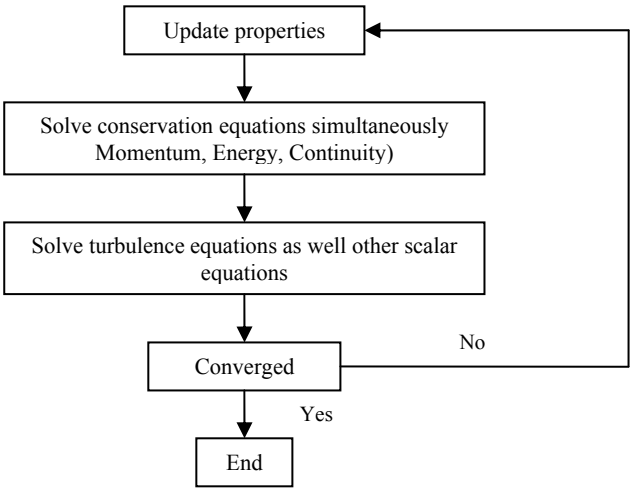

Figure 3.5: FLUENT coupled solver.

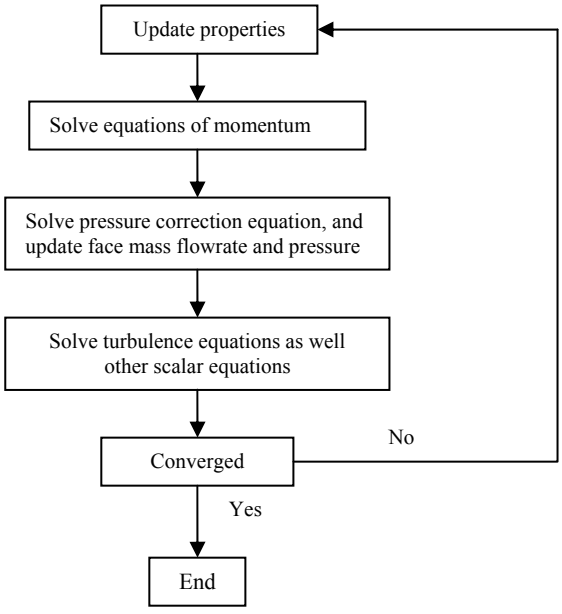

Figure 3.6: FLUENT segregated solver.

As shown in Figures (3.5 and 3.6), flow diagrams of numerical solvers of both coupled and segregated solvers, including the steps of each. Usually the solver performance is obtained by the discretisation schemes specification and it is not likely to make a priori selection of the solver. Nonetheless, the capabilities of current FLUENT do not have support for the coupled solver with the multiphase modelling. The segregated solver, therefore, is often utilized for multiphase modelling and has been used in this thesis of two–phase flow in pipe simulation.

3.9.1 Discretisation

As referred in section (3.7), most of the CFD codes utilize a finite volume method, which is able to convert the governing equations to algebraic equations that are solved numerically. The finite volume approach includes the combination of governing equations relating to each control volume, which leads to discrete equations that preserve each quantity based on the control volume. Discretisation of these governing equations can be demonstrated more simply using the generic transport equation of a scalar quantity ϕ as written in the following form (Ferziger *et al*., 1999):

$$\frac{\partial}{\partial t}(\rho\phi) + \nabla \cdot (\rho U\phi) = \nabla \cdot (\rho\Lambda\nabla\phi) + S_{\phi} \tag{3.42}$$

where (Λ) presents the scalar diffusivity of scalar (ϕ), while S_{ϕ} describes the source term.

When integrated with the equation of generic transport over a control volume, the developing equation usually includes the face values of variables ϕ (ϕ_e, ϕ_w, ϕ_n, and ϕ_s). These variables are represented in terms of the nodal values of the variable ϕ, such as ϕ_E ,ϕ_W ,ϕ_P ,ϕ_S , and ϕ_N. The available CFD codes as FLUENT gives different options of algorithms that can be used to complete this target in conjunction with first and second order upwind, power law, third order MUSCL (Monotone Upstream-centered Scheme for conservation laws), and QUICK (Quadratic Upstream Interpolation for Convective Kinetics) schemes. More information about these schemes is provided in FLUENT 6.2 Manual.

Several discretisation schemes such as the first and second order upwind, as well as QUICK are used for momentum, turbulence and phase volume fraction. Usually the first order upwind scheme gives a stable solution, thus results in better convergence which has less time compared with higher order discretisation schemes.

3.9.2 Under Relaxation

The ultimate equations of discretisation in a finite volume have a linear form, which is written as follows:

$$x\phi = y + \sum_i x_i \phi_i \tag{3.43}$$

where x and y are linearised constants. This equation is solved iteratively for ϕ until the convergence is obtained. To prevent the calculation from fluctuations, however, it is necessary to control the difference in consecutive values of ϕ. Typically, this can be achieved using an under relation factor, which minimizes the change of ϕ attained throughout the consecutive iterations. When the Equation (3.43) is modified, then it can be written as:

$$\phi_{new} = \phi_{old} + \alpha \Delta\phi \tag{3.44}$$

$$\Delta\phi = \left(y + \sum_i x_i \phi_i \right)_{new} - \phi_{old} \tag{3.45}$$

where α refers to an under relation factor, which has a value ranged from 0.1 to 1.

3.9.3 Pressure Velocity Coupling

Typically pressure velocity coupling in the CFD solver is solved to develop an equation for pressure from the continuity discrete equation. There are different approaches which are based on the pressure velocity algorithm, such as SIMPLE, SIMPLEC, and PISO. In general, The SIMPLE (semi–implicit pressure linked equation) algorithm is broadly utilized in existing CFD codes. It employs the

relationship between velocity and pressure corrections to impose the mass conservation in consequence to get the pressure. While the velocities are typically calculated by a segregated solver, it is also coupled with the phases. The equation of pressure correction is derived based on total volume continuity and is solved. Following this the pressure and velocities are adjusted to assure the satisfaction of the continuity constraint (FLUENT 6.2 User's Guide, 2005).

Therefore, using the SIMPLE algorithm, the equation of pressure velocity is affected by divergence difficulties, except if some under–relaxation is used. The velocity components usually are under–relaxed to make this algorithm more powerful. One of the factors that restrict the use of the SIMPLE algorithm is that the new velocities and their related fluxes cannot satisfy the momentum balance after the pressure correction equation is solved. Therefore, the calculation has to be iterated until the balance equation is fulfilled. The modified form of SIMPLE algorithm has been utilized in Eulerian–Eulerian simulations in this research as given in more detail in Chapter 5.

Another scheme which is one of the SIMPLE algorithm categories is the PISO (Pressure–Implicit with Splitting of Operators) scheme. It is derived from the higher degree of the approximate relation among the velocity and pressure corrections. In contrast with the SIMPLE algorithm, it has the ability to do two further corrections, these are skewness and neighbour correction. The advantage of using this algorithm is that it allows a fast convergence rate and sufficient accuracy without loss (FLUENT 6.2 User's Guide, 2005).

3.10 Conclusions

In this chapter Computational Fluid Dynamics (CFD) techniques have been reviewed and their capabilities of modelling two–phase flow also have been summarised. In addition, an overview of the available CFD codes, turbulence models, and related issues of modelling two–phase flow were introduced. A detailed description of the dispersed Multi-fluid flow modelling (Eulerian–Eulerian, Volume of Fluid, and Eulerian–Lagrangian) was given, including the conservation equations that have been used in each approach. No studies have been reviewed relating to two–phase flow in

pipes using CFD simulation. This part will be covered in subsequent chapters, which will include discussion of droplet hydrodynamics, flow pattern, liquid holdup and pressure drop.

3.11 Bibliography

Bakker, A. and L. M. Oshinowo (2004). Modeling of turbulence in stirred vessels using Large Eddy Simulation. *Chemical* Engineering *Research and Design*, 82, 1169-1178.

Bakker, A., A. H. Haidari and L. M. Oshinowo (2001). Realize greater benefits from CFD, fluid/solids handling. *AIChE's CEP magazine*, March, 45-53.

Chen, P., M. P. Dudukovic and J. Sanyal (2005). Three-dimensional simulation of bubble column flows with bubble coalescence and breakup. *AIChE Journal*, 51, 696-712.

Constantinescu, G. S. and K. D. Squires (2003). LES and DNS investigations of turbulent flow over a sphere at Re = 10,000. *Flow, Turbulence and Combustion*, 70, 267-298.

De Schepper, S. C. K., G.J. Heynderickx and G. B. Marin (2008). CFD modeling of all gas liquid and vapor liquid flow regimes predicted by the Baker chart. *Chemical Engineering Journal*, 138(13), 349-357.

Delnoij, E., J. A. M. Kuipers and W. P. M. van Swaaij (1999). A three-dimensional CFD model for gas-liquid bubble columns. *Chemical Engineering Science*, 54, 2217-2226.

Domgin, J., D. G. F. Huilier, H. Burnage and P. Gardin (1997). Coupling of a lagrangian model with a CFD code: Application to the numerical modelling of the turbulent dispersion of droplets in a turbulent pipe flow. *Journal of Hydraulic Research*, 35, 473-488.

Drew, D. A. (1983). Mathematical modeling of two-phase flow. *Annual Reviews in Fluid Mechanics*, 15, 261-291.

Ferziger, J. H. and M. Perić (1999). Computational models for fluid dynamics (*Second edition*). Springer, Berlin.

FLUENT 6.2 User's Guide (2005), FLUENT Inc., Lebanon, NH.

Gaylard, A. (2001). In: Computational fluid dynamics in practice. Rhodes, N. (Editor). Professional Engineering Publishing.

Hjertager, L. K., B. H. Hjertager and T. Solberg (2002). CFD modelling of fast chemical reactions in turbulent liquid flows. *Computers & Chemical Engineering*, 26(4-5), 507-515.

Hossain, A., J. Naser, A. M. K. McManus and G. Ryan (2003). CFD Investigation of particle deposition and distribution in a horizontal pipe. *Presented at the 3th international conference on CFD in the Minerals and Process Industries*, Melbourne, Australia, 10-12 December.

Jaworski, Z. and P. Pianko-oprych (2002). Two-phase laminar flow simulations in a kenics static mixer. The Standard Eulerian and Lagrangian Approaches, *Transactions IChemE, Chemical Engineering Research and Design*, Part A, 80, 910-916.

Launder, B. E. and D. B. Spalding (1974). The numerical computation of turbulent flows, *Computer Methods in Applied Mechanics and Engineering*, 3(2), 269-289.

Li, J. (1995). Calcul d'interface affine par morceaux (Piecewise Linear Interface Calculation). *C. R. Acad. Sci. Paris S´er. II*, 320, 391–396.

Lopez de Bertodano, M., S. -J. Lee, Jr. R. T. Lahey and D. A. Drew (1990). The prediction of two-phase distribution phenomena using a Reynolds stress model. *Journal of Fluids Engineering*, 112, 107-113.

Morsi, S. A. and A. J. Alexander (1972). An investigation of particle trajectories in two-phase flow systems. *Journal of Fluid Mechanics*, 55(2), 193-208.

Noh, W. and P. Woodward (1976). SLIC (simple line interface calculation), in: A. van de Vooren, P. Zandbergen (Editions.), *Proceedings of the 5th International Conference on Fluid Dynamics*, 59: Lecture Notes in Physics, Springer, Berlin, 330–340.

Oberkampf, W. L. and T. G. Trucano (2002). Verification and validation in computational fluid dynamics. *Progress in Aerospace Sciences*, 38, 209–272.

Prasad R. O., A. Bakker and E. M. Marshall (1998). Numerical modeling of mixing processes what can LES offer? *Presented at the Annual Meeting of the AIChE*, Session 238, Nov. 15-20, Miami Beach.

Puckett, E. G. (1991). A volume-of-fluid interface tracking algorithm with applications to computing shock wave refraction, in: H. Dwyer (Edition), *Proceedings of the 4th International Symposium on Computational Fluid Dynamics*, Davis, CA, 933–938.

Puckett, E. G., A. S. Almgren, J. B. Bell, D. L. Marcus and W. G. Rider (1997). A high order projection method for tracking fluid interfaces in variable density incompressible flows. *Journal of Computational Physics*, 130, 269–282.

Ranade, V. (2002). Computational flow modeling for chemical reactor engineering. Academic press.

Rashmi G. W., T. S. Y. Choong, S. A. Hussain, M. Khalid and T. G. Chuah (2009). Numerical study of dispersed oil–water turbulent flow in horizontal tube. *Journal of Petroleum Science and Engineering*, 65, 123–128.

Shaw, C. T. (1992). Using computational fluid dynamics. Prentice Hall International (UK) Ltd.

Ubbink O. (1997). Numerical prediction of two fluid systems with sharp interfaces. *Ph.D. Thesis*, Dept. of Mechanical Engineering, Imperial College of Science, Technology & Medicine.

Van Wachem, B. G. M. and A. E. Almstedt (2003). Methods for multiphase computational fluid dynamic. *Chemical Engineering Journal*, 96(1-3), 81-98.

Versteeg, H. K. and W. Malalasekera (1996). Introduction to computational fluid dynamics: the finite volume method: Addison-Wesley.

Zaleski, S. (2005). Interface tracking-VOF, in: Lecture Given at Course: Industrial two-phase flow CFD, von Karman Institute for Fluid Dynamics, Belgium.

Chapter 4

Numerical Simulation of Flow Pattern and Droplets Hydrodynamic using Volume of fluid (VOF) Model

As oil and gas developments are moving into deeper waters, production strategies are becoming more challenging due to the aggressive environment, and the problems associated with deep water. In general, oil and gas wells have flowlines that transport hydrocarbons, water, or chemicals between the platforms and manifolds, satellite wells and onshore facilities. These flow lines are normally buried on the sea bed. There is a high risk of water accumulation in the low spot sections during shutdown operations. During the restart operation, gas contracts and displaces the water, creating droplets as a result of disturbing the liquid film. This phenomenon of breaking up of the liquid film in the high velocity gas phase is very complicated. Understanding the hydrodynamics of droplets in a gas is of engineering importance.

In this chapter, we have attempted to simulate the droplet dynamics for two–phase flows in a horizontal flow conduit using the Volume of Fluid approach. The objective of this investigation is to study the flow pattern and drop hydrodynamics in gas dominated restarts in a low spot flowline. This will assist us to gain a better understanding of the liquid displacement during restart and to predict the operating conditions which have a high risk of hydrate formation. Various simulations of air–oil and air–water are performed to study the effect of different operating parameters. The effect of gas superficial velocity, liquid patching, low spot depth, and liquid viscosity on flow pattern and droplet formation is investigated into 0.5 m diameter and 55 m long. Both 2D and 3D simulations are performed in which all the predicted flow patterns are compared with Backer flow map.

4.1 Introduction

Exploration and production of oil and gas has moved into deep offshore waters with extreme conditions such as high pressure and low temperature since onshore reservoirs have been depleted. Typically the pipelines are used to transport the crude oil and gas from offshore to the processing facilities. In such systems, two–phase flow is more likely to take place during the transportation of hydrocarbons and gas condensate. Different flow patterns are expected to be generated, such as stratified, dispersed, slug, annular flow etc.

As mentioned in Chapter 2, several authors have reported their studies on two–phase flow in the conduit with different orientation angles (horizontal, vertical, and inclined). Therefore, the pipeline configuration is typically curved due to the topography of the sea floor. The accumulated water is most likely to accumulate in parts of the low sections, which can lead to a high risk of hydrate formation during restart operations. The consequence of this can result in a blockage to the pipeline, which is considered a very important challenge to the offshore deep–water development. The earlier practice of hydrate control strategy is usually based only on hydrate equilibrium data provided, without considering the other system features, such as the physical design of the production system, fluid properties, and two–phase distribution. The consequence of this could lead to quite a conservative approach providing a significant negative impact on the project economy. Overcautiousness however is due to the lack of knowledge and understanding of the hydrate formation and plugging tendencies of carrying two or multi–phase at any flowing conditions. One of the objectives of flow assurance is to optimize the hydrate control strategy in order to minimize the capital and operational costs.

The current state–of–the art in the subject of hydrate control has not yet developed to establish criteria and an experimental methodology that would assist us to find conclusively whether safe operation within the hydrate zone (expressed by pressure–temperature plot) is possible or not. Few cases are reported where certain production systems have been sufficiently operated inside the hydrate area. Moreover, the cause of such behaviour is due to the natural surfactants, which exist with the crude oil.

These surfactants provide self prevention of the hydrate plugging as seen in the literature review in Chapter 2. Some case studies based on field data have shown that multi–fluid transportation with up to 30% of water into the hydrate region is possible without adding any inhibitor. This behaviour is called "self–inhibition through natural surfactants" in which hydrate formation is not avoided, but under specific conditions pipeline blockage is prevented by transporting the hydrate as slurry flow.

The first attempt to examine the two–phase flow in a curved pipeline was conducted by Fitreman (1975). He studied the stability of two–phase gas–liquid flow in the curved section of a pipe by conducting a theoretical and experimental study. Leporcher *et al*. (2002) investigated the hydrate plugging of multi–phase flow in flow loops consisting of a two parts horizontal section with 140 m, 0.05 m diameter with a low pipe section about 22 m long and around 1 m depth. The author studied various parameters, such as levels of stagnant liquid before restart, different gas restart velocities, pipe geometry, and different fluid systems (gas–water, and gas–water–oil), to examine the impact on hydrate plugging.

It was found that the most significant case is at the low restart gas velocity throughout the accumulated stagnant water, where the plugging took place immediately and was controlled by the gas flow rate. In the case of three phases, it was found that the oil layer can delay the plugging time or even prevent it, especially in the case of low water level, while at high gas velocity no hydrate plugging was noted. The author concluded that the high energy hydrodynamic restart procedure would allow restarting the production inside the hydrate zone, whereas the low energy restart would assist hydrate plug formation.

The result obtained provides some preliminary input to the actual field operations. Therefore, more research is needed in order to investigate the risk of hydrate plugging in different pipe geometries. Volk *et al*. (2007) investigated the hydrate plugging of multi–phase flow in a horizontal stainless steel flow loop of 0.076 m, including the low section with and without an inhibitor. Different experiments at the low spot were performed at various operating conditions of restart gas flowrates and water fractions

that ranged from 0.15–0.25 ft/s and from 5–75%, respectively. Two different flow patterns were observed, theses were dispersed and segregated flow. Moreover, low gas restart velocities had a significant impact on the plugging tendency.

Such systems of multi–phase flow requires a better understanding of multi–phase transient flow patterns to assist in understanding the mechanisms of hydrate plug formation. In addition they also examined the effect of water fraction, and found that the importance of transient flow pattern which depends on the water fraction, liquid loading, pipe geometry, restart velocity, and two–phase distribution. The author noted that the water level plays a crucial role in the hydrate plugging in which the probability of hydrate formation is proportional to the water level. Furthermore, the plug can take place at a low water fraction, depending on the operating conditions and the pipe geometry.

Volk *et al*. (2007) studied also the effect of water salinity, since the produced water will not be clean, but will be brine with various salinities. The influence of the salt hydrodynamic is relatively well understood and known however the effects of salinity on hydrate kinetics, particle agglomeration, and plug formation is not understood. Different experiments were performed to study the effect of salinity on the plug development throughout the restart in the low point pipe sections. The experiment concluded that the salinity had an effect on the hydrate formation rate and also affected the flow patterns. However, these experiments demonstrated that an understanding of the transient flow patterns is required when studying hydrate plugging in low section pipelines. Therefore, further work is needed to provide a better understanding of the flow pattern risks at low liquid loading.

In this chapter, the Volume of Fluid model is employed to investigate the effects of restart gas superficial velocity at different liquid patching on the flow pattern, in a 0.5 m diameter and 55 m long tube. All the fluids used are assumed to be incompressible and isothermal. The Baker flow map is used to find out the accuracy of the obtained flow pattern. The effects of restart gas velocity, liquid patching and the level of low sections are studied both with air–water and air–oil two phases flow. A brief

comparison between the simulation flow pattern and Baker chart is reported, also between 2D and 3D simulations.

4.2 Multiphase Flow Modeling

As mentioned before, multiphase flow processes consist of several different flow patterns according to the operating conditions. Three steps need to be considered when modelling multiphase flow. The first step is to determine the number of phases. The next step involves the formulation of the governing equations which describe the multiphase flow. The numerical simulation of any flow problem requires solving the basic flow equations that describe the conservation of momentum, mass and energy in the control volume. The last step in the multiphase flow modelling consists of the solution of these governing equations.

In order to study the hydrodynamics of droplets and flow patterns in horizontal pipelines, including low spots, an existing CFD code is used. For this purpose, the Volume of Fluid (VOF) model in an Eulerian–Eulerian method is chosen for the two–phase flow simulation, in which the grid is fixed and the fluids are assumed to behave as continuous media. In the VOF model, an Eulerian scheme is shared by both phases, combined with a reformulation of the interface forces on a volumetric basis, as will be illustrated next.

4.2.1 Solution Procedure

The VOF model in ANSYS FLUENT 12.1 has been used to simulate the flow pattern and the droplet formation. In this model, as mentioned before in section (3.8.1.1), the progress of gas–liquid interface is tracked using the distribution of the liquid fraction (α_l) in the computational cell. It is equal to zero in the gas phase and unity in the liquid phase. However, the interface of two–phase presents in the cell, where the liquid fraction ranges from 0−1. The finite volume discretisation scheme is employed for interface tracking. There are different discretisation schemes available with the explicit scheme for VOF that are first order upwind, second order upwind, Compressive Interface Capturing Scheme for Arbitrary Meshes (CICSAM), modified

High Resolution Interface Capturing (HRIC), and Quadratic Upstream Interpolation for Convective Kinetics (QUICK). The CICSAM method was used to track the interface accurately. The surface tension was taken into account and given a constant value (0.073 N/m), and the k–ε turbulence model was applied to model the phase turbulence.

4.2.1.1 Equation of Continuity (conservation of mass)

$$\frac{\partial}{\partial t}(\rho)+\nabla.(\rho u_i)=0 \tag{4.1}$$

4.2.1.2 Conservation of Momentum (Navier–Stokes equation)

One momentum equation is shared by all phases, and is solved all through the entire domain.

$$\frac{\partial}{\partial t}(\rho u_i)+\nabla.(\rho u_i u_j)=-\nabla p+\nabla.\left[\mu(\nabla u_i+\nabla u_j)\right]+\rho g_i+F_i \tag{4.2}$$

The term on the left hand side represents the convection and the other four terms on the right side represent the pressure, diffusion, the body force of the gravity and the external body force, respectively.

4.2.1.3 The Volume Fraction Equation

The interface tracking between two phases of *gas–liquid* is achieved by solving the continuity equations of the liquid phase volume fraction, which can be written as:

$$\frac{\partial \alpha_l}{\partial t}+(U_i.\nabla)\alpha_l=0 \tag{4.3}$$

This equation of volume fraction is not solved for the gas phase volume fraction, which is calculated based on the following constraint:

$$\alpha_g + \alpha_l = 1 \tag{4.4}$$

where α_g and α_l are the volume fraction of gas and liquid phase, respectively.

4.2.2 Turbulence Model

The turbulence model of k–ε that is available in ANSYS FLUENT 12.1 was utilized to model the turbulence in the continuous phase (gas). A turbulence model is commonly used for simulating turbulence eddies. This model takes into account the transport of turbulence velocity and length scale. It utilizes a transport equation for the length scale, which provides a distribution of the length scale even in the case of complex flow, such as two–phase flow in a pipeline, with which the present research is concerned.

4.2.3 Physical Properties

At any given cell, the properties and variables of a two–phase mixture are obtained either by the volume fraction contributions or presented purely. However, the two–phase mixture properties used in the transport equations are found by the existence of the gas–liquid phase in each control volume. The density of the mixture in each cell can be expressed by:

$$\rho_{mix} = \alpha_l \rho_l + \alpha_g \rho_g = \alpha_l \rho_l + (1 - \alpha_l)\rho_g \tag{4.5}$$

And the viscosity of the mixture is calculated in the same manner:

$$\mu_{mix} = \alpha_l \mu_l + \alpha_g \mu_g = \alpha_l \mu_l + (1 - \alpha_l)\mu_g \tag{4.6}$$

where ρ_l, μ_l, ρ_g and μ_g are the density and viscosity of liquid and gas phase, respectively.

4.2.4 Differencing Scheme / Solution Strategy and Convergence Criterion

The momentum equation was solved using a first order up–wind differencing scheme, while the scheme of Pressure Implicit with Splitting of Operators (PISO) pressure–velocity coupling was utilized for the pressure–velocity coupling scheme, as is recommended for usual transient calculation. Applying the PISO scheme allows for a quick convergence without any significant loss of accuracy. The PRESTO scheme was used for pressure discretisation. Other schemes that lead to strong divergence or to slow convergence are linear or second order schemes. As large body forces such as surface tension and gravity take place in the multiphase flows, the pressure gradient and body force expressions into the equation of momentum were almost in equilibrium compared to the small contributions of viscous and convective terms. Segregated algorithms converge poorly unless partial equilibrium of body forces and pressure gradient is taken into consideration.

The equation of liquid volume fraction (4.3) was solved by applying an explicit time–marching scheme, and the maximum Counter number was set to 0.25. The values of under relaxation factors for momentum and pressure were 0.7 and 0.3, respectively. With respect to turbulence parameters, intensity and hydraulic diameter specifications were employed. A time step value of 0.001s was used during the simulations.

4.3 Description of the Pipeline Geometry and Operating Conditions

To investigate the flow pattern and hydrodynamic behaviour of continuous droplets forming in a pipeline, different sets of simulations were performed in a 2-D approach using VOF model. The simulations were carried out in a pipeline with 0.5 m diameter, and a total length of 55 m. The pipe is divided into two sections, where the low point section is approximately 10 m long with 1 m depth and the horizontal section is the main simulation section, and is 45 m long. These sections are shown in Figures (4.1 and 4.2). The low section diameter was patched by different initial liquid levels, ranging from 0.2–0.5 m, as shown in Figure (4.3).

The simulations were performed with a fixed mesh size, which was coarse at the low section and finer at the horizontal section in order to capture the flow pattern and the drop formation. Table (4.1) summarizes the physical properties of water, oil and air that were used in this study. For all simulations, a no–slip condition was applied to the pipe walls. The influence of the gravitational force on the flow was taken into account. At the pipe inlet, a velocity inlet boundary condition was employed, and a pressure outlet boundary was imposed to avoid difficulties with backflow at the pipe outlet. All simulations were performed under the atmospheric pressure (1 atm) and room temperature (25^{o}C), where the comparison of flow pattern was validated against the Baker (1954*)* flow map. The initial liquid patching and the gas filling in the low point section were:

- Patched with 0.2 m of water, which is considered a low liquid loading, corresponding to a fraction of 7% water and 93% air. The horizontal section was filled with pure air.

- Patched with 0.3 m of water, which is considered a medium liquid loading, corresponding to 21% water and 79% air fraction. The horizontal section was 100% air.

- Patched with 0.5 m of water, which is considered a high liquid loading with 30% water and 70% air fraction. The horizontal section was fully filled with air.

Figure 4.1: Pipeline Schematic

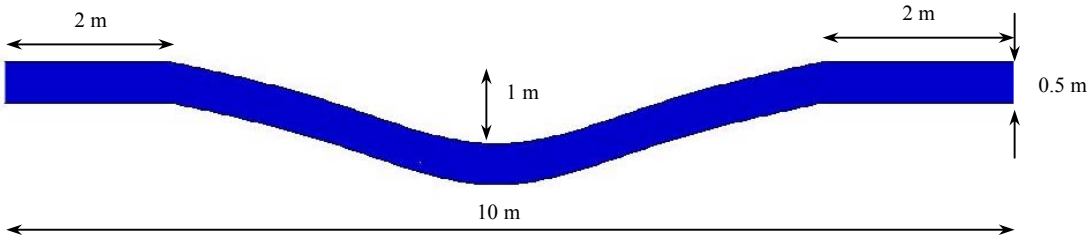

Figure 4.2: Schematic of low point

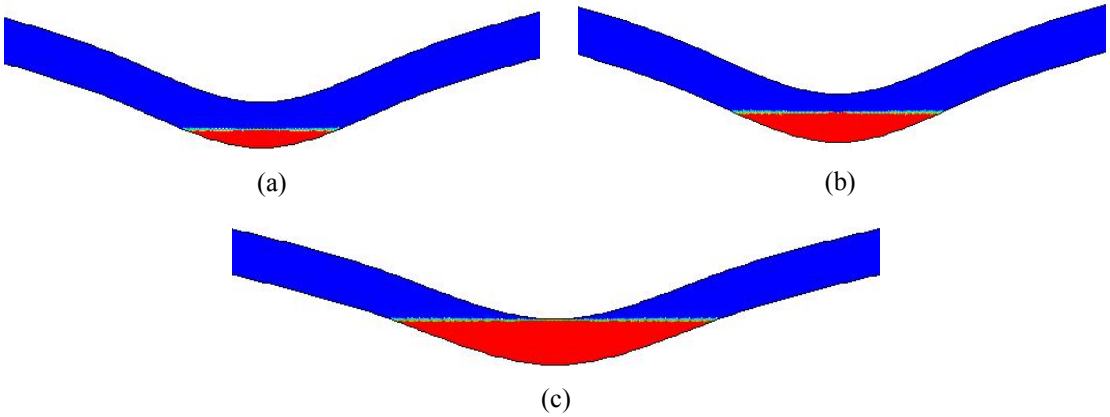

Figure 4.3: Initial patched liquid phase: (a) 20cm, (b) 30cm, and (c) 50cm.

4.4 Air–water Simulation Results and Discussion

4.4.1 Low Liquid Patching with Different Restart Gas Velocities

In order to investigate the effect of gas superficial velocity on the flow pattern, simulations of air–water flow were performed with different restart gas velocities, ranging from 5–20 m/s, and with constant patched liquid of 0.2 m. Low restart gas superficial velocity of 5 m/s, created a slow gas–liquid interface displacement until it reached to the horizontal section of the pipe. It took approximately 1 second as shown in Figure (4.4), while some of liquid returned to the low section due to not enough acceleration. Therefore, some of the water was observed in the low section (see Figure 4.5–a). The remainder settled down into the horizontal section as a very thin film of a few millimetres thickness, and reached to the end of the pipe. At medium gas superficial velocity of 10 m/s, the liquid in the low point reached the horizontal section within hundreds of iterations, or around 0.5 seconds as shown in Figure (4.4–b), where the water phase was not seen in the low section. All of the liquid was carried over and was located in the horizontal section, in which the interface configuration was flat, as seen in Figure (4.5–b). This is a similar interface configuration that was observed in the case of low gas superficial velocity of 5 m/s, as shown in Figure (4.5–a). Therefore, for low liquid loading simulations with low and medium superficial gas velocity, the gas–liquid interface remained almost flat. This represented a situation of the flow pattern resulting in a stratified flow.

At higher gas superficial velocities of 15 and 20 m/s, most of the water in the low spot was taken out quickly, within less than 0.5 seconds, as shown in Figure (4.6–a). As a result, the water was accumulated, remained in the horizontal section, and formed a thin film on the bottom pipe wall before it was dispersed.

Table 4.1: Physical Properties of Water and Air (T = 298 K and P = 101,325 Pa)

Fluid	ρ (kg/m^3)	μ (Pa.s)	σ (N/m)
Water	1000	0.001	0.073
Air	1.225	1.789×10^{-05}	-
Oil	865	0.04	0.032

The high gas velocity, therefore, generates more turbulence and penetrates the liquid phase (water) with a much stronger force, when compared to low and medium velocities. However, at a high gas superficial velocity of 15 m/s, at a dispersed or an annular flow, it was observed as droplets flow in the core phase (gas). Additionally, a small amount of liquid film covered the circumference of the pipe, as shown in Figure (4.6–b). The superficial gas velocity of 20 m/s formed tiny drops at the tube outlet, and more drops were expected to form as the film continues to flow. The generated flow was considered as churn flow, as shown in Figure (4.6–c). The low liquid patching, however, illustrates the risk for hydrate plugging at high superficial gas velocities of 15 and 20 m/s simulations, due to the flow pattern observation.

(a) (b)

Figure 4.4: Gas–liquid interface displacement from the low point for variant superficial gas velocity: (a) 5m/s, and (b) 10m/s.

(a) Some of the water, is remaining in the low section after 35 seconds, and rest of it, creates flat interface.

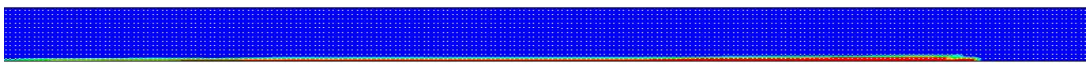

(b) For gas superficial velocity of 10m/s, the interface between gas-liquid is almost flat at the end of pipe after 15 seconds.

Figure 4.5: Sketch of water distribution with low and medium restart gas velocity.

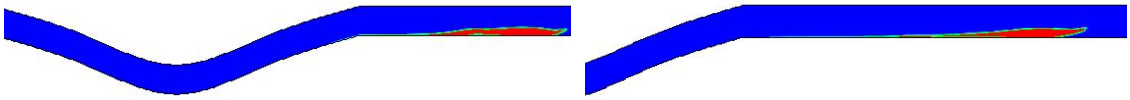

(i) (ii)

(a) (i) The water is displaced completely from the lower section of the pipe for 15m/s, and (ii) The water in low point section is displaced completely after around 0.2 seconds for 20m/s.

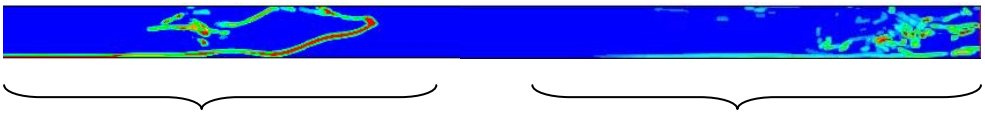

2 seconds 3 seconds

(b) At gas velocity of 15m/s, liquid film starts to be disturbed after 2 seconds and about 40m from the pipe entrance, after 3 seconds and at the pipe outlet, it is clear that the flow becomes dispersed/or annular.

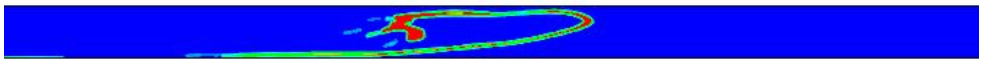

(c) The liquid film is lifted up and started to form droplets at the end of pipe for 20m/s.

Figure 4.6: Sketch of water distributions with high restart gas velocity.

4.4.2 Medium Liquid Patching with Different Restart Gas Velocities

For a medium liquid patching of 0.3 m and a low gas superficial velocity of 5 m/s, some of the water was displaced within 1 second as shown in Figure (4.7–a). After that, the remaining water at the top of the low section fell back into the bottom of the low segment due to insufficient velocity. The rest of the liquid created a very thin liquid film on the horizontal section in which a stratified flow was observed, as shown in Figure (4.7–b). At medium and high gas velocity of 10, 15, and 20 m/s, most of the water accumulated in the horizontal section, and not much water was left at the low point in the first second as shown in Figure (4.8). The entire water fraction was located in the horizontal section in which different flow patterns were observed. At a gas superficial velocity of 10 m/s, the gas–liquid interface started to breakup at 3 seconds and at around 30 m from the pipe entrance, this created some droplets that

remained in the system until the pipe outlet. The observed flow pattern was similar to the dispersed flow as shown in Figure (4.9–a), whereas at 15 m/s of gas superficial velocity, the interface was not disturbed until the end of the tube in which the observed flow pattern is similar in behaviour to slug flow at 2 seconds, and then develops into a dispersed flow at the pipe outlet after 3 seconds as shown in Figure (4.9–b). At the highest gas superficial velocity of 20 m/s, the interface started to interrupt around 2 seconds of flowing time, and created some droplets in which the observed flow pattern was churn flow, as shown in Figure (4.9–c). Therefore, the risk of hydrate plugging is expected at medium and high gas superficial velocity of 10, 15, and 20 m/s, respectively, due to the observed flow pattern of dispersed and churn.

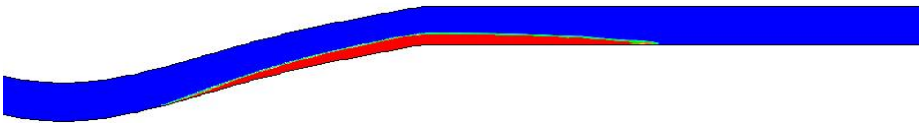

(a) The gas-liquid interface behaviour at 1 second for low velocity 5m/s.

(b) The liquid fraction at the low point after 27 seconds with a thin film of water in the horizontal section.

Figure 4.7: Shows the gas–liquid interface behaviour at low velocity 5m/s and medium liquid patching.

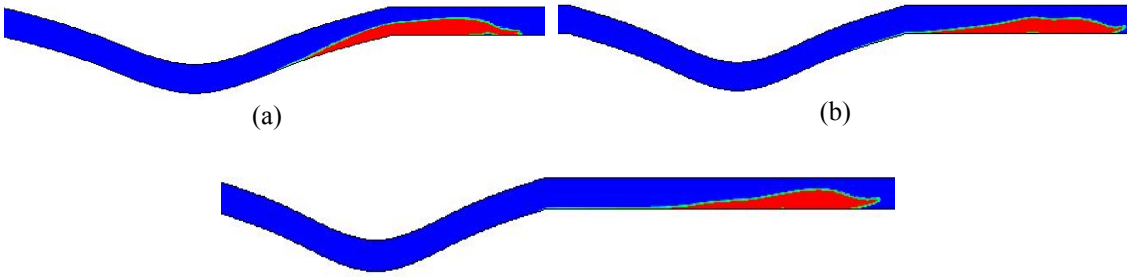

Figure 4.8: Shows the effect of gas superficial velocity on medium liquid patching 30cm after 0.5 seconds, (a) 10m/s, (b) 15m/s, and (c) 20m/s.

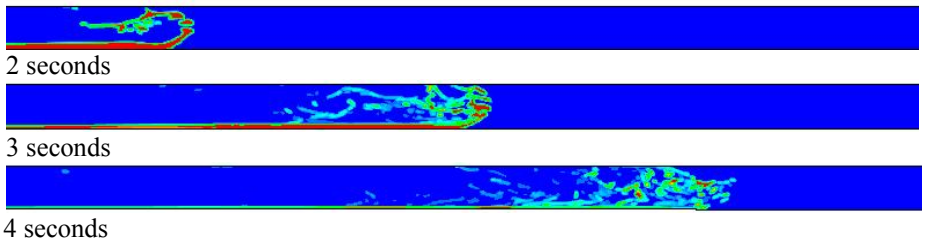

(a) 10m/s

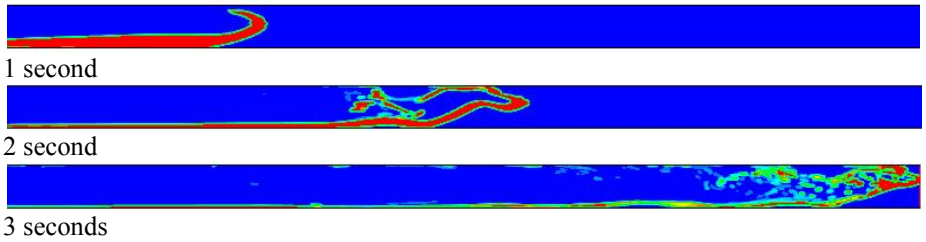

(b) 15m/s

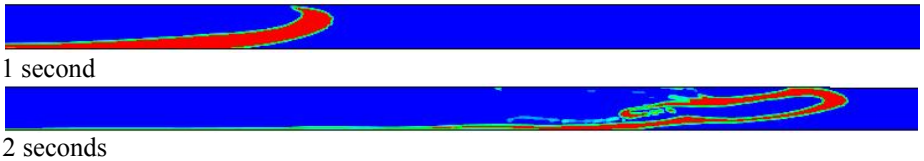

(c) 20m/s

Figure 4.9: Shows the effect of various gas superficial velocities on the gas-liquid interface in the horizontal section at medium liquid patching, (a) 10m/s, (b) 15m/s, and (c) 20m/s.

4.4.3 High Liquid Patching with Different Restart Gas Velocities

In the case of high liquid patching of 0.5 m, and low gas superficial velocity of 5 m/s, the flow observation was similar to the previous liquid patching of 0.2 and 0.3 m, and resulted in a stratified flow. Most of the liquid was taken out of the low section within 1 second, but some of it remained in the low section even after 53 seconds of flowing time, as shown in Figure (4.10). The two phases of gas and liquid in the horizontal section were almost separated and formed a flat layer of water until 4 seconds of flowing time. After that the liquid film was disrupted, resulting in the formation of a number of small droplets. Nevertheless, this situation did not develop into a dispersed flow, as was expected from the flow observation at 6 seconds, due to not enough turbulent force to keep interrupting the liquid film, which created more droplets. As a result, the droplets began to deposit on the bottom wall of the pipe, and the two phases are segregated by a liquid film. This observation was seen after 14 seconds, as shown schematically in Figure (4.11). The generated flow pattern at this liquid patching and low gas superficial velocity can be recognised as a stratified flow.

In comparison, with medium and high gas superficial velocities, the water fluid was predominately accumulated in the horizontal section. The entire water fraction was carried over from the low spot within 1 second, as shown in Figure (4.12). The disruption of the liquid film took place in the horizontal section. At a medium gas velocity of 10 m/s, the gas–liquid interface started to interrupt at 3 seconds and formed a few droplets. More droplets were formed as the flow carried on, some of which stuck to the wall, while the remaining fraction was transported with the bulk phase, as shown in Figure (4.13–a). This behaviour of the flow pattern can be characterized as churn flow. At a high gas superficial velocity of 15 m/s, the interface of gas–liquid was disrupted at approximately 3 seconds of flowing time at the pipe end. At the gas velocity of 20 m/s, the water phase moved as a chunk until it reached the conduit outlet after 2 seconds. At this time, it began to form small drops, in which the observed flow was similar to churn flow behaviour. The main drawback with high liquid patching is that it increases the risk of hydrate plugging due to the flow pattern observation. This occurs especially at 10, 15 and 20 m/s, in contrast with a low superficial gas velocity of 5 m/s, and is considered a low risk of hydrate formation.

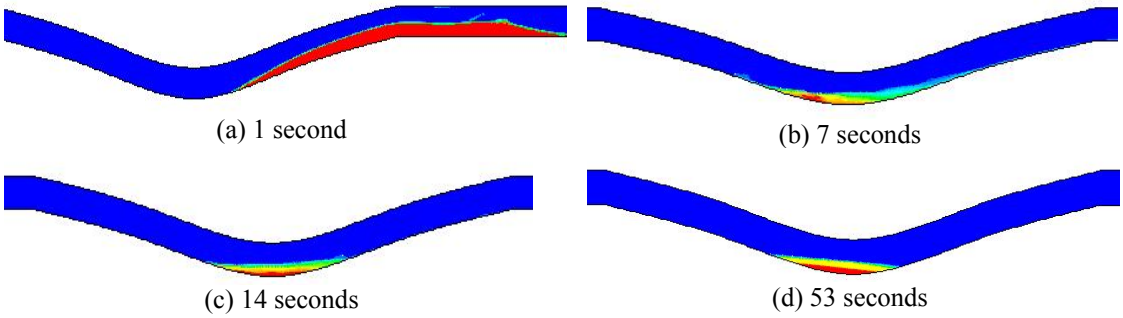

Figure 4.10: Shows the behaviour of the gas-liquid interface and water contours in the low point section for high liquid patching 50cm and low velocity 5m/s at different times.

Figure 4.11: Low gas superficial velocity (5m/s) and high liquid patching behaviour in the horizontal section.

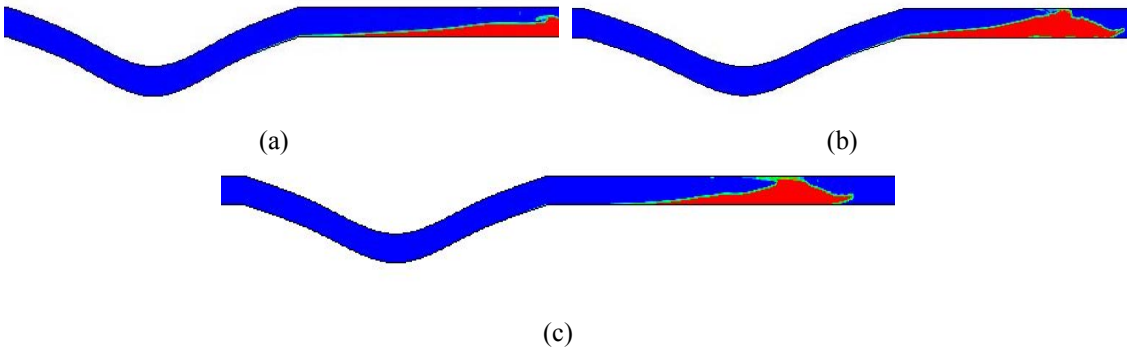

Figure 4.12: Shows the gas-liquid interface behaviour at a low point section for high liquid patching 50cm and at different gas velocities: (a) 10m/s, (b) 15m/s, and (c) 20m/s at 1 second of flowing time.

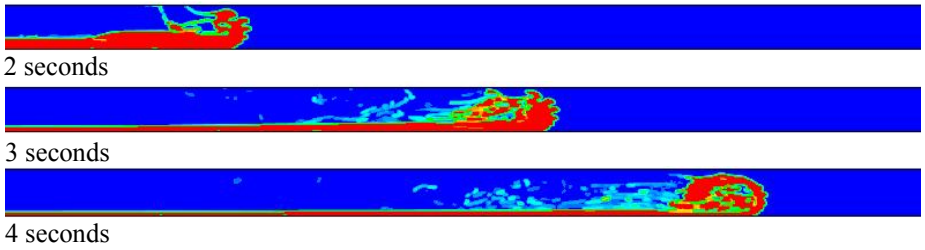

(a) 10m/s

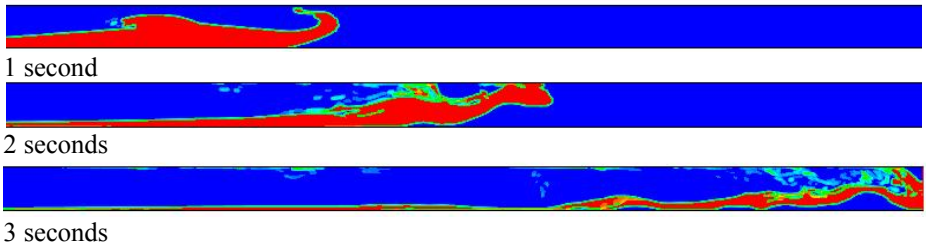

(b) 15m/s

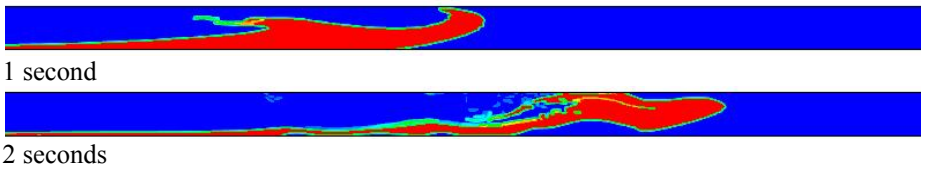

(c) 20m/s

Figure 4.13: Medium and high restart gas velocities with high liquid patching behaviour in the horizontal section.

4.4.4 Compare the Flow Pattern Simulation with Flow Map for 1m Low Section Depth

In this work Baker's flow map in Figure (4.14) is used to identify and compare the obtained flow pattern as a result of CFD two–phase flow simulation. The flow chart demonstrates the various boundaries of flow pattern zones as functions of a mass flux of gas, which is expressed by (*G*), and the ratio of mass fluxes of liquid and gas phase, which is expressed via (*L/G*). The dimensionless parameters ψ and λ are expressed by Equation (4.7) and (4.8), respectively. They are included when the gas–liquid combination is different from the standard combination, at which both parameters are equal to unity, such as in this case where the gas and liquid are defined by air and water.

$$\psi = \frac{\sigma_w}{\sigma}\left[\left(\frac{\mu_L}{\mu_W}\right)\left(\frac{\rho_W}{\rho_L}\right)^2\right]^{1/3} \tag{4.7}$$

$$\lambda = \left[\left(\frac{\rho_G}{\rho_A}\right)\left(\frac{\rho_L}{\rho_W}\right)\right]^{0.5} \tag{4.8}$$

In all simulation cases, the flow pattern of two–phase air–water flow was obtained under the atmospheric pressure (101.325 kPa) and room temperature (298 k). The mass flux of each phase of air and water was calculated to find out the corresponding flow pattern according to the Baker flow map. Based on the physical properties of each phase of air and water, the dimensionless parameters (ψ, λ) are equal to 1 in this situation. In the case of low liquid patching (0.2m), Table (4.2) presents the flow pattern obtained from different cases of simulation as a result of various restart gas superficial velocities.

As can be seen from Table (4.2) the predicted flow patterns using the Baker chart are quite adequate compared with the CFD simulations, especially at low and medium gas superficial velocities of 5 and 10 m/s respectively. At higher gas velocities all the

obtained flow patterns are not predicted accurately with the flow pattern expected from the Baker flow map.

Table 4.2: Flow Patterns for Low Liquid Patching (0.2m) at Different Restart Gas Superficial Velocities

G (kg/s.m^2)	*L* (kg/s.m^2)	*L/G*	Gas velocity (m/s)	Flow pattern
2.2	4.29	1.95	5	Stratified flow
7.3	32.85	4.5	10	Stratified flow
15.3	159.1	10.4	15	Annular flow
25.6	689.7	24.6	20	Churn flow*

* The flow pattern is predicted roughly because the Baker map does not include this flow regime.

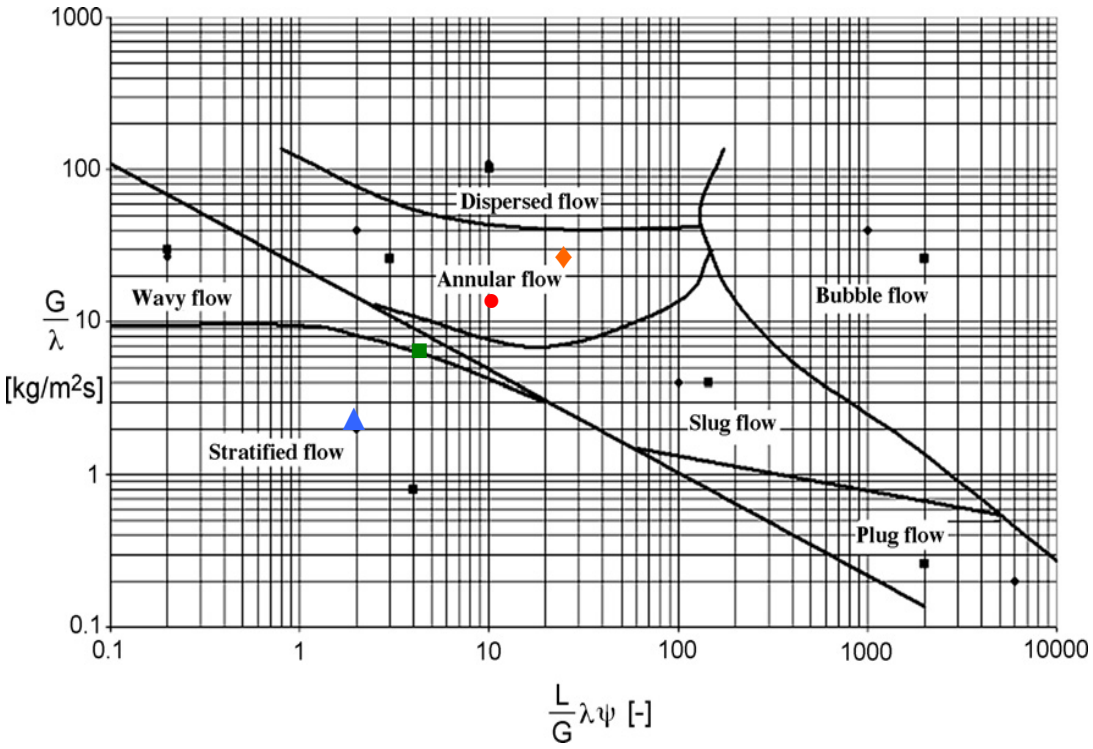

Figure 4.14: Comparison of flow pattern simulation with Baker flow map for 1m low section depth and low patched liquid at different gas velocities, ▲ 5m/s, ■ 10m/s, ● 15m/s, and ♦ 20m/s.

This could be due to the air–water flow simulation which was performed in 2D geometry instead of 3D, which predicts the flow pattern more accurately. Alternatively it could also be due to the flow map which is typically constructed based on specific operating conditions and pipe size. In order to visualize the flow pattern as seen in reality, 3D pipe geometry was constructed and the result will be given in section (4.6) for comparison with a 2D simulation. In addition, the remaining liquid in the low section was obtained for a different restart gas velocity. The final liquid holdup in the low section is affected by the restart gas velocity. Figure (4.15) shows how, for initial liquid patching, the final remaining liquid reaches a value for each velocity, unless the velocity is insufficient to displace any liquid. During the restart, if the gas velocity is not high enough to carry the water over, some of it will remain in the lower section of the conduit. This can be noted especially in the low gas superficial velocity of 5 m/s. Moreover, it can be noted the amount of liquid (water) that is left in the low section increases as the initial liquid patching increases.

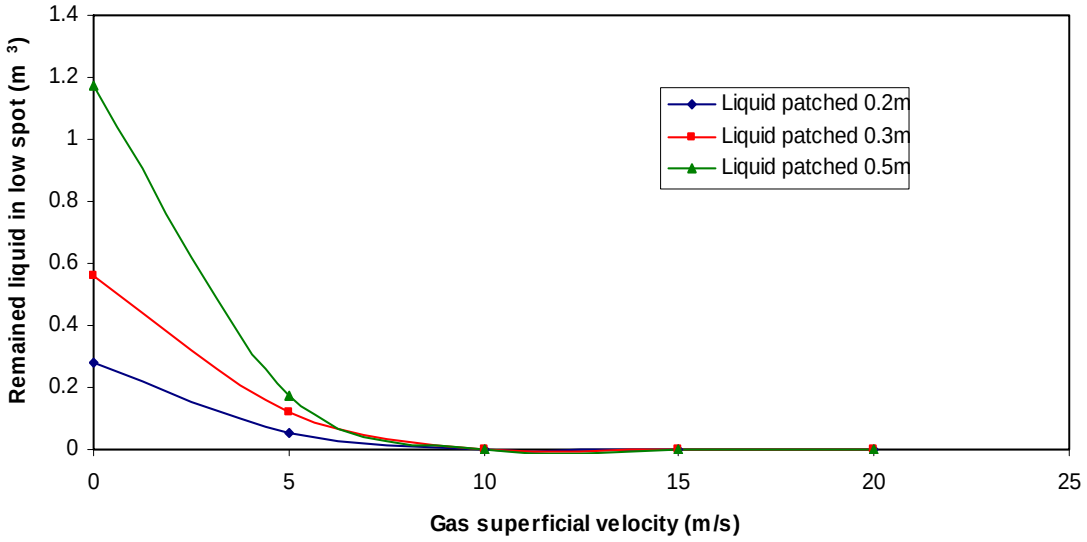

Figure 4.15: The remaining liquid at the low point at different gas superficial velocity for a 1m low spot depth.

4.4.5 The Effect of Low Spot Depth

The effect of low section depth on the flow pattern and droplet formation was studied with different restart gas superficial velocities ranging from 5 to 20 m/s. Various simulations were carried out in 2D, in which the low point section was patched by liquid (water) ranging from 0.2–0.5m. The new low section depth is changed to 2 m as shown in Figure (4.16).

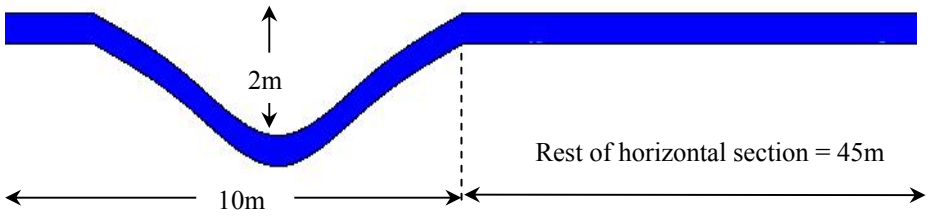

Figure 4.16: A new low section geometry with 2m depth.

4.4.5.1 Low Liquid Patching with Different Restart Gas Velocities

The results obtained for low liquid patching of 0.2 m with a low restart gas velocity of 5 m/s, were very interesting. At the beginning of 2 seconds, the gas phase started to displace the water from the low section, and the liquid film observed in the horizontal section was flat. Some of the liquid fell down to the low section as a result of insufficient velocity. The gas–liquid interface was disrupted at 3 seconds because of the generated turbulent force, which was not enough to lift the water up to the horizontal section, but led to the forming of some of the droplets as shown in Figure (4.17–a). In comparison with Figure (4.17–b) that represents the low point section of 1m at 3 seconds, where just a little liquid fraction was left at the bottom and created a very thin film at the horizontal section. It is obvious from these two figures that the depth of the low section has a significant influence on droplet formation. Figures (4.17–c and d), illustrate the water fraction contours, which are left at the lower pipe section even after 30 seconds. This means the gas superficial velocity of 5 m/s is still not sufficient to take out the entire water phase from the low channel point.

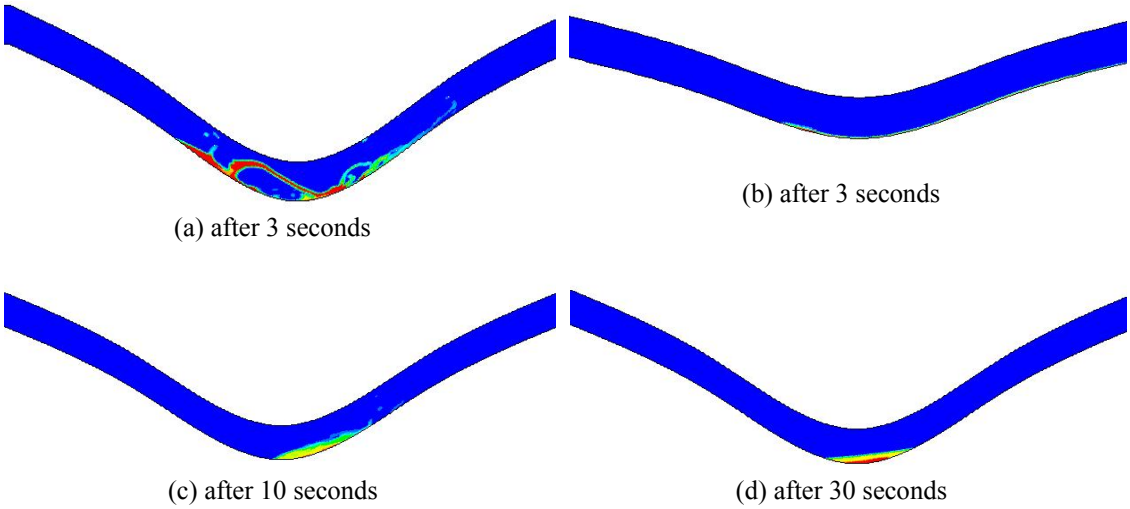

Figure 4.17: Sketch for water fraction in the low point with time at low velocity and liquid patched.

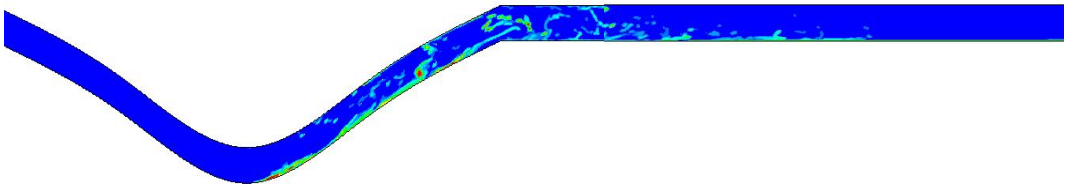

Figure 4.18: Water droplets contours in the low and horizontal section after 4 seconds.

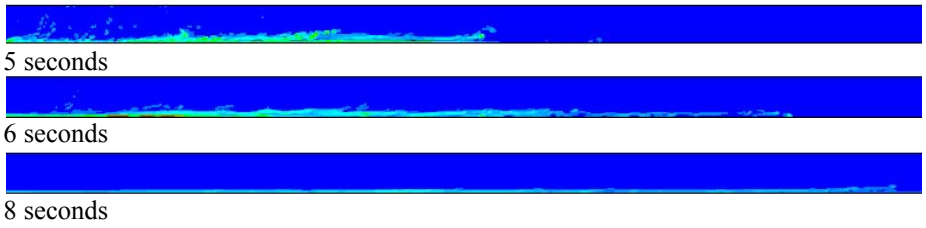

Figure 4.19: Gas-liquid interface behaviour with time for superficial gas velocity of 5m/s.

Figure (4.18) demonstrates the contour of the gas–liquid interface at a low gas superficial velocity after 4 seconds, in which formed droplets continue to exist in the system. At this stage, the flow pattern is similar to a dispersed flow where some drops move in the bulk phase. Around 5 seconds, the presence of these droplets could not be seen clearly and started to settle down. Consequently the two–phase was totally separated by a few millimetres of liquid film, which can be observed clearly after 8 seconds as shown in Figure (4.19). This scenario was controlled by two forces, which were acting on the droplet, these are the gravity and turbulence forces. As mentioned earlier when the turbulence force was inadequate to elevate and keep the droplet in the core phase, this resulted in the deposition of droplets on the bottom wall because of gravitational force, which is much higher. This led to a flattening of the interface where the stratified configuration became stable, as can be seen after 8 seconds.

After we have observed low gas superficial velocity of 5m/s, which does not have much effect on the flow pattern except in the first few seconds, the gas velocity is increased to 10 m/s and the water fraction was taken out from the low section in less than 1 second as shown in Figure (4.20–a). The gas–liquid interface broke off within 1 second and created some droplets, and the flow pattern could be recognised as a dispersed flow. The droplets, therefore, over time started to settle down and form a wavy interface that was similar to a stratified wavy flow as shown in Figure (4.21). The droplet movement is controlled by two forces as mentioned earlier, in which the generated turbulence force is not enough to lift the water layer. Therefore, the predominant force in the system was the gravitational force, which led to this behaviour of the flow pattern.

For high gas superficial velocity of 15 m/s, the whole water fraction was wiped out of the low spot, and the interface was also interrupted to form a few droplets within just 0.5 seconds. This gave an indication that the flow pattern obtained would be dispersed or annular flow (see Figure 4.20–b), but over time, the droplets had begun to evolve more drops and remained in the system until they reached the tube outlet, as shown in Figure (4.22). This is due to the high turbulence which keeps the droplets moving within the core gas phase. Therefore, as can be noted, the observed flow pattern was

dispersed flow. The same observation was noted at a gas superficial velocity of 20 m/s as shown in Figure (4.23).

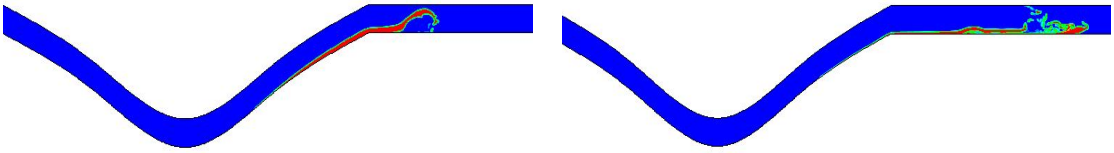

(a) at 0.5 seconds (b) at 0.5 seconds

Figure 4.20: Sketch for water fraction in the low point with time for different gas velocities: (a) 10m/s and (b) 15m/s.

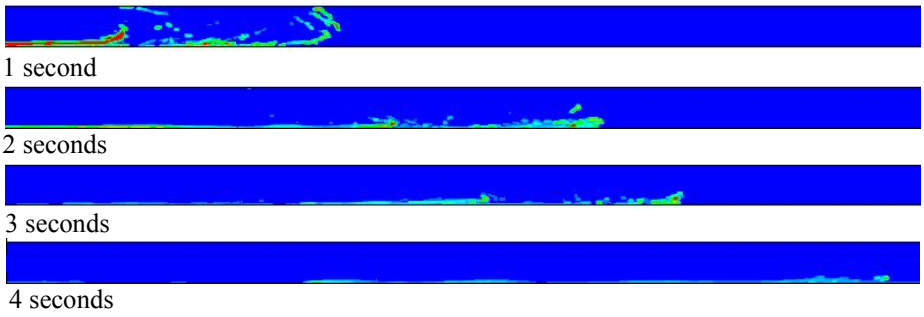

Figure 4.21: Gas-liquid interface behaviour with time for superficial gas velocity of 10m/s.

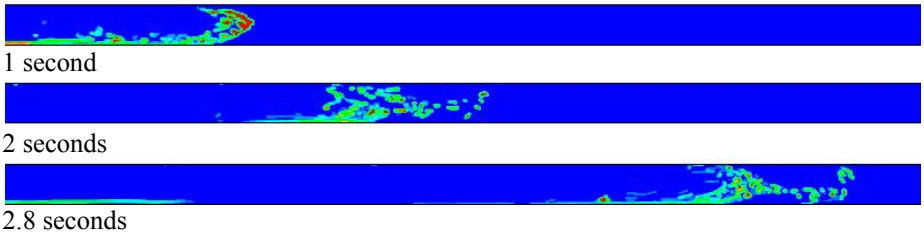

Figure 4.22: Gas–liquid interface behaviour with time for gas superficial velocity of 15m/s.

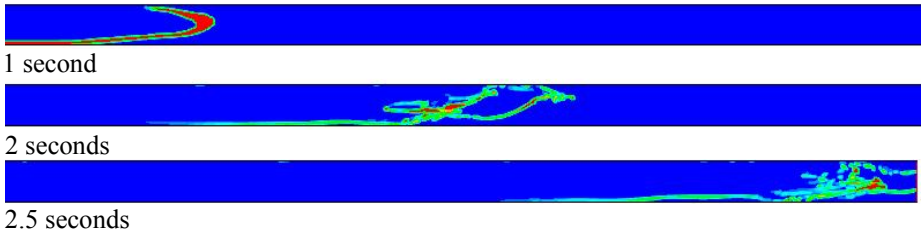

Figure 4.23: The gas–liquid interface behaviour with time for gas superficial velocity of 20m/s.

4.4.5.2 Medium Liquid Patching with Different Restart Gas Velocities

When the liquid patching increased to 0.3 m, almost 1.5 times that of low liquid patching, the flow behaviour and droplets hydrodynamics were investigated at different operating conditions of restart gas superficial velocity. Figure (4.24) demonstrates the liquid behaviour at low gas superficial velocity of 5 m/s, which was inadequate to take the whole water fraction out of the low point. It was expected that the low gas velocity of 5 m/s is insufficient to take the water out since it had the same behaviour at low liquid patching.

Figure (4.24) shows the formation of small droplets at the low point after around 3 seconds. These droplets began to progress in the first 5 m of the horizontal section as shown in Figure (4.25), in which the obtained two–phase behaviour at 4 seconds was comparable to the previous simulation of low liquid patching, as seen in Figure (4.18). Subsequently the droplets started to fall back because of insufficient acceleration to carry on the water phase. They deposited and created a wavy flow at around 6 seconds as shown in Figure (4.25). The liquid fraction in the low section started to settle down after 10 seconds as shown in Figure (4.24–k and l), as well as in the horizontal section where the water phase most likely spread over the total length of 45 m. This water layer was only a few millimetres and became completely flattened after 8 seconds. The observed flow pattern can be described as a stratified flow as shown in Figure (4.25).

It can be concluded that the behaviour of two–phase flow at medium liquid patching is quite similar to low liquid patching in terms of droplet formation and deposition time, as well as the flow behaviour which is exhibited by small droplets and waves on the gas–liquid interface.

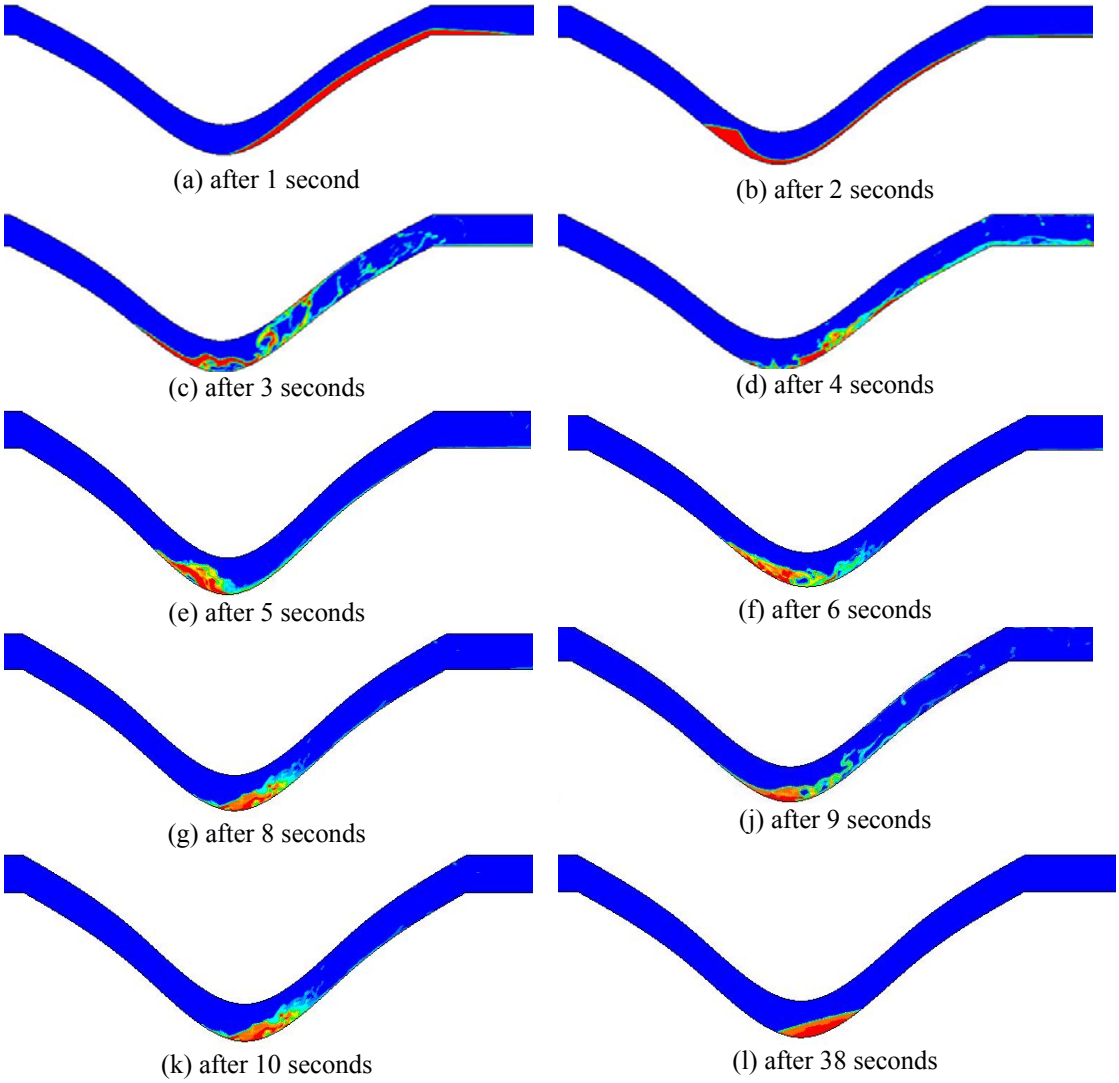

Figure 4.24: Sketch of water fraction behaviour at the lower section of pipe for 5m/s at different flow times.

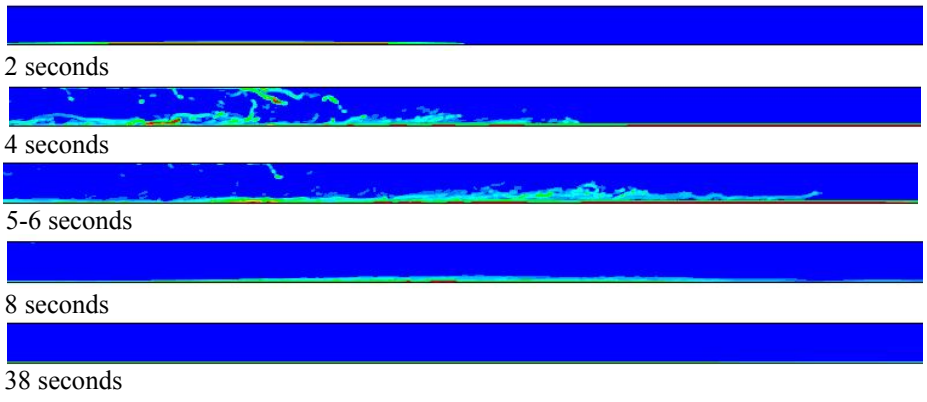

Figure 4.25: Behaviour of gas–liquid interface in horizontal section at medium liquid patching and 5m/s gas velocity.

At a medium gas superficial velocity of 10 m/s, the water fraction almost carried out of the low point section within 1 second, in which the interface was disturbed, and formed a few small droplets as can be seen in Figure (4.26). In contrast with the previous simulation of low liquid loading with the same superficial gas velocity as seen in Figure (4.21), the interface disrupted and created some droplets, which had not occurred at medium liquid patching. The reason for this is due to the increase of water volume in the second simulation, which affected the water mass. The lower volume provided lower mass and was much easier to elevate. The gravitational force was the predominate force, and led to a smooth or flat interface, which can be characterised as a stratified flow, as shown in Figure (4.26).

At a high gas superficial velocity of 15 m/s, the simulation results were very interesting. The entire water fraction in the low section was pushed out quickly to the horizontal section within 0.5 seconds (see Figure (4.27)). Later on the interface was interrupted and produced some droplets that become visible at 2 seconds. They continued to increase and grow with the flowing time until they reached the end of pipeline after around 3 seconds, as seen in Figure (4.28) which demonstrates these two stages.

From the observation at a high gas velocity of 15 m/s, the flow pattern can be classified as dispersed flow and represents a high risk of hydrate formation due to the formation of droplets which remain in the system, flowing with the bulk phase until the conduit outlet. In this scenario, at the appropriate conditions of low temperature and high pressure the droplets will most likely react with the gas phase and will form hydrate particles. These particles will stick with each other and plug the channel quickly. This flow behaviour can be one of the conditions of gas hydrate formation.

At a high superficial gas velocity of 20 m/s, the liquid fraction in the low section was also taken out rapidly to the horizontal section. The gas–liquid interface took different shapes. At 1 second the liquid phase moved as a chunk without disturbance, but at 2 seconds it started to break up and generated a few droplets, which were connected

with and without liquid film. This situation continued until the two–phase left the pipeline as shown in Figure (4.29). The recognised flow pattern was churn flow.

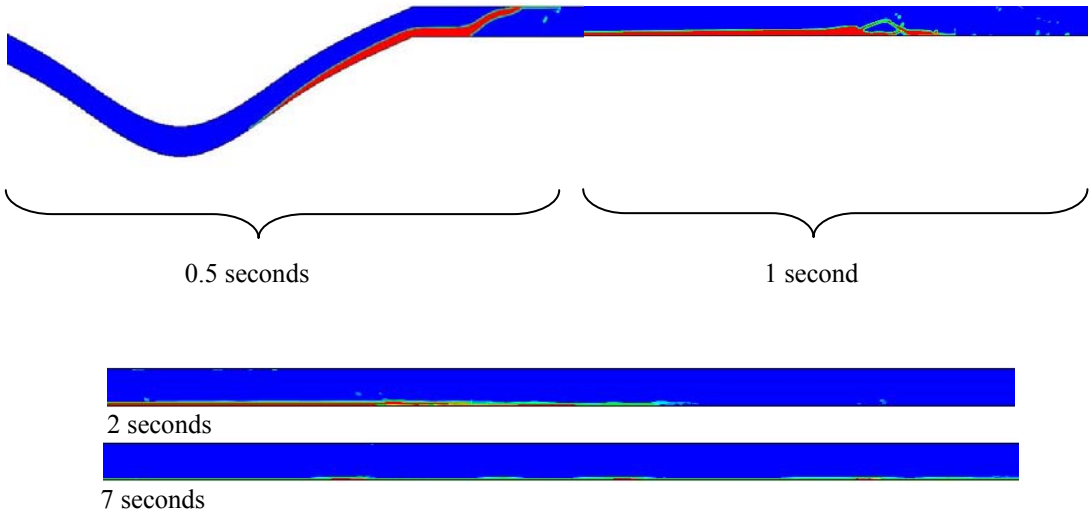

Figure 4.26: Sketch of two-phase behaviour at superficial gas velocity 10m/s with different flow time.

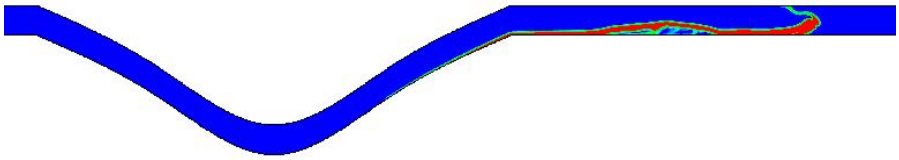

Figure 4.27: Water contours in the low and horizontal section for 15m/s at 0.5 seconds of flow time.

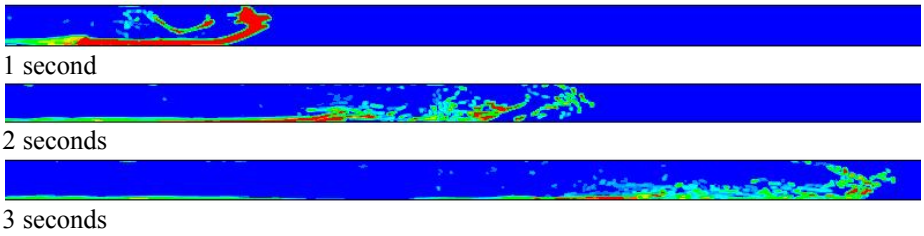

Figure 4.28: Sketch of gas-liquid interface for 15m/s at different flow times.

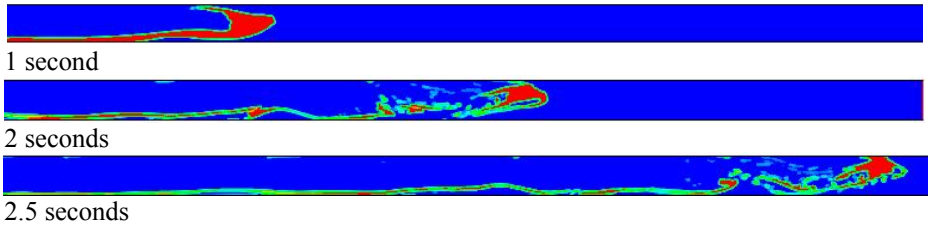

Figure 4.29: Sketch of gas-liquid interface for 20m/s at different flow times.

4.4.5.3 High Liquid Patching with Different Restart Gas Velocities

At a low gas superficial velocity of 5 m/s, it was clear that some of the liquid was taken out of the low section in the first second as shown in Figure (4.30–a). After a while some of the water fell back, due to insufficient velocity. This situation was expected since at low and medium liquid patching it was not taken out. In addition, the water film in the low section was interrupted at 3 seconds of flowing time, as shown in Figure (4.30–c). Owing to that, some droplets formed and developed in the first segment of the horizontal channel as shown in Figure (4.30–d to j). The liquid fraction settled down in the low section after 54 seconds of flowing time as shown in Figure (4.30–k), in which the water layer in the horizontal section became flatter. The observed flow can be described as a stratified flow.

At a medium gas superficial velocity of 10 m/s, some of the water fraction was pushed out of the conduit lower section at 0.5 seconds. After a while some of the water fluid remained in the low section due to insufficient force to take it out as shown in Figure (4.31). Later, at around 1 second, the gas–liquid interface was just a bit disturbed at the beginning of the horizontal section and formed a few small droplets as shown in Figure (4.32). Nevertheless, at a high liquid loading, the water layer just started to break off around 2 seconds, resulting in the formation of a few droplets at around 3 seconds, and then deposited rapidly at the end of the pipe segment at around 45 m as shown in Figure (4.32). It can be noted that the formation of droplets over time varies. It depends on the liquid patching, in which low liquid patching corresponds to less time and the reverse is true for high liquid patching. The observed flow was mainly a stratified and wavy flow as shown in Figure (4.32).

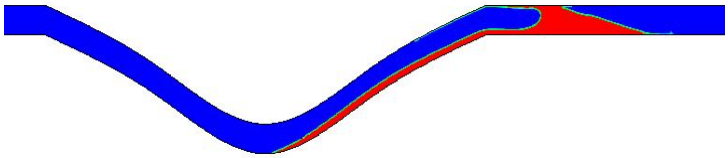

(a) 1 second

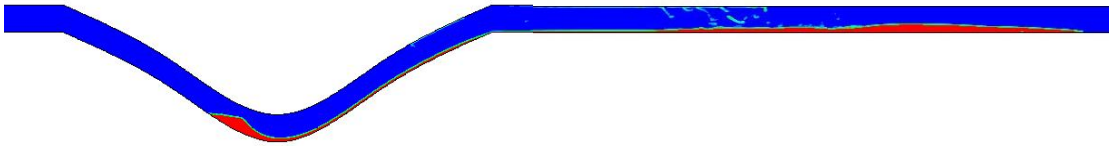

(b) 2 seconds

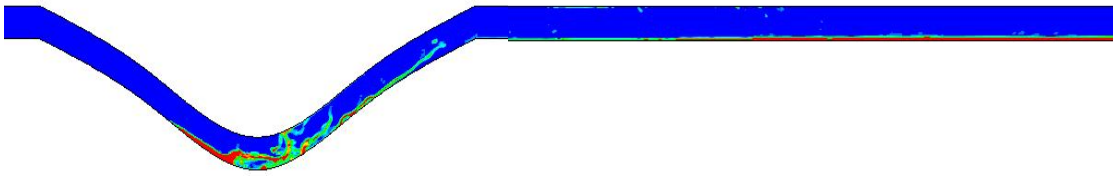

(c) 3 seconds

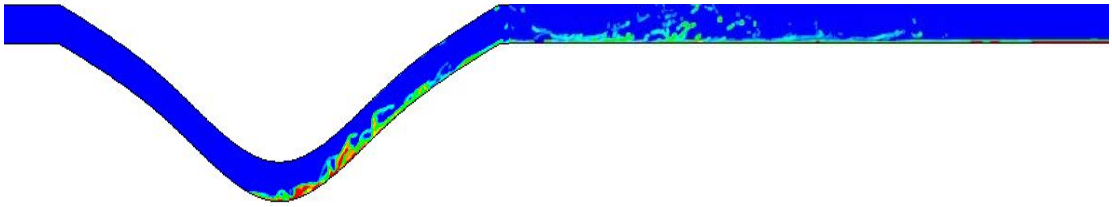

(d) 4 seconds

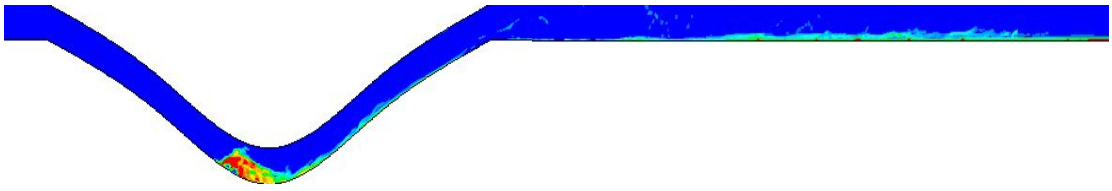

(e) 5 seconds

(f) 6 seconds

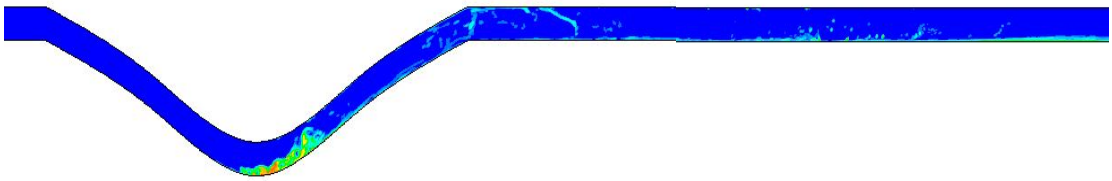

(g) 7 seconds

(h) 8 seconds

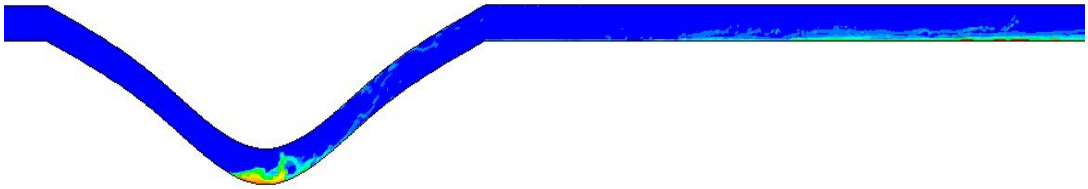

(i) 9 seconds

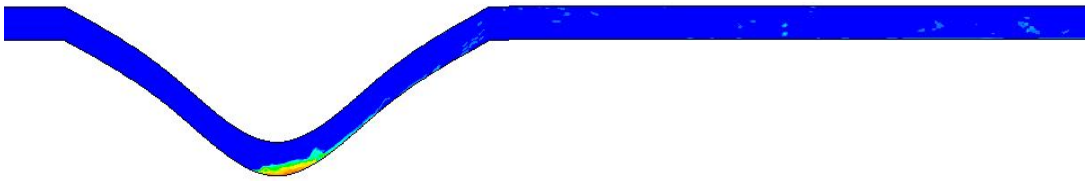

(j) 10 seconds

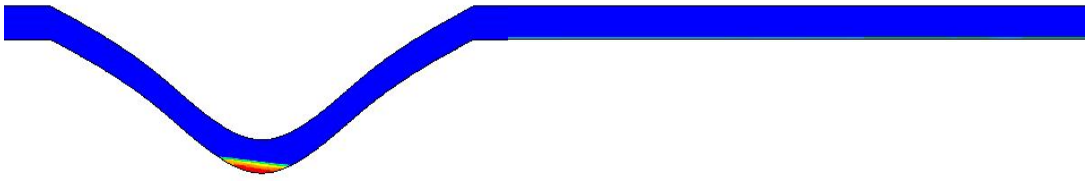

(k) 54 seconds

Figure 4.30: Water contours at low and horizontal sections at variant flow time for 5m/s and high liquid patching.

At a high gas velocity of 15 m/s, the water contours were very similar to previous simulations in terms of flow pattern. The water fraction in the low section moved towards the horizontal section in less than 0.5 seconds. The interface was interrupted at 1 second and generated some droplets that become visible and easy to observe, as shown in Figure (4.33). They continued to develop through the pipeline until they reached the end after 3 seconds as shown in Figure (4.33). From the observation the flow pattern seems identical to that found in the previous simulation results of low and medium liquid patching; it can be classified as dispersed flow. This signifies the high risk of hydrate formation due to the droplet formation and the existence in the system. Therefore, this flow behaviour is considered as high risk of hydrate formation.

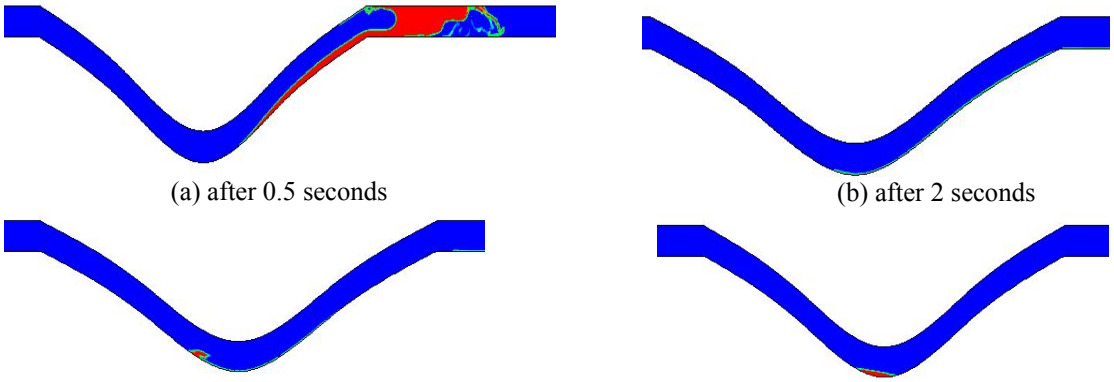

Figure 4.31: Water contours at the low section at different flow times for medium gas velocity and high liquid patching.

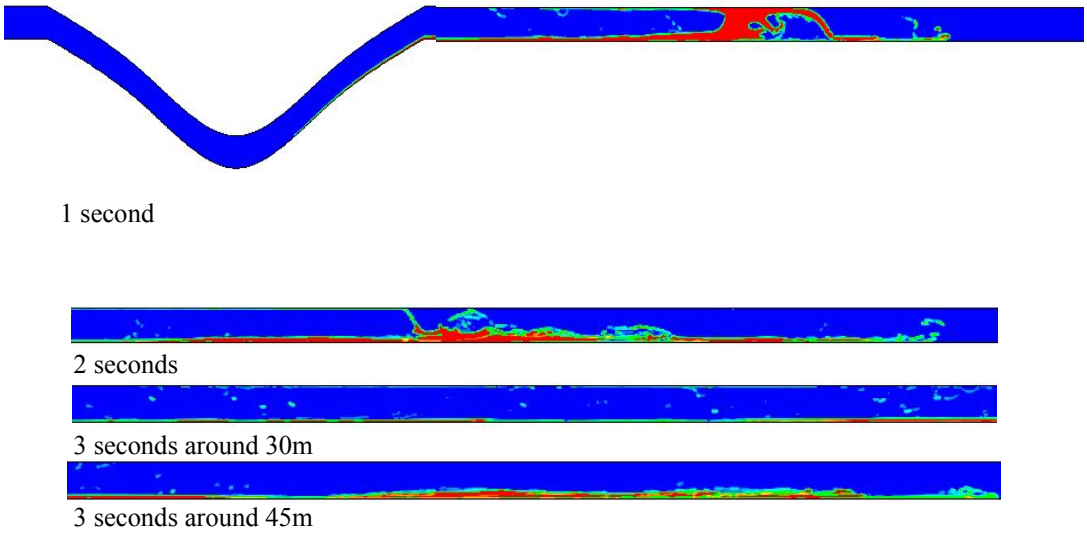

Figure 4.32: Sketch of water contours and flow pattern at superficial gas velocity of 10 m/s and high liquid patching.

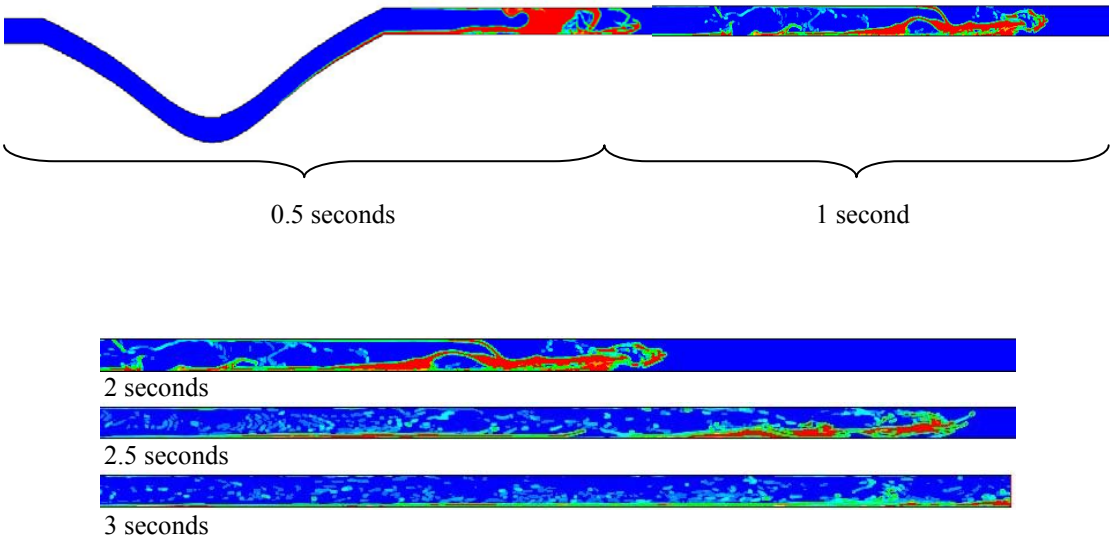

Figure 4.33: Sketch of water contours and flow pattern at superficial gas velocity of 15m/s and high liquid patching.

When the gas superficial velocity had increased further to 20 m/s; it became obvious that the liquid fluid was completely and quickly taken out from the low section. This was expected since it was achieved at a critical gas velocity of 15 m/s. The observed flow pattern is categorised as churn flow, in which the entire liquid phase flows as a chunk in the bulk phase, and some drops form behind as shown in Figure (4.34). This flow behaviour was considered less risky of hydrate formation at this pipe length, but as the pipe length increases the risk of hydrate plugging also increases.

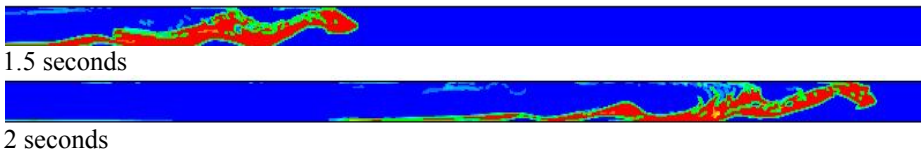

Figure 4.34: Sketch of water contours and flow pattern at superficial gas velocity of 20m/s and high liquid patching.

4.4.5.4 Compare the Flow Pattern Simulation with Flow Map for 2 m Low Section Depth

The same idea in section (4.4.4) has been used where the mass flux of air and water phase was computed to find the corresponding flow pattern according to the Baker chart. Since the same two–phase flow was used, so the dimensionless parameters are equal to 1 based on the physical properties of the air and water phase. In the case of low liquid patching, Table 4.3 demonstrates the flow patterns that have been obtained from different simulations as a result of various restart gas superficial velocities.

Table 4.3: Flow Patterns for Low Liquid Loading at Different Restart Gas Superficial Velocities for 2m Low Section Depth

G (kg/s.m^2)	L (kg/s.m^2)	L/G	Gas velocity (m/s)	Flow pattern
2.2	1.34	0.61	5	Stratified flow
7.3	13.87	1.9	10	Stratified flow
15.3	84.21	5.54	15	Annular flow
25.6	394.3	15.4	20	Dispersed flow

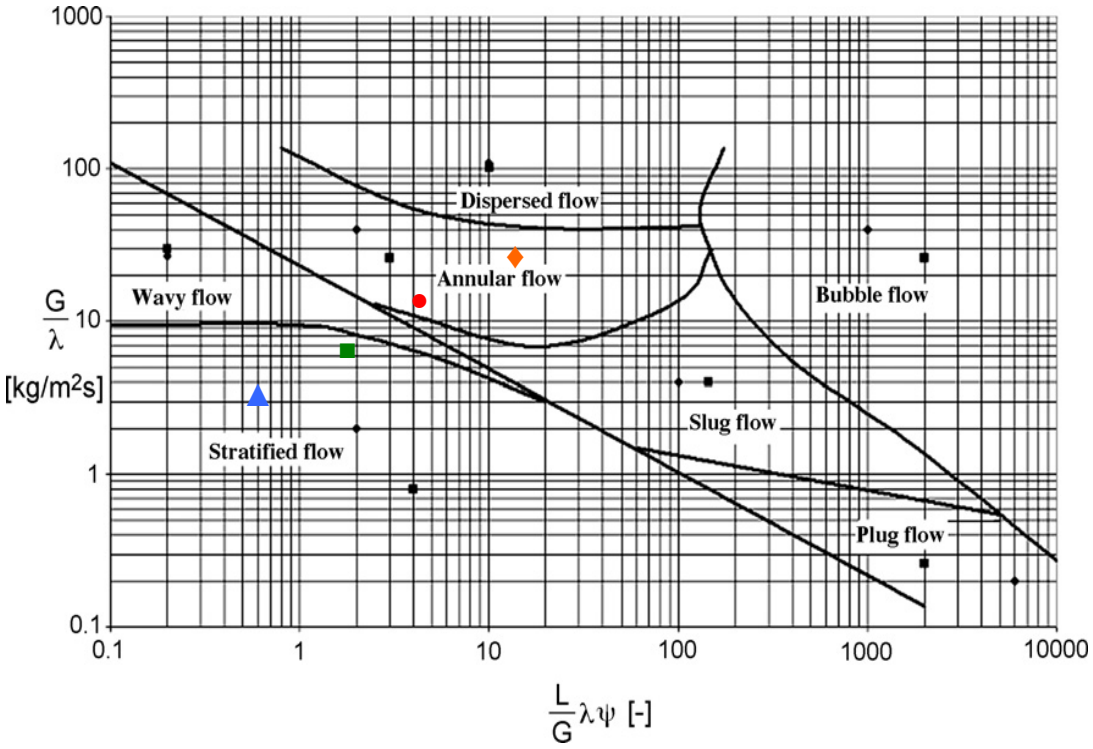

Figure 4.35: Compares flow pattern simulation with Baker flow map at 2m low section depth and low patched liquid at different gas velocities, ▲5m/s, ■10m/s, ●15m/s, and ♦20m/s.

It can be noted from Table (4.3) that the predicted flow patterns using the Baker chart are quite acceptable compared with the CFD simulations, especially at low and medium gas superficial velocities of 5 and 10 m/s respectively (see Figure (4.35)). While at high gas superficial velocities of 15 and 20 m/s, the flow patterns were reasonably predicted, but not precisely. The reason for this prediction may be due to the same two points that have been mentioned earlier. Firstly, that the simulation was performed into two–dimensional, not three–dimensional geometry. Secondly, it is also because of the flow map, which is typically constructed from specific operating conditions and tube size. This issue will be investigated in 3D pipe geometry in order to visualize and predict the flow pattern more accurately (see section 4.6).

Figure (4.36) shows the simulation results of the remaining water in the low section with a 2 m low spot. It can be seen that the required or critical gas superficial velocity to wipe the water phase out of the pipe low section was increased to above 10 m/s, since the depth of the low section had been increased. In comparison with a 1 m low section depth, the gas superficial velocity of 10 m/s was adequate to take the water fluid from the bottom to the top section of the conduit. The low section depth therefore can be considered as one of the parameters that affects the amount of water at the low point. Furthermore, it also has a minor effect on the flow pattern at a few seconds of restart flowing time of a low gas superficial velocity.

Figure (4.36) shows also how for an initial liquid holdup, the final liquid holdup in the low section reaches a value for each velocity. During the restart operation, if the gas velocity is not high enough to hold the water over, some of it will be located in the lower section of the channel. This can be seen particularly at low and medium gas superficial velocities of 5 and 10 m/s. Moreover, the observation was that the amount of liquid (water) left at the low section was similar at 1m depth, in which the liquid holdup increases as the initial liquid loading increases.

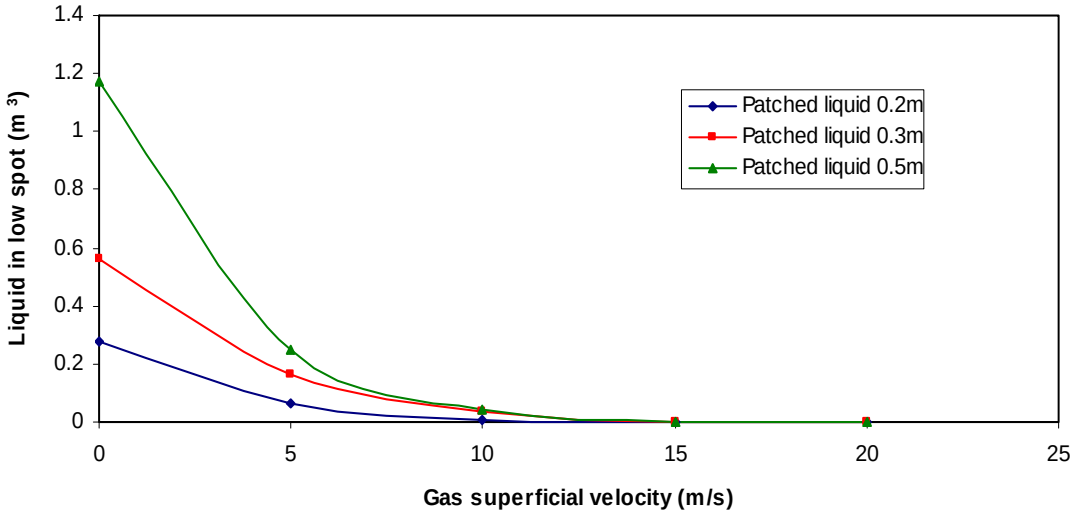

Figure 4.36: Experimental results of water lift in the low section for the second low spot.

4.4.6 The Risk of Flow Pattern

Two different flow pattern maps were developed based on the various restart gas superficial velocities. They indicate the conditions in which the risk of hydrate formation is either low or high. At 1 m of low section depth, situations with a low risk of hydrate plugging were observed at low and medium liquid patching with low restart gas superficial velocity. The observed flow pattern was mainly stratified flow, which is considered as low risk of hydrate plugging due to minimal disturbance taking place at the gas–liquid interface, and no droplets being generated. The high risk hydrate regions are considered to be found in those conditions in which the two–phase flow is totally mixed, such as dispersed and churn flow. The observation of these two flow patterns has been seen at the operating conditions of medium and high liquid patching, or at medium and high gas superficial velocity as shown in Figure (4.37).

At the low section depth of 2 m, the flow map is relatively similar to the previous flow map of 1 m depth. The regions of low risk of hydrate formation have been observed at different liquid patching with low and medium restart gas superficial velocity. The observed flow pattern was mainly a stratified or stratified wavy. These flow patterns are considered as low risk due to the water layer configuration, which is flat or wavy. In contrast, the high risk areas are considered to be those of high restart gas superficial velocity (15 and 20 m/s) in which the observed flow was dispersed or churn flow as shown in Figure (4.38).

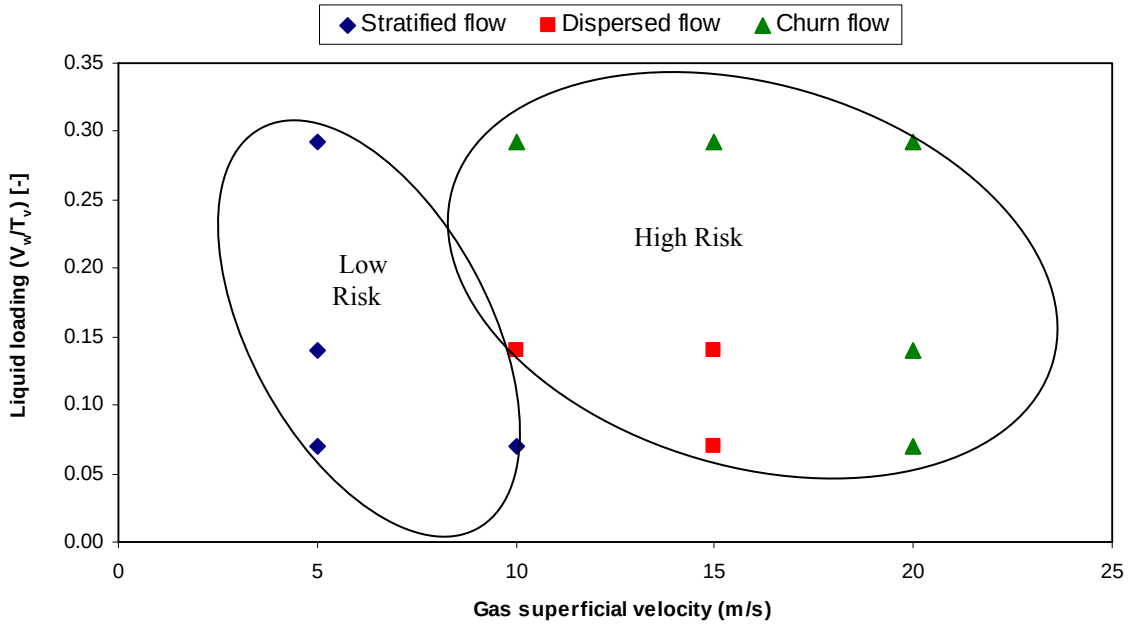

Figure 4.37: Flow pattern map indicates high and low risk areas of 1m low section depth.

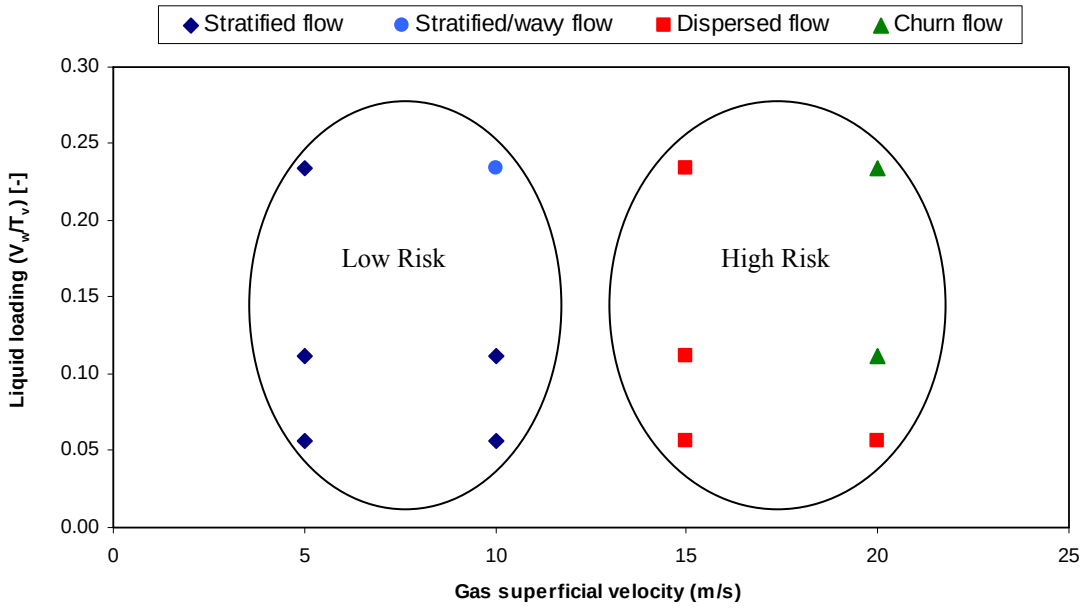

Figure 4.38: Flow pattern map indicates high and low risk areas of 2m low section depth.

4.5 Air–oil Simulation Results and Discussion

In order to investigate the effect of fluid property on the droplet hydrodynamic and liquid displacement, oil is used as a disperse phase, and its property is given in Table (4.1). Various simulations of air–oil two–phase flow were performed in 2D, using the VOF model. The simulation is performed in the same pipe size (see Figure 4.1) with a 1 m depth of low section and under the same operating conditions of pressure and temperature of 101.325 kPa and 298 k, respectively. The boundary conditions, which are applied for the pipe inlet and outlet, are velocity inlet and pressure outlet, while a no–slip wall boundary is applied to the wall. The restart gas superficial velocity and initial liquid patching are similar to those used in water–air simulation.

4.5.1 Low Oil Patching with Different Restart Gas Velocities

Similar to the air–water simulations, other simulations were also conducted, using a pure patched oil phase of 0.2 m with a low restart gas superficial velocity of 5 m/s. The results obtained were very similar to air–water simulation, since the air velocity was not enough to take the oil phase out of the low spot, although the oil fraction was displaced in the first 1-2 seconds during which the oil film was flat. Some of the liquid fell down to the low section because of the insufficient velocity and high oil viscosity. As a result some of the oil was left in the low section, and the flow pattern observed was a stratified flow as shown in Figure (4.39).

At a medium gas superficial velocity of 10 m/s the simulation result showed that the oil phase wiped out of the low spot to the horizontal section in the first second. A few drops were formed and clearly observed within the gas phase. They kept flowing until left the pipe at 4 seconds. After a while it reached the final equilibrium during which some of the oil was left in the low section, and the rest of it settled down as a thin film in the horizontal section as seen in Figure (4.40). The flow pattern in this scenario behaved as dispersed flow.

At a high gas superficial velocity of 15 and 20 m/s, the oil moved out of the low section quickly due to the high turbulence of gas velocity. The gas–liquid interface

was interrupted in the first 1–3 seconds, during which the droplets started to form. They continued flowing in the system until they reached the pipe outlet at 5.5 seconds. The observed flow was an obvious dispersed flow as shown in Figure (4.41). For the gas superficial velocity of 20 m/s the entire oil fraction accumulated in the horizontal section, while the oil film began to break up and create some drops, which remained flowing to the pipe end as shown in Figure (4.42). The observation flow can be considered as churn flow.

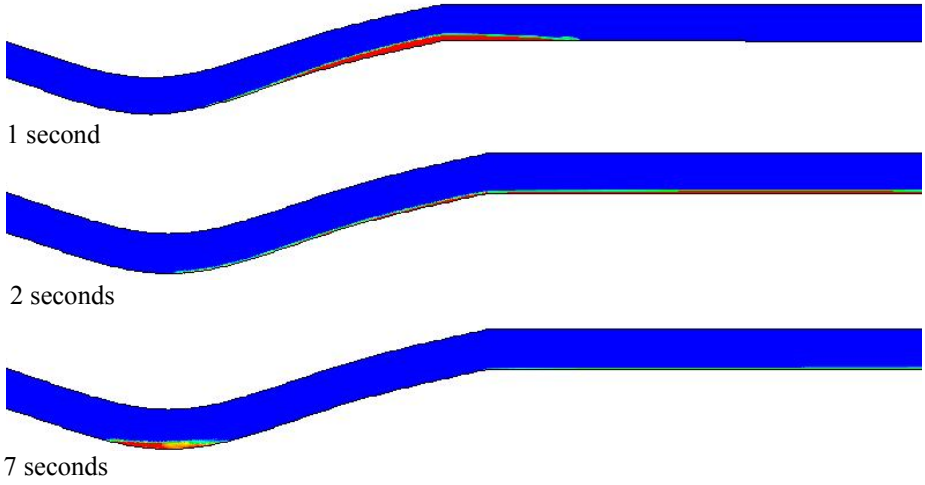

Figure 4.39: Sketch of oil fraction behaviour at the lower section of pipe for 5m/s at different flow times and low oil patching.

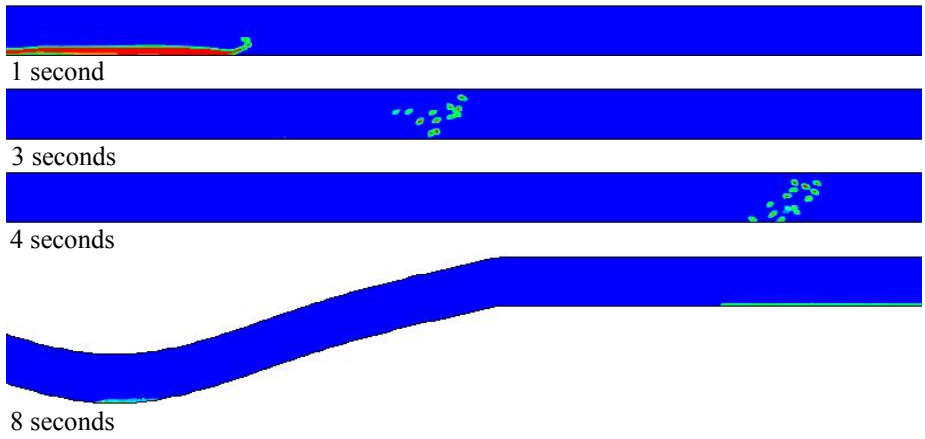

Figure 4.40: Sketch of air-oil interface for 10m/s at different flow times and low oil patching.

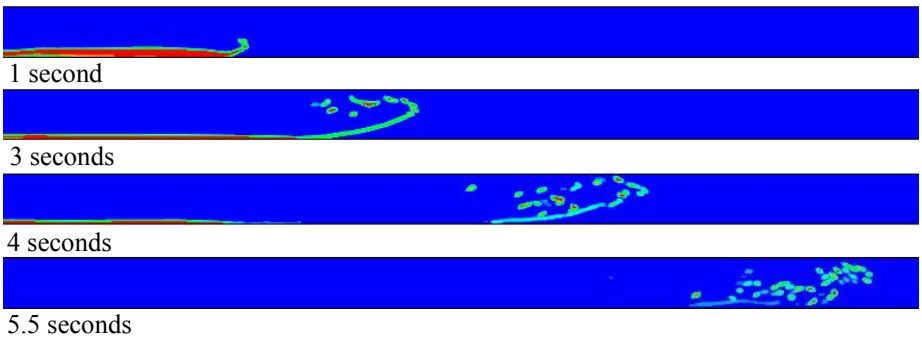

Figure 4.41: Sketch of air-oil interface for 15m/s at different flow times and low oil patching.

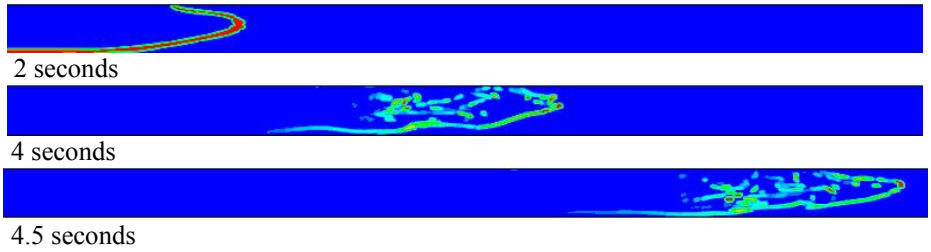

Figure 4.42: Sketch of air-oil interface for 20m/s at different flow times and low oil patching.

4.5.2 Medium Oil Patching with Different Restart Gas Velocities

At medium oil patching (0.3m) and a low gas velocity of 5 m/s, the flow behaviour did not change and the oil fraction remained in the low section, some of it remaining on the horizontal pipe section as a thin layer of oil, as shown in Figure (4.43). The observed flow pattern was similar to low oil patching, a stratified flow. At medium gas velocity of 10 m/s the majority of oil was wiped out of the low section in the first 1 second, then the interface was interrupted and formed droplets. These droplets remained flowing in the system until they passed the pipe length of 55 m, as shown in Figure (4.44). A small portion of the oil was left behind in the low section after the flow reached equilibrium, as shown in Figure (4.45). The observed flow was noted as dispersed flow.

At high gas superficial velocity of 15 m/s the simulation results showed that the whole oil phase fraction at the low section was taken out within 1 second and the liquid film began to disturb at 2 seconds. The formation of droplets kept increasing and flowing

throughout the conduit until it reached the distance of the pipe end at 55 m, as shown in Figure (4.46). The flow behaviour is categorized as churn flow.

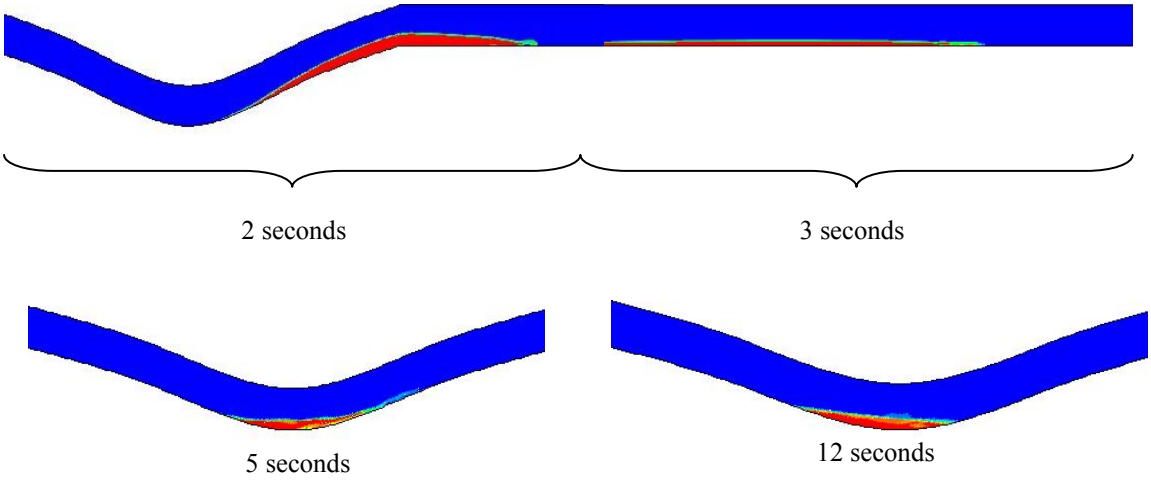

Figure 4.43: Sketch of air-oil interface at oil patching 0.3m for 5m/s at different flow times.

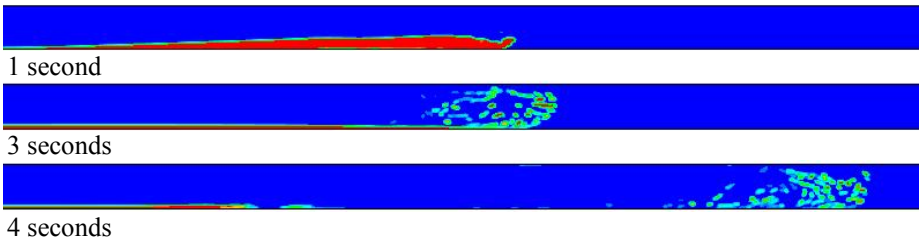

Figure 4.44: Sketch of air-oil interface at 0.3m oil patching for 10m/s at different flow times.

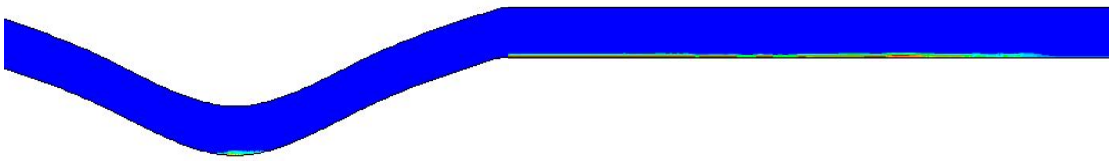

8 seconds

Figure 4.45: Sketch of air–oil interface at 0.3m oil patching for 10m/s at 8 second flow time.

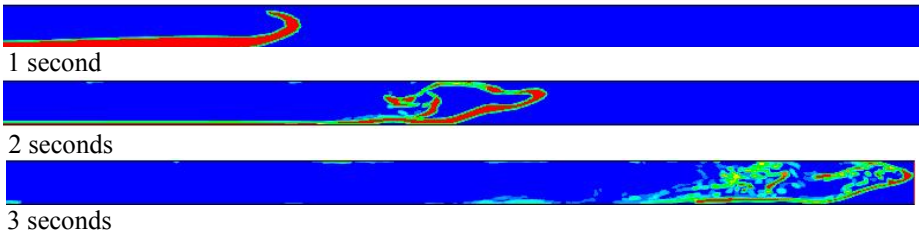

Figure 4.46: Sketch of air-oil interface for 15m/s at different flow times at medium liquid patching.

4.5.3 High Oil Patching with Different Restart Gas Velocities

At a low gas superficial velocity of 5 m/s and high oil patching of 0.5 m, it is clear that some of the liquid moved out of the low section within a few seconds. In a while, some of the oil fell back due to inadequate velocity and high viscosity. This situation was expected since at low and medium liquid patching a small amount of oil was left in the low section as seen in Figure (4.47). Therefore, the observed flow did not differ from the previous one at a low gas velocity; it was described as a stratified flow.

At a medium gas superficial velocity of 10m/s, most of the oil fraction was pushed out of the pipe lower segment within 1 second. After a while the oil film was interrupted and began to form droplets in which the film moved toward the pipe end as shown in Figure (4.48). The flow observation was noted as churn flow. At high gas velocities of 15 and 20 m/s the oil contours were very similar. The oil phase in the low section moved rapidly to the horizontal section. At around 2 seconds, the interface had just begun to interrupt and generated a few droplets that continued to increase in the system until they reached the pipe end at 3 seconds in the case of 15 m/s. At 20 m/s of gas velocity the interface only started to break up closer to the pipe end at around 50 m, and a few droplets formed. The observed flow in both cases was similar to churn flow.

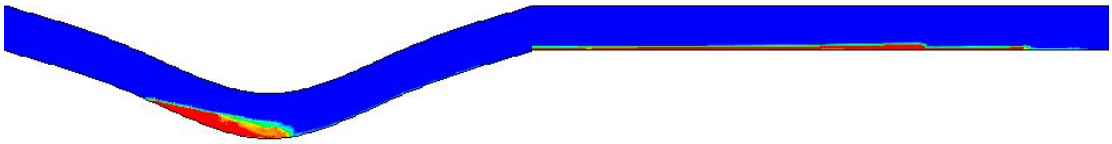

8 seconds

Figure 4.47: Sketch of air-oil interface for 5m/s at different flow times and high oil patching.

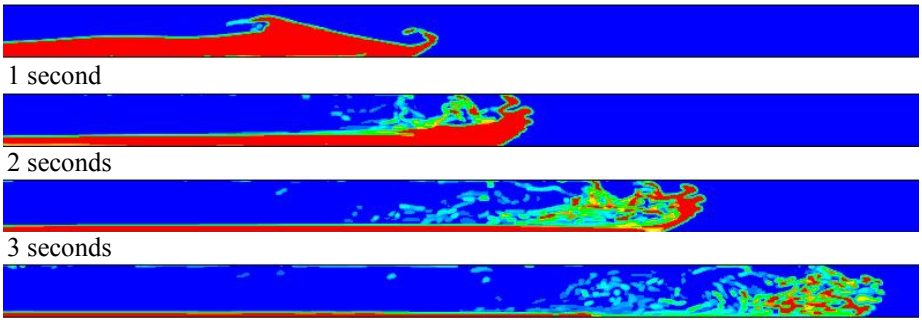

Figure 4.48: Sketch of air-oil interface for 10m/s at different flow times and high oil patching.

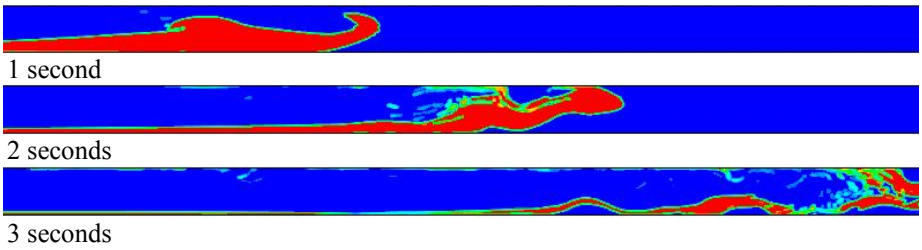

Figure 4.49: Sketch of air-oil interface for 15m/s at different flow times and high oil patching.

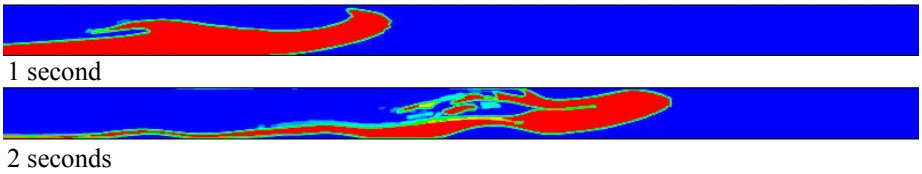

Figure 4.50: Sketch of air-oil interface for 20m/s at different flow times and high oil patching.

4.5.4 Liquid in the Low Section

In order to study the effect of fluid properties on liquid displacement from the low section, oil is used with the physical properties as shown in Table (4.1). The result illustrates that for high oil viscosity, the remaining oil in the low section is considerably higher than the water fluid. At low gas velocity of 5 m/s and low liquid patching, the oil had a higher residue of liquid than the water. Even at higher a velocity of 15 m/s, more liquid (oil) was actually removed, but it was still a small fraction in the low spot compared with the water as shown in Figure (4.51). Furthermore, the critical gas velocity in oil simulation was higher than when using water fluid at low and medium oil patching. A velocity of 15 m/s was insufficient to wipe the liquid (oil) completely out of the low section whereas 10 m/s had been enough to take out the water phase, as shown in Figure (4.52). It can be concluded that fluid viscosity plays a significant role in liquid displacement.

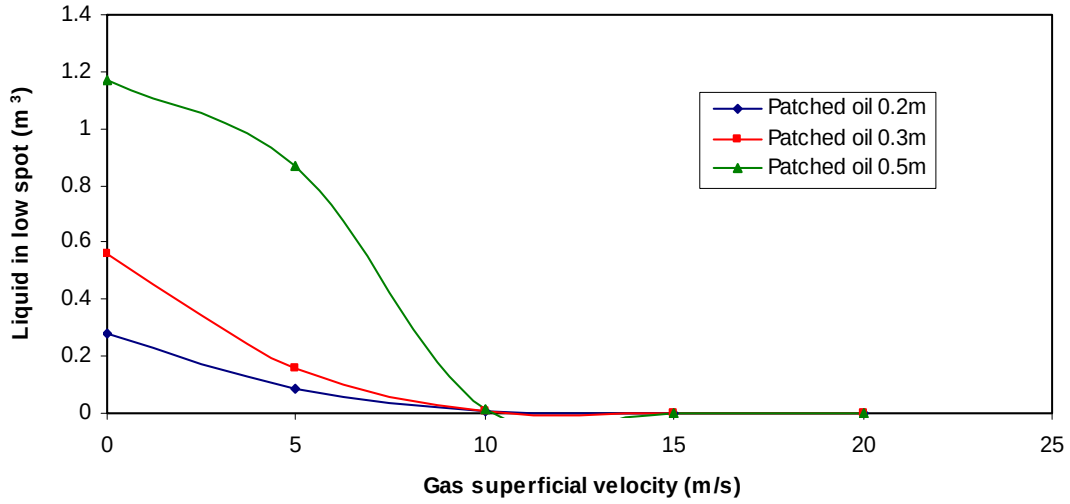

Figure 4.51: Experimental results of remained oil in the low section for 1m depth.

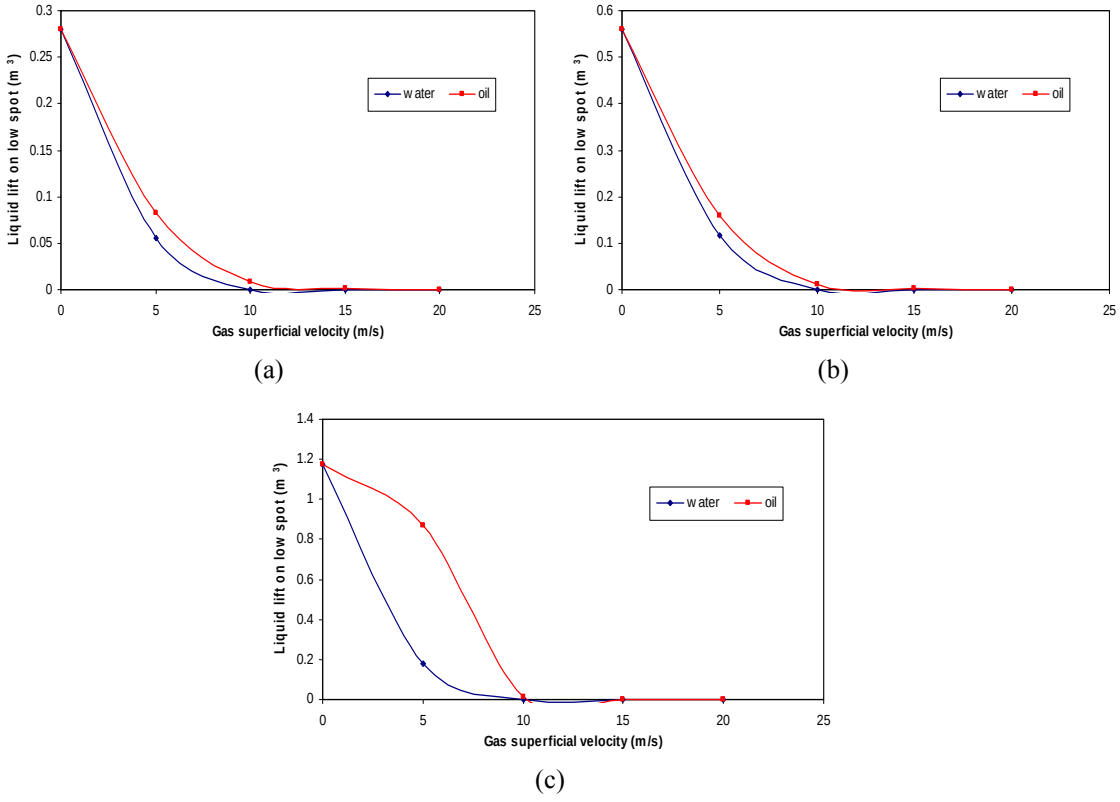

Figure 4.52: Comparison between oil and water left in the low section for 1m low spot depth at different liquid patching: (a) 0.2 m, (b) 0.3 m, and (c) 0.5 m.

4.6 Comparison between 2-D and 3-D VOF Simulation for Water with Constant Gas Restart Velocity

In order to compare the observed flow patterns obtained using 2D pipe geometry, two different simulations using the VOF model were conducted with 3D conduit geometry of 0.5 m diameter and 55 m in length, including a low section of 1m depth as shown in Figure (4.53). In the present study, the mesh was generated using Gambit and imported into ANSYS FLUENT 12.1, in which the calculations were conducted. Within the 3D geometry, a fixed mesh scheme was examined since the simulation takes a long time, between 3 to 5 days for one simulation. A structured hexahedral grid (1,985,000 cells) is used because it is suitable when solving the case under unsteady state. The time step selected is small 10^{-4} seconds, which required less iteration per time step. To achieve better convergence, under relaxation factors were adjusted and kept constant as 0.3, 0.7, and 0.8, and were applied for pressure, momentum, and turbulence kinetic energy parameters as given in the FLUENT document. The boundary conditions employed are given in section 4.3. A case study of fixed gas superficial velocity with a medium stagnant liquid (water or oil) was performed. The initial patched liquid level in the low section is 0.3 m. The simulation in 2D geometry took around 6 seconds real time, whereas in 3D it was simulated for around 6 seconds real time with the same computational time. Snapshots for both simulations at the same restart gas superficial velocity (15 m/s) and real time are shown in Figure (4.54).

The comparison between the two cases of simulation in terms of flow pattern and droplet hydrodynamic shows that the flow pattern was slightly different when simulated in a 3D domain. This interesting behaviour can be attributed due to the limitations of the 2D VOF solution algorithm of FLUENT that might increase the drag on liquid. Therefore, it can be concluded that 2D VOF simulations can provide reasonable results but not as accurate as those that can be achieved with 3D simulations.

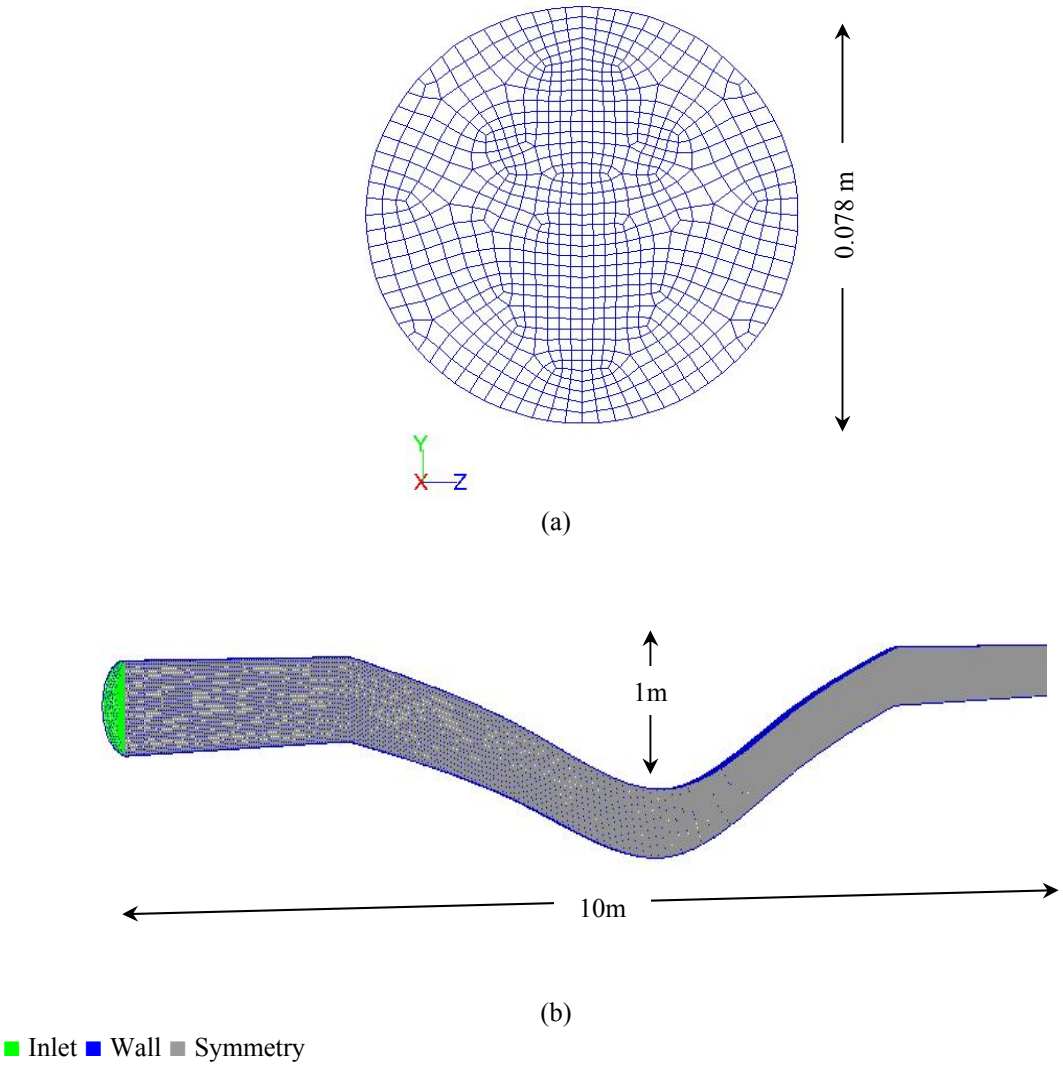

Figure 4.53: Typical computational domain grids representing the flow domain discretisation for a bended pipe: (a) View of inlet meshed pipeline (b) View of the meshed 3–D low section, and (c) View of the meshed horizontal pipeline.

In the three–dimensional simulation of air–water flow, the effect of restart gas superficial velocity of 15 m/s with the initial patched liquid of 0.3 m on the flow pattern was quite similar to that observed with 2D simulation, as shown in Figure (4.54–a). It can also be noted that the water phase was taken out of the low section in less than 0.5 seconds in the 3D simulation, while in the 2D simulation, it was taken out in around 1 second. The flow behaviour at 1 second of flowing time was quite similar, where the liquid film began to lift up, but with slight differences in the interface configuration. The air–water interface at 2 seconds was also quite similar in both simulations in which a liquid film was created along the bottom pipe wall, while the interface configuration was slightly different. In the 3D simulation, the water layer covered the pipe perimeter, and some drops were located in the core phase. However in the case of the 2D simulation, the water layer was distributed on the pipe edge, and some drops flowed in the core phase. Schematically the description of both cases are shown in Figure (4.54–a).

The predicted flow patterns using the two different dimensions were similarly quite descriptive. Another simulation was conducted under the same conditions of a restart gas velocity and low section level, but with high liquid patching of 0.5 m. The flow pattern observation at 1 second in two and three–dimensional simulations was quite similar, in which most of the liquid film remained on the bottom pipe wall while some of it rose up. At 2 seconds of flowing time, the air–water interface began to break off and produced few drops, whereas the liquid film remained on the bottom tube wall. The liquid film remained down at 3 seconds of flowing time with more developed drops. Therefore, the prediction of flow pattern using 2D and 3D simulations was quite reasonable, but the interface configuration was slightly different as shown schematically in Figure (4.54–b). In order to verify the flow pattern result, the flow pattern was obtained using the Baker (1954) flow map. Figure (4.55) shows the flow pattern obtained from each simulation of 2D and 3D. Clearly the 3D simulation prediction was much more accurate in comparison to the 2D simulation, which had provided a reasonable prediction.

The main difference between 2D and 3D simulations is not a surprise, since the 2D simulation does not take into account the shape of the cross sectional area of the pipe, which in sequence affects the shape of the droplets. Therefore the flow is not symmetrical as in the simulation case of full 3D geometry.

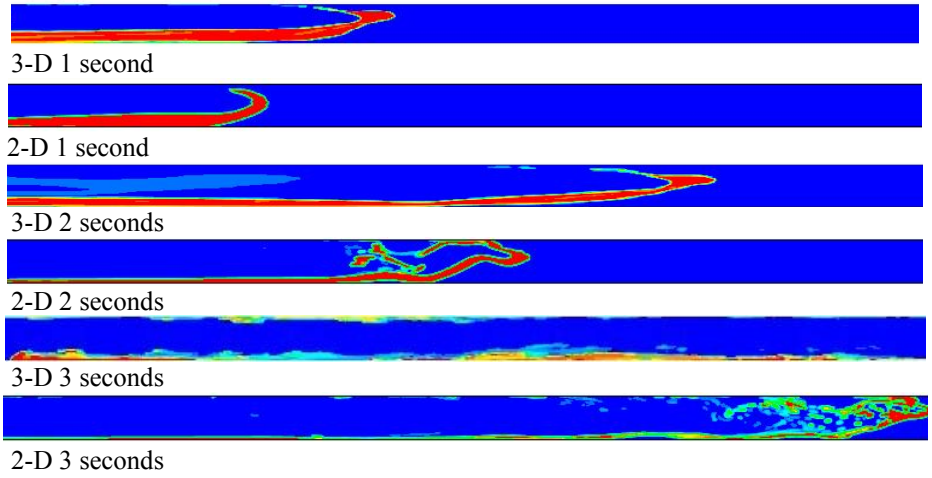

(a) Water patching 0.3 m

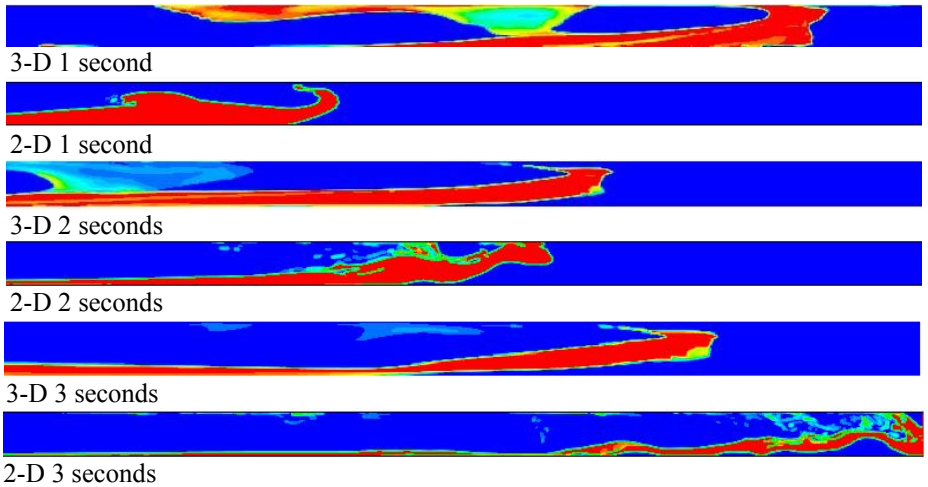

(b) Water patching 0.5 m

Figure 4.54: Comparison between 2D and 3D simulation of air–water flow at 15 m/s at different water patching.

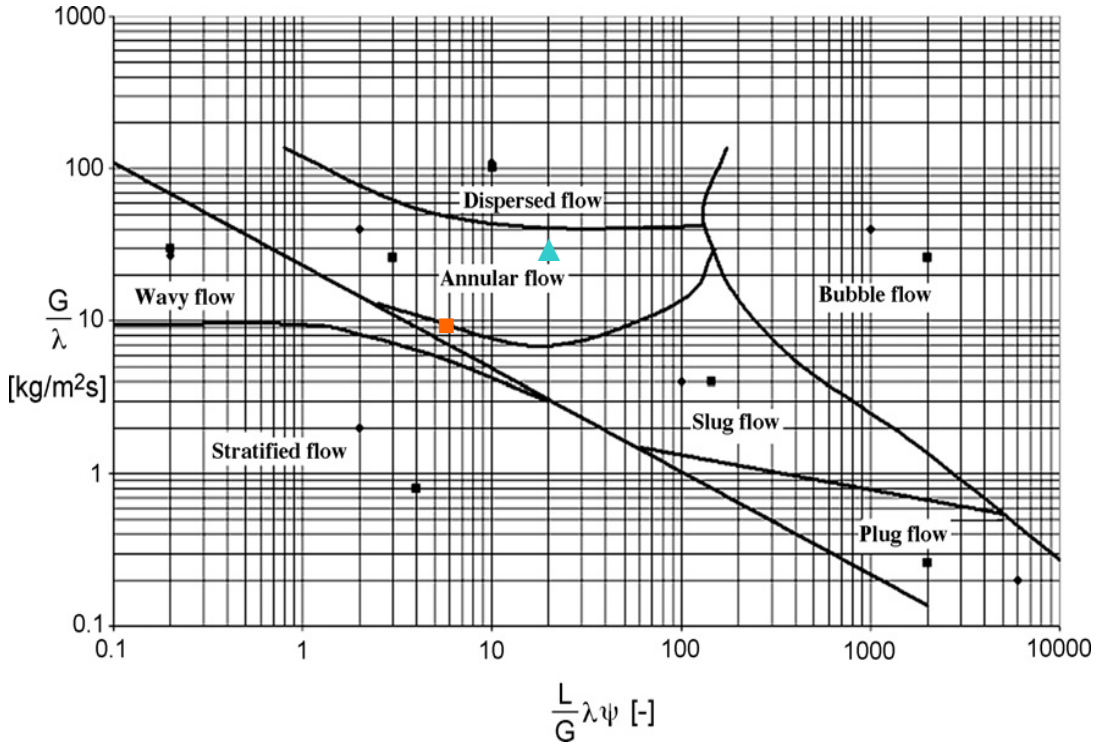

Figure 4.55: Comparison between 2D ■ and 3D ▲ simulation results of flow patterns with the Baker chart at 15m/s and 0.3m water patching.

4.7 Conclusions

This study aimed to provide some information about the droplet hydrodynamic and the flow behaviour in bend pipelines in order to find out the risk of hydrate formation. The simulation results have been obtained using the VOF approach. The effect of restart gas superficial velocity and various stagnant liquids in the low section were investigated in both 2D and 3D geometries. It is obvious that the liquid remaining in the low section of pipe decreases with an increase in gas superficial velocity, and the amount of liquid depends on the fluid properties as observed with water and oil fluid. The fluid's properties such as density and viscosity have a significant role in liquid displacement from the low section, in which viscosity proposes more resistance to flow, while the density makes it difficult for liquids to flow up to the horizontal pipe section. Moreover, the flow pattern is also strongly dependent on the restart gas's superficial velocity as well as the patched liquid in the low section. A low gas superficial velocity with various patched liquids of 0.2–0.5 m shows no risk of

hydrate formation due to the observed flow pattern, and is often a stratified flow. However as the restart gas velocity is increased, regardless of initial liquid patching, hydrate formation is more likely to be observed when the flow can be described as annular, churn or dispersed flow.

The prediction of flow pattern using 3D geometry was more accurate and reliable compared to the 2D simulation, which provided a reasonable prediction of flow patterns appearing in the Baker map, specifically at low gas velocity. The results obtained by the 2D simulation can be considered as an initial start for studying the flow behaviour at bend pipes. In order to validate the simulation result of the VOF model more accurately, it is necessary to conduct experimental work to determine the validity of the model more accurately, instead of using the flow map which is generated for specific operating conditions and pipe sizes.

4.8 Bibliographies

Fitremann, J. M. (1976). The stability of gas-flow over a stagnant liquid in a pipe and the onset of slugging. *International Journal of Multiphase Flow,* 3, 117-122.

Leporcher, E., K. Kinnari, C. Labes-carrier, Ph. Maurel and W. Vandersippe (2002). Multiphase flow: Can we take advantage of hydrodynamic conditions to avoid hydrate plugging during deepwater restart operations? *The SPE Annual Technical Conference and Exhibition*, San Antonio, Taxes, 29 September-2 October.

Volk, M., E. Delle-Case and A. Coletta (2010). Investigations of flow behavior formation in well-head jumpers during restart with gas and liquid. Technical Report, University of Tulsa.

Volk, M., E. Delle-Case and D. Estanga (2007). Risk-based restarts of untreated subsea oil and gas flowlines in the GoM. Technical Report, University of Tulsa.

Chapter 5

Modelling Pressure Drop and Liquid Holdup with Fixed Droplet Size using Eulerian–Eulerian Model

In this chapter, the three dimensional two–phase flow in a horizontal pipe has been investigated numerically. The steady state numerical simulations of two–phase gas–liquid stratified flow in a 0.078 m diameter and 7 m long pipe have been studied using the commercial CFD package FLUENT 12.1, in conjunction with a multiphase model. The Eulerian–Eulerian k–ε model was selected to describe the turbulence in continuous phase. Three fluids were used in this work with air representing the gas phase and water and oil representing the liquid phase. The purpose is to develop a model for predicting the pressure drop and liquid holdup at low liquid holdup and also to examine the behaviour of pressure drop and liquid holdup under different operating conditions. The numerical results in terms of pressure drop and liquid holdup are presented and discussed. The predicted results are noted to be in close agreement with previous results found in the literature. Moreover, it compared well with one of the existing correlations of two–phase pressure drop and liquid holdup.

5.1 Introduction

The stratified flow regime is frequently encountered in long distance transport pipelines (e.g. natural gas and oil flows) and in petrochemical and process plants. The requirements for economic design, optimization of operating conditions and assessment of safety factors create the need for quantitative information about such flows. In general, the flow patterns for two–phase flow in a horizontal pipe vary because of the role played by buoyancy. The prediction of pressure drop and liquid holdup in two–phase based on the flow conditions has been studied for decades. Many empirical correlations have been reported in the literature review in Chapter 2.

During the development stage of any gas field many problems have arisen within gas transmission lines, such as the existence of a small amount of liquid (Cawkwell and Charles, 1985). Condensation in gas pipelines commonly takes place because of the variation of temperature and pressure that occurs along the pipeline. The predominant flow regime in gas condensate pipelines with a small amount of liquid holdup is Stratified flow. Typically, the existence of liquids in the pipeline is lower than 200 bbl/MMSCFD and corresponding to 1.1% of liquid (Olive *et al*., 2003).

This amount of liquid can cause several operational problems such as increasing the pressure that leads to pipe burst and gas hydrate. Such problems can be avoided if an accurate prediction of two–phase liquid holdup and pressure gradient is obtained. These two system parameters are significant to pipeline size selection and downstream facilities. Owing to the inherent complexity of two–phase flows from a physical and numerical viewpoint, “general” applicable computational fluid dynamics (CFD) codes are non–existent. The reasons for the lack of fundamental knowledge on two–phase flows are three–fold:

1. Two-phase flow is a very complex physical phenomenon where many flow types can occur, and within each flow type several possible flow regimes can exist (annular, stratified flow, etc.).

2. The complex physical laws and mathematical treatment of phenomena taking place in the presence of the two–phase (interface dynamics, coalescence, break–up, drag, etc.) are still largely undeveloped. For instance, there is still no agreement on the governing equations (Ghorai and Nigam, 2006). Additionally, proposed constitutive models are empirical, but often lack experimental validation for the conditions under which they are applied.

3. The numerics for solving the governing equations and closure laws of two–phase flows are very complicated. Frequently two–phase flows demonstrate inherent oscillatory behaviour, requiring costly transient solution algorithms.

In spite of the major difficulties mentioned above, significant progress has been made in different areas of two–phase flow (Ghorai and Nigam, 2006). Many empirical correlations and phenomenological models have been proposed for the prediction of stratified gas–liquid flow parameters over the past two decades (Taitel and Dukler, 1976, Hart *et al*., 1989, Chen *et al*., 1997, Vlachos *et al*., 1999, and Fan *et al*., 2005). Due to the lack of knowledge about the distribution of wall shear in stratified pipe flows, expediential recourse is usually made to the relationship established in single–phase tube flow, with a resulting loss in the accuracy of the calculation. Computational fluid dynamics (CFD) techniques have been applied to the calculation of the stratified pipe flows.

One of the early CFD models of turbulent stratified flow in a horizontal conduit was presented by Shoham and Taitel, 1984. Solutions for turbulent liquid flows were obtained in horizontal and slightly inclined pipes of 25.4 mm diameter. Issa (1988) numerically simulated the stratified gas–liquid two–phase flow in pipes, using the standard k–ε turbulence model with the wall functions for each phase. Newton and Behnia (1988) obtained more satisfactory solutions for stratified pipe flow using a low Reynolds number turbulent model instead of wall functions.

In the present chapter, the CFD code ANSYS FLUENT 12.1 is used to develop a model for pressure drop and liquid holdup at low liquid loading and to understand the

pressure drop behaviour of gas–liquid two–phase in horizontal pipelines as well as the liquid holdup, which strongly influences the pressure drop in the system.

5.2 Development of Multiphase Flow Model

The gas–liquid two–phase flow in a pipeline is a complex multiphase and turbulent flow governed by mass and momentum conservation, turbulence transport, and interphase momentum transfer. Therefore, the following assumptions were made in developing a theoretical model that characterizes the gas–liquid (air–water/or oil) multiphase process.

I. The two–phase pipeline system temperature is constant at an ambient temperature of 25 ^{o}C, and the outlet pressure is at 1 atm, in which each phase is isothermal and incompressible.

II. The two–phase flow is assumed to be a stratified flow based on the two–phase superficial velocity and flow map (as shown in Figure 5.7), in which the gas phase is treated as the primary phase, while the liquid phase is treated as the secondary phase.

III. All droplets are assumed to be uniform in size and exhibit a spherical shape, and droplet coalescence and breakage are assumed to be negligible in this case study.

IV. Different phases move at different velocities which are identified here as physical velocity, and is calculated based on the volume fraction of each phase.

V. The drag force from the gas phase acting on the water droplets is included in the interphase momentum exchange.

VI. No external body force and virtual mass force are included in this simulation, but the effect of lift force on the droplet is assumed constant at 0.005 in order to math the experiment data.

VII. Each turbulence model is only applicable to the mixture in which two phases share the same turbulence quantities (e.g. k, ε).

The constant lift coefficient is by definition, a single value which can be either positive or negative. Therefore, it does not vary with local hydrodynamic conditions or other flow properties. Several gas–liquid studies in the past have successfully fitted both positive and negative constant lift coefficients to experimental data (Wang *et al*., 1986; Bel Fdhila, 1991; Lahey *et al*., 1993; Grossetete, 1995). For instance, for fully developed gas–liquid flows in a vertical pipe, the values of constant lift coefficient that resulted in a good fit to the experimental data were found to be in the range $0.01 \leq C_L \leq 0.15$ (Wang *et al*., 1986; Lahey *et al*., 1993).

Therefore, many investigators found it necessary to use lift coefficient values that are significantly less than the inviscid value of 0.5, and in some cases even negative, in order to match their experimental data. Therefore, the value of 0.005 was a good match with the experimental data.

5.3 Domain Description

In order to study the validity of the Eulerian–Eulerian approach for modeling the pressure drop and liquid holdup in a horizontal pipeline, 3D simulations were performed with air and water as continuous and dispersed phases, respectively. The geometry consisted of a straight horizontal pipe 78 mm in diameter. This value of the pipe diameter was chosen to be consistent with that normally used by Badie *et al*. (2000) for studying the pressure drop and liquid holdup. A pipe length of 7 m was used with three surface boundaries: inlet, outlet, and wall. The actual pipe length that was used in the experiment is 20 m, but 7 m was chosen because it was sufficient to obtain a fully developed velocity profile.

An unstructured mesh with tetrahedral cells was generated using Gambit 2.1.1 as shown in Figure (5.1). To optimise the mesh size it was necessary to carry out a mesh–independence study; this was done by performing a number of simulations with different mesh sizes, starting from a coarse mesh and refining it until the results were no longer dependent on the mesh size. The 3D mesh obtained thus contained approximately 204,300 tetrahedral cells.

5.4 Solution Procedure

One of the FLUENT turbulence models has been used to simulate the pressure drop and liquid holdup in a horizontal pipeline. In the FLUENT's Eulerian–Eulerian model, as mentioned early in Chapter 3, the gas–liquid volume fraction in the cell is equal to unity. The phases are assumed to share space in proportion to their volume fractions so as to satisfy the continuity relationship.

$$\sum_{i=1}^{n} \alpha_i = 1 \qquad \text{where } n \text{ is the number of phases} \qquad (5.1)$$

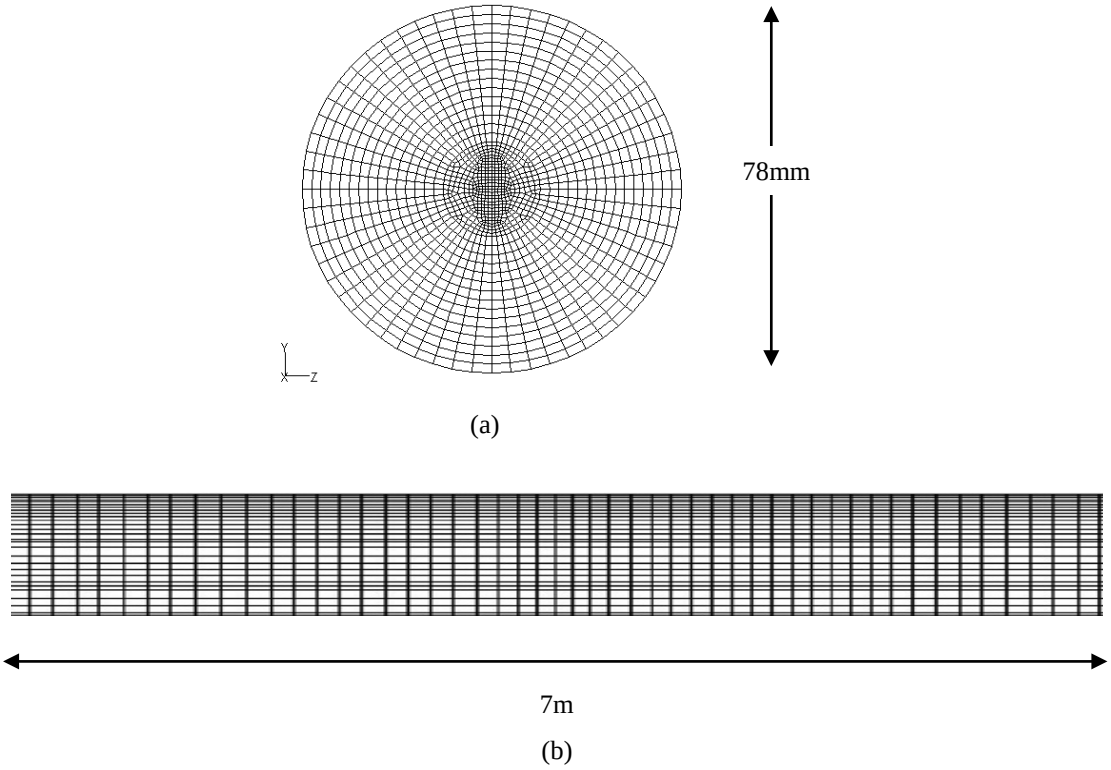

Figure 5.1: (a) Inlet view of 3-D meshed model (b) View of the meshed 3-D pipeline.

5.4.1 Mass Conservation Equation

The mass conservation equation for any phase can be written as:

$$\frac{\partial \rho_i}{\partial t} + \nabla.(\rho_i \vec{v_i}) = 0 \tag{5.2}$$

5.4.2 Momentum Conservation Equation

Each phase has its momentum equation that is solved through the whole domain. It can be expressed as follows:

$$\frac{\partial}{\partial t}(\alpha_i \rho_i \vec{v_i}) + \nabla.(\alpha_i \rho_i \vec{v_i} \vec{v_i}) = -\alpha_i \nabla p + \alpha_i \rho_i \vec{g} + \nabla.\bar{\bar{\tau}}_i + \sum_{n=1}^{m} \vec{R_{ij}} + \vec{F_i} + \vec{F}_{lift,i} \tag{5.3}$$

Where $\bar{\bar{\tau}}$ is the i^{th} phase stress-strain tensor, F_i is an external body force, $F_{lift,i}$ is a lift force, R_{ij} is an interaction force between phases, and p is the pressure shared by all phases.

5.4.3 Turbulent Model

As mentioned earlier in Chapter 3, different turbulence models are available in FLUENT 12.1. The most widely used model is k–ε model, which has been utilised to simulate the turbulence eddies and to model the turbulence in the continuous phase. Among the k–ε models, the Renormalization Group (RNG) k–ε model is employed. Choudhury (1993) derived the Renormalization Group (RNG) k–ε model statistically from the Navier–Stokes equation. It averages the higher energy levels in the flow statistically and produces the lower energy level properties as a result. The RNG k–ε model can be utilized to obtain both high and low Reynolds number flow affects while the Standard k–ε model can only acquire the effects of high Reynolds number flows. Therefore, the RNG k–ε model is more accurate and usable for a greater range of flows.

The transport equations of the RNG k–ε model are as follows:

$$\frac{\partial}{\partial t}(\rho k)+\frac{\partial}{\partial x_i}(\rho k u_i)=\frac{\partial}{\partial x}\left(\alpha_k \mu_e \frac{\partial k}{\partial x_i}\right)+G_k+G_b-\rho\varepsilon-\mathrm{Y}_m+S_k \tag{5.4}$$

$$\frac{\partial}{\partial t}(\rho \varepsilon)+\frac{\partial}{\partial x_i}(\rho \varepsilon u_i)=\frac{\partial}{\partial x_j}\left(\alpha_\varepsilon \mu_e \frac{\partial \varepsilon}{\partial x_j}\right)+C_{1\varepsilon}\frac{\varepsilon}{k}(G_k+C_{3\varepsilon}G_b)-\frac{\mathrm{C}_{2\varepsilon}^{*}\rho\varepsilon^2}{k} \tag{5.5}$$

where $C_{1\varepsilon}$ and $C_{2\varepsilon}$ are the empirical constants, which are equal to 1.42, and 1.68, respectively (FLUENT Inc. 2008).

5.4.4 Wall Treatment

Enhanced wall treatment in the near wall was used. In this approach, the whole domain is subdivided into a viscosity–affected region and a fully–turbulent region based on the turbulent Reynolds number, Re_y, defined as:

$$\mathrm{Re}_y=\frac{\rho y\sqrt{k}}{\mu} \tag{5.6}$$

5.5 Eulerian–Eulerian Model Description

In order to solve the modeling equations for different cases, the type of solver, number of phases, fluid properties, and operating and boundary conditions have to be specified.

5.5.1 Solver Formulation

Both segregated and coupled solvers are available with FLUENT. Using either method will solve the integral equations for conservation of mass and momentum and other scalar equations. The segregated solver has traditionally been used for incompressible flows while the coupled formulation has a performance advantage over the segregated solver for high speed compressible flows. Furthermore, the segregated solver normally takes a shorter time to converge solutions and requires less

memory. However, like all Eulerian–Eulerian simulations, the segregated solver was selected with a steady state condition.

5.5.2 Operating Conditions

The operating conditions include gravity, density and pressure. A gravitational acceleration of -9.81m/s^2 is defined in the 'Y' direction. The horizontal pipeline is assumed to be an open system for which the operating pressure of 101.325 kPa is defined. The specification of an operating density is needed to improve the convergence behaviour, and therefore, the approximate bulk density value is used as the lower phase density at the operating density.

5.6 Boundary and Initial Conditions

Air and water/or oil were taken as gas and liquid phase. A single characteristic droplet size (100 µm) for water and oil was utilised in all simulations to provide closure for drag calculation. At the inlet pipe boundary condition, velocity inlet was used to define the actual velocity of each phase. A uniform velocity across the pipe cross section was used in all the simulations. Individual velocities of the phases were calculated to determine continuous and dispersed phase. The initial value of liquid holdup was calculated using the Hart *et al*. correlation (1989).

$$U_w = \frac{U_{s,w}}{\alpha_w} \qquad U_g = \frac{U_{s,g}}{(1-\alpha_w)} \tag{5.7}$$

At the outlet of the pipe a pressure outlet boundary condition was implemented. Zero static pressure (gauge) which is equal to the atmospheric pressure (1 atm) was specified at the outlet in all cases. A wall boundary condition was used to bind the fluid and the solid region. A 'No–slip' boundary condition was imposed at the wall. The turbulent gas-liquid flows are considered to be symmetric about the centre plane. A Symmetry boundary condition was used to reduce the computational cells to half, thus reducing the computational time.

5.7 Interphase Forces

The drag coefficient, which is used to account for the drag on a droplet in the presence of adjacent drops, and is given by the following expressions (Ishii and Chawla, 1979), depends on the Reynolds number.

The drag coefficient for the stock regime is computed as follows

$$C_D = \frac{24}{\mathrm{Re}}, \mathrm{Re} < 1 \qquad \mathrm{Re} = \frac{D_p \rho_g \Delta V}{\eta_m} \tag{5.8}$$

The effective viscosity is,

$$\frac{\eta_m}{\eta_g} = (1 - \alpha_d)^{-2.5} \tag{5.9}$$

Droplet volume fraction is given by (Roscoe and Brit (1952), Brinkman (1952)),

$$\alpha_d = \frac{\alpha_l}{\alpha_l + \alpha_g} \tag{5.10}$$

The drag coefficient for the viscous regime is computed as follows,

$$C_D = \frac{24}{\mathrm{Re}}\left(1 + 0.1\mathrm{Re}^{0.75}\right) \qquad 1 > \mathrm{Re} < 1000 \tag{5.11}$$

The drag coefficient for the Newton's regime is computed as follows,

$$C_D = \frac{2}{3}(D_p / \lambda_{RT})\left[\frac{1 + 17.67 f^{6/7}}{18.67 f}\right]^2 \qquad \mathrm{Re} < 1000 \tag{5.12}$$

The Rayleigh–Taylor instability wavelength,

$$\lambda_{RT} = \left(\frac{\sigma}{g.\Delta\rho}\right)^{1/2} \tag{5.13}$$

5.8 Numerical Technique

All of the Eulerian–Eulerian simulations were carried out with two different phase flows, such as air–water and air–oil where the gas and liquid are taken as primary and secondary phases, respectively. All of the equations of two–phase 3D turbulence flow were solved in each cell of the computational domain. In the present Eulerian–Eulerian model, turbulence was modeled using k–ε model. A renormalization group of k–ε (RNG k–ε) was used while the enhanced wall treatment functions proposed by Kader (1981) were used to specify the wall boundary conditions.

All model equations were solved in a segregated, iterative fashion. Calculations were performed in a time dependent mode and a first order upwind scheme was used for the discretisation of momentum, volume fraction, k, and ε for a few iterations, and then was switched to second order for all of them except volume fraction to Quick, whereas a phase–coupled SIMPLE algorithm was used for pressure velocity coupling. Under relaxation factors used for pressure and momentum were 0.3 and 0.05 respectively. The same time step of 0.001 seconds was used throughout the simulation. For turbulence parameters, intensity and hydraulic diameter specifications were found to be quite useful. The convergence criteria for residuals were set to 1×10^{-4} for each time step.

In order to reduce computational time for these memory intensive simulation studies all simulations were performed on high speed clusters, which includes 8 processors. Simulations were performed until a fully developed flow field was ensured by examining the overall mass balance and time history of the relevant flow variable.

5.9 Validation of CFD Model

To achieve validation of the Eulerian–Eulerian model used in this study the pressure drop and liquid holdup were compared with the experimental data for a similar horizontal pipeline specification (Badie *et al*., 2000). The objective here was to attempt and validate the CFD model as much as possible so as to establish confidence in the numerical results. The various stages of the validation process are described below.

5.9.1 Examination of Turbulence Models

Several turbulence models were available for utilization. Each turbulence model has advantages, disadvantages, limitations, and appropriate flow regimes. A large family of turbulence models exists in the literature, yet there are no quantitative guidelines for choosing an appropriate turbulence model for a multiphase flow.

This section concentrates on an assessment of three turbulence models, which are standard k–ε, RNG k–ε, and realizable k–ε. The model tests were conducted in a horizontal pipe having an internal diameter of 0.078 m and a length of 7 m. Prior to examining each turbulence model, the standard k–ε, RNG k–ε, and realizable k–ε models were chosen for a grid independent test.

The following Figures (5.2 and 5.3), illustrate the relationship between the pressure gradient and liquid holdup against superficial water velocity at constant droplet size and superficial air velocity of 100 μm and 20 m/s, respectively. It can be seen that RNG k–ε model had close agreement with the experimental data in terms of pressure gradient and liquid holdup, and had less percentage of error. Therefore, this model has been chosen for further sensitivity analysis.

5.9.2 Grid–independent Test

The aim of the grid–independent test was to verify the minimum grid resolution required to generate a solution that is independent of the grid used. In this test, the initial value of liquid volume fraction was calculated using the Hart *et al*. (1989) correlation. The droplet diameter was constant at 1×10^{-4} m, and three different mesh sizes were used for grid generation. These were 110,330, 204,300, and 401,200.

Table (5.1) shows a comparison between three CFD turbulence models with respect to the experimental data in which the pressure gradient was chosen at a constant superficial gas and liquid velocity. The CFD pressure gradient decreases as the grids become finer. The errors (δ) further indicates that the mesh cell number of 204,300 is insignificant compared with other two–mesh sizes of 110,330 and 401,200 respectively. In general, a total of 204,300 cells are acceptable for the pipe meshing.

Table 5.1: Effect of Grid Size on Pressure Drop Using RNG k-ε Model at a Constant Superficial Water Velocity 0.025m/s

Mesh	Gas superficial velocity (m/s)								
	15			20			25		
	Pressure gradient (Pa/m)								
	CFD	Exp.	δ%	CFD	Exp.	δ%	CFD	Exp.	δ%
110,330	61.36	46.97	30.64	102.18	89.11	14.67	155.46	177.17	12.25
204,300	53.63	46.97	14.18	93.51	89.11	4.94	135.94	177.17	23.27
401,200	44.38	46.97	5.5	80.27	89.11	9.92	115.69	177.17	34.70

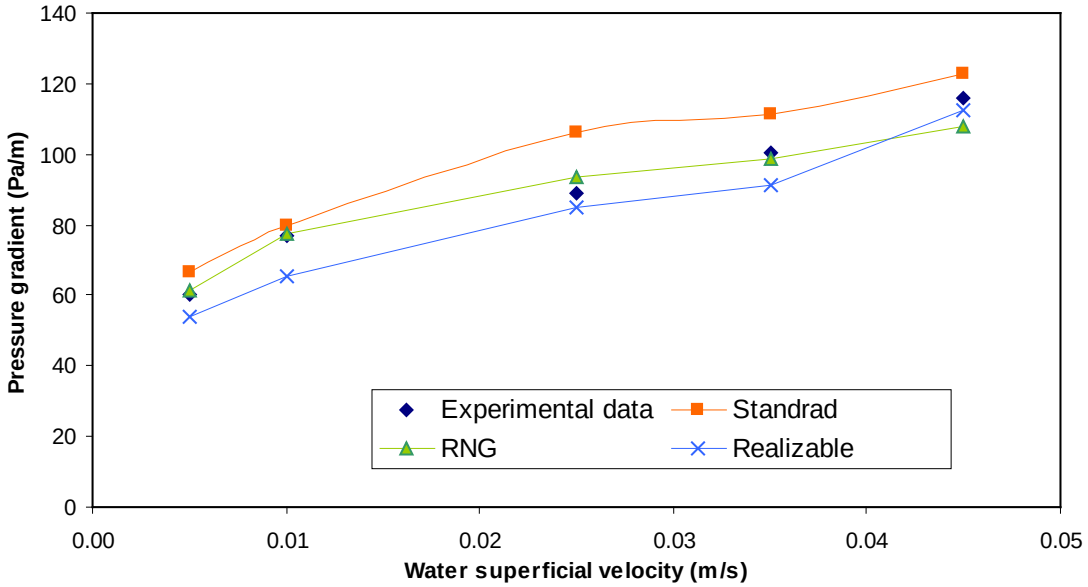

Figure 5.2: Shows the comparison of pressure gradient between the experimental data and different turbulence k–ε models.

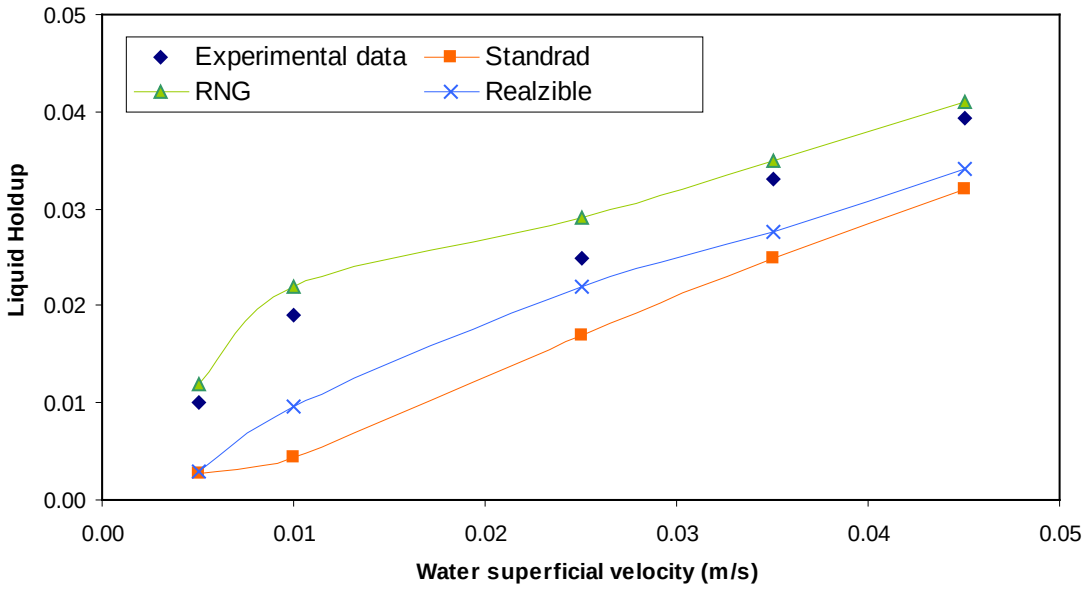

Figure 5.3: Shows the comparison of liquid holdup between the experimental data and different turbulence k–ε models.

5.9.3 The Variation of Pressure Drop and Liquid Holdup through the Pipeline

The simulations were performed to achieve results under fully developed flow conditions in the 0.078 m inside diameter and 7 m long horizontal pipe using the CFD code FLUENT 12.1 for the air–water system. The two–phase superficial gas and liquid velocities varied from 15 to 25m/s and from 0.02 to 0.05m/s, respectively, where the average liquid holdup is ranged from 0.006 to 0.055. The simulation results were compared qualitatively and quantitatively with the experimental data from the literature (Badie *et al*., 2000).

From Figure (5.4), it can be noted that the vast decrease in the liquid holdup comprises a decrease in pressure gradient in the first 2 m. After that the liquid was pushed to the pipe outlet, where its value started to increase until reached a steady state. On the other hand, the pressure gradient begun to fluctuate until it reached a steady state as can be seen in Figure (5.5). Both the pressure drop and liquid holdup reach a steady state value after 6 m of pipe length. Therefore, the results were reported at the outlet of the pipe.

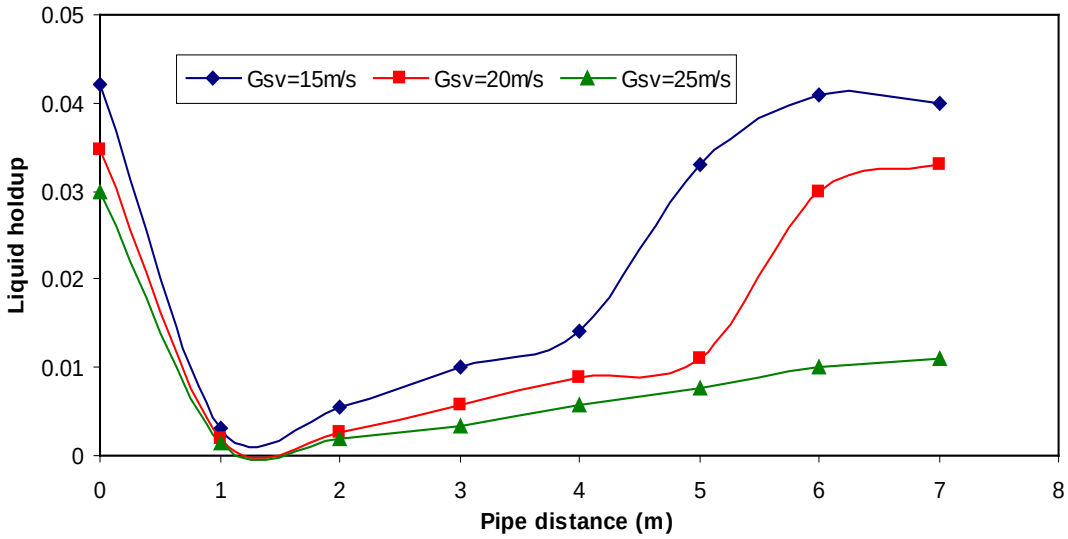

Figure 5.4: Shows the liquid holdup across the pipeline.

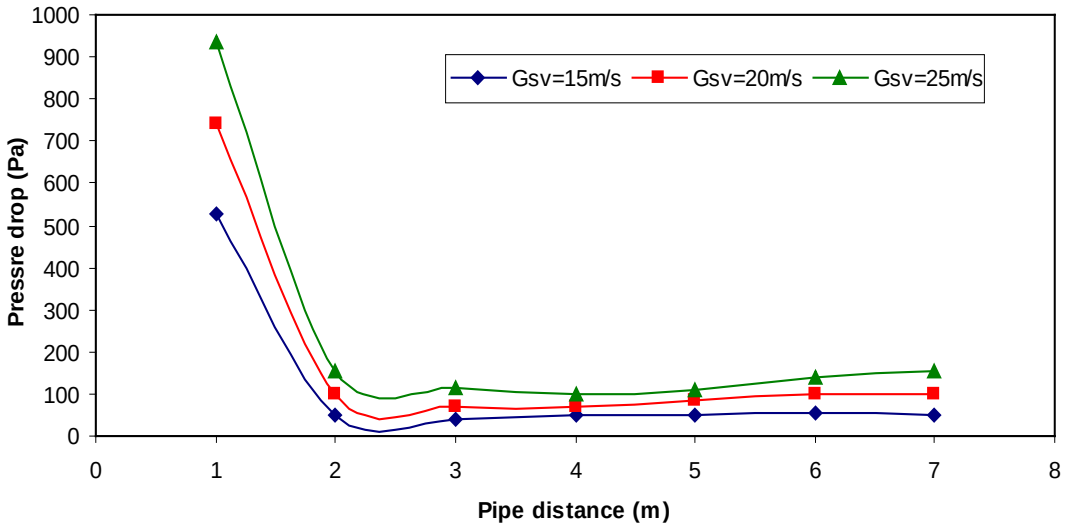

Figure 5.5: Shows the pressure drop across the pipeline.

5.9.4 Liquid Holdup

Figure (5.6) shows contours of water volume fraction for a constant superficial water velocity of 0.035 m/s and different superficial gas velocity of 15 m/s, 20 m/s, and 25 m/s, respectively. The water contours in Figure (5.6–a and b) show the water phase is settled at the bottom of the pipe, where the interface between two–phase (air–water) is almost flat and with some waves on the top. This flow regime is called stratified–wavy, and is similar to the flow pattern observed by Badie *et al*. (2000) (see Figure 5.7). As can be seen for all three cases, a stratified–wavy flow regime is observed. The liquid holdup decreases with an increase in gas superficial velocity.

At a high superficial gas velocity of 25 m/s, the liquid film reduces significantly compared to the other two velocities. This is because at a high superficial gas velocity, some of the liquid fraction will be lifted up as droplets. These velocities also fall on the borderline between annular and stratified–wavy flow as shown on Figure (5.7). One needs to switch between the drag models and use finer grid sizes in order to capture the regime change in the CFD. As this involves higher computational work for the present study we limited our attention to the stratified wavy flow.

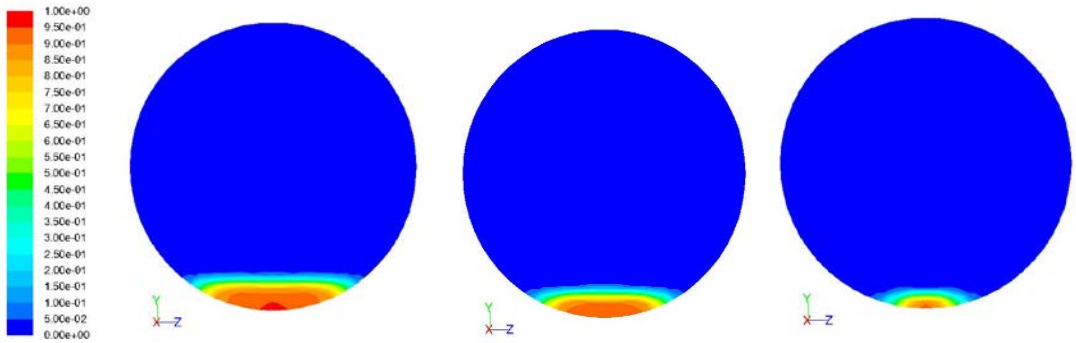

Figure 5.6: Shows liquid holdup contours at outlet for constant superficial water velocity 0.035 m/s and variant superficial gas velocity (a) 15 m/s, (b) 20 m/s, and (c) 25 m/s.

The liquid holdup is considered an important parameter for a multiphase flow. The simulations were conducted under constant superficial water velocity with various superficial gas velocities in one case and the reverse. The simulation results are compared with the experimental data of Badie *et al*. (2000) for several air–water velocities and initial liquid holdups as shown in Figures (5.8 and 5.9). The comparison is also made with the model proposed by Hart *et al*. (1989). The superficial gas velocity is kept constant at Figure (5.8), while the superficial liquid velocity is treated as a parameter.

As can be seen, the liquid holdup increased with an increase in the superficial liquid velocity at a constant gas velocity. The CFD predictions are able to capture this trend. It can be noted that the CFD simulations show close agreement with the experimental data for low and medium superficial gas velocity (15 and 20 m/s) for all the superficial liquid velocities. Furthermore, the CFD model illustrates better agreement with the experimental data than the model developed by Hart *et al*. (1989). Similarly Figure (5.9) illustrates the effect of superficial gas velocity on the liquid holdup. The CFD simulations show close agreement with 15 and 20 m/s superficial gas velocity. In contrast at high superficial gas velocity of 25 m/s, the model predictions deviated from the experimental data.

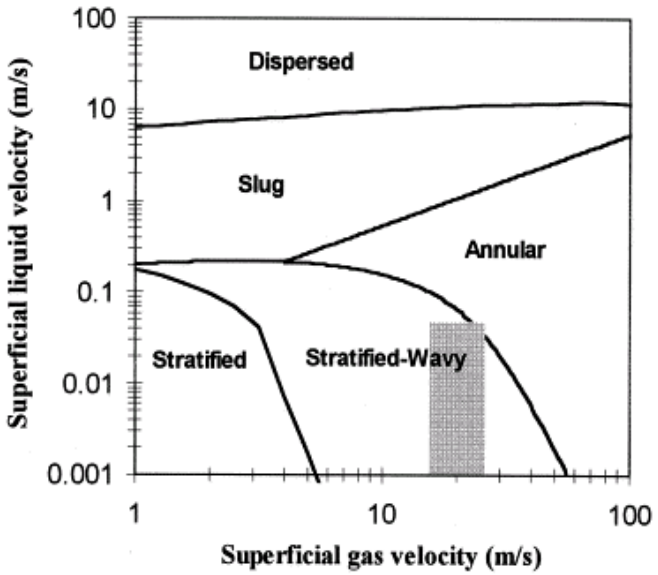

Figure 5.7: Region of air–water flow data plotted on (Taitel and Dukler, 1976) flow pattern map.

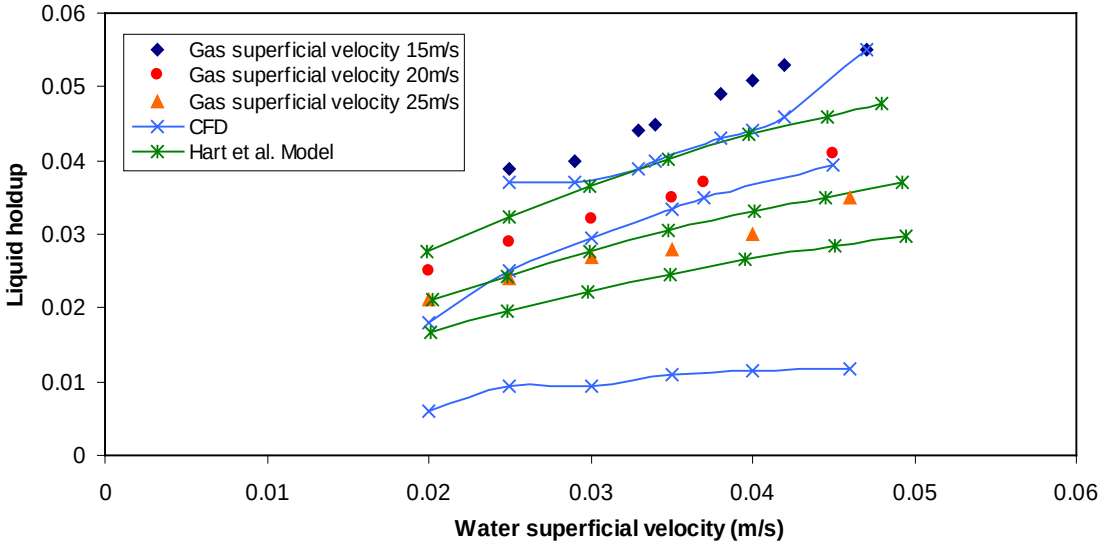

Figure 5.8: Shows liquid holdup at different superficial gas velocity and constant liquid superficial velocity.

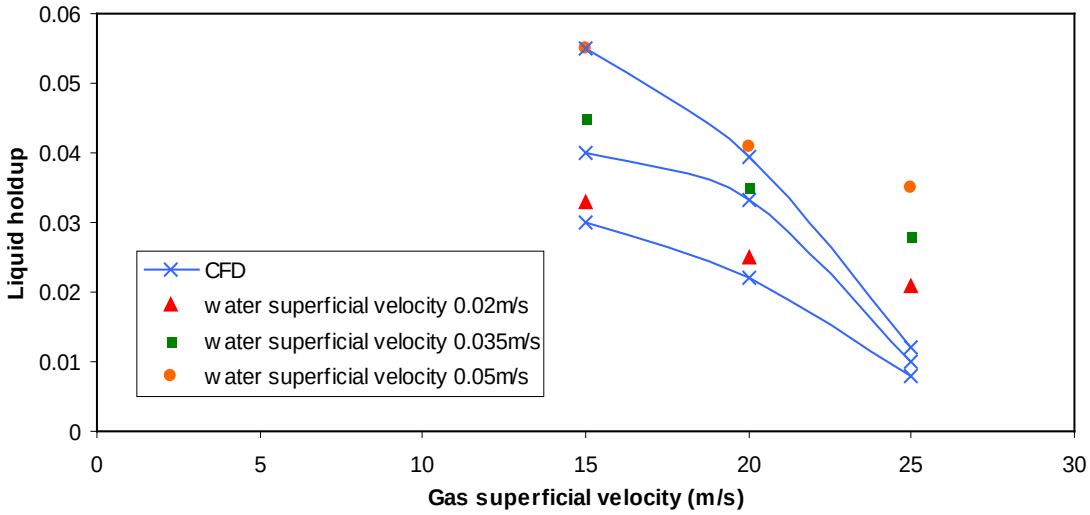

Figure 5.9: Shows liquid holdup at different superficial gas velocity and constant superficial liquid velocity.

5.9.5 Pressure Gradient

In order to study the effect of a superficial velocity of gas and liquid on the pressure gradient of two–phase flow in horizontal pipes, different simulation studies were performed with several air and water superficial velocities ranging from 15 to 25m/s, and 0.02 to 0.05m/s, respectively. The results were compared with experimental data (Badie *et al*., 2000) and also with the models developed by Hart *et al*., (1989) and Chen *et al*. (1997). Figure (5.10) shows the relationship between the superficial water velocity and pressure gradient in which the superficial gas velocity is kept constant.

It can be noted that the pressure gradient increases with the superficial water velocity as shown on Figure (5.10–a and b). The rate of increase can be seen clearly as the superficial gas velocity also increased. At low superficial gas velocity the pressure gradient changes cannot be distinguished with variant superficial water velocity, and is represented as a straight line.

The pressure gradient results at low superficial gas velocity are well predicted by CFD simulations with respect to experimental data. In contrast the Hart *et al*. (1989) and Chen *et al*. (1997) developed models over predicted the pressure gradient at low and medium superficial gas velocities of 15 and 20 m/s respectively. However at high superficial gas velocity, the Hart and Chen models predicted pressure gradient quite well with respect to the Badie experimental data, especially at low superficial water velocity according to the Hart model, and at medium superficial water velocity according to the Chen model, where the CFD result under predicted.

Figure (5.11) demonstrates the effect of superficial gas velocity on the pressure gradient at a stable superficial water velocity. It can be observed that an increase in the water superficial velocity at a constant gas superficial velocity leads to a substantial increase in the pressure gradient. In addition, it shows a close agreement with low and medium gas superficial velocities of 15 and 20 m/s respectively, and deviated at high gas superficial velocity (25 m/s). This is due to the fact that when the gas flow rate is increased, a greater friction of pipe wall is covered by a rough

interface formed between the liquid and gas, which leads to an increased friction factor and pressure gradient.

The validation of the model used in this study is achieved by comparison with experimental data. The results were in close agreement in particular at a superficial gas velocity lower than 25 m/s. Therefore, the model can be used for studying the effect of different parameters on the pressure drop and liquid holdup in a horizontal pipeline. In order to study these parameters, such as mass flux and initial liquid holdup, on the pressure drop and liquid holdup simulations were performed for a series of liquid holdup at a constant gas and liquid superficial velocity.

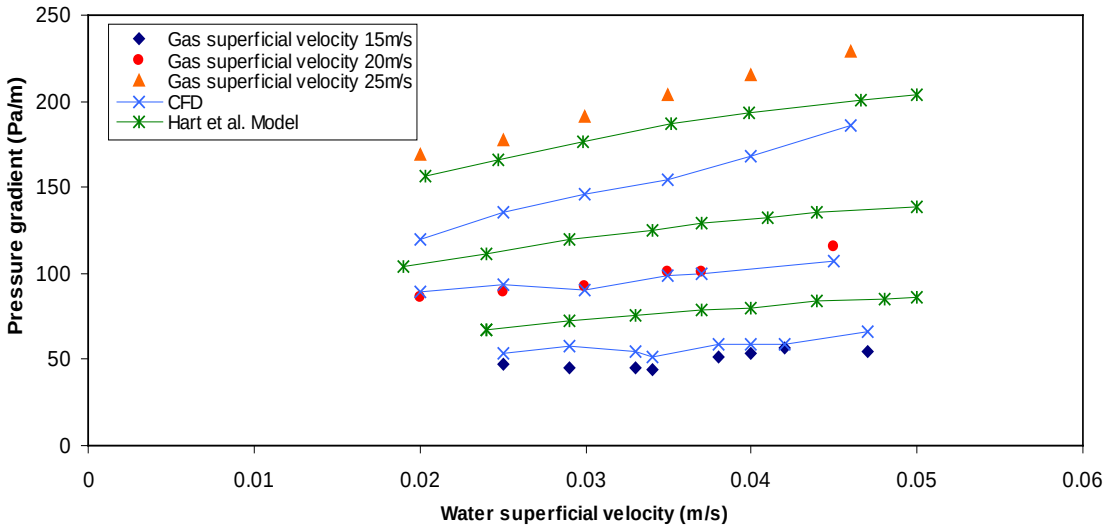

(a)

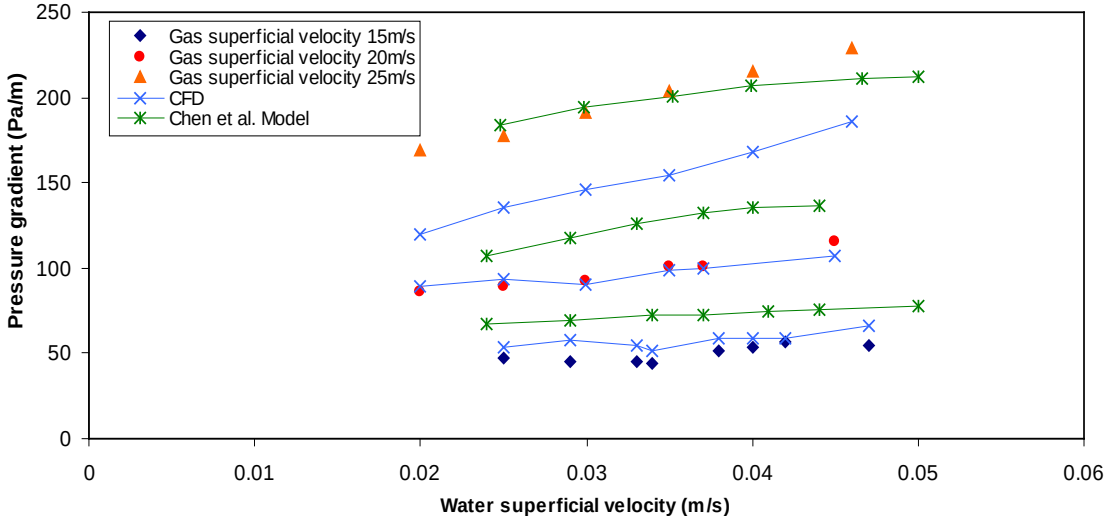

(b)

Figure 5.10: Shows CFD comparison of pressure gradient with an experimental data and (a) the Hart *et al.* model and (b) the Chen *et al*. model.

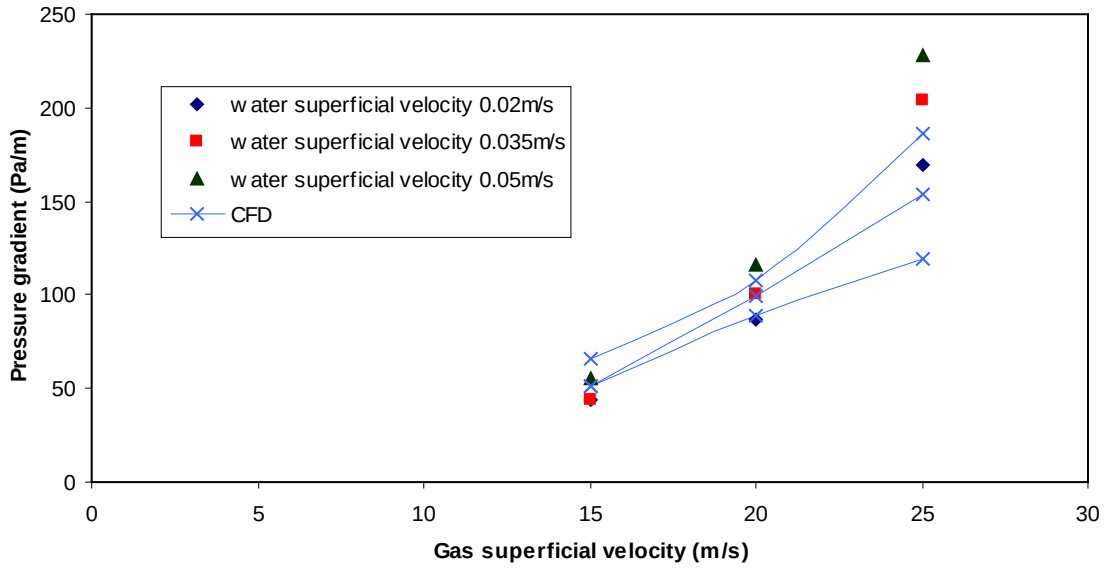

Figure 5.11: Shows CFD comparison of pressure gradient with an experimental data.

5.10 Effect of Different Parameters on Pressure Drop and Liquid Holdup

5.10.1 Effect of Droplet Size

This section has investigated the effect of droplet diameter on the pressure gradient and liquid holdup at a high gas superficial velocity of 25 m/s. The previous simulations were performed under constant droplet diameter (100 μm), where the result deviated from the experimental data. Moreover, as we know that the droplet sizes are not uniform in reality, it varies (e.g. from 10–1000 μm). The droplet size is examined to capture the effect on the two–phase pressure drop and liquid holdup parameters. The simulation was performed under a fixed droplet diameter of 300 μm.

Figure (5.12) represents the pressure gradient versus superficial water velocity at a constant superficial gas velocity of 25 m/s. The CFD prediction result of pressure gradient at a drop size of 300 μm is found to have closely followed the experimental data as shown in Figure (5.12). It can also be observed that the CFD simulations data confirm close agreement with the experimental data at a constant high gas superficial velocity of 25 m/s with entire range of liquid (water) superficial velocities. In addition, the CFD model confirms agreement with the experimental data, compared to the model developed by Hart *et al*. (1989). On the other hand, Figure (5.13) demonstrates the effect of water superficial velocity on the liquid holdup at a constant gas superficial velocity of 25 m/s.

The CFD simulation results of a 300 μm drop size also show closer agreement with the experimental data compared with the previous case study of 100 μm drop size. It can also be observed clearly in Figure (5.14–b), in which the interface between the two–phase is more obvious in comparison with the first simulation with 100 μm, as shown in Figure (5.14–a), and represents the stratified flow. Additionally, at a 300 μm droplet diameter, the model predictions of liquid holdup are predicted well at low water superficial velocities between 0.02–0.025 m/s. At medium and high water superficial velocities above 0.03 m/s, the CFD predictions of liquid holdup data are over predicted compared with the model by Hart *et al*. (1989).

As mentioned earlier, one needs to look carefully at the effect of droplet size in terms of introducing more than one phase of the water droplet. The breakage and coalescence process of the droplet may also have an impact on the system parameters of pressure drop and liquid holdup.

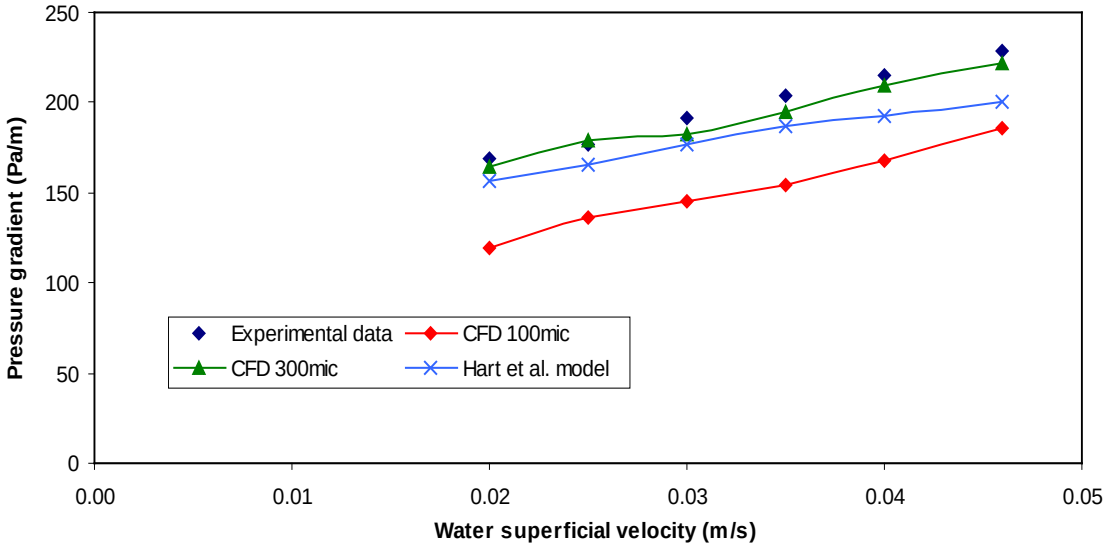

Figure 5.12: Demonstrates the effect of water superficial velocity on pressure gradient at high gas superficial velocity.

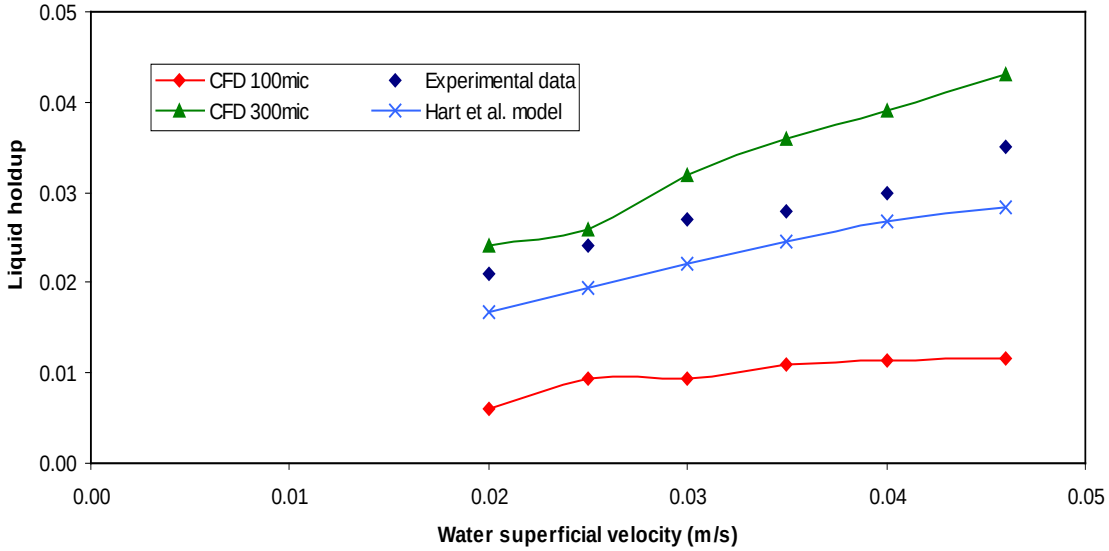

Figure 5.13: Demonstrates the effect of water superficial velocity on liquid holdup at high gas superficial velocity.

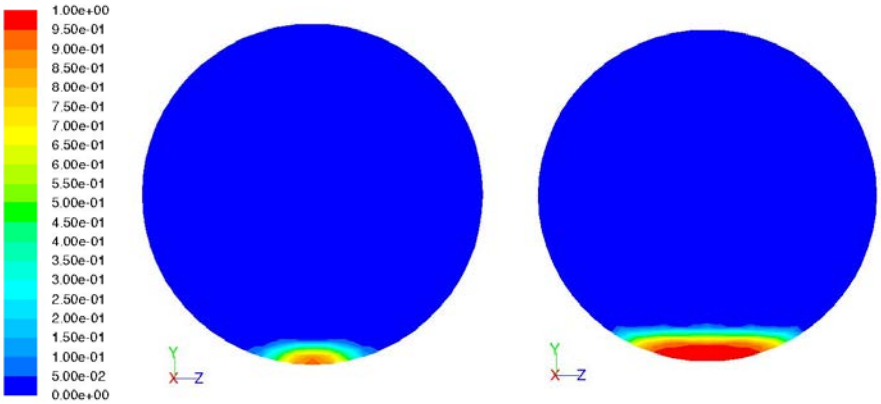

(a) (b)

Figure 5.14: Shows liquid holdup contours at outlet for constant superficial gas velocity (25m/s) and variant droplet size: (a) 100µm, and (b) 300µm.

5.10.2 Effect of Gas Mass Flux

In order to study the effect of gas mass flux on the pressure drop and liquid holdup, further simulations were performed for the same pipe size in which the input water fraction and water mass flux were treated as a constant, and gas mass flux as a parameter; this ranged from 10 to 30 kg/m^2.s. The pressure drop data is shown in Figure (5.15) as a function of gas mass flux. It can be seen clearly that an increase in the gas mass flux at a constant initial water holdup led to a substantial increase in the pressure drop as shown in Figure (5.15), even for low input water fraction. When the gas mass flux increases, a greater friction of the pipe wall is covered by a rough interface formed between the liquid and the gas, leading to an increased friction factor and pressure drop. The tendency of this result is consistent with reported experimental studies (Meng *et al.*, 2001 and Olive *et al.*, 2003). In addition, it can be noted that an increase initial liquid holdup leads to a sharp increase in the pressure drop.

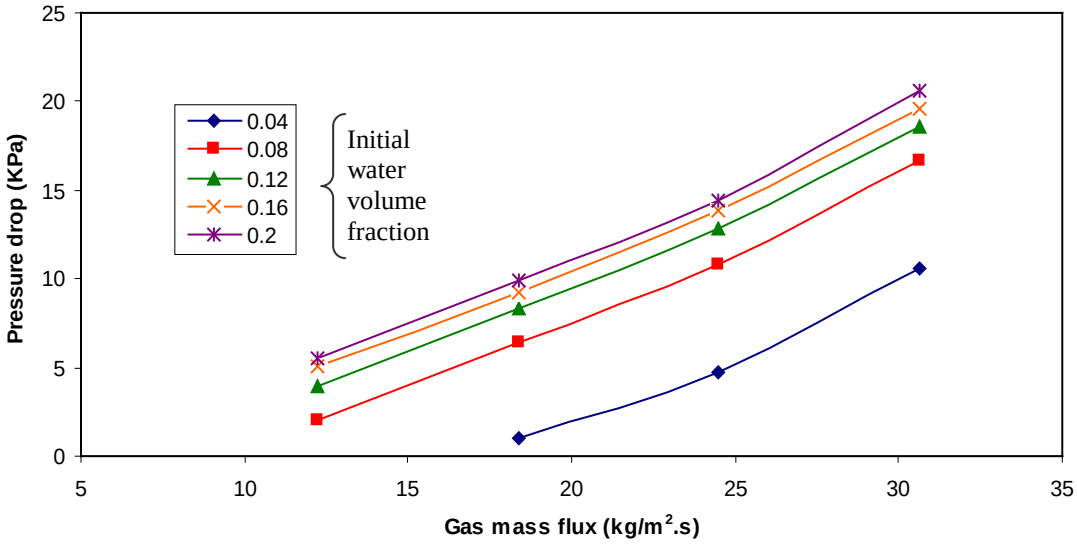

Figure 5.15: Shows CFD pressure drop versus different gas mass flux at constant water fraction.

On the other hand, the simulation results obtained of liquid holdup for air–water flow were plotted versus gas mass flux with different initial water fractions which varied from 0.04 to 0.2, and are treated as a factor in Figure (5.16). It can be observed that the liquid holdup decreases with increasing gas mass flux at different initial water holdup. This is due to the increase of the interfacial shear stress at larger velocity differences between the gas and liquid fluid, where this result of decreasing liquid holdup with increasing gas mass flux was expected. This observation was similar to that reported in experimental data of gas–liquid flow with low liquid loading in horizontal pipes by Meng *et al*. (2001).

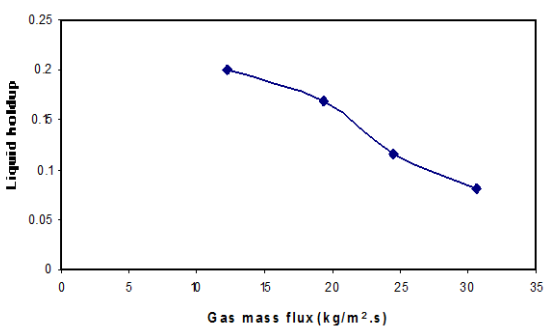

(a)

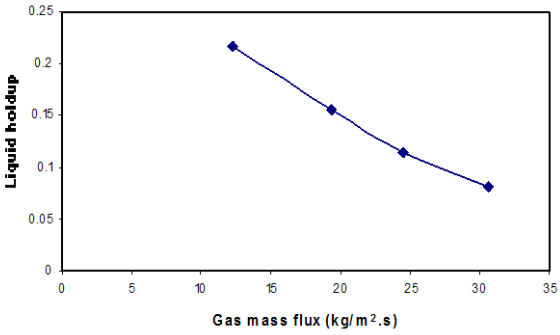

(d)

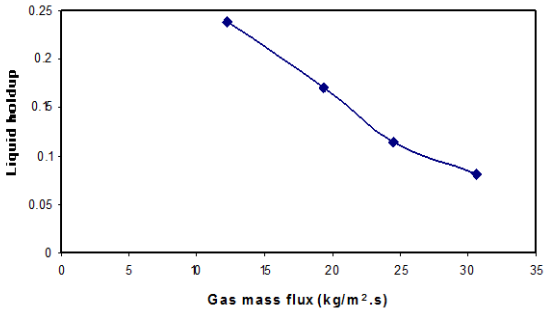

(b)

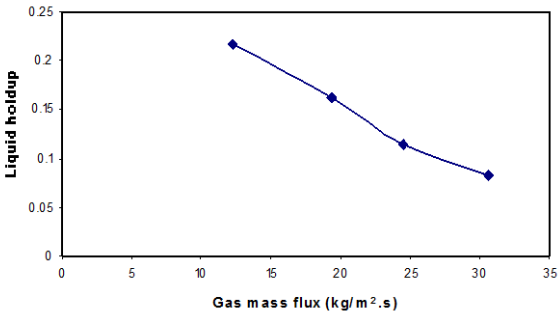

(e)

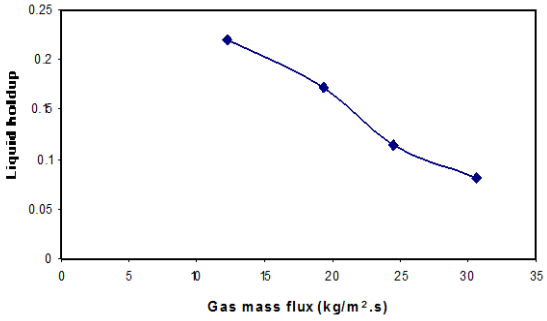

(c)

Figure 5.16: Shows CFD water holdup versus different gas superficial velocity at different initial water fractions (a) 0.04, (b) 0.08, (c) 0.12, (d) 0.16, and (e) 0.2.

5.10.3 Effect of Initial Water Holdup

In this section, the input water fraction is treated as a parameter and is varied from 0.04 to 0.2, in which the mass flux of both phases; gas and liquid, are kept constant. Figure (5.17) demonstrates the effect of initial liquid holdup on the pressure drop at constant total mass flux. It can be observed that the values of pressure drop in the horizontal pipe tend to go in the same direction as that varied by the values of water volume fraction. The instantaneous values of pressure drop always increased with an increase in the initial water fraction. At a high water fraction above 0.1, the increase of pressure drop is considered insignificant in comparison with that where the water fraction is lower than 0.1. In other words, the presence of a small amount of liquid increases the pressure drop significantly, while the increase of mass flux results in a rapid increase in the pressure drop.

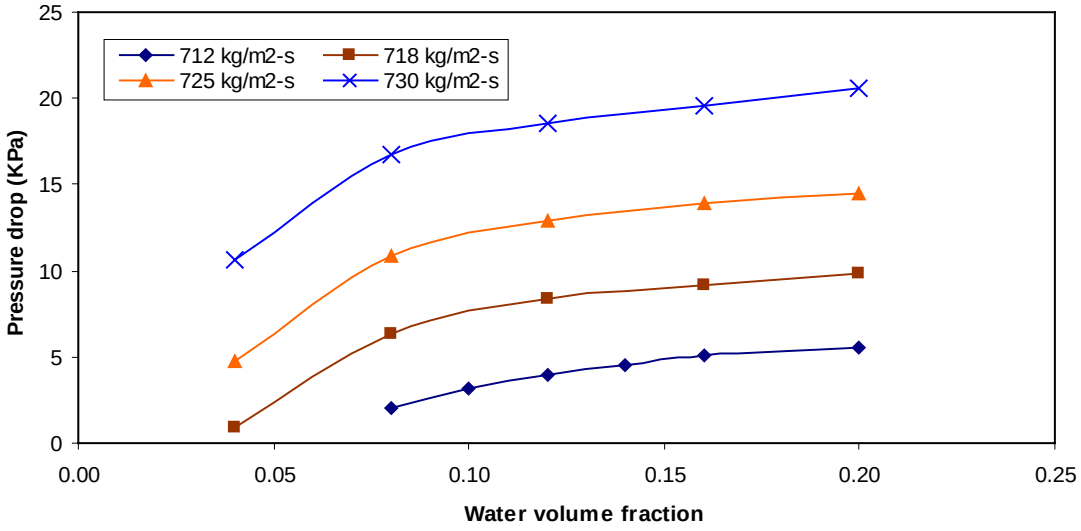

Figure 5.17: Shows CFD pressure drop versus different initial water fraction at constant total mass flux.

5.10.4 Effect of Water Mass Flux

In this section the water mass flux is treated as a parameter where the gas mass flux and liquid fraction are kept constant. As shown in Figure (5.18) the pressure drop increases as the water mass flux increases, where this increase was proportional and sharp. The same trend was observed for the liquid holdup, which increased with the water mass flux. Figure (5.19) shows the effect of water mass flux on the final liquid holdup at a constant gas mass flux.

As can be noted, the increase of liquid holdup was rapid at a low water mass flux, but when the water mass flux increased the variation of liquid holdup was insignificant. This is due to the high water mass flux or velocity which led to entrain some of the liquid into various sized drops. The residence time of these drops depends on their size, and the flow turbulence as well. Therefore, at low water superficial velocity/or mass flux, the liquid interface is not easily interrupted unless the primary phase velocity is quite high, and will also be less liquid entrained. In other words, the change of water mass flux increases the pressure drop significantly, while the liquid holdup increases rapidly and then becomes almost steady.

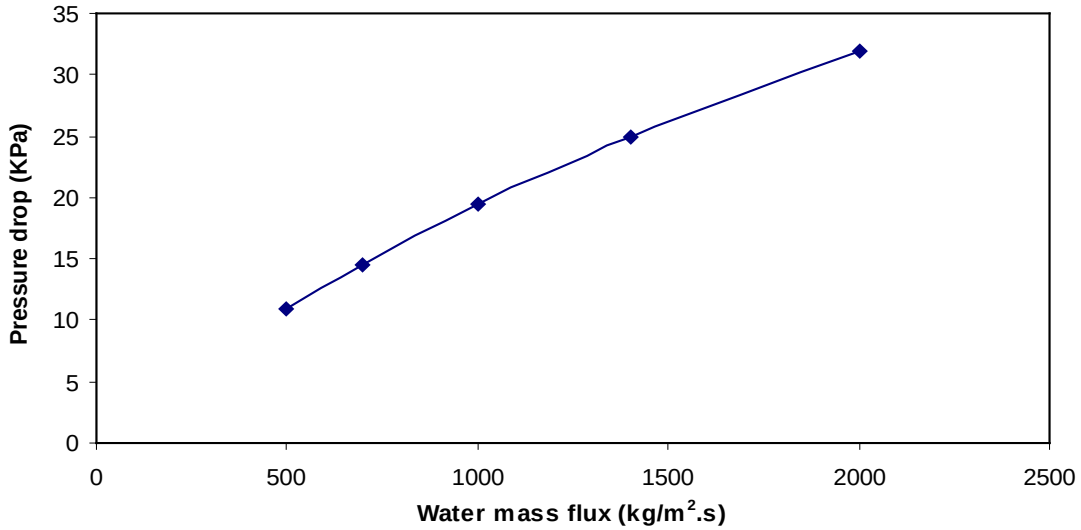

Figure 5.18: Shows the effect of water mass flux on pressure drop at constant water fraction and gas mass flux.

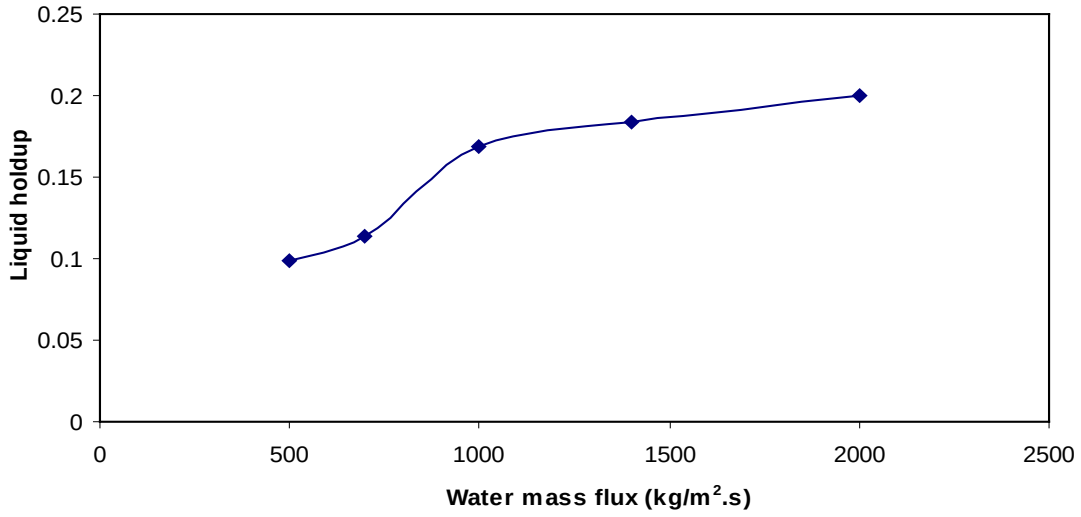

Figure 5.19: Shows the effect of water mass flux on liquid holdup at constant water fraction and gas mass flux.

5.11 Simulation Result of Air–oil Two–phase Flow

The simulations of two–phase flow air–oil were carried out in the same pipe geometry with 0.078m and 7m long horizontal pipes to obtain the effect of system operating parameters as well as the viscosity on the pressure drop and liquid holdup. The mass flux of two–phase air and oil is used as an inlet boundary condition, and varied from 12 to 30 kg/m^{2}s and 40 to 1300 kg/m^{2}s respectively, and the average oil volume fractions varied from 4 to 20%. The simulation is conducted under standard conditions of temperature and pressure at 25 ^{o}C and 1 atm. The simulation results are taken at the pipe outlet for liquid holdup, and at the inlet for pressure drop since the gauge pressure at the outlet is zero.

5.11.1 Effect of Initial Oil Holdup

To investigate the effect of oil volume fraction on the pressure drop, various simulations were performed and the results are illustrated in Figure (5.20). The total mass flux is kept constant while the oil volume fraction is treated as a parameter. It can be noted from Figure (5.20) that at a two–phase mass flux less than 90 kg/m^{2}s the effect of the oil fraction is considered insignificant, where the pressure drop is almost kept constant. On the other hand, at high two–phase mass flux, it can be clearly observed that the pressure drop varies with the oil volume fraction. In the case of mass flux (92.3 kg/m^{2}s), the pressure drop is decreased quickly and then increased, while at a higher two–phase mass flux (104.5 kg/m^{2}s) the pressure drop is decreased rapidly and then continues to decrease at a constant rate.

As the total flow rate increased, more drops would expect to entrain in the inner pipe, leading to a decrease the real area of the gas. At a constant input liquid volume fraction the increase of gas mass flux/superficial velocity will lead to an increase the pressure drop of two–phase as shown in Figure (5.21). Moreover, the increases of input liquid volume fraction combined with increasing mass flux are enlarged, and hence there is a reduction of the wetted area of the pipe wall. The result of this will lead to a reduction in the pressure drop as shown in Figure (5.21–e).

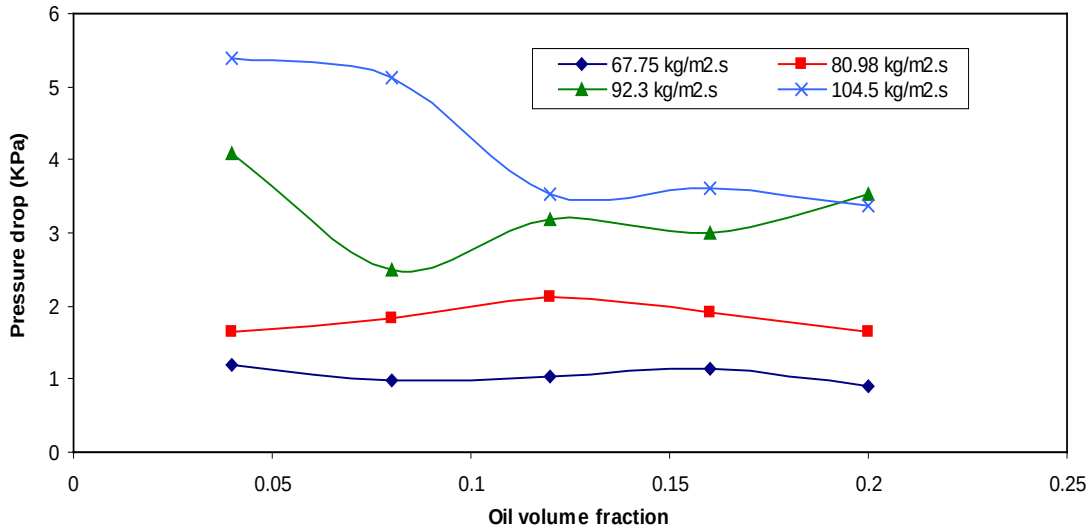

Figure 5.20: Shows the effect of oil volume fraction on pressure drop at constant two–phase flux.

5.11.2 Effect of Gas Mass Flux

To examine the effect of gas mass flux or superficial velocity on the two–phase pressure drop, the gas mass flux is treated as a parameter and the oil mass flux and volume fraction are kept constant. Figure (5.21–a to e) shows the effect of gas mass flux that is treated as a parameter on the two–phase air–oil pressure drop at a constant oil mass flux. As the gas mass flux/or superficial velocity increased at a constant oil volume fraction, the pressure drop increased sharply. An interesting phenomenon was noted for the pressure drop, which decreased at a high oil fraction of 0.2 when the gas mass flux increased from about 25 to 30 kg/m^2.s.

The result of the liquid holdup was plotted versus the gas mass flux with an initial liquid (oil) holdup, and is treated as a parameter in Figure (5.22–a to e). It can be noted that the final liquid (oil) holdup decreases as the gas mass flux/or superficial velocity increases. The reason for this decrease is due to the higher drag exerted on the oil phase at the interface, by the fast movement of gas phase that led to the liquid flowing faster, leaving a smaller amount of liquid in the pipe at any time. An interesting observation was made at a high oil fraction of 0.2 in Figure (5.22–e). An

increase in the gas mass flux to around 20 kg/m^{2}s caused the liquid holdup to increase instead decreasing in comparison to other oil fractions in Figure (5.22–a, b, c, and d).

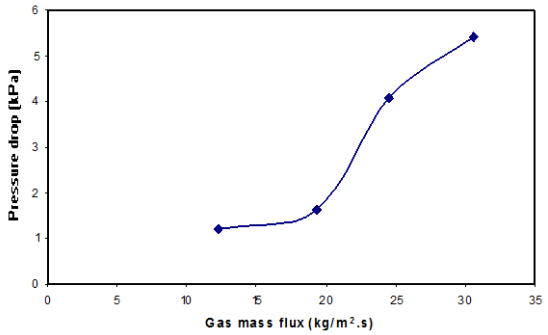

(a)

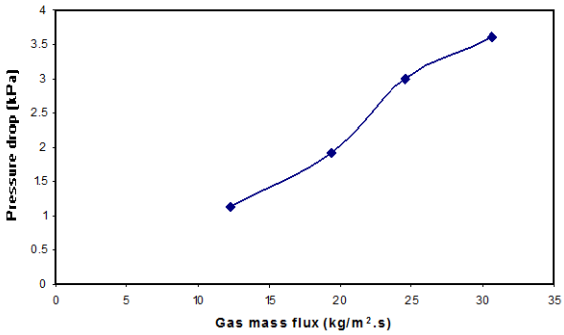

(d)

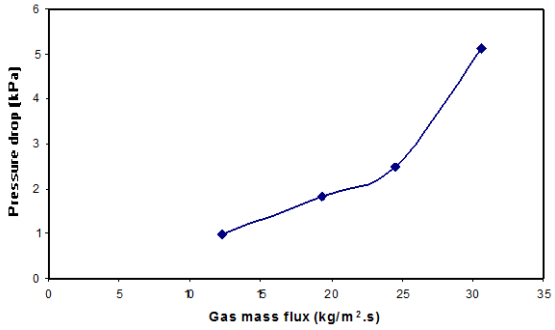

(b)

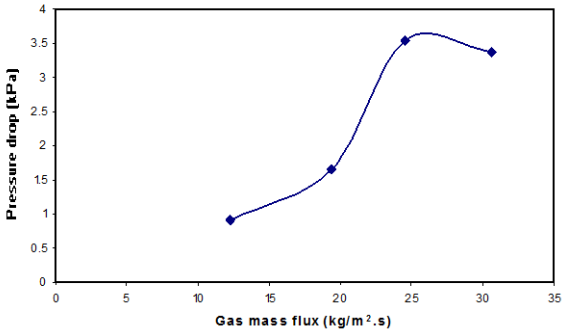

(e)

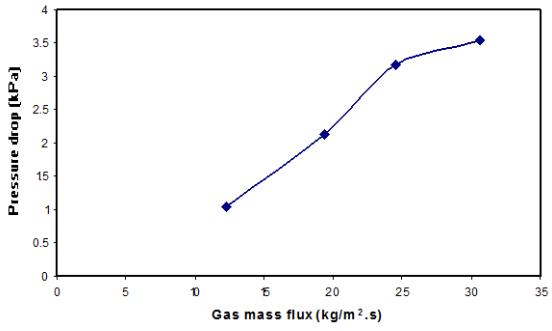

(c)

Figure 5.21: Demonstrates the effect of gas mass flux on pressure drop at a constant input oil volume fraction: (a) 0.04, (b) 0.08, (c) 0.12, (d) 0.16, and (e) 0.2.

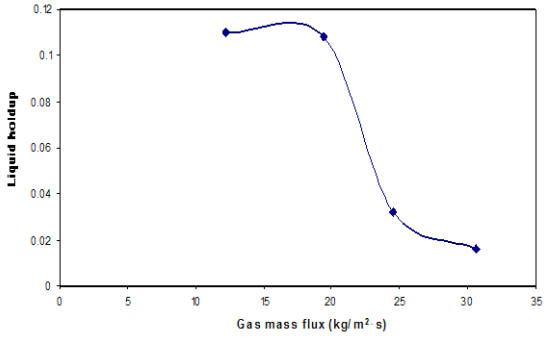

(a)

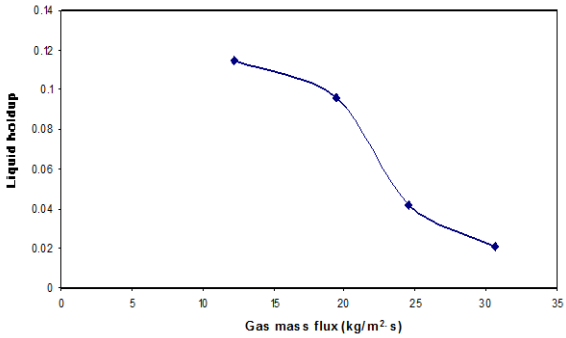

(d)

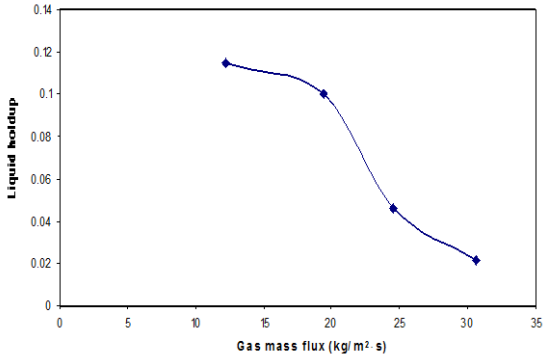

(b)

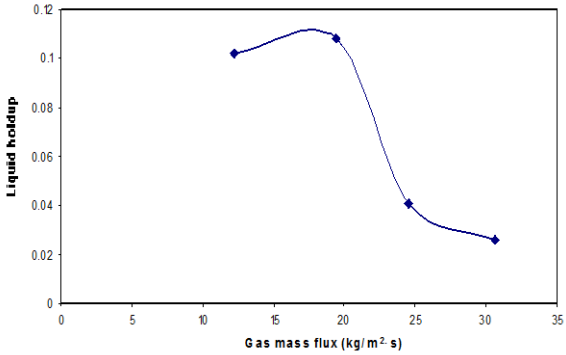

(e)

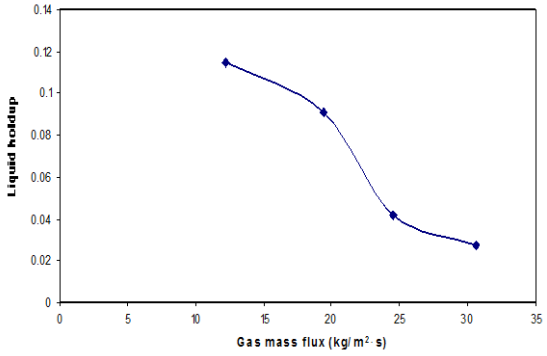

(c)

Figure 5.22: Demonstrates the effect of gas mass flux on liquid holdup at a constant input oil volume fraction: (a) 0.04, (b) 0.08, (c) 0.12, (d) 0.16, and (e) 0.2.

5.11.3 Effect of Oil Mass Flux

In order to investigate the effect of oil mass flux/or superficial velocity which is treated as a parameter on the two–phase pressure drop and liquid holdup, the gas mass flux and oil fraction are treated as constants. As shown in Figure (5.23), the pressure drop results were plotted against the oil mass flux. The result demonstrates that the pressure drop increases with the increase of oil mass flux/superficial velocity. This increase was initially sharp, and then the rate of increase can be described as linear. Moreover, the pressure drop is increased slightly between the mass flux values of around 850 and 1300 kg/m^{2}s compared to low mass fluxes. An increase in the oil mass flux/superficial velocity at a constant gas mass flux and oil fraction leads to an increase in the final oil holdup value as shown in Figure (5.24).

The rate of increase of oil holdup with mass flux is less than linear, since the local liquid velocity also increases with increasing oil mass flux. The reason for this is due to a faster moving of the liquid phase, which leads to it covering a greater segment of the pipe and wetting a greater fraction of the pipe wall.

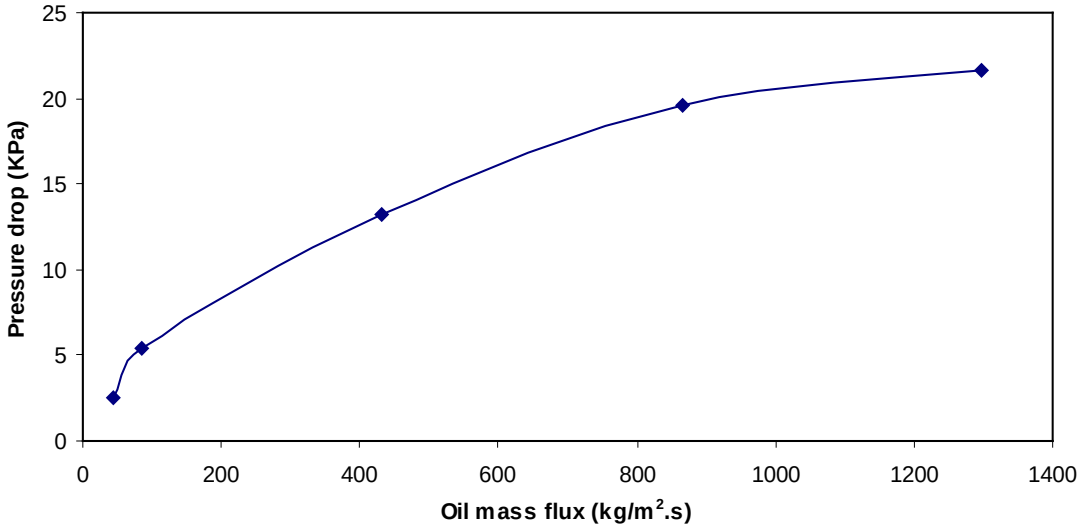

Figure 5.23: Shows the effect of oil mass flux on pressure drop at constant gas mass flux and liquid volume fraction.

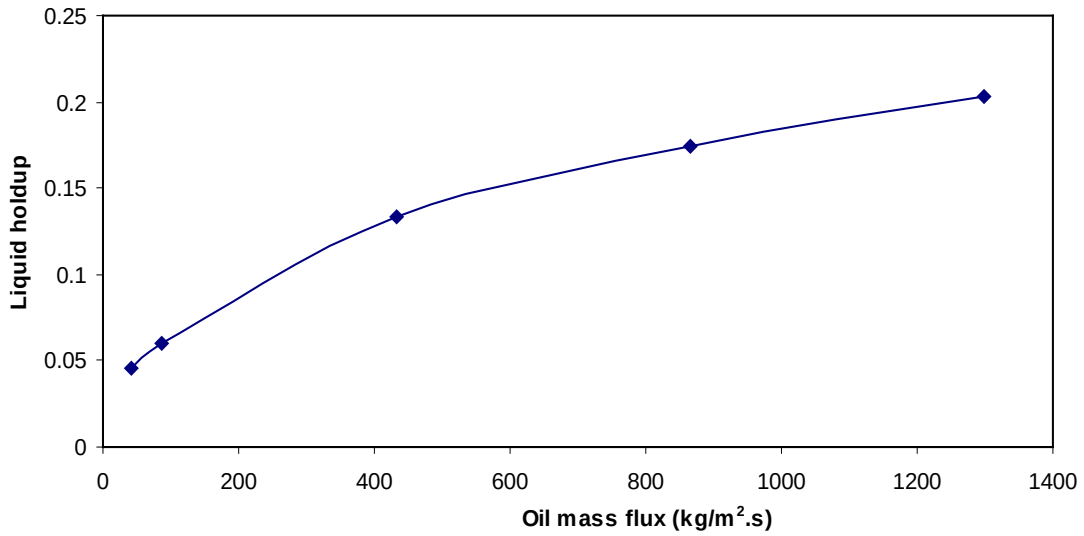

Figure 5.24: Shows the effect of oil mass flux on liquid holdup at constant gas mass flux and liquid volume fraction.

5.11.4 Comparison between Air–oil and Air–water Flow Results

The two–phase pressure drop range of air–oil at a constant gas mass flux and liquid volume fraction is between 2.5–21 kPa as shown in Figure (5.23), while for air–water two–phase pressure drop, with the same condition of gas mass flux/superficial velocity and water volume fraction, the pressure drop range was between 10–31 kPa as shown Figure (5.18). This difference in the pressure drop results was possibly due to the two liquid phase's oil and water viscosity difference.

For air–oil two–phase flow, the existence of a small amount of liquid decreased the pressure drop considerably, especially for high two–phase mass flux as shown in Figure (5.20). The effect of increasing liquid volume fraction on pressure drop was insignificant at low two–phase mass flux (67.75 and 80.98 kg/m^{2}s), but it was limited for high mass flux (92.3 and 104.5 kg/m^{2}s) to a volume fraction of 0.04–0.12. This phenomenon was much more significant for air–water flow. The liquid fraction of 0.08 increased the pressure drop higher than at the air–oil flow as shown in Figure (5.17).

For air–oil two–phase flow, it was observed that the pressure drop decreased when the liquid volume fraction increased from 0.04–0.12 at a high superficial gas velocity of 20–25 m/s. This phenomenon was not seen with air–water two–phase flow where the two–phase pressure drop was noted to increase until the increase in the liquid fraction was less significant on the pressure drop change.

The result obtained for the liquid holdup for air–water was greater than for the air–oil two–phase flow. In the case of air–water two–phase flow, the range of liquid holdup was 0.2–0.24 for a gas mass flux of 12.25 kg/m^{2}s, which corresponds to 10 m/s and 0.08–0.084 for 30.63 kg/m^{2}s (corresponding to 25 m/s). On the other hand, the air–oil liquid holdup range was 0.1–0.12 for a gas mass flux of 12.25 kg/m^{2}s and 0.016–0.027 for a gas mass flux of 30.63 kg/m^{2}s. Moreover, the phenomenon of decreasing the liquid holdup with the increase in the initial liquid volume fraction was observed for varying gas mass flux values/superficial velocities in both cases of two–phase flow. However as the liquid holdup at air–water is greater than for air–oil, this could be that the flow pattern in each of these two–phase flows is different, annular flow for air–water and stratified wavy flow for air–oil. This would be expected due to the viscosity difference.

5.12 Comparison of CFD Result with An empirical Correlation

As mentioned in Chapter 2, different empirical correlations have been developed based on experimental data for calculating the pressure drop and liquid holdup. One of these correlations is the Beggs and Brill (1973) (labelled “B–B”) correlation analysis. This is based on experimental data for air–water flow in small tubes with various inclination angles and has been widely used to describe the pressure drop in a horizontal pipe of two–phase flow that may be encountered in oil and gas transportation, although numerous empirical or semi–empirical models are available in the literature.

The Beggs and Brill correlation can be used to find the friction pressure loss and the hydrostatic pressure difference, which is not included here since the pipeline used is horizontal. The two–phase flow pattern defined as Segregated, Intermittent or

Distributed is obtained based on the Beggs and Brill parameters. Then the liquid holdup and *in-situ* density of two–phase mixture is computed based on the flow regime. The gas–liquid two–phase flow friction factor is obtained based on the input ratio of two–phase and the Fanning friction factor. Based on this the friction pressure drop can be estimated using the input mixture properties of two phases.

5.12.1 Identified Flow Pattern

To identify the flow pattern, transition lines are obtained as follows:

$$\left.\begin{aligned} L_1 &= 316\lambda^{0.302} \\ L_2 &= 92.52\times10^{-5}\lambda^{-2.4684} \\ L_3 &= 0.1\lambda^{-1.4516} \\ L_4 &= 0.5\lambda^{-6.738} \end{aligned}\right\} \tag{5.14}$$

Where L_1, L_2, L_3, and L_4 are Beggs and Brill parameters, and λ is the initial liquid holdup that is calculated using this equation:

$$\lambda = \frac{u_l}{u_m} \tag{5.15}$$

Where u_l is the liquid velocity and u_m is the mixture velocity. The flow pattern is determined either from the existence of a flow pattern map or based on the following conditions of the correlation as:

$$Fr_m = \frac{u_m^2}{gD} \tag{5.16}$$

To find out one of the flow patterns (Segregated, Intermittent or Distributed), the following conditions are applied:

- The flow is described as Segregated if

$\lambda < 0.01$ and $Fr_m < L_1$ or $\lambda > 0.01$ and $Fr_m < L_2$

- The flow is described as Transition if

$\lambda \geq 0.01$ and $L_2 < Fr_m \leq L_3$

- The flow is described as Intermittent if

$0.01 \leq \lambda < 0.4$ and $L_3 < Fr_m \leq L_1$ or $\lambda \geq 0.4$ and $L_3 < Fr_m \leq L_4$

- The flow is described as Distributed if

$\lambda < 0.4$ and $Fr_m \geq L_1$ or $\lambda \geq 0.4$ and $Fr_m > L_4$

5.12.2 Two–phase Pressure Drop

In order to calculate the pressure drop due to friction, the empirical parameter "S" is obtained using one of the following formulas based on the "*y*" value.

if $1 < y < 1.2$, then

$$S = \ln(2.2y - 1.2) \tag{5.17}$$

Otherwise

$$S = \frac{y}{-0.0523 + 3.182y - 0.8725y^2 + 0.01853y^4} \tag{5.18}$$

where *y* can be defined as,

$$y = \ln\frac{\lambda}{\alpha} \quad \text{and} \quad \alpha = \frac{A\lambda^B}{Fr_m^C} \tag{5.19}$$

where *A*, *B* and *C* are constants and depend on the flow regime

The two–phase friction factor is obtained from equation (5.19) based on no–slip friction factor, which is based on no–slip Reynolds number that is calculated as follows:

$$\mathrm{Re}_{ns} = \frac{\rho_{mix} V_{mix} D}{\mu_{mix}} \tag{5.20}$$

The Blasius equation for the Fanning friction factor can be written as:

$$f_{ns} = \frac{x}{\mathrm{Re}_{ns}^{n}} \tag{5.21}$$

where x = 16 and n = 1.0 for laminar flow (Re < 2000), while x = 0.079 and n = 0.25 for turbulent flow (Re > 2000). The two-phase friction factor is calculated as:

$$f = f_{ns} e^{s} \tag{5.22}$$

The two –phase pressure drop due to friction can be expressed as:

$$\Delta P = \frac{2 f \rho_{mix} V_{mix}^{2}}{D} \tag{5.23}$$

5.12.3 Liquid Holdup Correlation

The liquid holdup correlation used in this investigation, is the Mukherjee and Brill (1985) (Labelled “M–B”) correlation developed for different pipe inclination angles. In this research we will focus on the horizontal segment and exclude the uphill section of the correlation. The general liquid holdup correlation is presented in the equation (5.24) below.

$$H_L = \exp\left[\left(C_1 + C_2 \sin\theta + C_3 \sin^2\theta + C_4 N_L^2 \right) \frac{N_{gv}^{C_5}}{N_{Lv}^{C_6}} \right] \tag{5.24}$$

The second and third terms in the equation are equal to zero because the pipe is horizontal. C_1, C_2, C_3, C_4, C_5, and C_6 are regression coefficients depending on flow direction uphill, downhill and horizontal. N_{gv}, N_{Lv}, and N_L are the gas velocity number, liquid velocity number and liquid viscosity number, respectively. They can be obtained as follows:

$$N_{gv} = v_{sg}\left(\frac{\rho_l}{g\sigma_l}\right)^{0.25} \tag{5.25}$$

$$N_{Lv} = v_{sl}\left(\frac{\rho_l}{g\sigma_l}\right)^{0.25} \tag{5.26}$$

$$N_L = \mu_L\left(\frac{g}{\rho_l\sigma_l^3}\right)^{0.25} \tag{5.27}$$

5.12.4 Results and Discussion

The Beggs and Brill correlation has been tested at two different initial liquid (water/or oil) volume fractions. Figure (5.25) demonstrates the CFD simulation results of the pressure drop of two–phase air–water flow against the gas mass flux that was treated as a parameter and compared with the calculated values of the Beggs and Brill correlation. In general, the results of the pressure drop show close agreement between the CFD and the Beggs and Brill correlation.

This correlation gives satisfactory predictions for air–water systems, where it performs better at high gas mass flux/superficial velocity and at low liquid holdup of 0.08 (see Figure (5.25–a)), while it performs quite reasonably at high liquid holdup of 0.2 (see Figure (5.25–b)). Generally, the CFD prediction is quite accurate where it produces the same trend in comparison with the Beggs and Brill correlation, but the CFD pressure drop results of one fixed drop size is under predicted over ranged gas mass fluxes. On the other hand, the predicted pressure drop of air–oil two–phase flow by the Beggs and Brill correlation shows agreement with the CFD simulation results, as shown in Figure (5.26).

The Beggs and Brill correlation agrees quite well with the air–oil pressure drop data over the entire range of gas mass flux. The CFD pressure drop result at high liquid holdup of 0.2 deviates from the correlation (as shown in Figure (5.26–b) and indicates that the pressure drop was not affected by increasing the gas mass flux whereas the correlation is contrary to that. In general, the result of the CFD pressure drop of air–oil is in close agreement with the Beggs and Brill correlation in comparison with the air–water pressure drop simulation result, but the CFD result of air–oil still shows as under predicted at both a low and high input liquid volume fraction. The tendency of the two-phase air-water increasingly underpredict the pressure drop for increasing gas fluxes at low and high liquid holdups may arise as a result of different flow regimes not being explicitly accounted for. These are conditions in which the slip factor is high, and the flow is expected to be inhomogeneous. This deviation increased at a high liquid holdup and high gas mass flux/superficial velocity, therefore the pressure drop deviation is much higher in the case of air–water rather than air–oil two–phase flow.

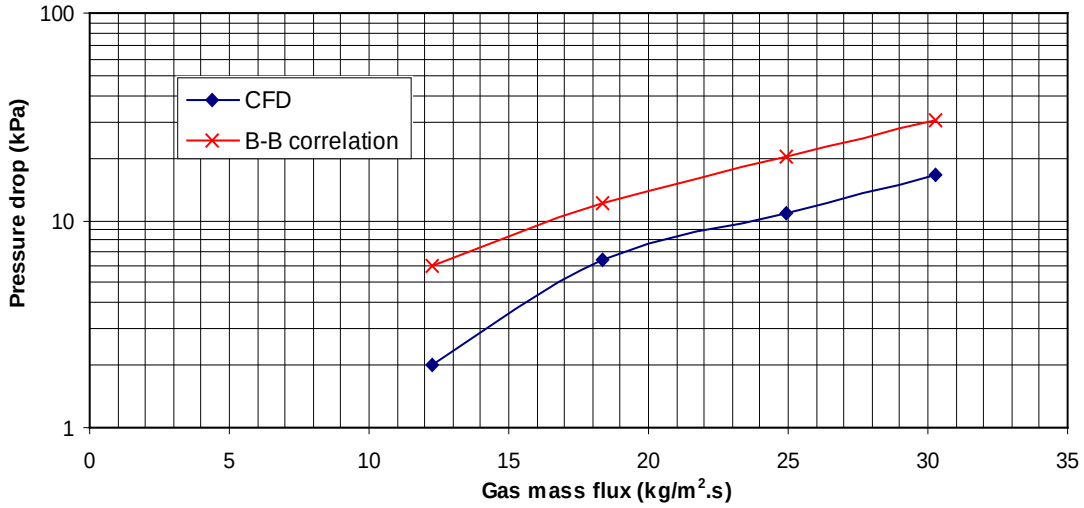

(a)

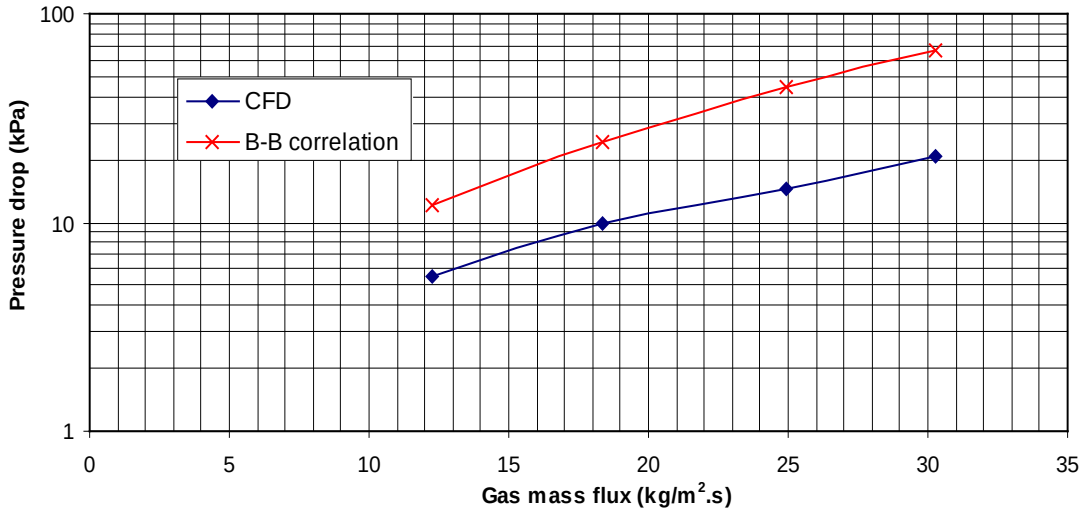

(b)

Figure 5.25: Shows comparison between the CFD and the B–B correlation pressure drop of air–water at different gas mass flux and constant liquid volume fraction (a) 0.08 and (b) 0.2.

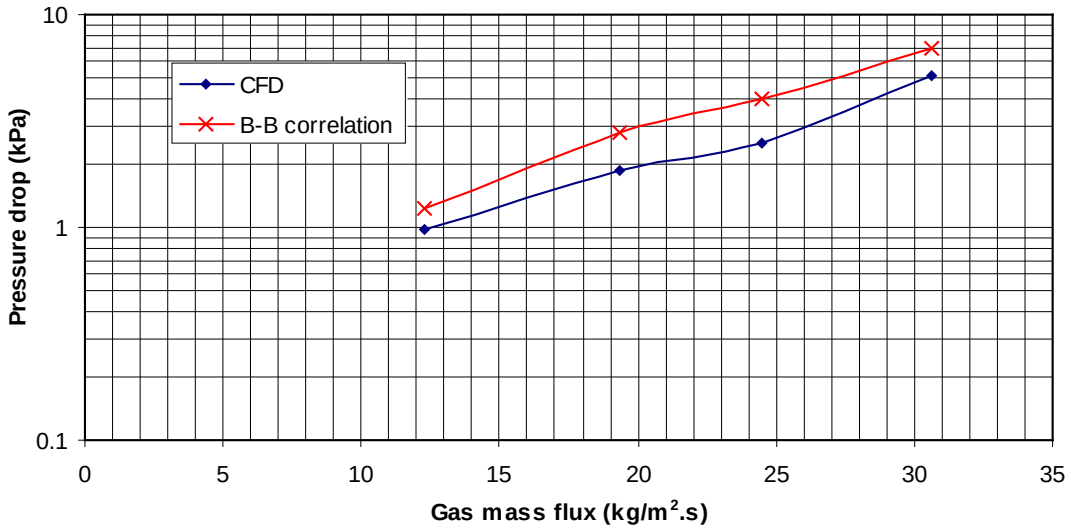

(a)

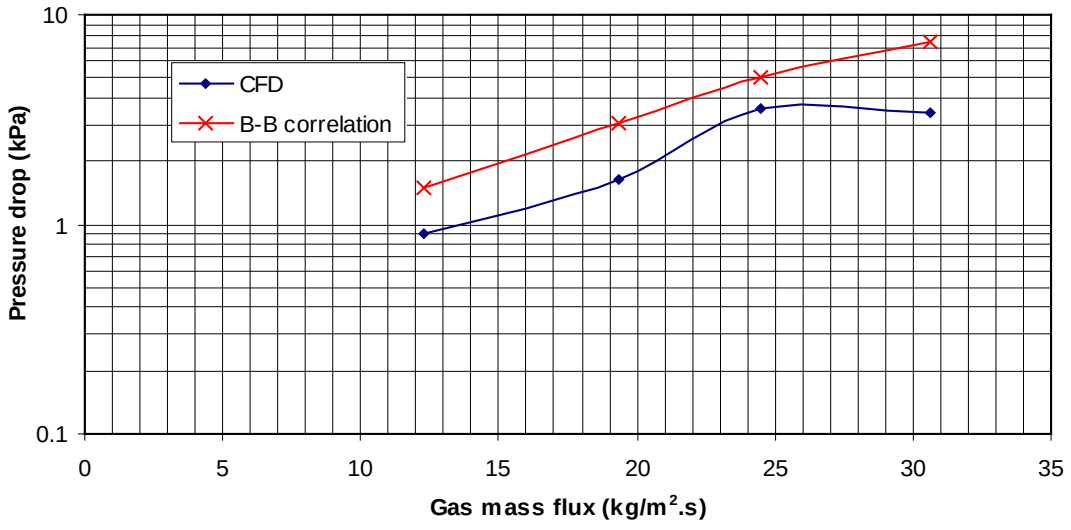

(b)

Figure 5.26: Shows comparison between the CFD and the B–B correlation pressure drop of air–oil at different gas mass flux and constant liquid volume fraction (a) 0.08 and (b) 0.2.

The graphs of the pressure drop comparison data, graphs of the predicted CFD simulation liquid holdup of water and oil versus calculated the liquid holdup using the Mukherjee and Brill correlation, plotted against gas mass flux values as presented in Figures (5.27 and 5.28). The result illustrates that the holdup predicted data via the Mukherjee and Brill correlation is accurately predicted in the case of air–water flow at different input liquid volume fractions of 0.08 and 0.2, as shown in Figure (5.27–a and b) respectively. Moreover, it can be noted that the liquid holdup decreased with the increasing mass flux of gas, and both the results of the CFD and the correlation have the same trend, where the CFD result is slightly under predicted. In the case of air–oil the prediction of the CFD liquid holdup was also under predicted in comparison with the Mukherjee and Brill correlation, as can be seen in Figure (5.28–a and b).

The results of the CFD and correlation are quite reasonable and show that the liquid holdup also decreases with increasing gas mass flux, where both of them have quite a similar trend. In addition, the CFD result of liquid holdup is under predicted with the deviation increasing in the case of the high input liquid fraction of 0.2 as shown in Figure (5.28–b). At a low gas mass flux the liquid holdup results from the CFD is quite far from the correlation, and also shows when the mass flux of gas increased. The CFD liquid holdup increased slightly, where the correlation results are opposed to that. In general, the CFD liquid holdup prediction is quite reasonable in both the cases of air–water and air–oil two–phase flow, in which the deviation of the liquid holdup is significantly larger in the situation of air–oil flow.

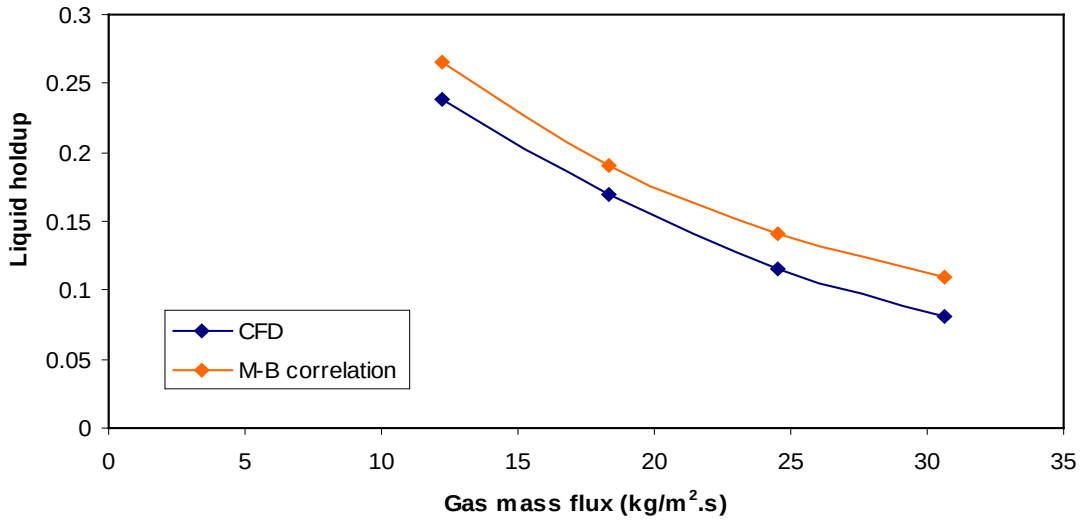

(a)

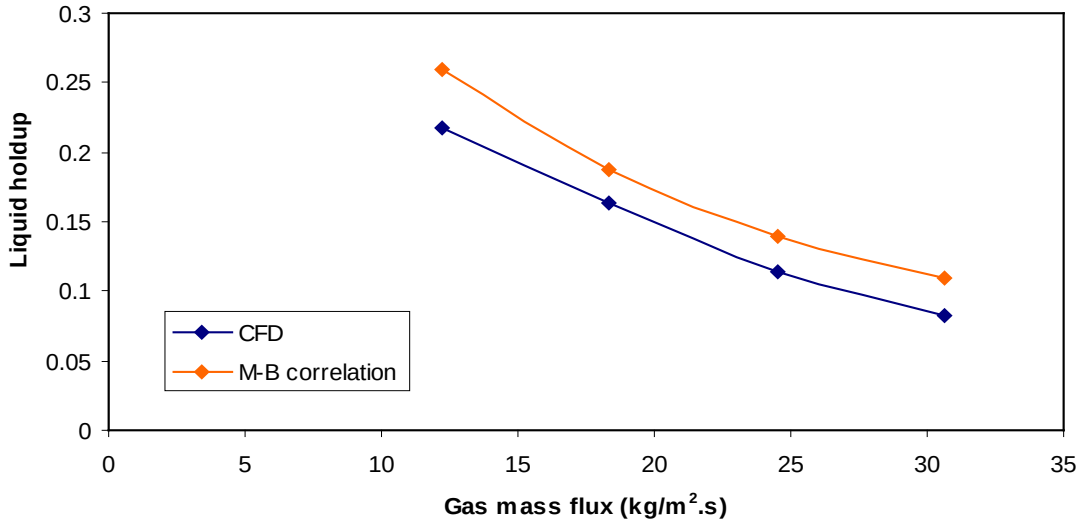

(b)

Figure 5.27: Shows liquid holdup comparison between the CFD simulation and the M–B correlation results at variant gas mass flux and constant water volume fraction: (a) 0.08 and (b) 0.2.

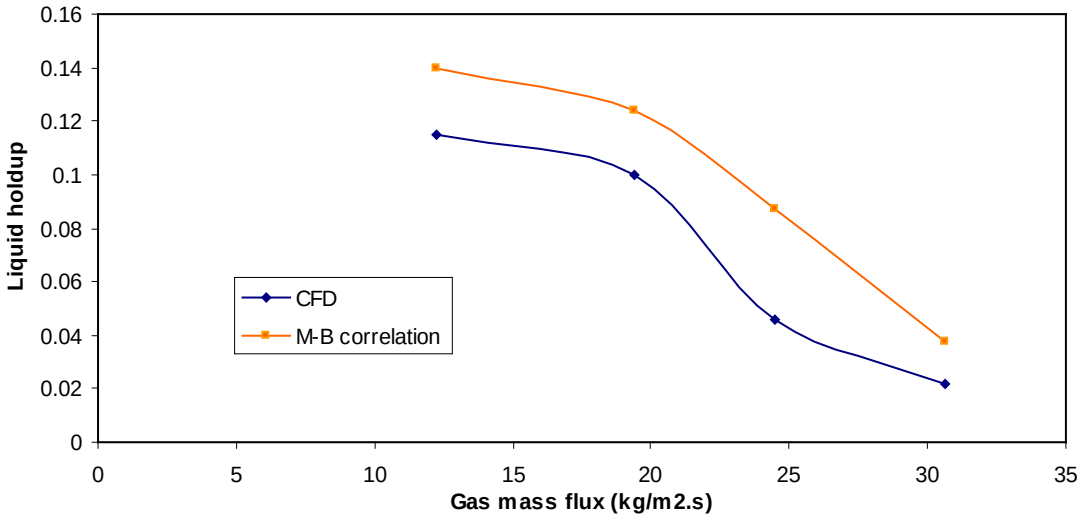

(a)

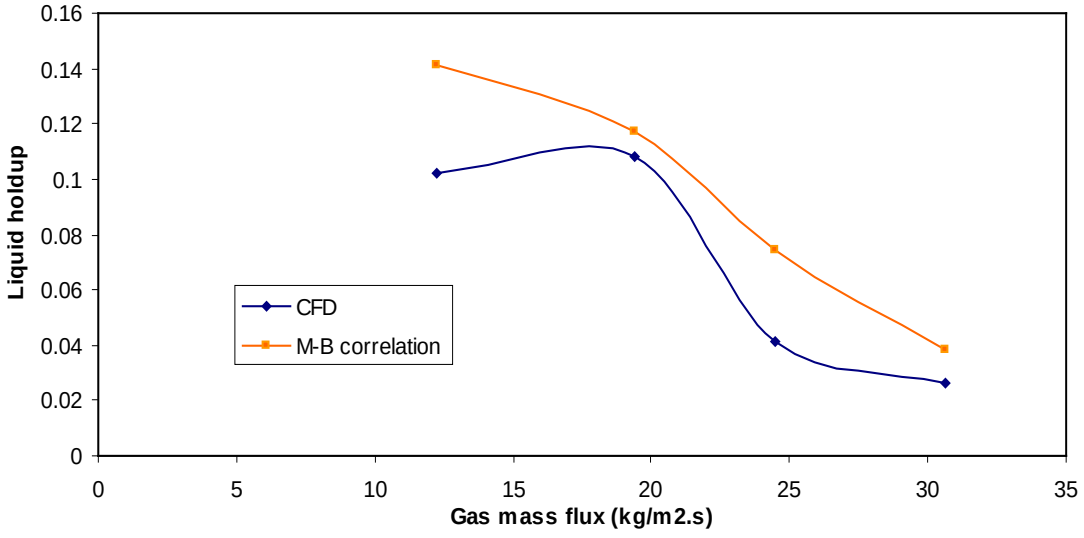

(b)

Figure 5.28: Shows liquid holdup comparison between the CFD simulation and the M–B correlation result at variant gas mass flux and constant oil volume fraction: (a) 0.08 and (b) 0.2.

5.13 Conclusions

The following conclusions can be derived based on the results that are achieved from this investigation:

Various multi–phase turbulence models available in ANYSY FLUENT 12.1 are applicable to low liquid loading. These models include three high Reynolds number k–ε models which are standard k–ε, RNG k–ε, and realizable k–ε, and are utilized to examine the pressure drop in a horizontal pipe. It was found that the RNG k–ε model is the most appropriate model to predict the pressure drop in comparison with the experimental data that is available in the literature, and the existing models of Hart *et al*. (1989) and Chen *et al*. (1997). Moreover, a new drag coefficient has been implemented to account for the drag on a droplet by using the Ishii and Chawla (1979) expression. There is good quantitative agreement with the experimental data with the Renormalization Group (RNG) k–ε model for different superficial gas velocity and a wide range of superficial water velocities. It was observed that the pressure gradient increased with the system parameters, such as the drop size, water and gas superficial velocity and the water volume fraction.

The liquid holdup decreased with respect to gas mass flux/superficial velocity, but increased with the water mass flux/superficial velocity. The deviation of pressure gradient and liquid holdup obtained throughout the CFD simulation with respect to the experimental data (Badie *et al*., 2000) was found to be relatively small at low superficial gas velocities. Furthermore, when the two empirical correlations that have been examined (Beggs and Brill (1973), and Mukherjee and Brill (1985)) against the CFD simulation results of pressure drop and liquid holdup, it was noted that they gave closer agreement with the air–oil system rather than the air–water system, but shows reasonable agreement over the entire gas mass flux/superficial velocity.

The pressure drop data for air–water was found to be much higher than for air–oil systems. This is due to the viscosity difference. It can be concluded that the CFD simulation, which is more efficient and economic, can be employed as an alternative to the empirical correlation to obtain the pressure gradient and liquid holdup in two–

phase flow in horizontal pipelines. It is recommended that further investigation of the pressure drop and liquid holdup prediction be conducted by using a population balance equation that takes into account the droplet breakage and coalescence.

5.14 Bibliography

ANSYS-FLUENT Inc (2008). FLUENT 12.0, ANSYS-FLUENT Inc, Lebanon, N.H.

Badie, S., C. P. Hale, C. J. Lawrence and G. F. Hewitt (2000). Pressure gradient and holdup in horizontal two phase gas-liquid flows with low liquid loading. *International Journal of Multiphase Flow*, 26, 1525-1543.

Beggs, H. D. and J. P. Brill (1973). A study of two–phase flow in inclined pipes. *Journal of Petroleum Technology*, 25, 607-617.

Bel Fdhila, R'Bei (1991). "Analyse experimentale et modeelisation d'un ecoulement vertical a bulles un elargissement brusque", PhD thesis, L'Institute National Polytechnique de Tolouse, Tolouse, France.

Cawkwell, M. G. and M. E. Charles (1985). Pressure, temperature predicted for two-phase pipelines. *Oil and Gas Journal*, 85, 101-107.

Chen, X. T., X. D. Cai and J. P. Brill (1997). Gas–liquid stratified-wavy flow in horizontal pipelines. *Journal Energy Resources Technol*ogy, 119(2), 209-216.

Chhabra, R. P., S. I. Farooqi and J. F. Richardson (1984). Isothermal Two Phase Flow of Air and Aqueous Polymer Solutions in a Smooth Horizontal Pipe. *Chemical Engineering Research Design*, 62, 22-32.

Chisholm D. (1967). A theoretical basis for the Lockhart-Martinelli correlation for two-phase flow. *International Journal of Heat Mass Transfer*, 10, 1767-1778.

Choudhury, D. (1993). Introduction to the renormalization group method and turbulence modelling. FLUENT Inc. Technical memorandum TM-107.

Fan, Y., Q. Wang, H. Zhang, C. Sarica and T. J. Danielson (2005). A model to predict liquid holdup and pressure gradient of near-horizontal wet-gas pipelines. *The SPE Annual Technical Conference and Exhibition*, Dallas, Texas, 9-12 October.

Ghorai, S. and K. D. P. Nigam (2006). CFD modeling of flow profiles and interfacial phenomena in two-phase flow in pipes. *Chemical Engineering and Processing*, 45(1), 55-65.

Grossetete, C. (1995). "Caraterisation experimentale et simulations de l'evolution d'un ecoulemnt diphasique a bulles ascendant dans un conduite verticale", Collection de notes internes de la Direction des Études et Recherches. Electricité de France.

Hart, J., P. J. Hamersma and J. M. H. Fortuin (1989). Correlations predicting frictional pressure drop and liquid holdup during horizontal gas-liquid pipe flow with a small liquid holdup. *International Journal of Multiphase Flow*, 15(5), 947-964.

Ishii, M. and T. C. Chawla (1979). Local drag laws in dispersed two-phase flow. NUREG/CR-1230, ANL-79-105.

Issa, R. I. (1988). Prediction of turbulent, stratified, two-phase flow in inclined pipes and channels. *International Journal of Multiphase Flow*, 14(1), 141-154.

Kader, B. A. (1981). Temperature and concentration profiles in fully turbulent boundary layers. *International Journal of Heat and Mass Transfer*, 24(9), 1541-1544.

Lahey Jr., R.T., M. Lopez de Bertodano and O.C. Jones Jr. (1993), "Phase distribution phenomena in complex geometry conduits", *Nuclear Eng. and Design*, 141, 177-201.

Lockhart, R. W. and R. C. Martinelli (1949). Proposed correlation of data for isothermal two-phase, two-component flow in pipes. *Chemical Engineering Progress*, 45(1), 39-48.

Mukherjee, H. and J. P. Brill (1985). Pressure drop correlation for inclined two–phase flow. *Journal of Energy Resources Technology*, 107, 549-554.

Newton, C. H. and M. Behnia (1998). Numerical calculation of turbulent stratified gas-liquid pipe flows. *International Journal of Multiphase Flow*, 24(5), 327-337.

Olive, N. R., H. -Q. Zhang, Q. Wang, C. L. Redus and J. P. Brill (2003). Experimental study of low liquid loading gas–liquid flow in near-horizontal pipes. *Journal of Energy Resources Technol*ogy, 125, 293-298.

Roscoe, R. and J. Brit (1952). *Applied Physics*, 3, 267-269.

Shoham, O. and Y. Taitel (1984). Stratified turbulent-turbulent gas-liquid flow in horizontal and inclined pipes, *AIChE Journal*, 30(2), 377-385.

Taitel, Y. and A. E. Dukler (1976). Model for predicting flow regime transitions in horizontal and near horizontal gas–liquid flow. *AIChE Journal*, 22, 47-55.

Vlachos, N. A., S. A. Paras and A. J. Karabelas (1999). Prediction of holdup, axial pressure gradient and wall shear stress in wavy stratified and stratified/atomisation gas/liquid flow. *International Journal of Multiphase Flow*, 25(3), 365-376.

Wang, S.K.,S.J. Lee, J. Jones, O. C. and J. Lahey, R. T., "3-D Turbulence Structure and Phase Distribution Measurements in Bubbly Two-Phase Flows", *Int. J. Multiphase Flow*,13, 327-343 (1987).

Chapter 6

Prediction of System Parameters and Drop Size Distribution using CFD and Population Balance Equation

In the present Chapter, numerical aspects of the coupling between the population of droplets and the surrounding fluid are exposed. This contribution focuses on the combined Computational Fluid Dynamics (CFD) and Droplet Population Balance Model (DPBM), where the DPBM is solved as part of the CFD code.

The droplet population balance equations are solved by the Quadrature Method of Moments (QMOM). The droplet size distribution in gas–liquid air–water horizontal co–current annular flow is investigated through a CFD–PBM coupled model. Also the pressure drop and liquid holdup are obtained and compared with k–ε model of constant droplet size (presented in Chapter 5) and with an empirical correlation. The Eulerian–Eulerian k–ε approach is utilized as the framework of this model, and the population balance equation is used to obtain the dispersed liquid droplet diameter distribution where the droplet size distribution is investigated in different pipe sizes of 0.0953 and 0.078 m inside diameter. The Turbulent coalescence kernel and Luo's breakup kernel are used in this investigation.

6.1 Introduction

A number of different flow regimes can exist for the simultaneous co–current of two–phase flow in a pipeline. In the transport of two–phase gas–liquid mixtures in a conduit with a small amount of liquid, the expected flow pattern is characterized by a wavy interface and drops in the core phase (gas). In this situation, the dynamics of the film and the liquid droplets is significant in obtaining the pressure drop and liquid holdup in the conduit (Fore and Dukler, 1995; Simmons and Hanratty, 2001).

The most common flow is annular flow, which can take place at all pipe inclination angles, and the liquid fraction carried as droplets can differ from zero to one. Droplets deposit on the wall and form some waves that exist on the liquid film while some droplets are entrained in the core phase (gas). For a fully developed flow, the liquid entrained fraction as droplets is illustrated as a balance between the two mechanism rates of atomisation and deposition. The prediction of such phenomena requires knowledge of the distribution of droplet sizes in the gas phase (Simmons and Hanratty, 2001).

The measurement of droplet size in annular flows has been studied by Azzopardi (1997). Different techniques have been used to find the droplet size distribution. Tatterson *et al*. (1977) utilized charge removal from an insulated probe. Wicks and Dukler (1966) employed a needle bridging technique in which two needles were placed at a small distance apart and connected to a battery and a resistance. The droplets larger than the gap completed the circuit and led to an electrical pulse. By changing the needle gap, the cumulative size distribution was obtained. Semiat and Dukler (1981) and Lopes and Dukler (1985) utilized a laser grating technique that generated a local measurement of velocity and droplet size.

The previous techniques were unable to detect small droplets lower than 100 μm. Therefore, further work has demonstrated that these techniques cause significant error in measuring the volume median size since a significant proportion of the volume is carried by small drops with a diameter less than 100 μm. Further refinements were

made to the laser–grating technique by Fore and Duker (1995). These allowed the measurement of very small droplet sizes such as 10 μm.

Several measurement techniques which have been used to obtain the droplet size distribution in horizontal and vertical pipes can be found in Simmon and Hanratty (2001). For numerical studies, this type of flow pattern (annular) in the horizontal pipe has received less attention in the literature than other flows such as bubbly flow, even though this flow is very common in industrial processes such as the transport of hydrocarbons. Some of the numerical studies that have been conducted in a horizontal pipe, for example: Ekambara *et al*. (2008) have employed the two–phase Multiple Size Group (MUSIG) model to study the internal phase size distribution of horizontal bubbly flow. In this model, the continuous bubble size distribution is divided into a series number of discrete size classes.

The mass conservation of each class fraction is balanced using source terms that describe the inter–fraction mass transfer as a result of bubble coalescence and breakage processes. Typically, the MUSIG model requires considerable computational time and resources in order to obtain accurate numerical predictions for system parameters and size distribution. Dorao *et al*. (2009) have investigated numerically the evolution of the droplet size distribution by modelling the interaction between the droplet and the film based on the statistical method resembling the population balance equation. They found the distribution of droplet size and a liquid film are strongly based on entrainment and deposition processes. The numerical experiments are demonstrated and show the modelling framework principles.

Li *et al*. (2010) have examined the performance of population balance models using Average Bubble Number Density technique to predict the phase size distribution, avoid fraction, interfacial area concentration, and superficial velocity of two–phase air–water flows in a horizontal pipe. The results obtained have achieved agreement with the experimental data, but with some inconsistency at specific locations of the pipe as a result of the insufficient resolution of the turbulent model. They have

concluded that some challenging issues still need to be addressed in order to improve the prediction parameters of gas–liquid bubbly flow in a horizontal conduit.

This Chapter presents the population balance equation and the available techniques to solve it, and also demonstrates the available coalescence and breakage kernels. Furthermore, the droplet size distribution in gas–liquid horizontal co–current annular flow is investigated through a CFD in conjunction with population balance model (PBM) coupled model. A two fluid Eulerian approach is used as the framework of this model and a population balance equation is used to obtain the dispersed liquid droplet diameter distribution, pressure drop and liquid holdup of two–phase. Turbulent and Luo models for coalescence and breakup kernels are utilized in this study.

6.2 Population Balance Equation

In practice, during two–phase flow applications, droplets can break and aggregate due to droplet–droplet and droplet–fluid interactions. Under these circumstances, a constant droplet size model might not be suitable for predicting the correct thermo–fluid dynamics of the gas–liquid two–phase flow. A single droplet size model cannot properly describe the interfacial interactions that take place between the phases, such as the mass and heat transfer and interfacial forces. Therefore, in order to develop the system design and optimization, depending on droplet–film interactions, new simulation tools are needed to take into account the evolution of the droplet size distribution resulting from breakage and aggregation or coalescence phenomena in two–phase flows. Typically, this can be performed using the population balance modelling framework for illustrating the populations' evolution of entities (i.e. droplet, bubble, or particle).

Usually, population balances are encountered in a number of scientific and engineering disciplines. They are used to study crystallization, polymerization, precipitation, food processes, particle size distribution (PSD) of crushed material or dispersed liquid and rain drop formation etc. Although there are a few cases in which the analytical solutions of population balance equations are available, numerical

techniques are important in most practical applications. Such techniques are required to be accurate and with a relatively low computational cost.

There are many numerical approaches available which satisfy the accuracy requirement. Some of these methods are the Monte Carlo method (Smith 1998b, Ramkrishna 2000), the methods of classes (CM) (Batterham *et al*. 1981, Hounslow *et al*. 1988, Lister *et al*. 1995, Kumar and Ramkrishna 1996a, Kumar and Ramkrishna 1996b, Vanni 2000, Ramkrishna 2000), the Quadrature method of moments (QMOM) (McGraw 1997, McGraw and Wright 2003, Marchisio *et al*. 2003b, Marchisio *et al*. 2003a), the direct quadrature method of moments (DQMOM) (Fan *et al*. 2004, Marchisio and Fox 2005) and, in some simple cases, the standard method of moments (SMM)). A review of population balance approaches applicable to CFD can be found in Jakobsen *et al*. (2005).

The population balance equation (PBE) is a simple continuity statement. It can be derived as a balance for droplets in some fixed subregion of internal–coordinate and physical space. Based on the population balance method, the dispersed phase is expressed for a density function n (ζ, r, t) where ζ is the property of dispersed phase (i.e. volume, area, mass), r is the spatial vector position, and t is the time. The population balance equation can be written as (Ramkrishna, 2000):

$$\left.\begin{aligned}&\underbrace{\frac{\partial f(\zeta;r.t)}{\partial t}}_{accumulation}+\underbrace{\nabla_{r}.[u(\zeta;r,t)f(\zeta;r,t)]}_{convection}+\underbrace{\nabla_{\xi}.\left[\dot{\zeta}(\zeta;r,t)f(\zeta;r,t)\right]}_{growthrate}=\\&\underbrace{H_{B,a}(f,\zeta;r,t)}_{Birthdueto\ aggregation}+\underbrace{H_{D,a}(f,\zeta;r,t)}_{Dearthduetoaggregation}+\underbrace{H_{B,b}(f,\zeta;r,t)}_{Birthdueto\ breakup}+\underbrace{H_{D,b}(f,\zeta;r,t)}_{Deathdueto\ breakup}\end{aligned}\right\} \quad (6.1)$$

where ζ represents the internal coordinate space vector whose terms might be described by surface area, volume etc, while r indicates the divergence in the physical space or external space. The first and second terms on the right hand side of the Equation (6.1) accounts for birth and death events related to coalescence processes; the third and fourth terms account for birth and death events due to breakage processes.

By assuming that the volume of the particles is the only internal coordinate, the field is homogeneous and the internal coordinate is time independent. Equation (6.1) can be written as:

$$\frac{\partial f(v;t)}{\partial t} = H_{B,a}(f,v;t) + H_{D,a}(f,v;t) + H_{B,b}(f,v;t) + H_{D,b}(f,v;t) \tag{6.2}$$

The source and sink terms on the right hand side can be modeled as:

$$\left.\begin{aligned} H_{B,a}(f,v;t) &= \frac{1}{2}\int_0^v a(v-v',v')f(v-v',t)f(v',t)dv' \\ H_{D,a}(f,v;t) &= -f(v,t)\int_0^\infty a(v,v')f(v',t)dv' \\ H_{B,b}(f,v;t) &= \int_v^\infty \gamma(v')b(v')p(v/v')f(v',t)dv' \\ H_{D,b}(f,v;t) &= -b(v)f(v,t) \end{aligned}\right\} \tag{6.3}$$

where a (v,v') is the coalescence rate between droplets of size v and v'; b (v) is the breakup rate of droplets of size v; $\gamma(v')$ represents the number of fragments, or daughter droplets, generated from the breakup of a droplet of size v' and $p\ (v/v')$ is the probability density function for a droplet of size v to be generated by the breakup of a droplet of size v'. Then, $p\ (v/v')\ dv$ is the fraction of daughter droplets having a size between v and $v + dv$, generated by the breakup of droplets of size v'.

The moments of the droplet size distribution are defined as:

$$m^{(k)}(t) = \int_0^\infty f(v;t)v^k dv \tag{6.4}$$

The moments give important statistical descriptions on the population. The zero order moment ($k = 0$) represents the total number density of the population; the first order moment ($k = 1$) is the total mass per unit of volume of the population, and the

fractional moments, k = 1/3 and k = 2/3 gives information on the mean diameter and on the mean surface area, respectively.

6.3 Closure Models for Coalescence and Breakage

6.3.1 Breakage Models

The breakage rate expression consists of the breakage frequency g, that describes the droplets splitting function per unit of time and the probability density function (PDF) β, which represents the distribution of the daughter droplets from the splitting mother particle (Christian *et al*., 2009):

$$g(v')\beta(v|v') \tag{6.5}$$

Different models of breakage rate of droplets or bubbles are developed by several authors (Alopaeus *et al*., 2002, Coulaloglou and Tavlarides, 1977; Hagesaether *et al*., 2002; Lehr *et al*., 2002; Luo and Svendsen, 1996; Martínez–Bazán *et al*., 1999a; Prince and Blanch, 1990; Andersson and Andersson, 2006a). The breakage expression accounts for the interaction of a single drop with the turbulent continuous phase in which the droplet undertakes breakage if the turbulent kinetic energy transmitted to the droplet is higher than its surface energy (Coulaloglou and Tavlarides, 1977).

In most models, the researchers made an assumption that droplet or bubble deformation and breakup occurs under the influence of local pressure fluctuations in a locally isotropic flow field, or on the arrival of turbulent eddies to the surface of the droplets. The new droplet diameter is mainly dependent on the turbulent energy dissipation. To obtain the daughter droplet distribution, it is necessary to specify the number of daughter droplets. Valentas *et al*. (1966) utilised a normal density function for the daughter droplet distribution that assumes binary breakage.

As an alternative to using the binary breakup assumptions in the other models, a beta distribution by Bahmanyar *et al*. (1991) can illustrate more than two daughter droplets. Other PDFs are developed by Martínez–Bazán et al. (1999b) or Diemer and

Olson (2002). Binary breakup is more appropriate for bubbles but usually not for droplets in which more than two daughter droplets are formed (Schmidt, 2006). A review of daughter size distributions and breakage models in the literature can be found in Wang *et al*. (2003) and in Lasheras *et al*. (2002). The experimental investigation and modelling of breakage phenomena and daughter droplet or bubble distribution in gas–liquid and liquid–liquid two–phase flow systems is a current research area (Andersson and Andersson, 2006b; Eastwood *et al*., 2004; Maaß *et al*., 2007; Maaß *et al*., 2009; Vankova et al., 2007).

6.3.2 Coalescence Models

The process of droplet coalescence takes place due to the interaction between two droplets and the turbulent continuous phase. The coalescence process among the droplets is expected to occur if the intervening liquid film has sufficient contact time to be drained out (Chatzi and Lee, 1987). The coalescence source expressions take into account the aggregation kernel that considers the probability of successful collisions between two droplets (v and v'). It is usually explained as the result of two quantities, which are the collision frequency h and the coalescence efficiency λ.

$$a(v, v') = h(v, v') \times \lambda(v, v') \tag{6.6}$$

Most of the models are based on the assumption of film drainage (Coulaloglou and Tavlarides, 1977; Chesters, 1991; Luo (1993), Prince and Blanch (1990), Tsouris and Tavlarides, 1994). Other methods replaced the film drainage by using a mechanism derived from the effect of the collision impact (Sovová, 1981) but could not achieve acceptance. The influence of mass transfer is generally neglected while the droplet–droplet coalescence is very sensitive to changes in local chemical composition (Simon and Bart, 2002). Therefore, coalescence phenomena are complicated to tackle, and there are only a few models in the literature that have a predictive character.

The coalescence mechanism in gas–liquid systems was not fully understood until recently and is still an important research topic (Eiswirth and Bart, 2008; Henschke *et*

al., 2002; Simon, 2004; Tobin and Ramkrishna, 1999). Some of the well known models, which are available in the literature, such as Coulaloglou and Tavlarides (1977), Luo and Svendsen (1996), Martínez–Bazán *et al*. (1999) and Prince and Blanch (1990), where the Luo and Svendsen (1996) model was applied in this study.

6.4 Numerical Techniques

Analytical solutions of PBEs were presented in some cases where the coalescence and breakup kernels have a simple form and when the particle size distribution (PSD) has a specific initial shape (Scott 1968, McCoy and Madras 2003). In some situations the analytical solution of the PSD is available, but some properties of the PSD, such as mean diameter and mean surface area, are derived using numerical integration of the analytical solution. This method computationally is more expensive than solving the PBE via discretisation approaches. Nevertheless, the analytical solutions can be a valuable source for validating and testing numerical techniques; it can also be validated against experimental data, which is considered the easiest way for validation.

In industrial applications of practical interest, numerical methods are needed to solve the PBE. The most common techniques employed are the methods of Classes, the methods of moments, and the Monte Carlo method. Therefore, the three most common techniques that are available in the CFD application: the standard methods of moments (SMM), the quadrature method of moments (QMOM), and the discrete method (DM), will be reviewed.

6.4.1 The Discrete Method

The discrete technique is also called the classes or sectional method, and was developed by Hounslow *et al*. (1988), Litster *et al*. (1995), and Ramkrishna (2000). In the discrete technique, the entity population (i.e. droplet, bubble or particle) is discretised into a finite number of size intervals, which describe a set of discrete size classes or bins. The benefit of this method is robust numerics that lead to discovering the particle size distribution (PSD) directly. This approach is more valuable when the

range of particle sizes is identified before and does not span more than two or three orders of magnitude. In this situation, the particle population can be discretised by a small number of size intervals and the size distribution, which is combined with fluid dynamics can be obtained. On the other hand, the disadvantage of this method is that it is computationally expensive when using a large number of intervals or bins that must be identified.

The population balance equation (6.1) can be written in terms of droplet size (v) and volume fraction excluding the growth and nucleation processes.

$$\frac{\partial}{\partial t}(\rho_w \alpha_v) + \nabla.(\rho_w u_v \alpha_v) = \rho_w V_v (B_{B,v} - D_{B,v} + B_{D,v} - D_{D,v}) \tag{6.7}$$

where ρ_w is the density of water phase and the α_v is the volume fraction of droplet size (v), expressed as:

$$\alpha_v = N_v V_v \qquad \text{where } v = 0, 1, \ldots N-1 \tag{6.8}$$

$$N_v(t) = \int_{V_v}^{V_{v+1}} n(V,t)dV \tag{6.9}$$

V_v is the volume fraction of droplet size v. The droplet birth and death rates are described as follows:

$$B_{B,v} = \sum_{v''=1}^{N} \sum_{v'=1}^{N} a_{v''v'} N_{v''} N_{v'} x_{v''v'} \zeta_{v''v'} \tag{6.10}$$

$$D_{B,v} = \sum_{v'=1}^{N} a_{vv'} N_v N_{v'} \tag{6.11}$$

$$B_{D,v} = \sum_{v'=v+1}^{N} k(V_{v'}) N_{v'} \beta(V_v | V_{v'}) \tag{6.12}$$

$$D_{D,v} = k(V_v) N_v \tag{6.13}$$

6.4.2 The Standard Method of Moments

The standard method of moments (SMM) is an effective approach compared to the discrete population balance approach. The SMM was developed by Randolph and Larson (1971); it is an alternative method for solving the population balance equation. In this method, the population balance equation is described via a set of transport equations that represent the moments of the distribution. The *i*th moment is identified by coupling the number density of the entire particle space weighted with the particle property raised to its *i*th power.

It is usually sufficient to solve only a few equations of moment, usually between three to six equations. This can significantly reduce the number of equations to be solved in contrast with the discretised technique. The advantage of this approach is valuable when the entire distribution is not required to be presented and certain average and total quantities are sufficient to characterize the particle distribution. In general, the first four moments are the most commonly used where the zeroth moment describes the total number density, the second moment describes the total surface area per unit volume, and the third moment signifies the total mass density. The disadvantages of this approach are that exact closure of the right–hand side of Equation (6.1) is possible only in cases of constant aggregation and size–independent growth, and that breakage modelling is difficult.

In the SMM approach, assumptions about the size distribution are not needed, and the moment equations are described with a formula that is created in a closed form including only the moment's functions. Nonetheless, the requirement of this exact closure leads to a serious constraint, where the aggregation term (with the exception

of the constant aggregation kernel) and breakage phenomena cannot be described as functions of moments.

The SMM method is derived from taking moments of the PBE with respect to the internal coordinate of the entity (i.e. M is droplet size). For the homogeneous system, the ith moment can be written as:

$$m_k(t) = \int_0^\infty M^k n(M;t) dM \tag{6.14}$$

The first four moments ($k \in$ 0, 1, 2, 3) m_0, m_1, m_2, m_3 are the most significant as mentioned earlier, since they are related to the total number density, the total length, the total surface area per unit volume, and the total volume density, respectively. Furthermore, these quantities can be used in this approach to find out the mean droplet size that can be defined as follows:

$$N_{total} = m_0 \tag{6.15}$$

$$L_{total} = m_1 \tag{6.16}$$

$$A_{total} = K_a m_2 \tag{6.17}$$

$$V_{total} = K_v m_3 \tag{6.18}$$

$$d_{32} = \frac{m_3}{m_2} \tag{6.19}$$

6.4.3 The Quadrature Method of Moments

The quadrature method of moments (QMOM) was developed by McGraw (1997) when he studied the growth of size–dependence in aerosols. Later it used for aggregation problems by Barrett and Webb (1998). Wright *et al*. (2002) have also

developed a QMOM approach to treat a bivariate aerosol distribution. Furthermore, the approach was developed for aggregation–breakage processes by Marchisio (2003a, 2003c). This method has a similar advantage compare to the SMM in terms of computational costs, but replaces the exact closure needed by SMM with an approximate closure. This leads to employing the QMOM approach in a wide range of applications with no limitations. On the other hand, the QMOM approach has a disadvantage in that it may destroy the shape of the distribution, and information regarding the distribution is only stored in its moments. The *i*th moment is described by integrating the function of population number density with respect to specific population property, such as droplet sizes, weighted with this property raised to its *i*th power. The *k*th moment can be then identified as:

$$m_k(x,t) = \int_0^\infty n(L,x,t)L^k dL \tag{6.20}$$

where L represents the droplet size. When i is equal to zero, it means the zero moment, which signifies the total number of particles per unit volume, and when the value of i is equal to three the third moment describing the volume fraction (volume concentration) of the entities (droplet, bubble, or particle). The QMOM tracks the population moments, for instance the zero and third moments, instead of its size. Therefore, it is not based on the minimum and maximum particle sizes; it depends on the Product–Difference algorithm to obtain weights and abscissas from the moments that needs the solution of an eigenvalue problem in terms of the population low order moments.

6.5 Mathematical Modelling

The aim of this investigation is to obtain complete information on the droplet size distribution and system parameters of two–phase air–water flow in three–dimensional horizontal pipes. As mentioned in Chapter 3, multiphase CFD models are considered significant tools that can be used for different chemical and mineral processes. Such a method utilizes numerical techniques for solving the conservation equations for a

given flow geometry and boundary conditions. Therefore, using the CFD coupled with a population balance model for capturing phenomena such as interface interactions, turbulence for heat and mass transfer, and momentum is seen as relevant for the particular problem. The governing equations of the flow and the population balance terms of the coalescence and break–up kernels are described in detail in the following sections.

6.5.1 Mass Conservation Equation

The numerical simulation is based on the concept of the two fluids Eulerian–Eulerian model that is derived from the ensemble–average mass and momentum transport equations for each fluid. The gas phase is considered as a continuum and the liquid phase (droplets) as the dispersed phase, these equations can be expressed without the interface mass transfer as follows:

Continuity equation of the gas phase:

$$\frac{\partial}{\partial t}(\rho_g \alpha_g) + \nabla.(\rho_g \alpha_g u_g) = 0 \tag{6.21}$$

Continuity equation of the liquid phase:

$$\frac{\partial}{\partial t}(\rho_l \alpha_l f_i) + \nabla.(\rho_l \alpha_l u_l f_i) = S_i \tag{6.22}$$

where f_i is the volume fraction of droplets of group i ($f_i = \alpha_{li} / \alpha_l$) and S_i is the source term, which accounts for the death and birth of droplets as a result of coalescence and breakage processes. Based on the assumption that is given in Chapter 5 that there is no mass transfer between two–phase, the term of S_i is equal to zero at constant and uniform droplet size, but in this situation of coalescence and breakage, S_i term can be computed as:

$$S_i = B_i^B + B_i^C - D_i^B - D_i^C \qquad \text{where } i = 1, 2, \ldots\ldots, N \tag{6.23}$$

The terms on the right side of the equation $B_i^B, B_i^C, D_i^B,$ and D_i^C represent the birth and death due to breakage and coalescence of droplets, respectively. The birth and death rate of droplets due to the coalescence and breakage can be written as:

$$\left.\begin{aligned} B_i^C &= \frac{1}{2}\int_0^V a(v-v',v')n(v-v')n(v')dv' \\ D_i^C &= \int_0^\infty a(v,v')n(v)n(v')dv' \\ B_i^B &= \int_{\Omega_v} pg(v')\beta(v/v')n(v')dv' \\ D_i^B &= g(v)n(v) \end{aligned}\right\} \tag{6.24}$$

The droplet number density n (v) is described as the droplet volume fraction using the following formula:

$$\alpha_l f_i = n_i V_i \tag{6.25}$$

where V_i expresses the droplet volume fraction of group i. It is necessary to provide a model that describes each of these phenomena of coalescence and breakage. The breakage of droplets in turbulent dispersions used a model developed by Luo and Svendsen (1996). They assumed the breakage of droplets is binary and the model is derived from the isotropic turbulence theories. The droplet breakage rate of volume v into volume size of v' can be found as:

$$\frac{\Omega(v,v')}{(1-\alpha_l)n_j} = C\left(\frac{\varepsilon}{d_j^2}\right)^{1/3}\int_{\zeta_{\min}}^1 \frac{(1+\zeta)^2}{\zeta^{11/3}}\exp\left(\frac{12c_f\sigma}{\beta\rho_g\varepsilon^{2/3}d_j^{5/3}\zeta^{11/3}}\right)d\zeta \tag{6.26}$$

$$c_f = f^{2/3} + (1-f)^{2/3} - 1 \tag{6.27}$$

where:

ε	= the energy dissipation rate per unit of gas mass
ζ	= the size ratio between a particle and an eddy in the inertial sub–range
C and β	= empirical constants 0.923 and 2.0, respectively, and are based on droplet breakage in a turbulent dispersion system
c_f	= the increase coefficient of surface area
f	= the breakage volume fraction

The coalescence of two–droplet is modelled using the turbulent model. The coalescence process can take place via two methods that are viscous and inertial subrange mechanisms. The viscous subrange mechanism is used when the particles sizes are smaller than the Kolmogorov microscale. The collision rate of particles is influenced by the local shear within the eddy, it is expressed by the Saffman and Turner (1956) developed relation that can be written as:

$$a(L_i, L_j) = \varsigma_T \sqrt{\frac{8\pi}{15}} \dot{\gamma} \frac{(L_i + L_j)^3}{8} \tag{6.28}$$

$$\dot{\gamma} = \frac{\varepsilon^{0.5}}{\upsilon} \tag{6.29}$$

where ς_T and $\dot{\gamma}$ represent the pre–factor which accounts for the capture efficiency coefficient of turbulent collision, and the shear rate, respectively.

The second mechanism of inertial subrange applies in the case where particle sizes are bigger than the Kolmogorov microscale or smallest eddy. Therefore, they are dragged via the velocity fluctuations in the flow field. In this situation, the aggregation rate is described by Abrahamson's model (1975):

$$a(L_i, L_j) = \varsigma_T 2^{3/2} \sqrt{\pi} \frac{(L_i + L_j)^2}{4} \sqrt{U_i^2 + U_j^2} \tag{6.30}$$

where U_i and U_j are the mean velocity of particle *i* and *j*, respectively.

Higshitani *et al*. (1968) developed relationship for the empirical capture efficiency coefficient of turbulent collision, which demonstrates the hydrodynamic and attractive interaction between colliding particles. It can be written as follows:

$$\varsigma_T = 0.732\left(\frac{5}{N_T}\right)^{0.242} \quad ; N_T \geq 5 \tag{6.31}$$

where N_T describes the ratio between the Van der Waals and the viscous forces, it can be expressed as:

$$N_T = \frac{6\pi\mu(L_i + L_j)^3\,\dot{\lambda}}{8H} \tag{6.32}$$

$$\dot{\lambda} = \sqrt{\frac{4\varepsilon}{15\pi\upsilon}} \tag{6.33}$$

where H and $\dot{\lambda}$ are the Hamaker constant and the deformation rate, respectively.

6.5.2 Momentum Transfer Equations

The momentum conservation of multiphase flows can be described using the volume averaged momentum equation as follows:

$$\frac{\partial}{\partial t}(\rho_g\alpha_g u_g) + \nabla.(\rho_g\alpha_g u_g u_g) = -\alpha_g\nabla p + \rho_g\alpha_g g - \nabla(\alpha_g\tau_g) + F_{gl} \tag{6.34}$$

where:

u_g = the volume averaged velocity vector

p = the pressure

g = the gravity

τ_g = the phase shear stress tensor

F_{gl} = the interface force term between gas and liquid phases

The right hand side expression of Equation (6.34) demonstrates the forces which are acting on the gas phase. These forces include the pressure gradient, gravity, the viscous stress term and the interface momentum forces. The pressure is equally identified in each phase and the effective viscosity of the viscous stress term includes the laminar viscosity and turbulent component in the turbulence situation. The only interfacial force considered between the two phases could arise from the drag force in which other forces are neglected. The cause of drag force is due to the resistance that is generated by the movement of the body in the gas fluid. Viscous stress produces skin drag and pressure distribution around the travelling body leading to create a form drag. The drag force expression can be described in the following form:

$$F_D = \frac{3}{4d_d} C_D \alpha_d \rho_c |u_c - u_d|(u_c - u_d) \tag{6.35}$$

where d_p and C_D are the droplet diameter and the drag coefficient accounts for the character of the flow around the droplets, respectively. The drag coefficient has been modelled using the same expression of the Ishii and Chawla (1976) drag model that is used in Chapter 5.

6.5.3 Turbulence Equations

Turbulence that is generated by the continuous phase is taken into consideration. The very common single–phase turbulence models are typically utilized to model the gas phase turbulence in Eulerian–Eulerian multiphase simulations. In the current study the RNG k–ε model developed by Choudhury (1993) is employed. The governing equations for kinetic energy and turbulent dissipation terms are expressed by the following equations:

$$\frac{\partial}{\partial t}(\rho k)+\frac{\partial}{\partial x_i}(\rho k u_i)=\frac{\partial}{\partial x}\left(\alpha_k \mu_e \frac{\partial k}{\partial x_i}\right)+G_k+G_b-\rho\varepsilon-\mathrm{Y}_m+S_k \tag{6.36}$$

$$\frac{\partial}{\partial t}(\rho\varepsilon)+\frac{\partial}{\partial x_i}(\rho\varepsilon u_i)=\frac{\partial}{\partial x_j}\left(\alpha_\varepsilon \mu_e \frac{\partial \varepsilon}{\partial x_j}\right)+C_{1\varepsilon}\frac{\varepsilon}{k}(G_k+C_{3\varepsilon}G_b)-\frac{\mathrm{C}^*_{2\varepsilon}\rho\varepsilon^2}{k} \tag{6.37}$$

where $C_{1\varepsilon}$ and $C_{2\varepsilon}$ are the RNG k–ε model constants, which are equal to 1.42, and 1.68, respectively (FLUENT Inc. 2008).

6.6 Method of Solution

The first case of simulation was performed in a three–dimensional horizontal pipe with dimensions of 0.0953 m ID and 10 m long to examine the CFD–PBM model for the prediction of drop size distribution and validate that against the experimental data of Simmons and Hanratty (2001). The rest of the simulations were conducted in the same pipe size that is used in Chapter 5. The gas phase (air) was considered as a continuous phase and the liquid phase (water) was considered as a dispersed phase. For the description of the population balances in the present case the QMOM was chosen for modelling the drop size distribution where the droplet size ranged from 10–1000 μm.

For the boundary conditions the general method with velocity-inlet at the inlet and pressure outlet condition at the outlet were applied, but the volume fraction of the dispersed phase at the inlet was assumed. The surfaces of the upper and the bottom pipe wall were defined with no–slip wall boundary conditions. All flow conditions at the inlet were similar to the experiments (Simmons and Hanratty, 2001). The 3D mesh obtained thus included approximately 936,000 tetrahedral cells.

The computational grid is shown in Figure (6.1). Enhanced wall treatment modeled the near wall region. The simulations were performed unsteady where the time step was chosen as 0.001 seconds and is found to be sufficient to produce results independent of the choice of time step and thus utilized here.

Unsteady simulations were carried out using the first order implicit solver which was adopted to achieve the final solution in this study. The solution of the above equations was performed in the commercial CFD package ANSYS FLUENT 12.1 coupled with the population balance model. For the discretisation in space first order upwind schemes were utilized for momentum, turbulent kinetic energy, turbulent dissipation rate, and liquid moment and the QUICK scheme was used for the volume fraction. The simple algorithm was employed for the pressure–velocity coupling. For the under–relaxation factors, standard values were used without modification except that the momentum 0.05 was used.

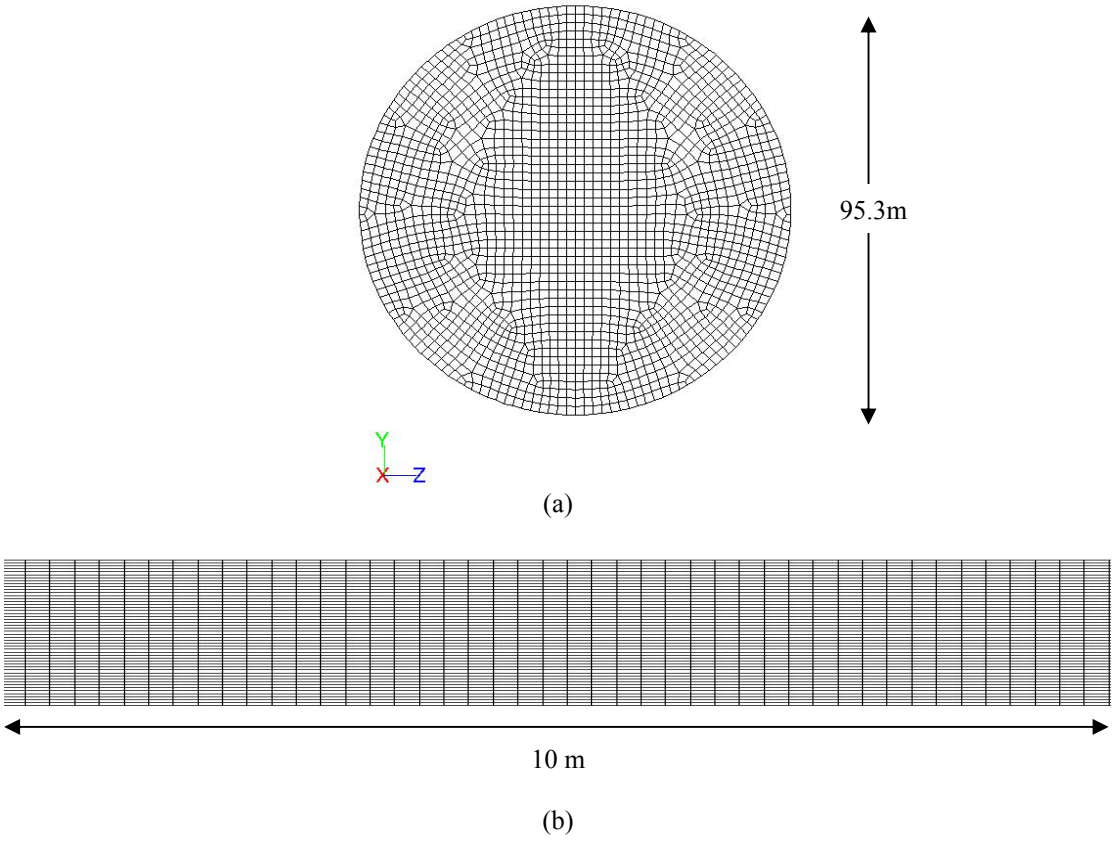

Figure 6.1: computational grid (a) inlet and (b) horizontal view.

6.7 Results and Discussion

6.7.1 Comparing CFD–PBM Model with an Experimental Data

The droplet size distribution is the focus of this section where the simulation results for the air–water two–phase flow in a horizontal pipeline and the operating conditions carried out by Simmons and Hanratty (2001) are presented for two cases. In the first case the gas and liquid superficial velocities are 36 and 0.041 m/s and the second case gas superficial velocity was increased to 50 m/s and the liquid superficial velocity kept constant.

The simulations conducted by the QMOM approach for solving the population balance equation used the first four moments. Fixed time steps were used for the simulations. The droplet distributions and a comparison with the experimental data are demonstrated. Figure (6.2) illustrates the droplet size distribution of the CFD–PBM model prediction, which is compared with the experimental data at gas superficial velocities of 36 and 50 m/s and a constant liquid superficial velocity of 0.041 m/s. The model of coupled CFD–PBM is able to predict the drop size distribution reasonably well, based on the coalescence and breakage models.

The present model provides fairly reasonable droplet size distribution (DSD) and also close agreement with the experimental diameter between 1 and 10 μm. After that the droplet size distribution trend started to deviate from the experimental result at a diameter greater than 10 μm. However, the model performs well at small droplet diameters and exhibits a sharp peak around the 100 μm region compared with the experimental data. This means that the predicted breakup and the coalescence effects are underestimated for droplets bigger than 10 μm. The original Luo and Svendsen model can only give good predictions for small sized droplets. It is not clear if it is the effect of the coalescence kernel, breakup kernel, or their limitations. A possible explanation is that the existent of coalescence and breakup mechanisms are mostly designed for gas bubble phase in the bubble column and they are accurate under certain working conditions. Luo and Svendsen's model cannot accurately capture the liquid droplet size distribution in annular flow. Thus, future work is needed for more

accurate coalescence and breakup kernels developed specifically for liquid droplets in gas-liquid annular flow.

However, there are few possibilities to improve the model of Luo and Svendsen. For example, only binary breakup is assumed in the model that is suitable in the case for gas bubbles, but not in situations where more than two daughter droplets are formed. In consideration of this fact, the model still gave a good result which can be used to study the droplet size distribution and prediction of pressure drop and liquid holdup parameters in pipes with a 0.078 m diameter and 7 m length.

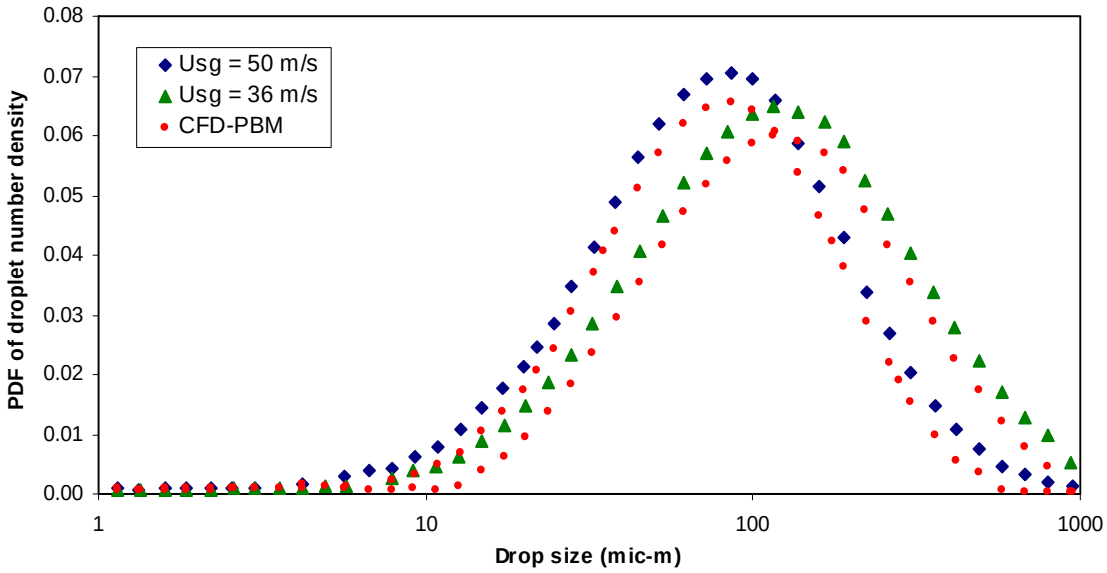

Figure 6.2: Droplet size distributions through the pipe at liquid superficial velocity of 0.041m/s.

6.7.2 Effect of Gas Superficial Velocity

6.7.2.1 Droplet Size Distribution (DSD)

Figure (6.3) shows the probability density function (PDF) result for droplet number density for the present CFD–PBM coupled model in a horizontal pipe with 0.078 m diameter. The simulated droplet size distribution is plotted at a constant aggregation and using the aggregation kernel of the turbulent model, where there are constant gas and liquid velocities of 15 and 0.7 m/s, respectively.

It can be noted that there is a peak in the droplet diameter size, which represents a balance point between the coalescence and breakup processes. From the perspective of a liquid droplet, the coalescence is a negative effect for its diameter while the breakup process is a positive one, and the turbulent effect is the driving force for the two mechanisms. Different particle size distribution (PSD) has been observed at each scenario, and differences in the peak of droplet diameter at constant aggregation and using the aggregation kernel (turbulent model) are around 80 μm and 100 μm, respectively. Also the PDF of the droplet size was higher than in the case of using constant aggregation. This means that this scenario does not describe the droplet size distribution accurately.

Figure (6.4) demonstrates the droplet size distribution at various superficial gas velocities and a constant superficial liquid velocity of 0.7 m/s. It can be seen that there is no obvious increase in the small droplet size distribution as the gas superficial velocity is increased. This shift can be considered less important at medium and high gas superficial velocity. It can also be noted that there is a clear increase in the importance of large droplet sizes as the gas superficial velocity increased. The increase of gas velocity from 20 to 25 m/s does not show any change in the DSD of the large size (roughly around 900 μm). The CFD–PBM model exhibits the peak of around 100 μm at a low gas superficial velocity of 15 m/s, which means this drop diameter is the predominant one in the system.

Two other peaks of drop size at a gas superficial velocity of 20 and 25m/s were expected to present smaller droplet diameter as more turbulence was generated due to higher velocity, but the corresponding droplet size was quite similar and very close to each other around 300 μm. This drop size represents the predominant droplet diameter for both gas velocities of 20 and 25m/s. This means the increase of gas superficial velocity does not have much influence on the breakage and coalescence mechanism which presents the same predominant droplet size. This could possibly be due to the gas velocity not increasing enough. If it is increased further a different PDF shape with a different peak may be seen.

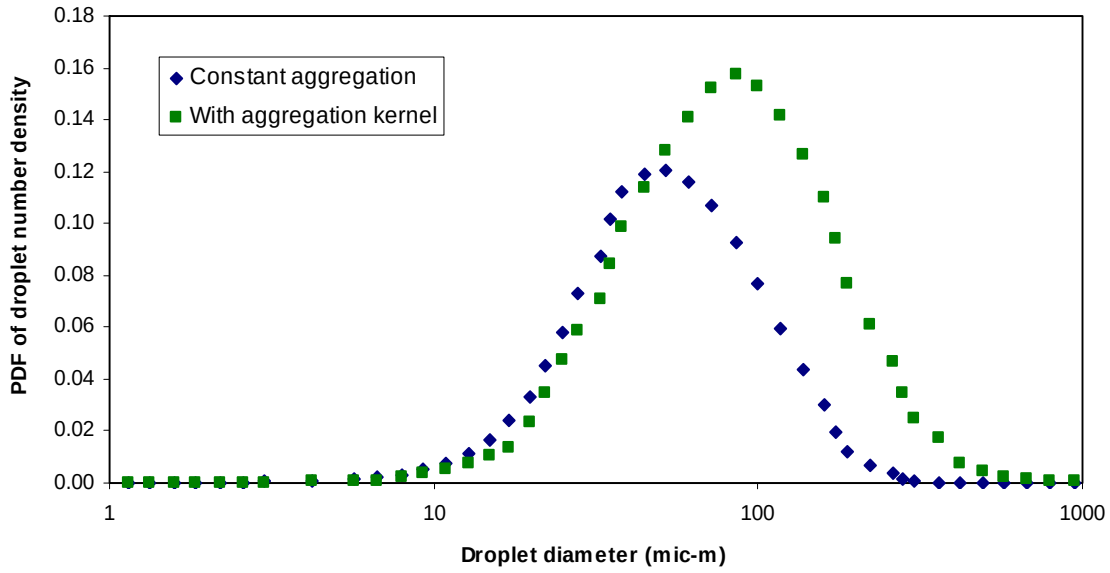

Figure 6.3: Droplet size distributions through the pipe size of 0.078m diameter at liquid and gas superficial velocities of 0.07 and 15m/s.

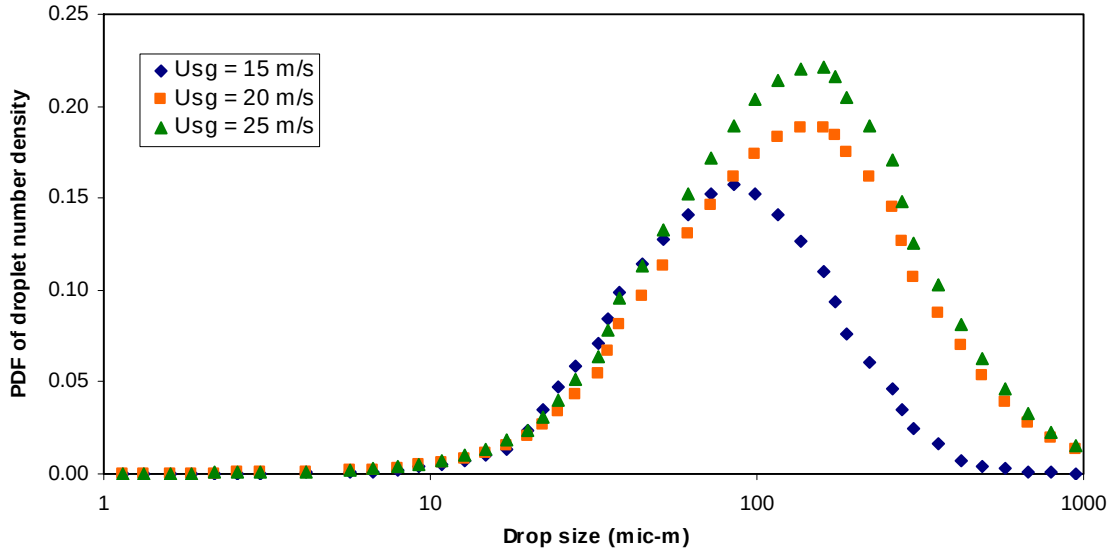

Figure 6.4: Droplet size distributions through the pipe size of 0.078m diameter at liquid superficial velocity of 0.07m/s.

6.7.2.2 Pressure Drop and Liquid Holdup

In contrast with the previous model presented in Chapter 5 of k–ε model of constant drop size for two–phase flow, in this Chapter the k–ε single drop size model is Labelled CFD without PBM to be compared with CFD with PBM. The obtained pressure drop result of two–phase air–water flow was higher in the case of the CFD–PBM model at a low gas mass flux of 12.5 kg/m^{2}s (corresponding to 10 m/s) and at a constant input water fraction of 0.08 as shown in Figure (6.5). Therefore, the result of CFD without PBM pressure drop is deviated from the correlation compared to the CFD with PBM pressure drop result, which exhibits comparatively less deviation at a low gas mass flux of 12.5 kg/m^{2}s.

At medium and high gas mass flux of between 18–25 kg/m^{2}s (corresponding to 15–20m/s), the prediction of pressure drop increased when compared to CFD without PBM, and became closer to the correlation prediction. At a high gas superficial velocity of 25m/s (around 32 kg/m^{2}s), the CFD with PBM model pressure drop prediction is quite similar to the CFD without PBM.

This gives an indication that the predominant droplet diameter into the system is around 100 μm due to the predicted pressure drop value from both models being almost comparable. Moreover, as concluded from Figure (6.4) the predominant droplet size was increased as the gas velocity increased, therefore, the result of the CFD–PBM model pressure drop at high gas velocity is under predicted. Thus the current result of pressure drop demonstrates a closer agreement with the correlation data, particularly at low and medium gas mass fluxes/or superficial velocities for the CFD with PBM model, where the result showed less deviation compared with the correlation, although it was slightly higher at CFD without BPM.

The obtained CFD data from the two–phase liquid holdup was plotted against the gas mass flux, which is treated as a parameter with a constant input water fraction of 0.08 as shown in Figure (6.6). In this figure, it can be observed that the two–phase flow liquid holdup of the CFD with BPM model has a higher liquid holdup prediction in comparison with the CFD without PBM model, and the Mukherjee and Brill

correlation at a low gas mass flux of 12.25 kg/m^{2}s or gas superficial velocity of 10 m/s. At a low gas mass flux we would expect a high amount of liquid holdup, due to the low turbulence that is generated as a result of low gas phase velocity.

In this situation, the droplets progress to settle down even for small droplet diameters, but the large droplets require high drag force to push them toward the pipe outlet. This result might be expected and considered as over prediction at this flow condition; however the empirical correlation analysis is not able to account for drop size variation.

At the medium gas mass flux between 18–25 kg/m^{2}s (corresponding to 15–20 m/s), the two–phase liquid holdup is fluctuating around the empirical correlation result. Sometimes the predicted liquid holdup of the CFD–PBM model is under and over prediction, but the predicted liquid holdup data is much closer and less deviated from the correlation result compared with k–ε of single drop size model. At a higher gas mass flux above 25 to 30 kg/m^{2}s (corresponding to 20–25 m/s), the CFD–PBM model predictions agree fully with the results of the Mukherjee and Brill correlation when compared to the Eulerian–Eulerian model of single droplet diameter.

At high gas velocity we would expect high turbulence and large drag force to be generated, and this could have a significant influence on the large droplet diameters. In general, the CFD–PBM model provides close agreement with the empirical correlation at medium and high gas velocities.

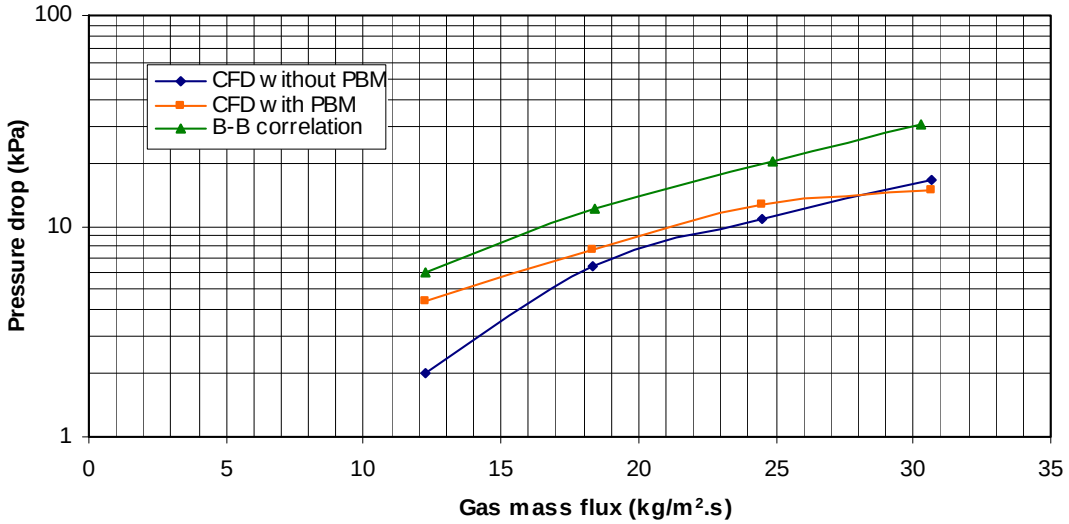

Figure 6.5: Comparison of predicted pressure drop with and without PBM against empirical correlation.

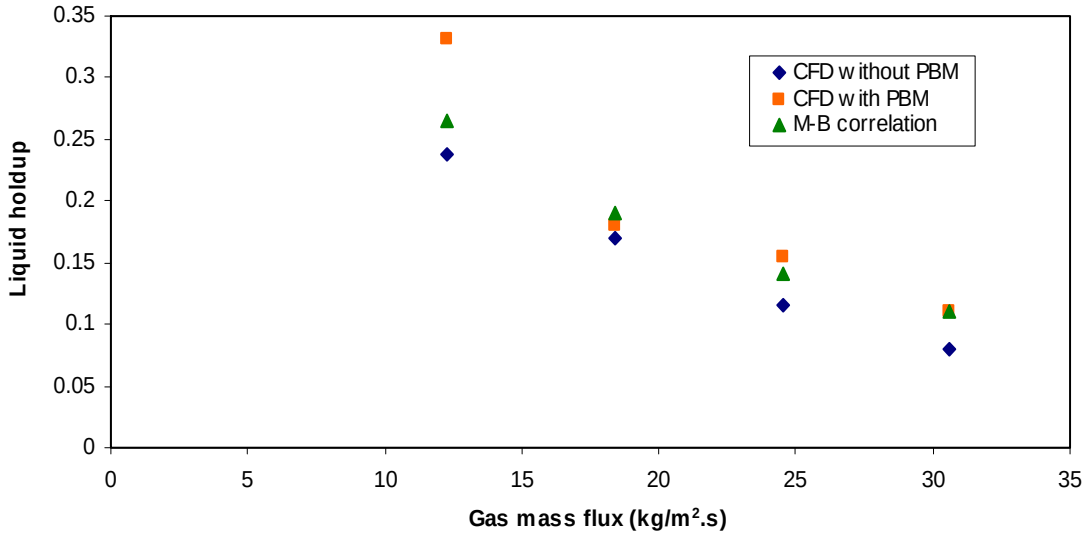

Figure 6.6: Comparison of predicted liquid holdup with and without PBM against empirical correlation.

6.7.3 Effect of Water Superficial Velocity

6.7.3.1 Droplet Size Distribution

Figure (6.7) shows the droplet size distribution data as a function of water superficial velocity and at a constant superficial gas velocity of 15 m/s. It can be seen that there is an obvious increase in the significance of small droplets as the superficial water velocity or flow rate is increased. At the inlet water superficial velocity of 0.7 m/s, the PDF of small droplets (less than 50 μm) is not changed where the shift of PDF of small droplets can be seen clearly at a higher rate of water superficial velocity of 1 m/s. Therefore the increase of water superficial velocity has a positive impact on the small droplets number density compared to gas superficial velocity that had minimal influence.

It can be seen that there is a peak across to the diameter size that describes the balance point between the coalescence and breakage mechanisms. It can be noted that the peak of the PDF of droplets increased with respect to water superficial velocity in which the droplet diameter corresponding to the first peak of 0.3 m/s water superficial velocity is around 110 μm, the droplet diameter corresponding to the second peak is around 90 μm, and the third peak is around 80 μm. However, it can be seen that as the water superficial velocity increase leads to a decrease in the droplet diameter, and this corresponds to the peak. Furthermore, the existence of large droplet diameters (larger than 500 μm) decreased as the water superficial velocity increased where it seems the droplet coalescence and breakage processes are controlled by turbulent force.

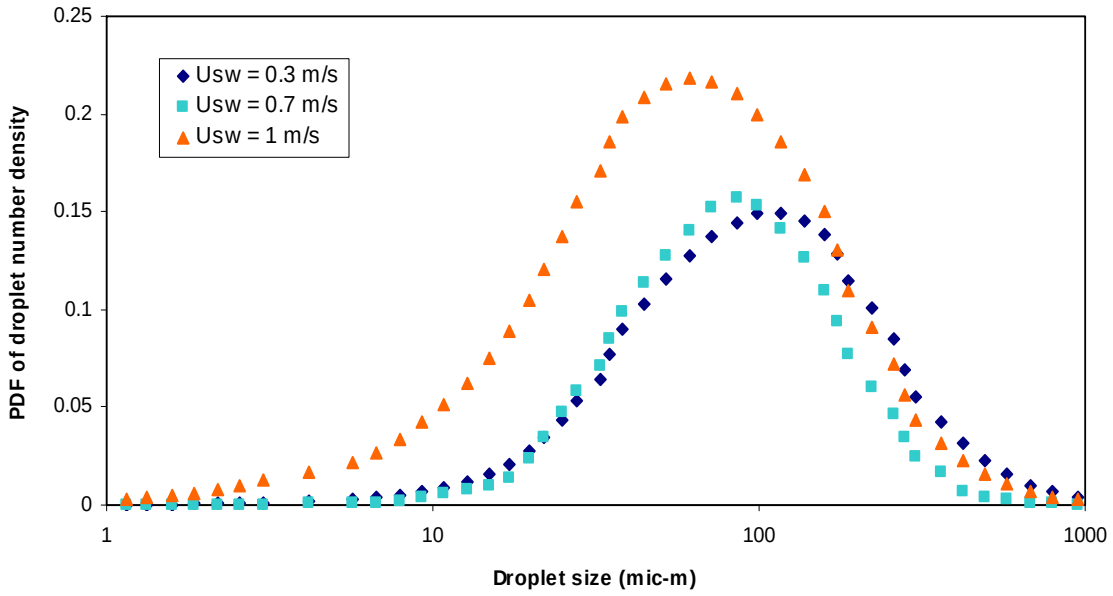

Figure 6.7: Droplet size distributions through the pipe size of 0.078m diameter at gas superficial velocity of 15m/s.

6.7.3.2 Pressure Drop and Liquid Holdup

The effect of water mass flux/or superficial velocity on the two–phase pressure drop and liquid holdup has been investigated at a constant gas mass flux and input water fraction of 24.5 kg/m^{2}s (20 m/s) and 0.08, respectively. Various CFD simulations were performed at different water mass fluxes that were ranged from 500–2000 kg/m^{2}s corresponding to a water superficial velocity of 0.5–2 m/s. The CFD data of two–phase pressure drop of air–water flow from different simulations are plotted in Figure (6.8).

At low water mass flux of around 500 kg/m^{2}s, the pressure drop of the CFD–PBM model is under predicted when compared to the k–ε constant drop size model, as well as the Beggs and Brill (1973) developed correlation. On the other hand, the Eulerian–Eulerian single fixed drop size model shows some agreement and follows closely the pressure drop of two–phase data from the empirical correlation.

At a medium water mass flux of 1000 kg/m^{2}s, the predicted CFD two–phase pressure drop data of both models with and without PBM are under predicted, compared to the empirical correlation in which the deviation of the CFD without PBM model is much less than the CFD with PBM approach.

Both model predictions at low and medium water mass fluxes have similar trends, in which the two–phase pressure drop is proportional to the water mass flux. At higher water mass flux above 1500 kg/m^{2}s, an interesting observation for two–phase pressure drop of CFD with PBM model that is totally deviated from the correlation and rapidly increased. This increase was significant in comparison with the fixed drop size model, which exhibits a similar trend to that of the developed correlation of Beggs and Brill (1973), with a tendency of over prediction compared to the correlation. Moreover, the CFD without PBM model predicted results are much better with less deviation from the correlation data as shown in Figure (6.8).

In general, the predicted two–phase pressure drop using two CFD models increases as water mass flux increases, except at high water mass flux where the CFD–PBM model is over predicted. This reflects the limitation of the two–phase flow empirical correlations, which do not take into account the drop size. Again it is important for the CFD two-phase flows in pipelines to be treated with concern, in particular when using gas–liquid drag and other forces that could be included. It might also be conducted as an experimental work in the same pipe size for a better understanding of the two–phase pressure drop and liquid holdup behaviour.

The other quantity examined with increasing water mass flux is the two–phase liquid holdup as shown in Figure (6.9). At the inlet water mass flux of 500 kg/m^{2}s, the data of k–ε with the population balance model are more close to and show less deviation from the correlation, rather than the k–ε model with a constant drop size. At a medium of water mass flux of 1000 kg/m^{2}s, the predictions of the CFD liquid holdup data of the two models are observed to be in close agreement with the correlation, and both strongly follow the same trend with a slight deviation.

At a higher water mass flux above 1500 kg/m^{2}s, the predicted CFD liquid holdup data of k–ε with the population balance model is over predicted and closely follows the same correlation trend in contrast with k–ε model with a constant drop size, which displays closer agreement with the correlation at mass flux of 1500 kg/m^{2}s, and which begins to deviate as the water mass flux increased. This situation is expected since the k–ε with the population balance model involves different drop sizes ranging from 10–1000 μm, in which the bigger size is expected to deposit quickly due to gravitational force, and the smallest size (such as 10 μm) would remain in the system longer due to the flow turbulence, as mentioned in Chapters 4 and 5.

The conclusion is that the two–phase liquid holdup prediction using the CFD of k–ε model with a constant drop size and k–ε with the population balance model increases as the water mass flux increases, and is closely predicted at medium water mass flux compared with low water mass flux which was under predicted. At high mass flux the liquid holdup of k–ε with the population balance model shows less deviation from the empirical correlation and increases as the mass flux of water increases.

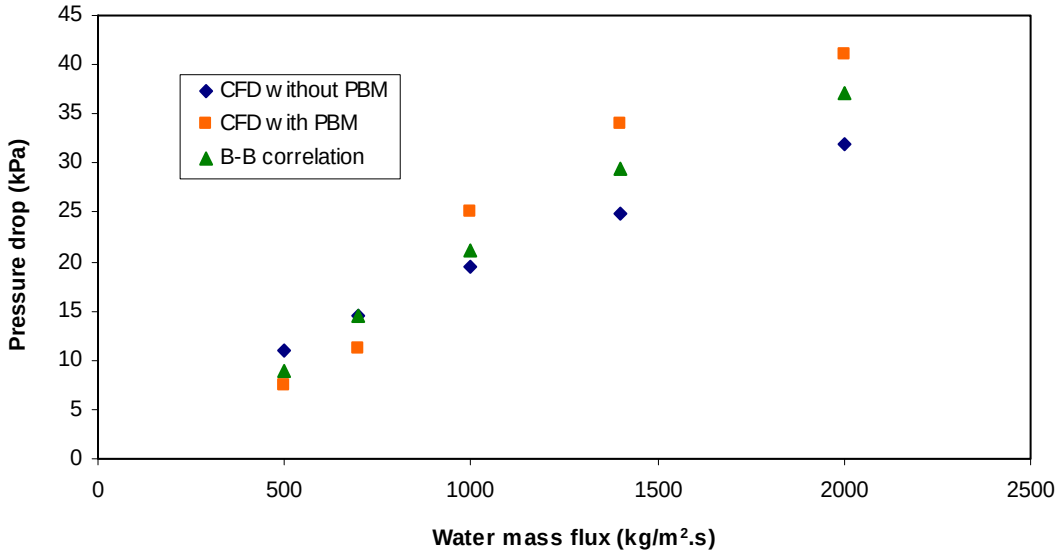

Figure 6.8: Comparison of predicted pressure drop with and without PBM against empirical correlation.

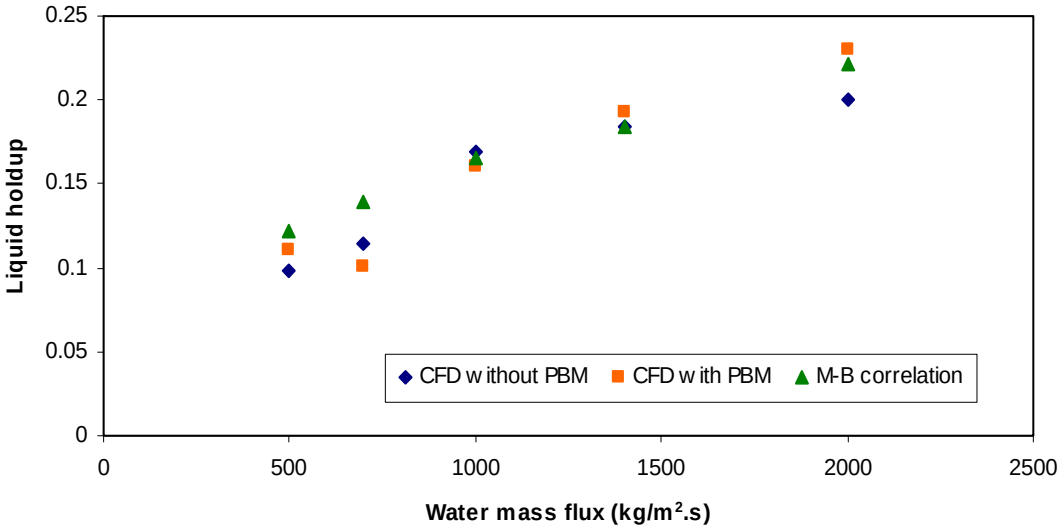

Figure 6.9: Comparison of predicted liquid holdup with and without PBM against empirical correlation.

6.8 Conclusions

In this Chapter, a CFD–PBM coupled model in the framework of ANSYS FLUENT 12.1 was intended to investigate the droplet's size distribution in a gas–liquid air–water annular flow system. Two phases are modeled by the Eulerian–Eulerian method and the turbulence is accounted for by a renormalization group k–ε model. For the solution of PBE, the Quadrature Method of Moments is used and particular coalescence and breakup kernels were utilized to demonstrate the droplet size distribution behaviour. The flow variables, such as gas and liquid superficial velocities are employed to examine the k–ε with population balance model for predicting the two–phase pressure drop and liquid holdup.

The results of using k–ε with the population balance model illustrate that the numerical prediction of droplet size distribution in annular flow using traditional coalescence and breakup kernels is possible. The results suggest that using the turbulent model and the Luo and Svendsen model for the aggregation and breakage kernel shows reasonable performance compared with the Simmons and Henratty (2001) experimental data covering all diameter ranges in the present investigation. The CFD–PBM model shows good predictions for small sized droplets. It is clear that the use of two models of the coalescence and breakage kernels leads to presentation of a reasonable result. Luo and Svendsen's model and turbulent model could not precisely capture the liquid droplet size distribution in annular flow. Therefore, further work is required for more accurate coalescence and breakup kernels developed specifically for liquid droplets in gas–liquid annular flow.

A comparison of computational data of k–ε model of constant droplet size and the CFD–PBM approach for the prediction of two–phase pressure drop and liquid holdup has been made. Also the computational data were compared with an empirical correlation reported in the literature. The pipe simulations were performed with a different mass flux of two–phase and constant input volume fraction of dispersed phase. The CFD–PBM model shows that the two–phase pressure drop and liquid holdup as well increase as the superficial velocity of air and water increase. Moreover, the gas and liquid mass flux had significant influence on the pressure drop,

and led to a rapid increase. In comparison with the single drop size model, the pressure drop data were lower than the CFD–PBM approach. The liquid holdup was also increased but at high mass flux rather than at low mass flux.

It can be concluded that this study showed that the introduced CFD–PBM model can lead to a reasonable prediction for two–phase pressure drop and liquid holdup compared to the k–ε model with a constant drop size, and gives a better understanding for the two–phase flow pressure drop and liquid holdup behaviour. However, in order to obtain more reliable CFD simulation data relating to droplet size distribution, pressure drop and liquid holdup of two–phase flow, an experimental work using the same pipe size dimensions to validate the data more accurately, rather than using an empirical correlation which provides a reasonable indication to the system parameters, is required.

6.9 Bibliography

Abrahamson, J. (1975). Collision Rates of Small Particles in a Vigourously Turbulent Fluid. *Chemical Engineering Science*, 30, 1371-1379.

Alopaeus, V., J. Koskinen and K. I. Keskinen (2002). Simulation of the population balances for liquid-liquid systems in a nonideal stirred tank. Part 2 Parameter fitting and the use of the multiblock model for dense dispersions. *Chemical Engineering Science*, 57, 1815-1825.

Andersson, R. and B. Andersson (2006a). Modeling the breakup of fluid particles in turbulent flows. *AIChE Journal*, 52 (6), 2031-2038.

Andersson, R. and B. Andersson (2006b). On the breakup of fluid particles in turbulent flows. *AIChE Journal*, 52 (6), 2020-2030.

Azzopardi, B. J. (1997). Drops in annular two–phase flow. *International Journal of Multiphase Flow*, 23, 1-53.

Bahmanyar, H. and M. J. Slater (1991). Studies of drop-break-up in liquid-liquid systems in a rotating disc contactor part I: conditions of no mass transfer. *Chemical Engineering Technology*, 14, 79-89.

Barrett, J. C. and N. A. Webb (1998). A comparison of some approximate methods for solving the aerosol general dynamic equation. *Journal of Aerosol Science*, 29, 31-39.

Batterham, R. J., J. S. Hall and G. Barton (1981). Pelletizing kinetics and simulation of full-scale balling circuits. In: *3rd International Symposium on Agglomeration*, Nürnberg, Germany, 136 (A).

Chatzi, E. and J. L. Lee (1987). Analysis of interaction for liquid-liquid dispersion in agitated vessels. *Industrial & Engineering Chemistry Research*, 26, 2263-2267.

Chesters, A. K. (1991). The modelling of coalescence processes in fluid-liquid dispersions. A review of current understanding. Trans IChemE, 69 (A), 259-281.

Choudhury D. (1993). Introduction to the renormalization group method and turbulence modelling. Fluent Inc. Technical memorandum TM-107.

Christian D., M. M. Attarakih and H. -J. Bart (2009). Coupling of CFD with DPBM for an RDC extractor. *Chemical Engineering Science*, 64, 721-732.

Coulaloglou, C. A. and L. L. Tavlarides (1977). Description of interaction processes in agitated liquid-liquid dispersions. *Chemical Engineering Science*, 32, 1289-1297.

Diemer, R. B. and J. H. Olson (2002). A moment methodology for coagulation and breakage problems: Part 3- generalized daughter distribution functions. *Chemical Engineering Science*, 57, 4187-4198.

Dorao, C. A., M. Fernandino, L. E. Patruno, P. M. Dupuy, H. A. Jakobsen and H. F. Svendsen (2009). Macroscopic description of droplet–film interaction for gas–liquid systems. *Applied Mathematical Modelling Journal*, 33 (8), 3309-3318.

Eastwood, C. D., L. Armi and J. C. Lasheras (2004). The breakup of immiscible fluids in turbulent flows. *Journal of Fluid Mechanics* 502, 309-333.

Eiswirth, R. T. and H. -J. Bart (2008). Experimental investigation of droplet-droplet coalescence in liquid-liquid systems. Proceeding International Solvent Extraction Conference ISEC 2008, Moyer, B. (Edition), *Canadian Institute of Mining, Metallurgy and Petroleum*, Montreal, 2, 1177-1182.

Ekambara, K., R. S. Sanders, K. Nandakumar and J. H. Masliyah (2008). CFD simulation of bubbly two–phase flow in horizontal pipes. *Chemical Engineering Journal*, 144, 277-288.

Fan, R., D. L. Marchisio and R. O. Fox (2004). Application of the direct quadrature method of moments to polydisperse gas-solid fluidized beds. *Journal of Aerosol Science* 139, 7-20.

Fore, L. B. and A. E. Dukler (1995). Distribution of drop size and velocity in gas–liquid annular flow. *International Journal of Multiphase Flow*, 21 (2), 137-149.

Hagesaether, L. (2002). Coalescence and break-up of drops and bubbles. *PhD thesis*, Norwegian University of Science and Technology, Trondheim, Norway.

Henschke, M., L. H. Schlieper and A. Pfennig (2002). Determination of coalescence parameter from batch-settling experiments. *Chemical Engineering Journal*, 85 (2), 369-378.

Higashitani, K., K. Yamauchi, Y. Matsuno and G. Hosokawa (1983). Turbulent coagulation of particles dispersed in a viscous fluid. *Chemical Engineering Journal Japan*, 16 (4), 299-304.

Hounslow, M. J., R. L. Ryall and V. R. Marshall (1988). A discretized population balance for nucleation, growth and aggregation. *AIChE Journal*, 34 (11), 1821-1832.

Hounslow, M. J., R. L. Ryall and V. R. Marshall (1988). A discretized population balance for nucleation, growth, and aggregation. *AIChE Journal*, 34 (11), 1821-1832.

Ishii, M. and T. C. Chawla (1979). Local drag laws in dispersed two-phase flow, NUREG/CR-1230, ANL-79-105.

Jakobsen, H. A., H. Lindborg and C. A. Dorao (2005). Modeling of bubble column reactors: progress and limitations. *Industrial and Chemical Engineering Research*, 44 (14), 5107-5151.

Kumar, S. and D. Ramkrishna (1996a). On the solution of population balance equations by discretization-i. a fixed pivot technique. *Chemical Engineering Science* 51 (8), 1311–1332.

Kumar, S. and D. Ramkrishna (1996b). On the solution of population balance equations by discretization-ii. a moving pivot technique. *Chemical Engineering Science* 51(8), 1333–1342.

Lasheras, J. C., C. Eastwood, C. Martínez-Bazán and J. L. Montañés (2002). A review of statistical models for the break-up of an immiscible fluid immersed into a fully developed turbulent flow. *International Journal of Multiphase Flow*, 28, 247-278.

Lehr, F., M. Millies and D. Mewes (2002). Bubble-size distributions and flow fields in bubble columns. *AIChE Journal*, 48, 2426-2442.

Li, C., G. H. Yeoh, S. C. P. Cheung and J. Y. Tu (2010). On modelling horizontal gas–liquid flow using population balance approach, *17th Australian Fluid Mechanics Conference*, Auckland, 5-9 December.

Lister, J. D., D. J. Smith and M. J. Hounslow (1995). Adjustable discretized population balance for growth and aggregation. *AIChE Journal*, 41(3), 591-603.

Litster, J. D., D. J. Smit and M. J. Hounslow (1995). Adjustable discretization population balance for growth and aggregation. *AIChE Journal*, 41 (3), 591-603.

Lopes, J. C. B. and A. E. Dukler (1985). Droplet sizes dynamics and deposition in vertical annular flow. US Nuclear Regulatory Commission, Washington DC, USA, Report NUREG/CR-4424.

Luo, H. (1993). Coalescence, breakup and liquid circulation in bubble column reactors. *PhD thesis*, University of Trondheim, Norway.

Luo, H. and H. F. Svendsen (1996). Theoretical model for drop and bubble breakup in turbulent dispersions. *AIChE Journal*, 42, 1225-1233.

Maaß, S., A. Gäbler, A. Zaccone, A. R. Paschedag and M. Kraume (2007). Experimental investigations and modelling of breakage phenomena in stirred liquid/liquid systems. *Chemical Engineering Research and Design*, 85, 703-709.

Maaß, S., S. Wollny, R. Sperling and M. Kraume (2009). Numerical and experimental analysis of particle strain and breakage in turbulent dispersions. *Chemical Engineering Research and Design*, 87, 565-572.

Marchisio, D. L. and R. O. Fox (2005). Solution of population balance equations using the direct quadrature method of moments. *Journal of Aerosol Science* 36(1), 43-73.

Marchisio, D. L., J. T. Pikturna, R. O. Fox and R. D. Vigil (2003a). Quadrature method of moments for population balance equations. *AIChE Journal*, 49(5), 1266-1276.

Marchisio, D. L., R. D. Vigil and R. O. Fox (2003b). Quadrature method of moments for aggregation-breakage processes. *Journal of Colloid and Interface Science*, 258, 322-334.

Marchisio, D. L., R. O. Fox and R. D. Vigil (2003c). Implementation of the quadrature method of moments in CFD codes for aggregation-breakage problems. *Chemical Engineering Science*, 58, 3337-33351.

Martínez-Bazán, C., J. L. Montañés and J. C. Lasheras (1999a). On the breakup of an air bubble injected into a fully developed turbulent flow. Part 1. breakup frequency. *Journal of Fluid Mechanics*, 401, 157-182.

McCoy, B. J. and G. Madras (2003). Analytical solution for a population balance equation with aggregation and fragmentation. *Chemical Engineering Science*, 58, 3049-3051.

McGraw, R. (1997). Description of aerosol dynamics by the quadrature method of moments. *Aerosol Science and Technology*, 27, 255-265.

McGraw, R. and D. L. Wright (2003). Chemically resolved aerosol dynamics for internal mixtures by the quadrature method of moments. *Journal of Aerosol Science*, 34, 189-209.

Prince, M. J. and H. W. Blanch (1990). Bubble coalescence and break-up in air-sparged bubble columns. *AIChE Journal*, 36, 1485-1499.

Ramkrishna, D. (2000). Population balances. Academic Press. San Diego.

Randolph, A. D. and M. A. Larson (1971). Theory of Particulate Processes: Analysis and Techniques of Continuous Crystallization. Academic Press, San Diego, CA.

Saffman, P. G. and J. S. Turner (1956). On the collision of droplets in turbulent clouds. *Journal of Fluid Mechanics*, 1, 16-30.

Schmidt, S. A. (2006). Populations dynamische Simulation gerührter Extraktionskolonnen auf der Basis von Einzeltropfen-und Tropfenschwarmuntersuchungen. *Dr.-Ing. Thesis*, Shaker Verlag, Aachen.

Scott, W. T. (1968). Analytic studies of cloud droplet coalescence i. *Journal of the Atmospheric Science*, 25, 54-65.

Semiat, R. and A. E. Dukler (1981). Simultaneous measurement of size and velocity of bubbles and drops: a new optical technique. *American Institute of Chemical Engineering Journal*, 27, 148-159.

Simmons, M. J. H. and T. J. Hanratty (2001). Droplet size measurements in horizontal annular gas–liquid flow. *International Journal of Multiphase Flow,* 27(5), 861-883.

Simon, M. (2004). Koaleszenz von Tropfen und Tropfenschwärmen. *Dr.-Ing. Thesis*, TU Kaiserslautern, Kaiserslautern.

Simon, M. and H. -J. Bart (2002). Experimental studies of coalescence in liquid-liquid systems. *Chemical Engineering Technology*, 25, 481-484.

Smith, M. (1998b). Constant-number monte carlo simulation of population balances. *Chemical Engineering Science*, 53(9), 1777-1786.

Sovova, H. (1981). Breakage and coalescence of drops in a batch stirred vessel–II. Comparison of model and experiments. *Chemical Engineering Science*, 36, 1567-1573.

Tatterson, D. F., J. C. Dallman and T. J. Hanratty (1977). Drop sizes in annular gas–liquid flow. *AIChE Journal*, 23, 68-76.

Tobin, T. and D. Ramkrishna (1999). Modeling the effect of drop charge in turbulent liquid-liquid dispersions. *Canadian Journal of Chemical Engineering*, 77, 1090-1104.

Tsouris, C. and L. L. Tavlarides (1994). Breakage and coalescence models for drops in turbulent dispersions. *AIChE Journal*, 40, 395-406.

Valentas, K.J. and N. R. Amundson (1966). Breakage and coalescence in dispersed phase systems. *Industrial & Engineering Chemistry Fundamentals*, 5, 533-542.

Valentas, K.J., O. Bilous and N. R. Amundson (1966). Analysis of breakage in dispersed phase systems. *Industrial & Engineering Chemistry Fundamentals*, 5, 271-279.

Vankova, N., S. Tcholakova, N. D. Denkov, V. D. Vulchev and T. Danner (2007). Emulsifiaction in turbulent flow 2. Breakage rate constants. *Journal of Colloid and Interface Science*, 313, 612-629.

Vanni, M. (2000). Approximate population balance equations for aggregation breakage processes. *Journal of Colloid and Interface Science*, 221, 143–160.

Wang, T., J. Wang and Y. Jin (2003). A novel theoretical breakup kernel function for bubbles/droplets in a turbulent flow. *Chemical Engineering Science*, 58, 4629-4637.

Wicks, M. and A. E. Dukler (1966). In-situ measurements of drop size distribution in two–phase flow: a new method for electrically conducting liquids. *3rd International Heat Transfer Conference*, Chicago.

Wright, D. L., R. McGraw and D. E. Rosner (2002). Bivariate extension of the quadrature method of moments for modeling simultaneous coagulation and sintering of particle populations. *Journal of Colloid and Interface Science*, 236, 242-251.

Chapter 7

Conclusions and Future Work

7.1 Summary and Conclusions

A comprehensive review of the literature revealed the obvious importance of gas–liquid flows in several industrial processes. However very few attempts to focus on using CFD to model the hydrodynamics and accurately predict fundamental multiphase characteristics such as the dispersed phase distribution, two–phase pressure drop and liquid holdup were found.

A review of the existence of two–phase flow maps in different inclination angles, and empirical correlations for two–phase pressure drop and liquid holdup prediction was also carried out. Production from oil and gas reservoirs is shifting into deeper waters which will be more challenging due to high pressure and low temperature conditions. With these conditions many problems may be encountered when transporting the hydrocarbon in flowlines to onshore facilities. During the shutdown operation there is a high risk of water accumulation in the low sections where, at the restart operation gas contracts and displaces the water, creating droplets as a result of disturbing the liquid film. Understanding the hydrodynamics of droplets in a gas is of engineering importance.

A few CFD studies investigated the two–phase pressure drop and liquid holdup in horizontal pipes. In particular, general closure for turbulent gas–liquid dispersions were not developed. The present work attempts to fill this gap by implementing a new drag coefficient in a commercial CFD code for better prediction of pressure drop and liquid holdup.

In this work, numerical investigation and modelling of the two–phase gas–liquid flow in bend and horizontal pipelines have been conducted. Two CFD approaches, which are the Volume of Fluid (VOF) and the Eulerian–Eulerian, have been employed for

this study. The VOF approach is used to study the droplet hydrodynamic and predict the flow pattern in bend pipes at different restart gas velocities using different patched liquids (i.e. water and oil). The k–ε two–fluid Eulerian model has been developed for predicting the pressure drop and liquid holdup of two–phase gas–liquid co current flow in horizontal conduits.

The primary objective of developing this model was to predict the two–phase pressure drop and liquid holdup, and also to study the behaviour of these parameters under specific operating conditions. Last but not least, the CFD–PBM model is introduced to study the physical processes of coalescence and breakup in two–phase flows. The evaluation of the model was performed by comparing experimental data obtained from the open literature and empirical correlations. A summary of the most important conclusions drawn from each chapter of this thesis is given in the next section.

7.1.1 Numerical Simulation of Two–phase Flow in Bend Pipelines

In Chapter 4, the applicability of interface tracking CFD modeling of two–phase flow in a bend pipeline was investigated using the VOF technique. The investigation is proposed to give some information about the droplet hydrodynamic and the flow behaviour in bend pipelines to find out the risk of hydrate formation. All simulations were performed under atmospheric pressure and room temperature for air–water and air–oil two–phase flows, with different restart gas superficial velocities and stagnant liquid levels.

The results obtained of the flow pattern observation are validated against the two–phase flow map of Baker (1954). The predicted results from the VOF approach appeared to provide reasonable agreement with the Baker chart. Moreover, the liquid fluid properties such as viscosity and density played a major role in the liquid displacement where the remaining liquid in the low section decreased as the restart gas superficial velocity increased. In general, the low restart of gas superficial velocity showed less risk of hydrate formation when compared to a high gas superficial velocity which generates annular or dispersed flow, and is considered to be

at high risk of hydrate formation. The low section depth also affected the flow pattern generation even at low restart gas velocity.

A flow map was developed based on the achieved result; it described the high and low risk regions of flow pattern based on the patched liquid in the low section and restart gas velocity. The three–dimensional VOF simulations can give more accurate observations to the flow pattern when compared to a two–dimensional simulation.

7.1.2 Development of E–E Model for Two–phase Flow in Horizontal Pipeline

In Chapter 5, the E–E two–fluid model has been developed for prediction of pressure drop and liquid holdup for two–phase gas–liquid flow with the existence of a small amount of liquid (typically around 1%). Different k–ε models, which are available in ANSYS FLUENT 12.1, such as standard k–ε, renormalization group k–ε, and realizable k–ε, were employed to predict the pressure drop and liquid holdup of two–phase flow in horizontal pipes, using constant droplet diameter (100 μm).

The RNG k–ε model provided a close agreement with the experimental data of Badie *et al*. (2000) by implementing a new drag coefficient, which was developed experimentally by Ishii and Chawla (1979). The developed CFD model also showed closer agreement when compared to the Hart *et al*. (1989) and Chen *et al*. (1997) models through a wide range of gas and water superficial velocities, specifically at low and medium velocities whereas at high gas velocity some deviation was shown.

The developed CFD model of constant droplet size was used to study the pressure drop and liquid holdup at various factors such as gas and water mass flux, and initial liquid holdup. The two–phase pressure drop increased as these factors also increased, while the liquid holdup decreased with respect to gas mass flux and increased with the water mass flux. It was also found that the pressure drop and liquid holdup of air–water flow is much higher than air–oil flow due to the difference in the properties of the two liquids.

7.1.3 Prediction of Droplet Size Distribution Using CFD–PBM Model

In Chapter 6, a CFD–PBM coupled model is introduced to account for the droplet size distribution in a gas–liquid annular flow system, and to investigate the pressure drop and liquid holdup. The QMOM model used in this thesis was derived in the research work of McGraw (1997) and is based on an alternative approach to the modeling of population balances.

The concept is to model the two–phase gas and liquid in the potentially more efficient Eulerian formulation in order to capture the full polydisperse nature of the two–phase flow. There are several breakup and coalescence models available in the FLUENT 12.1 for the population balance equation (PBE). The turbulent model and the Luo and Svendsen model for coalescence and breakage kernels were employed in this work.

The results obtained for the evolution of droplet sizes due to breakup and coalescence were predicted using the QMOM, which agreed with the experimental data of Simmons and Hanratty (2001). The CFD–PBM model demonstrated that the prediction of two–phase pressure drop and liquid holdup were improved when compared with k–ε model with constant drop size.

7.2 Recommendations for Future Work

In this section, the possibilities for advanced improvements to the droplet hydrodynamic study using the VOF model to predict pressure drop and liquid holdup and using the E–E k–ε model of constant droplet diameter and CFD–PBM model for two–phase flow in pipes and related challenges, are discussed.

7.2.1 Improvement to Droplet Hydrodynamic VOF model

- In order to validate the simulation result of the VOF model more accurately, it is necessary to conduct experimental work that takes into account the pipe sizes which are used in this work. This can provide more accurate results for the flow pattern, instead of using the flow map which is generated from a specific operating condition and pipe size.

- Chapter 4 focused on the risk of operating conditions and liquid patching that generate a specific flow pattern that possibly has a high risk of hydrate formation. It will be interesting to construct a new facility that will be able to form hydrates in order to know the regions in which the hydrate formation begins, and where they will essentially build up.

- All simulation experiments were performed for water and oil phase with restart gas fluid. The hydrate can also be formed in multiphase flow systems in an oil dominated system. To understand and find out the best operating parameter for hydrate formation in an oil/water mixture system with liquid restart, more liquid restart numerical experiments are needed in order to characterise the hydrodynamics of the droplet and the flow behaviour in a dense phase.

7.2.2 k–ε Model of Constant Droplet Size

- The main consideration that should be taken into account is inter–phase forces and turbulence modeling. For instance, drag force models are quite accurate only at certain conditions as seen with the Ishii and Chawla drag coefficient, but it does not give an accurate result at high superficial velocity. Therefore, switching among other drag coefficients that might provide good results at a high gas superficial velocity in order to minimize the deviation of pressure drop and liquid holdup data could be examined.

- Turbulence is still not a well understood physical problem and is complicated in multiphase flows. Future investigation should focus on the mechanisms of turbulence production and dissipation due to the interaction between the two phases. Also, the ability to accurately predict turbulence in the continuous phase should be tested.

- The use of other approaches to turbulence modeling for multi–phase, such as Direct Eddy Simulation, Reynolds Stress Model, and Large Eddy Simulation should also be assessed.

- Further validation of the proposed closure guidelines should be undertaken, preferably in two–phase flow in pipes. It might be necessary to include the effect of other interphase forces in addition to drag, lift and turbulent dispersion.

7.2.3 Improvements to CFD–PBM Model

- One of the biggest challenges in two–phase flow modeling is the accurate prediction of droplet size distribution. More emphasis should be given for modeling the physics of the breakup and coalescence mechanisms, which require assumptions about the daughter droplet distributions.

7.2.4 Recommendation on the Experimental Work

- Comprehensive experimental data on horizontal gas–liquid pipe flows are required in order to achieve accurate results. Particularly, experimental work should be conducted to obtain the two–phase flow map in bend pipes, as well as the droplet size distribution which would assist in developing better closure models for CFD. Such an experimental facility requires significant thought and resources, but will be invaluable to validate and refine the developed models.

7.3 Bibliography

Badie, S., C. P. Hale, C. J. Lawrence and G. F. Hewitt (2000). Pressure gradient and holdup in horizontal two-Phase gas-liquid flows with low liquid loading. *International Journal of Multiphase Flow*, 26, 1525-1543.

Baker, O. (1954). Design pipelines for simultaneous flow of oil and gas. *Oil and Gas Journal*, 53, 26.

Chen, X. T., X. D. Cai and J. P. Brill (1997). Gas–Liquid stratified-wavy flow in horizontal pipelines. *Journal of Energy Resources Technol*ogy, 119(4), 209-216.

Hart, J., P. J. Hamersma and J. M. H. Fortuin (1989). Correlations predicting frictional pressure drop and liquid holdup during horizontal gas-liquid pipe flow with a small liquid holdup. *International Journal of Multiphase Flow*, 15(5), 947-964.

Ishii M. and T. C. Chawla (1979). Local drag laws in dispersed two-phase flow, NUREG/CR-1230, ANL-79-105.

McGraw, R. (1997). Description of aerosol dynamics by the quadrature method of moments. *Aerosol Science and Technology*, 27, 255-265.

Simmons, M. J. H. and T. J. Hanratty (2001). Droplet size measurements in horizontal annular gas–liquid flow. *International Journal of Multiphase Flow,* 27(5), 861-883.